Multifractal intermittency of forced and free turbulence studied with the gyroscope cascade model

Xin Li

École des Ponts ParisTech

THÈSE DE DOCTORAT
de l'École des Ponts ParisTech

Multifractal intermittency of forced and free turbulence studied with the gyroscope cascade model

Intermittence multifractale de la turbulence forcée et libre étudiée avec le modèle de cascade de gyroscopes

École doctorale N° 531, Sciences, Ingénierie et Environnement (SIE)

Spécialité : Sciences et Techniques de l'Environnement

Thèse préparée au sein des laboratoires HM&Co et CEREA

Thèse soutenue le 21 Décembre 2022 , par
Xin LI

Composition du jury :

Klaus, FRAEDRICH Professeur Émérite, Max Planck Institute Hamburg	Rapporteur
Claude, CAMBON Directeur de Recherche Émérite, École Centrale de Lyon	Rapporteur
Ioulia, TCHIGUIRINSKAIA Directrice de Recherche, École des Ponts ParisTech	*Examinatrice*
Jisun, LEE Attachée de Recherche, Pukyong National University	*Examinatrice*
Daniel, SCHERTZER Professeur, École des Ponts ParisTech	*Directeur de thèse*
Yelva, ROUSTAN Chargé de Recherche, École des Ponts ParisTech	*Co-Directeur de thèse*

HM&Co HYDROLOGY METEOROLOGY and COMPLEXITY

cerea

INTERMITTENCE MULTIFRACTALE DE LA TURBULENCE FORCÉE ET LIBRE ÉTUDIÉE AVEC LE MODÈLE DE CASCADE DE GYROSCOPES

MULTIFRACTAL INTERMITTENCY OF FORCED AND FREE TURBULENCE STUDIED WITH THE GYROSCOPE CASCADE MODEL

By XIN LI,

A Thesis Submitted to the Sciences, Ingénierie et Environment in

Partial Fulfillment of the Requirements for

the Degree Sciences et Techniques de l'Environnement

Ecole des Ponts ParisTech
SCIENCES ET TECHNIQUES DE L'ENVIRONNEMENT (2022)
Champs sur Marne, Paris, France (Hydrology Meteorology et Complexity)

TITLE:	Multifractal intermittency of forced and free turbulence studied with the gyroscope cascade model
AUTHOR:	Xin LI Dr (Sciences et Techniques de l'Environnement), Ecole des Ponts ParisTech, France
DIRECTOR OF SUPERVISOR:	Daniel Schertzer
SUPERVISOR:	Yelva Roustan
NUMBER OF PAGES:	xxxvi, 231

Résumé

La turbulence est l'un des problèmes fondamentaux non résolus de la physique classique, en dépit de sa manifestation dans de nombreux domaines, y compris l'ingénierie, par exemple dans l'énergie éolienne. Ceci est lié à notre manque de connaissance des propriétés des équations déterministes 3D de Navier-Stokes (NS) aussi fondamentales que l'existence et l'unicité de ses solutions. Cela n'empêche pas les chercheurs et les ingénieurs de l'utiliser. À l'aide de méthodes statistiques, le mécanisme de la turbulence a été partiellement révélé, comme le processus de transfert d'énergie. Par exemple, des modèles de fermeture de la turbulence, tels que le modèle quasi-normal à amortissement turbulent markovianisé (EDQNM), ont été introduits pour tenir compte partiellement de la hiérarchie infinie des équations des moments statistiques générée par le terme non linéaire des équations de Navier-Stokes. Ils ont mis en évidence la possibilité d'une rétrodiffusion de l'énergie du pic du spectre énergétique vers les plus gros tourbillons et donc une modification de la loi de décroissance de l'énergie de la turbulence. Cependant, ces avancées ne prennent pas en compte la caractéristique fondamentale de la turbulence : l'intermittence, qui signifie que la turbulence est extrêmement hétérogène et conduit à une grande divergence entre les preuves empiriques et ces modèles. Nous avons donc choisi le modèle déterministe Scaling Gyroscope Cascade (SGC), pour étudier la multifractalité de l'intermittence.

Le SGC est basé sur une discrétisation parcimonieuse de la forme de Bernoulli des équations de NS dans l'espace de Fourier qui préserve bien l'interaction de la triade d'un tourbillon parent et de ses tourbillons enfants, générant étape par étape une forte intermittence.

Tout d'abord, les codes Python pour les trois méthodes de simulation numérique explicite - la méthode d'Euler, la méthode de Runge-Kutta du quatrième ordre et la méthode d'Adams-Bashforth asservie - sont présentés et testés afin de déterminer l'approche de simulation numérique la plus efficace pour le modèle SGC. Il ressort que la méthode d'Euler est la méthode de simulation numérique la plus efficace en comparant le temps d'exécution et la mémoire maximale. En outre, la structure spatiale du modèle SGC suggère que la complexité de calcul augmente de manière exponentielle avec le nombre d'étapes de la cascade.

Ensuite, l'intermittence du modèle SGC à de grands pas de cascade est étudiée en injectant différents forçages. L'existence de fluctuations spatio-temporelles est confirmée à l'aide d'une analyse statistique du flux d'énergie dans le domaine inertiel. La distribution de probabilité de ces fluctuations présente des queues beaucoup plus épaisses que celles d'une distribution gaussienne. Pour obtenir un aperçu plus détaillé, l'analyse est poursuivie dans le cadre de l'Universal Multifractal (UM), basé sur des cascades multiplicatives stochastiques qui sont à la fois stables et attractives. Ces cascades sont déterminées par seulement quelques paramètres UM qui sont physiquement significatifs pour tout modèle de cascade, y compris le SGC.

Parmi les différents résultats obtenus, nous démontrons que l'indice clé de multifractalité est significativement inférieur à 2, remettant ainsi en cause le modèle log-normal encore souvent utilisé pour la turbulence hydrodynamique.

Enfin, nous revisitons à l'aide du SGC la décroissance d'énergie d'une turbulence libre en tenant compte de l'intermittence. En raison de cette dernière, la mise en évidence du terme de rétrodiffusion d'énergie est plus complexe à démontrer, ainsi que ses impacts sur la loi de décroissance de l'énergie. Mais la phénoménologie reste la même, bien qu'avec des effets d'intermittence, par exemple, l'énergie est stockée à grande échelle par bouffées, et non plus de manière continue.

Mots clés- turbulence, intermittence; multifractalité; le modèle SGC; loi de décroissance de l'énergie libre; terme de rétrodiffusion, interactions triadiques non locales;

Abstract

Turbulence is one of the fundamental unresolved problems of classical physics, despite its manifestation in many fields, including engineering, for example in wind energy. This is linked to our lack of knowledge of properties of the deterministic 3D Navier-Stokes (NS) equations as basic as the existence and uniqueness of its solutions. This doesn't prevent researchers and engineers from using it. With the help of statistical methods, the mechanism of turbulence has been partially revealed, such as the energy transfer process. For instance, turbulence closure models, such as the Eddy Damped Quasi-Normal Markovian model, have been introduced to partially account for the infinite hierarchy of moment equations caused by the non-linear term in the NS equation. They have highlighted the possibility of backscattered energy from the energy spectrum peak to the largest eddies and therefore modification of the energy decay law of turbulence. However, these advancements do not take into account the fundamental characteristic of turbulence: intermittency, which means that turbulence is extremely heterogeneous and leads to a large discrepancy between the empirical evidence and these models. We therefore chose the deterministic Scaling Gyroscope Cascade (SGC) model, to investigate the multifractality of intermittency. SGC is based on a parsimonious discretisation of the Bernoulli's form of the NS

equations in Fourier space that well preserves the triad interaction of a parent eddy and its child eddies, generating step by step a strong intermittency.

Firstly, the Python codes for the three explicit numerical simulation methods - the Euler method, the fourth order Runge-Kutta method and the slaved Adams-Bashforth method - are presented and tested to determine the most efficient numerical simulation approach for the SGC model. It comes out that the Euler method is the most effective numerical simulation method by comparing the running time and maximum memory. Besides, the spatial structure of the SGC model suggests that the computing complexity increases exponentially with the number of cascade steps.

Then, the intermittency of SGC model at large cascade steps is investigated by injecting various forcings. The existence of spatial-temporal fluctuations is confirmed with the help of a statistical analysis of the energy flux in the inertial range. The probability distribution of these fluctuations has tails that are much heavier than those of a Gaussian distribution. To get more detailed insights, the analysis is pursued in the Universal Multifractal (UM) framework, based on stochastic multiplicative cascades that are both stable and attractive. These cascades are determined by only a few UM parameters that are physically meaningful for any cascade models, including the SGC.

Among the various obtained results, we demonstrate that the key multifractality index is significantly less than 2 thus questioning the log-normal model still often used for hydrodynamic turbulence.

Last but not least, we revisit with the help of SGC the energy decay of a free turbulence taking into account the intermittency. Due to the latter, the evidence of the energy backscatter term is more complex to demonstrate, as well as its impacts

on the energy decay law. But the phenomenology remains the same, although with intermittency effects, e.g., energy is stored at large scales by puffs, no longer in a continuous manner.

Key words- turbulence, intermittency; multifractality; the SGC model; free energy decay law; backscatter term, nonlocal triad interactions;

I would like to dedicate this thesis to my family, especially my grandmother who cared about me at her last moment.

Acknowledgements

It will start by giving special thanks to my superiors. I would like to thank Professor Daniel Schertzer, the thesis director, for his patience in cultivating my research ability. The thesis is greatly supported by the supervisor HDR Yelva Roustan's comprehensive and well-considered suggestions. Besides, I want to express my gratitude to the lab director Ioulia Tchiguirinskaia for her helpful advice when my research was not going well. With their guidance, I'm able to overcome all the challenges and gain the basic skills of doing research as well as a disciplined scientific research attitude.

Besides, I would like to thank my colleagues. Dr. Auguste Gires is always willing to provide a hand when I met some issues. Thanks to Catherine and Albertine to help me with administrative matters. The student representative Ángel García Gago always spares no effort to care about my study and mental health. To the rest of the group, those academic discussions inspired me a lot, and those amusing jokes at coffee time relieved my stress. I would like to thank my friends Zhizhao Wang and Yunyi Wang from CEREA and Dr.Sijia Kong from École des Mines de Paris for their accompany. I also like to express my gratitude to École des Ponts ParisTech for providing scholarship to fund my research study, as well as the laboratory HM&Co and CEREA. Thank you for all support. These time makes me grow and is cherished.

Table of Contents

List of Figures

List of Tables

Code Listings

List of Algorithms

Notation and Abbreviations

Notations

Notations

α_ℓ The exponent of scaling law of scale $\ell(t)$, 151

α_D The dissipativity is the power of negative Laplacian when $v\frac{\partial^2}{\partial x^2}$ is replaced by $-v(-\frac{\partial^2}{\partial x^2})^{\alpha_D}$, 152

α_e Exponent of energy decay law, 15

α_l Exponent of integral scale, 16

$\boldsymbol{f}$ Body force, 7

$\boldsymbol{k}$ Wave number, 9

$\boldsymbol{p}$ Pressure, 7

$\boldsymbol{r}$ Location vector, 7

$\boldsymbol{t}$ Time, 7

$\boldsymbol{u}$ Velocity which has vector, 7

$\delta_r \boldsymbol{u}(l)$ The velocity increment, 10

$\ell(t)$ A rather arbitrary scale of energy-containing eddies in the energy spectrum function, 151

$\ell_{d,\alpha_D}(t)$ The dissipation scale related to R_{α_D}, 152

∞ Infinite, 14

λ Separate ratio , 30

μ Increment of the energy flux at cascade step n, 30

ρ Density, 7

σ^2 The variance, 22

ε Energy flux rate or energy flux density, 8

$\widehat{\boldsymbol{u}}$ Velocity $\boldsymbol{u}$ in Fourier space, 17

A_n $\varepsilon_n = \lambda^{nc}$, 34

A_n^c $\varepsilon_n = 0$, 34

c Co-dimension, 28

C_s The prefactor of stationary of big eddies, 151

D Euclidean dimension, 28

D_F Fractal dimension, 26

$E(\boldsymbol{k})$ Energy spectrum, 9

F Fractal set, 27

$F(x)$ Dimensionless functions of the dimensionless wavevector x in the energy spectrum function, 151

$G(x)$ Dimensionless functions of the dimensionless wavevector x in the energy spectrum function, 151

$I(t)$ Loitsiansky integral, 15

K kinetic energy, 14

$L(t)$ Integral scale, 16

l_0 Initial scale, 28

l_I The demarcation scale between the anisotropic large eddy and the isotropic small eddies , 12

l_n Scale at steps n , 28

$L_s(t)$ Saffman invariant, 16

l_η Kolmogorov scale/ dissipation scale, 12

N The number of parts that the object exactly decomposed into, 27

n Cascade Step in most cases. The word layer is used as a synonym in explaining SGC model. Besdies, it is shell in GOY model (Gledzer 1973, Ohkitani and Yamada 1989) . The fact is that all of these terms refer to the same thing n. , 28

q The moments order, 10

$r(N)$ Similarity ratio or the inverse resolution, 27

R_{α_D} The modified Reynolds number, 152

$R_{ij}(l)$ Correlation function , 9

s The exponent of stationary of big eddies, 151

$S_q(l)$ The moments function, 10

$v_{turb}(k)$ $\mathbf{k}-$independent viscosity, 21

α One of UM parameters, multifractality index , 50

α^* kinematic pressure, 58

α_e Multifractality index obtained from ensemble analysis , 88

α_v The exponent of the velocity $v(t)$, 151

β^* The power spectrum exponent, 13

$\boldsymbol{\Omega}$ The rotation , 58

$\boldsymbol{\omega}$ The vorticity , 58

$\boldsymbol{e}$, 18

$\boldsymbol{M}$ The angular momentum, 58

$\boldsymbol{P}_{ij}$, 18

Δt The time step, 62

$\delta_{i,j}$ The Kronecker's δ, 18

$\delta_{i,j}$ The Kronecker's δ, 58

$\eta*$ Artificial dissipation cascade step , 69

γ_+ The positive singularity , 45

γ_- The negative singularity , 45

λ_k The arbitrary nonlocalness parameter , 59

$\lambda_{\boldsymbol{k}}$ Parameter to separate the local and nonlocal interactions , 21

∇ The nabla operator , 58

$\overline{\alpha}$ Averaged multifractality index obtained from all sub-series , 88

$\overline{\epsilon}$ The average of energy transfer rate , 13

$\overline{\widehat{\boldsymbol{u}}}$ Conjugate of $\widehat{\boldsymbol{u}}$, 17

$\overline{C_1}$ Averaged mean codimension obtained from all sub-series , 88

$\overline{q_s}$ The mean critical moment obtained from all sub-series , 88

τ Eddy turnover time, 13

τ_e Initial large-eddy turnover time, 81

$\theta_{k,p,q}$ The correlation relaxation time of the triad k, p, q, 155

ε_n The energy flux density at step n , 30

$\zeta(q)$ Exponent of the qth-order moment structure function, 10

$c(\gamma)$ Co-dimension function , 47

C_1 One of UM parameters, the codimension of singularity of the mean field, which equals its singularity. , 50

C_{1_e} Mean codimension obtained from ensemble analysis , 88

c_{ij} Sub-codimensions , 46

D The diameter of the pipe, 6

$E(t)$ System energy, 82

$E_m(t)$ Energy at wave number k_m, 82

H^* A measure of correlation, 13

$K(q)$ The moment scaling function, 48

L Scale of motion, 7

$L(t)$ Integral scale, 81

n_+ The number of more active steps , 45

n_- The number of less active steps , 45

$P(\nabla)$ The projector of nabla operator, 58

q_{s_e} Critical moment obtained from ensemble analysis, 88

Re Reynolds number, 7

$S(n)$ The storage space, 72

$T(n)$ Statement frequency, 75

t_f Maximum time, 82

U Velocity, 6

v Viscosity, 6

Operations

$\int$ Integral, 14

$\prod$ Product , 30

$\mathbf{\Omega}$ The divergence , 58

$\cdot$ Scalar product , 7

Δ The Laplace Operator , 58

∇ Gradient, 7

$\propto$ Proportional to, 13

curl The curl , 58

grad The gradient , 58

Abbreviations

RTE Gestionnaire du Réseau de Transport d'Electricité

NS Navier-Stokes

QNA Quasi-Normal Approximation

DIA	Direct Interaction Approximation
EDQNM	Eddy Damped Quasi-Normal Markovian
UM	Universal Multifractals
SGC	Scaling Gyroscope Cascade
DNS	Direct Numerical Simulation
GSI	Generalized Scale Invariance
TKE	Turbulence Kinetic Energy
DTM	Double Trace Moment
ODE	Ordinary Differential Equation
RK4	Fourth-order Runge-Kutta Method
ABF	Adams-Bashforth (ABF) Method
Max RSS	Maximum Resident Set Size
PDF	Probability Density Function

Chapter 1

Introduction

1.1 Background

Turbulence occur everywhere from life to scientific research, such as the mixing of cream in a coffee cup, flight, and chemical experiments. Rapid development of technologies motivates the study of turbulence to predict and control it. For example, when designing the structural load and safety in marine engineering, one of factors causing the movement of sediments and resuspension is turbulence in the bottom layer of the ocean. Besides, turbulence will enhance sound scattering, making studying sound transportation in the ocean more complex. Turbulence in the atmosphere is more important than ever to many fields since recent research [136] predicts a high frequency of atmospheric turbulence occurring and it will strengthen with climate change to which turbulent heat flux may play an important role, though

difficult to estimate [126]. Turbulence-related injuries in the flight, according to the International Air Transport Association [77], reach 25%. On the other side, Gestionnaire du Réseau de Transport d'Electricité (RTE) claims that renewable resource - wind energy in France has remarkable growth [37], as wind energy in 2020 generated 7.9% of electricity and the maximum average rate of coverage of consumption in 2021 reached 31.35%. This renewable resource is the kinetic energy available in the large-scale movements of air in the atmosphere [13], which is transported from the ground to the height and captured by wind turbines Fig 1.1[1]. It requires quantifying turbulence caused by converting the kinetic energy of wind into thermal energy [86]. However, the mechanism of turbulence is neither completely understood nor precisely predictable [87].

Figure 1.1: Wind turbines in Aveyron department of the Midi-Pyrenees region of France

In the absence of computer technique, turbulence research at the beginning has been largely focused on the analytical approximations through deterministic and stochastic approaches, since the Navier-Stokes (NS) equation (See 1.2.1), which is

[1]This figure is from JohnnyOneSpeed

the deterministic equation of turbulence, is still very challenging to guarantee and obtain the global existence of unique solutions. After the statistical method is proposed, significant achievements were achieved in the 20th century. The statistical description (See 1.2.2), which relies on the moments of velocity fluctuations from the NS equation, enables to study the dynamic of turbulence and gives generic properties, such as the energy spectrum and decaying energy. However, one of the challenges is an infinite hierarchy of enclosed moment equations caused by the nonlinear term, as the partial time derivative of moments n is determined by moments $n + 1$. In order to obtain a finite and closed set of equations, which is called closure scheme, this difficulty could be handed by truncating by a model.

Based on the assumption of homogeneous isotropic turbulence [131] and stationary statistics, the Kármán-Howarth [25] equations are introduced, which inspires statistic theory of turbulence and lays the foundation of "closure" approximations. Kolmogorov proposed the well-known assumption of turbulence (See 1.4, 1.5) relying on the cascade structure (See 1.3). This assumption has been used to testify the following closure models.

The Quasi-Normal approximation (QNA) [90] by assuming that the probability distributions of fluctuating velocity are normal distributions, closes the second and third-order moments equations. The fourth-order moments of the cumulant, which indicates the difference between the velocity distribution and normal distribution, are zero. Scientists have taken notice of this promising analytical approach because of its ability to achieve high Reynolds numbers and relative simplicity.

Kraichnan [60] noticed realizability problem of QNA that it violates the basic probabilistic inequalities and the energy spectrum obtained by the QNA model is

unphysical. So he proposed a field-theoretic closure called Direct Interaction Approximation (DIA) to solve this realizability problem, which provides the exact statistical solution to a stochastic model and saves many properties shown in the NS equation. The pity of DIA is that it is not consistent with Kolmogorov theory. Plus, Kraichnan [61] investigated the energy transfer process and revealed the importance of nonlocal triad interaction (See 1.6) in two-dimensional turbulence that transfers most of energy from large scale to small scale [96, 56]. The nonlocal triad interaction provides an approach to study the inner detail of the energy transferring in the scales of turbulence, but it questions Kolmogorov's theory due to the assumption of statistical independence of cascade motion.

Eddy Damped Quasi-Normal Markovian (EDQNM) Model [98], a DIA-based closure model, is the currently most accepted closure model. By introducing a phenomenological eddy damping rate, EDQNM avoids unphysical features, especially the realizability guaranteed by Markovianization assumption, so that it is consistent with Kolmogorov theory. It has been proven as an effective model to study the dynamics and transport properties of turbulence [48]. In the framework of EDQNM, some deep insights have been proposed through the nonlocal interactions. One of them is the backscatter term [74] becomes a non-neglected factor in the energy decay of turbulence, which reveals the mechanism of inverse energy [88] and provides a more accurate energy decay process.

Unfortunately, these advances haven't taken one of the most fundamental phenomena of natural turbulence: intermittency [8, 40] (See 1.7) into account, resulting in strongly non-Gaussian fluctuations over a wide range of space-time scales. Even though the traditional assuring scale invariance method by neglecting intermittency

can describe turbulence energy transport, which involves only the second-order moments, description for the higher-order statistical moments urgently needs to be corrected. Universal Multifractals (UM) based on multiplicative cascade models (See Chapter 2) have been introduced as a powerful tool to describe intermittency in a scale-invariant (scaling) framework, which emphasized extreme nonlinear variability. The multifractal analysis of empirical data, particularly from lab experiments and atmospheric in-situ/remotely sensed data, has rather consistently generated estimated UM parameters: multifractality index $\alpha \approx 1.5$ and mean codimension $C_1 \approx 0.25$. NS equation and stochastic cascades are sometimes disagreed, nevertheless. The Scaling Gyroscope Cascade (SGC) model [20] (See 3.1), which is based on a parsimonious discretization of Fourier transform of the Bernoulli's form of NS equation and preserves majority of the fundamental properties of NS equation, is therefore studied since it provides a more close statistical description of natural turbulence and shows intermittency.

This thesis initially investigates the efficient numerical approach for SGC model. The intermittency is next verified by energy flux of numerical simulated SGC model, and its temporal multifractality is analyzed by UM framework (See Chapter 4). Free energy decay process considering intermittency is studied by SGC model (See Chapter 5) to fill part of gap between scaling laws obtained by EDQNM and energy transferring process considering intermittency. Here, SGC model is simulated by direct numerical simulation (DNS), which is an ideal method to explore the dynamic and transitional process of turbulence in great detail under the rapid development of computing technology. It gets rid of the limitations of closure problems and analytical approaches and provides a great amount of information on turbulence. Related basic

knowledge is provided in the following.

1.2 Turbulence

Turbulence are disorder flows over time and space domain, and the motion is random and believed to be highly unpredictable. There is no precise mathematical definition, but a physical definition was first proposed in Reynolds experiment [104]. In this experiment, the flow was pumped into a long, straight circular pipe to get rid of vibration from the left side, which is shown in Fig 1.2[2].

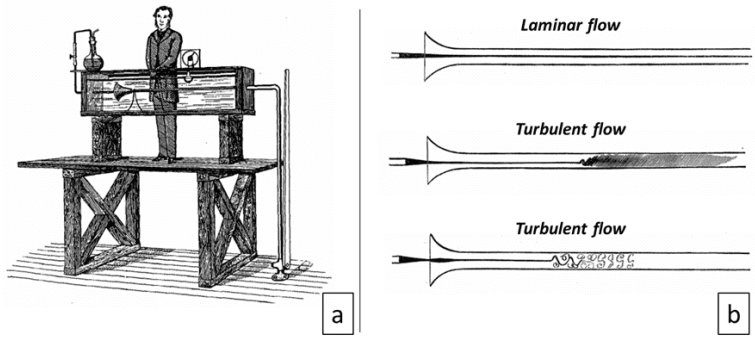

Figure 1.2: The Reynolds experiment

The injected water contains a stream of stained trickle, allowing to observe water motion in the glass tube clearly. This experiment was performed by independently varying velocity U, the diameter of pipe D, and by considering various molecular viscosity v. Hence, the parameter which characterizes turbulence is named as Reynolds number:

$$Re = \frac{UL}{v} \sim \frac{The\ inertial\ force}{The\ viscosity\ force} \tag{1.2.1}$$

[2]The figure is from https://clqtg10snjb14i85u49wifbv-wpengine.netdna-ssl.com/wp-content/uploads/2020/04

where L is the scale of motion which is D in Reynolds experiment. The critical value R_c suggested by Reynolds was the order of 2000. For $R > R_c$, the mixture of colored stream and surrounding water on the right side is irregular and random, which is turbulent flow. On the contrary, the unmixed stream is laminar flow.

1.2.1 The deterministic equation: NS equation

It's generally accepted that the equation governing turbulence is Navier-Stokes equation [92, 10]:

$$\frac{\partial \boldsymbol{u}}{\partial t} + (\boldsymbol{u} \cdot \nabla)\boldsymbol{u} = v\nabla^2 \boldsymbol{u} + \boldsymbol{f} - \frac{1}{\rho}\nabla p \tag{1.2.2}$$

where $\boldsymbol{u}$ is velocity vector which depends on time t and location vector $\boldsymbol{r}$; p is pressure; ρ is pressure; $\boldsymbol{f}$ is body force; ∇ represents gradient. For incompressible fluid, the divergence of velocity is

$$\nabla \cdot \boldsymbol{u} = 0. \tag{1.2.3}$$

It is of great importance that it characterizes the constant transfer of physical quantities in the fluid. The unsteady-state term, which is the first item on the left side of Eq 1.2.2, is the rate of changed momentum of fluid per unit volume. The advection term, which is the second item on the left side of Eq 1.2.2, represents the momentum that flows in and flows out of control surface. The right side of Eq 1.2.2 is pressure term, external forcing, and viscous dissipation, which contributes to momentum of dissipation of Newtonian viscous fluids. Unfortunately, the existence of rigorous mathematical unique solution for incompressible Navier-Stokes equation hasn't been obtained so far due to its complexity [107] resulting from the non-linear term and infinite-dimensional problem.

NS equation follows three basic physical laws: the conservation of mass, Newton's second law, and energy conservation. Energy transfer rate [58] is defined as the energy per mass per time that passes through a spherical shell in Fourier space:

$$\varepsilon = -\frac{1}{2}\frac{\partial}{\partial t}(\boldsymbol{u}\cdot\boldsymbol{u}). \tag{1.2.4}$$

It is conserved by the nonlinear term of NS equation assuming $v = 0$, $f = 0$ and density is constant.

Moreover, NS equation is symmetrical so that many properties are invariant under these conditions. These symmetries are:

1. Space-translations: $t, \boldsymbol{r}, \boldsymbol{u} \mapsto t, \boldsymbol{r} + l, \boldsymbol{u}, l \in \mathbb{R}^3$
2. Time-translations: $t, \boldsymbol{r}, \boldsymbol{u} \mapsto t + \tau, \boldsymbol{r}, \boldsymbol{u}, \tau \in \mathbb{R}$
3. Galilean transformations: $t, \boldsymbol{r}, \boldsymbol{u} \mapsto t, \boldsymbol{r} + \boldsymbol{U}\boldsymbol{t}, \boldsymbol{u} + \boldsymbol{U}, \boldsymbol{U} \in \mathbb{R}^3$
4. Parity: $t, \boldsymbol{r}, \boldsymbol{u} \mapsto t, -\boldsymbol{r}, -\boldsymbol{u}$
5. Rotations: $t, \boldsymbol{r}, \boldsymbol{u} \mapsto t, R\boldsymbol{r}, R\boldsymbol{u}, R \in SO(3, \mathbb{R})$
6. Scaling: $t, \boldsymbol{r}, \boldsymbol{u} \mapsto e^{1-a}t, e\boldsymbol{r}, e^a\boldsymbol{u}, e \in \mathbb{R}_+, a \in \mathbb{R}$

The first four symmetries can be explained as Galilean invariance and scaling symmetry is obvious under the limit $v \to 0, \boldsymbol{f} \to 0$. A hidden scaling symmetry [81] of NS equation ($v \to 0$) is introduced from rescaling around suitably defined Lagrangian scaling centres, which is different from Galilean invariance.

1.2.2 Statistical approach

When Reynolds number of NS equation is high, the degrees of freedom are huge and turbulence is very sensitive to small disturbances and errors. It's impossible to trace and predict turbulence because of its random instantaneous motion. After Taylor [132] suggested that the motion of turbulence can be studied as the stochastic process, statistical method [65] is introduced as one of the important research approaches to quantify turbulence, e.g., the averages, probability distribution functions, spectra, correlations. One of statistical methods is correlation function:

$$R_{ij}(l) = \langle \boldsymbol{u}_i(\boldsymbol{r}) \cdot \boldsymbol{u}_j(\boldsymbol{r}+l) \rangle. \tag{1.2.5}$$

This correlation function describes the relationship of velocity at different locations. Kármán and Howarth in 1938 [25] proposed a self-similar law for this spatial correlation function of velocity during studying decay of three-dimensional isotropic turbulence at a high Reynolds number.

Many physical quantities of turbulence are related to the correlation function. For example, energy spectrum [5] which is under assumption of homogeneous, describes the distribution of average kinetic energy wave number space $\boldsymbol{k}$:

$$R_{ii}(l) = \int_{-\infty}^{\infty} e^{-ikl} E(t) dk \Rightarrow E(\boldsymbol{k}) \equiv \frac{1}{2} \int \int_{|\boldsymbol{k}|} \phi_{ii}(\boldsymbol{k}) d\sigma(\boldsymbol{k}) \tag{1.2.6}$$

where $\phi_{ii}(\boldsymbol{k}) = \int \int \int_{-\infty}^{+\infty} e^{i\boldsymbol{k}\cdot\boldsymbol{r}} R_{ii}(\boldsymbol{r}) d\boldsymbol{r}$ is three-dimensional.

To avoid the difficulty to determine probability density function with few parameters, the moment of high order q [3] providing approximation is:

$$\langle [\boldsymbol{u}(\boldsymbol{r}+l) - \boldsymbol{u}(\boldsymbol{r})]^q \rangle = \langle (\delta_r \boldsymbol{u}(l))^q \rangle = S_q(l), \tag{1.2.7}$$

where

$$\delta_r \boldsymbol{u}(l) = \boldsymbol{u}(\boldsymbol{r} + l) - \boldsymbol{u}(\boldsymbol{r}) \tag{1.2.8}$$

is velocity increment. Assuming that turbulence are maintained at a steady state by external forces, the right sides of Eq 1.2.7 under assumption of homogeneous and isotropic is independent of time, direction, and selected spatial point $\mathbf{r}$, so it is simplified to a velocity component relating only to the magnitude of distance l, which is named as structure function:

$$S_q(l) \propto l^{\zeta(q)}, \tag{1.2.9}$$

where $\zeta(q)$ is the exponent of the qth-order moment structure function.

Fruitful conclusions were built on assumption of statistical theory, such as the well-known K41 theory. What's more, strongly anisotropic systems are studied by Generalized Scale Invariance (GSI) [115, 78]. It's actually self-affine generated by the pullback transforms and differential dilations/contractions operators. In two dimensions, the operators could be represented by off-diagonal matrices.

1.3 Energy cascade

Richardson [105] is considered that laid the foundation for turbulence structure as he first introduced the energy cascade to describe scaling law of turbulence. Part of Richardson's poem describing turbulence is

"Big whorls have little whorls,

Which feed on their velocity;

And little whorls have lesser whorls,

And so on to viscosity."

It suggests that turbulence are full of eddies of different sizes. Large-scale eddies in Fig 1.3, which are like tanks and contain energy continuously, obtain energy from the outside and transport energy to small-scale eddies by the inertia of fluid, while small-scale eddies whirling faster will consume energy and turn it into heat by viscous fraction. The inertia range, which depends on Reynolds number, is between large-scale energy storage and small-scale energy consumption. The dissipation exists at all scales but could be neglected in the inertial range.

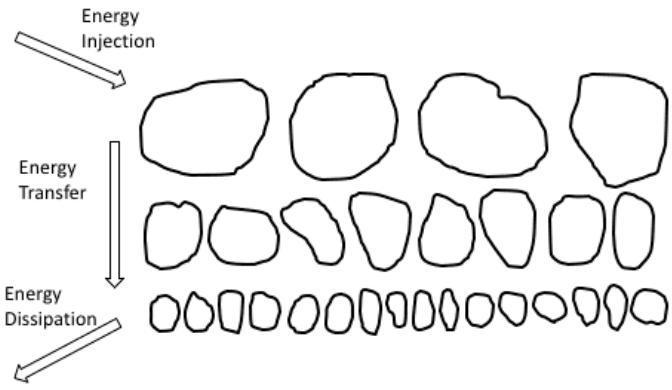

Figure 1.3: The cascade

After introducing cascade, turbulence research has been greatly motivated by cascades for a long time. Based on Richardson's cascade structure, Kolmogorov [58] proposed a statistical theory of turbulence, which measures statistical quantities of turbulence. Moreover, achievements in multiplicative cascade models suggest the importance of the cascade is far more significant.

1.4 Kolmogorov assumption

Here, the well-known Kolmogorov assumption, which quantitatively describes energy distribution between scales and is considered as the fundamental advancement of turbulence research, is explained. To start, several hypotheses are proposed to get rid of large anisotropic eddies, which are affected by the boundary condition.

Lemma 1 ***The hypothesis of local isotropy:*** *When Reynolds number is high enough, the motion of turbulence at small scales $l < l_I$ is statistically isotropic, where l_I is the scale dividing isotropic eddies from those anisotropic large eddy.*

Lemma 2 ***The similarity hypothesis:*** *At sufficiently high Reynolds number, the motions of turbulence at small scale ($l_\eta < l < l_I$) are in a statistically universal form as shown in Fig 1.4, which is uniquely determined by dissipation rate ε and independent of v. l_η is Kolmogorov scale ($Re_\eta = 1$) where dissipation starts.*

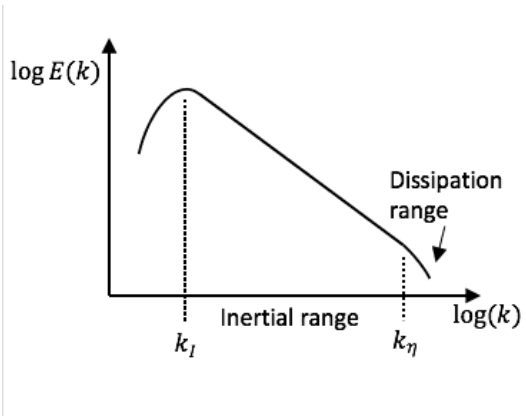

Figure 1.4: The inertial range. k is wave number, which has $k \propto \frac{1}{l}$.

Now it's possible to describe the uniform characteristic in inertial range. Kolmogorov assumed the dissipation rate is the mean $\langle \varepsilon \rangle = \overline{\varepsilon}$ in whole energy transferring

process to reveal spatial distribution of turbulence. Due the Eq 1.2.4, the dissipation rate is [25]

$$\epsilon \propto \frac{\boldsymbol{u}^2}{\tau} = \frac{\boldsymbol{u}^2}{l/\boldsymbol{u}} = \frac{\boldsymbol{u}^3}{l}, \tag{1.4.1}$$

where τ is eddy turnover time. Eq 1.4.1 yields that the mean square of velocity increment between two points is two-thirds powers of the distance.

Lemma 3 ***Structure function:*** *The second-order structure function depends on length scale l and mean dissipation rate $\bar{\epsilon}$:*

$$S_2(l) \propto l^{2H^*} \sim (\bar{\epsilon} l)^{2/3}, \tag{1.4.2}$$

where H^* is a measure of correlation.

Therefore, famous $-5/3$ energy spectrum [95] is obtained from the definition of energy spectrum Eq 1.2.6.

Lemma 4 ***Kolmogorov-Obukhov spectrum:*** *Scaling law of spectrum in inertial range is:*

$$E(k,t) \propto \bar{\epsilon}^{2/3} k^{-\beta^*} = \bar{\epsilon}^{2/3} k^{-5/3}, \tag{1.4.3}$$

where β^* is power spectrum exponent.

Besides, relationship between the second-order structure function and energy spectrum is

$$\beta^* = 1 + \zeta(2) \approx 1 + 2H^*, \tag{1.4.4}$$

where $\zeta(2)$ is the second-order-moment structure function exponent.

Variety of experiments [110, 47] and theories [14] since the 1950s have confirmed that the micro-structure of turbulence is what predicted by Kolmogorov and Obukhov- the second-order structure function of turbulence obeys $\frac{2}{3}$ law, and the one-dimensional spectrum of turbulence obeys $-\frac{5}{3}$ power law.

1.5 Energy decay law

The dynamics of turbulence are generally referred to energy transferring from large eddies to small eddies, which maintains motion of turbulence. Without external forces, the kinetic energy (TKE) of fully developed turbulence will be consumed by the viscosity term. Therefore, free energy decay law is one of the key characteristics to reveal the mechanism of turbulence, which could be widely applied to rapid expansion of wind energy [55]. Until now, plenty of research on the free energy decay laws has been carried out. Even though there is a general agreement on the kinetic energy of freely decaying turbulence that decays with time, the exponent of energy decay law is still debatable.

According to the definition of energy spectrum, kinetic energy is

$$K \equiv \frac{1}{2} R_{ii}(0) = \int_0^{+\infty} E(k,t) dk. \tag{1.5.1}$$

Kármán and Howarth [25] firstly suggest energy decay is self-similar for scales outside the dissipation range. Batchelor and Townsend [7] investigated the decay of homogeneous isotropic three-dimensional turbulence at a high Reynolds number and predicated energy decay law in the initial period when viscous dissipation and inertia

forces are of comparable importance, is

$$K(t) \propto t^{-1}, \tag{1.5.2}$$

whereas energy decay law in the final period after which inertia forces are negligible is

$$K(t) \propto t^{-\frac{5}{2}}. \tag{1.5.3}$$

Comte-Bellot and Corrsin [23] obtained that energy decay obeys a power law

$$K(t) \propto t^{\alpha_e} \tag{1.5.4}$$

where exponent α_e is less than -1. George in 1992 [45] confirmed this conclusion that exponent α_e should be between $-\frac{5}{2}$ and -1 and explicit value is decided by the behavior of energy spectrum near $k \to 0$. By assuming Loitsiansky integral

$$I(t) = -\int \boldsymbol{r}^2 R_{ii}(\boldsymbol{r}, t) d\boldsymbol{r} \tag{1.5.5}$$

is an invariant, Kolmogorov [57] derived

$$K(t) \propto t^{-\frac{10}{7}}. \tag{1.5.6}$$

Besides, the freely decaying turbulence with this assumption is commonly known as Batchelor turbulence.

However, Proudman and Reid in 1954 [103] and Batchelor and Proudman in 1956 [6, 88] proved that Loitsiansky scale isn't an invariant, which brings questions to $-\frac{10}{7}$

energy decay law. Saffman [111] therefore proposed that the second integral moment of velocity correlation is an invariant:

$$L_s(t) = \int R_{ii}(\boldsymbol{r}, t) d\boldsymbol{r} \neq 0, \tag{1.5.7}$$

which is named as Saffman invariant, and the exponent α_e associated with this hypothesis which is referred as Saffman turbulence is $-\frac{6}{5}$. Both measurement data and experimental data of freely decaying grid-generated turbulence [23, 64, 91] have verified it.

Actually, energy decay process is dominated by contributions from small wave numbers as a consequence of exponential factor in the integrand, so its power-law decay during the final period results from a behavior of $E(k, 0)$ $(k \to 0)$. Energy decay law $\alpha_e = -\frac{10}{7}$ corresponds to the energy spectrum $E(k, 0) \sim k^4$ at large scale, while energy decay law $\alpha_e = -\frac{6}{5}$ is related to spectrum $E(k, 0) \sim k^2$.

Meanwhile, integral scale l measuring the correlation distance between two terms of distance or time has a power law:

$$L(t) = \frac{\int_0^\infty k^{-1} E(k, t) dk}{\int_0^\infty E(k, t) dk} \propto t^{\alpha_l}. \tag{1.5.8}$$

Exponent α_l in Batchelor turbulence is $\frac{2}{7}$ obtaining from constant $u^2 l^5 = const$, whereas it is $\frac{2}{5}$ in Saffman turbulence resulting from constant $u^2 l^3 = const$.

More detailed research on energy decay process will be discussed in Chapter 5.

1.6 The nonlocal triad interaction

Although a clear big picture of turbulence in which energy spectrum and energy decay obey self-similar law has been obtained, the microcosm mechanism dominated energy transferring in the scales of turbulence is also of great importance. Actually, triads interaction preserves detailed conservation of kinetic energy that provides significant information about the way nonlinear interactions occur between these modes. Fourier analysis of NS equation, an infinite set of ordinary differential equations, could be projected into a plane perpendicular to the wave vector due to incompressibility eliminating longitudinal motion. Thus, the quadratic nonlinearity decomposes into three Fourier modes interactions, which is named as triad interaction by Kraichnan [60].

Velocity $\boldsymbol{u}(\boldsymbol{x},t)$ of homogeneous turbulence in Fourier space is:

$$\widehat{\boldsymbol{u}}(\boldsymbol{k},t) = \frac{1}{(2\pi)^3}\int \boldsymbol{u}(\boldsymbol{x},t)e^{i\boldsymbol{k}\cdot\boldsymbol{x}}d\boldsymbol{x}, \tag{1.6.1}$$

which satisfies conjugate symmetry:

$$\widehat{\boldsymbol{u}}(-\boldsymbol{k},t) = \overline{\widehat{\boldsymbol{u}}}(\boldsymbol{k},t). \tag{1.6.2}$$

Continuity equation Eq 1.2.3 indicates

$$\boldsymbol{\kappa}\cdot\widehat{\boldsymbol{u}} = 0, \tag{1.6.3}$$

where κ is wave number. When any vector $\widehat{\boldsymbol{V}}$ decomposes into:

$$\widehat{\boldsymbol{V}} = \widehat{\boldsymbol{V}}^{\parallel} + \widehat{\boldsymbol{V}}^{\perp}, \tag{1.6.4}$$

where component $\widehat{\boldsymbol{V}}^{\parallel}$ is parallel to $\boldsymbol{\kappa}$ and component $\widehat{\boldsymbol{V}}^{\perp}$ is normal to $\boldsymbol{\kappa}$. Then component of $\widehat{\boldsymbol{V}}^{\parallel}$ becomes

$$\widehat{\boldsymbol{V}}^{\parallel} = \boldsymbol{e}(\boldsymbol{e}\cdot\widehat{\boldsymbol{V}}) = \boldsymbol{\kappa}(\boldsymbol{\kappa}\cdot\widehat{\boldsymbol{V}})/\kappa^2 \iff \widehat{V}_j^{\parallel} = \frac{\kappa_j\kappa_k}{\kappa^2}\widehat{V}_k, \tag{1.6.5}$$

where the unit vector $\boldsymbol{e}$ equals $\boldsymbol{e} = \boldsymbol{\kappa}/\kappa$. Unit vector Due to Eq 1.6.4, component $\widehat{\boldsymbol{V}}^{\perp}$ has

$$\widehat{\boldsymbol{V}}^{\perp} = \widehat{\boldsymbol{V}} - \boldsymbol{\kappa}(\boldsymbol{\kappa}\cdot\widehat{\boldsymbol{V}})/\kappa^2 \iff \widehat{V}_j^{\perp} = \boldsymbol{P}_{ik}\widehat{V}_k, \tag{1.6.6}$$

where $\boldsymbol{P}_{ij}$ is projection tensor allowing that component Eq 1.6.6 is the projection of $\widehat{\boldsymbol{V}}$ onto the plane normal to $\boldsymbol{\kappa}$:

$$\boldsymbol{P}_{ij}(\boldsymbol{\kappa}) \equiv \delta_{jk} - \frac{\kappa_j\kappa_k}{\kappa^2}. \tag{1.6.7}$$

Projection tensor

Regarding momentum conservation on an fluid element, it yields [139]

$$\frac{\partial u_j}{\partial t} + \frac{\partial u_j u_k}{\partial x_k} = v\frac{\partial^2 u_j}{\partial x_k \partial x_k} - \frac{1}{\rho}\frac{\partial p}{\partial x_j}, \tag{1.6.8}$$

the equation for time evolution of velocity vector is obtained by its Fourier transform:

$$\frac{d\widehat{u}_j}{dt} + v\kappa^2\widehat{u}_j = -i\kappa_j\widehat{p} - \widehat{V}_j \tag{1.6.9}$$

where $\widehat{V}_j$ is derived from Fourier transform of nonliear term of Eq 1.6.8. Due to Eq 1.6.3, $\widehat{V}_j$ has:

$$\kappa^2\widehat{p} = i\kappa_j\widehat{V}_j \Rightarrow \widehat{V}_j^{\parallel} = \frac{\kappa_j\kappa_k}{\kappa^2}\widehat{V}_k = -i\kappa_j\widehat{p}, \tag{1.6.10}$$

which indicates that $-\widehat{V}_j^{\parallel}$ is balanced by pressure term. Hence, Eq 1.6.9 turns into:

$$\frac{d\widehat{u}_j}{dt} + v\kappa^2\widehat{u}_j = -(\delta_{ij} - \frac{\kappa_j\kappa_k}{\kappa^2})\widehat{V}_k = -P_{ij}\widehat{V}_k = -\widehat{V}_j^{\perp} \tag{1.6.11}$$

Now it's time to give out $\widehat{V}_j$:

$$\widehat{V}_j(\boldsymbol{\kappa}, t) = i\kappa_k \sum_{\boldsymbol{\kappa'}} \widehat{u}_j(\boldsymbol{\kappa'})\widehat{u}_k(\boldsymbol{\kappa} - \boldsymbol{\kappa'}), \tag{1.6.12}$$

Eq 1.6.11 becomes

$$(\frac{d}{dt} + v\kappa^2)\widehat{u}_j(\boldsymbol{\kappa}, t) = -i\kappa_l \boldsymbol{P}_{jk}(\boldsymbol{\kappa}) \sum_{\boldsymbol{\kappa'}} \widehat{u}_k(\boldsymbol{\kappa'}, t)\widehat{u}_k(\boldsymbol{\kappa} - \boldsymbol{\kappa'}, t). \tag{1.6.13}$$

It shows time evolution of velocity $\widehat{u}(\boldsymbol{\kappa}, t)$ are related to velocities at wave number $\boldsymbol{p} = \boldsymbol{\kappa'}$ and $\boldsymbol{q} = \boldsymbol{\kappa} - \boldsymbol{\kappa'}$ ($\boldsymbol{\kappa} = \boldsymbol{k}$). These three wave vectors $(\boldsymbol{k}, \boldsymbol{p}, \boldsymbol{q})$ in Fig 1.5 forms a triangle

$$\boldsymbol{k} + \boldsymbol{p} + \boldsymbol{q} = 0. \tag{1.6.14}$$

Hence, the elementary interactions between this triad $(\boldsymbol{k}, \boldsymbol{p}, \boldsymbol{q})$ resulting from the quadratic nonlinearity conserves energy.

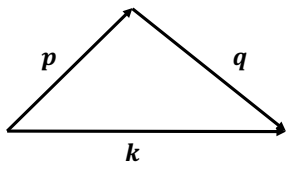

Figure 1.5: The triad interaction

The triad interaction in Fig.1.6a whose wave numbers' length are almost same, is local.

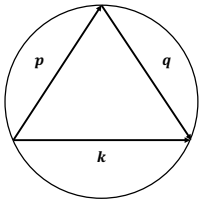

(a) The local triad interaction

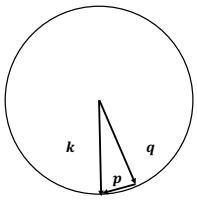

(b) One kind of nonlocal triad interactions

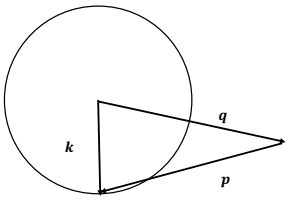

(c) Another kind of nonlocal triad interactions

Figure 1.6: Three kinds of triad interaction

Conversely, the triad interaction in Fig 1.6b,1.6c is nonlocal when one of wave numbers' length is smaller:

$$\boldsymbol{q} \ll \boldsymbol{p} \sim \boldsymbol{k}, \tag{1.6.15a}$$

$$\boldsymbol{p} \ll \boldsymbol{q} \sim \boldsymbol{k}, \tag{1.6.15b}$$

$$\boldsymbol{k} \ll \boldsymbol{p} \sim \boldsymbol{q}. \tag{1.6.15c}$$

The nonlocal triad interaction makes energy locally exchanged between two larger

wave numbers. Plus, the nonlocal triad interaction in Eq.1.6.15c could be represented by $\boldsymbol{k}-$independent viscosity $v_{turb}(k)$ [63], which has widely applied to the subgrid models for homogeneous turbulence. Kraichnan [61] investigated energy transfer process and confirmed the importance of nonlocal triad interaction, which has been demonstrated by more detailed studies [28, 30] through the DNS of Navier-Stokes turbulence and motives further research of energy transfer process [29, 138, 36, 96]. For instance, the parameter $\lambda_{\boldsymbol{k}}$ to separate the local and nonlocal interactions [71]

$$\frac{max(\boldsymbol{k},\boldsymbol{p},\boldsymbol{q})}{min(\boldsymbol{k},\boldsymbol{p},\boldsymbol{q})} \geq \lambda_{\boldsymbol{k}}, \tag{1.6.16}$$

and the parameter that has been used by Lesieur is 2. Moreover, the backscatter term and intermittency based on nonlocal interactions will be discussed later.

1.7 The intermittency

Further investigation showed that structure function proposed by K41 theory, as well as scaling laws of energy dissipation rates at higher order moments, don't agree with experimental results. These significant deviations are caused by intermittency, which breaks self-similarity properties [41] and brings the scale invariance under doubt. For example, one of the shortcomings of K41 theory was that energy dissipation rate ϵ is uniform in space and constant in time. Moreover, it is not only the fundamental characteristic of natural turbulence [114, 31] but also a general phenomenon in geophysics [117], raising doubts about previous research.

The general concept of intermittency is that high activate part of field concentrates

into a small fraction, which is non-Gaussian distribution. As shown in Fig 1.7a, vertical velocity [46] [3] shows high values in the time $10h-15h$, which is more obviously observed in Fig 1.7b.

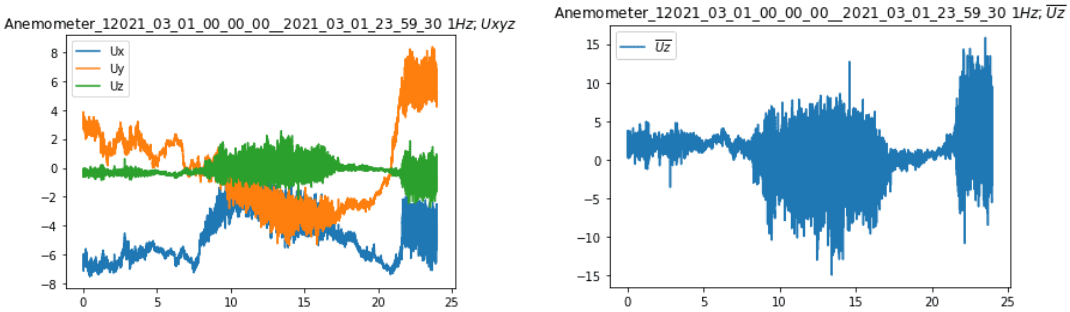

(a) The wind velocity (b) The normalized vertical wind velocity

Figure 1.7: The wind velocity exhibiting high intermittent. The time unit is an hour and resolution is 1Hz.

Intermittency was first introduced by Batchelor and Townsend [8] to describe spatial inhomogeneous energy caused by the stretching of vortex filaments that the fraction of available space for energy reduces as scale of eddies decreases. This spottiness of eddies whose scale is small is the internal intermittency of turbulence. Landau [68] noticed that intermittency should be taken into consideration in energy transferring process and claimed dissipation rate ε is a function of space and time. Later Kolmogorov [59] refined K41 theory and ε in K62 hypothesis is assumed to have a log-normal distribution

$$\sigma^2_{log\varepsilon} \sim A + alog(L/l) \tag{1.7.1}$$

where a is some universal constant, $\sigma^2_{log\varepsilon}$ is the variance and L is the largest scale.

[3] The data is from Hydrology Meteorology and Complexity laboratory of École des Ponts ParisTech, which is measured by one of 3D sonic anemometers (manufactured by Thies). It is installed at a wind farm located the southeast of Paris in France.

The second-order moment scaling function now is

$$S_2(l) \propto \varepsilon^{2/3} l^{2/3} \tag{1.7.2}$$

which is also known as refined similarity hypothesis.

More research about intermittency will be explained in Chapter 2.

1.8 Summary

Turbulence is unquestionably complicated, and given how important it is, its mechanism and properties have to be exposed. Some basic knowledge and significant advancements of turbulence that have been described above provide a brief comprehension of the dynamic of turbulence. The deterministic equation of turbulence is explained whose symmetries enable the maintenance of invariant properties. Although it hasn't been completed to give out a general solution to NS equation, statistical methods have been commonly used to characterize turbulence. Energy cascade structure greatly inspired turbulence research, such as the classic Kolmogorov assumption that provides the energy spectrum and energy decay law. Besides, the closure techniques, such as QNA and EDQNM, motivate the microcosmic description of turbulence, revealing triad interactions preserving energy conservation. Backscatter term resulting from nonlocal triad interactions generates reversed energy, which leads to a more detailed decay law using EDQNM approach. These theories, particularly the existence of the backscatter term and scaling laws are, however, called into

question by the fundamental property of natural turbulence: intermittency. Therefore, this research is carried out initially on the properties of intermittency, such as multifractality. Then the role of intermittency in scaling laws of natural turbulence is investigated.

Chapter 2

Multiplicative cascade models and Universal Multifractal framework

After realizing the importance of intermittency that is commonly observed by the distribution of velocity increments and of fragment sizes at small scales in turbulence, which results in the gap between classic models and reality, it captures researchers' attention. Due to its non-Gaussian and anomalously heavy tails distribution, the investigation of chaotic and nonlinear cascade driven by the vortex-stretching mechanism is challenging. The multiplicative cascades considering intermittency lead to significant improvements in bridging this gap, such as the simplest $\beta-$model. Moreover, the convergence of multiplicative cascade process based on the central limit theorem contributes to Universal Multifractal (UM) framework to quantity intermittency by two scaling invariant parameters- the multifractality index and mean codimension reflecting the similarity degree, which has been widely applied to describe the extreme nonlinear variability of many fields including the atmospheric turbulence. Two

UM parameters can be estimated by Double Trace Moment (DTM) technique. In this chapter, cascade models considering intermittency as well as the converged UM framework are explained.

2.1 The fractal geometry

As well known, fractal theory characterizing the simplest scale invariance-similarity degree, laid the foundation to overcome the challenge faced by traditional geometry in describing complex irregular events in the nature, and becomes a powerful tool for studying physical phenomena. It motivates the $\beta-$model that take intermittency into consideration.

Despite the fact that many studies significantly boosted the development of fractal theory [53], fractal came to light after Mandelbrot [82, 106] explained Richardson's empirical finding that the length of coast will be greatly exceeded under some dimensional measurements, as the lengths are different under different scale measurements. When the scale approaches 0, the length will be positive infinity. Therefore, he gave Hausdorff dimension [52] based on self-similar method and named as fractal dimension D_F. Fractal dimension D_F is the measure of geometric irregularity degree. Fractal dimension of the Britain coastline is 1.25. It is less than Euclidean dimension of the plane 2 and larger than Euclidean dimension of straight line 1. Moreover, fractal dimension describes self-similarity that is repeated at each scale. The fractal geometry allows to quantify the complexity of a chaotic system by fractal dimension of the converged attractor of trajectories in their phase space. Moreover, it has been widely applied to model the natural phenomena, for example, topographical surfaces, wind

activity [18], and rainfall fields.

A fractal set F [34] satisfies the followings:

(i) F has a fine structure, i.e. details on arbitrarily small scales;

(ii) F is too irregular to be described in traditional geometry, both locally and globally;

(iii) F has some form of self-similarity, perhaps approximate or statistical;

(iv) F in most cases is defined in a very simple way, perhaps recursively.

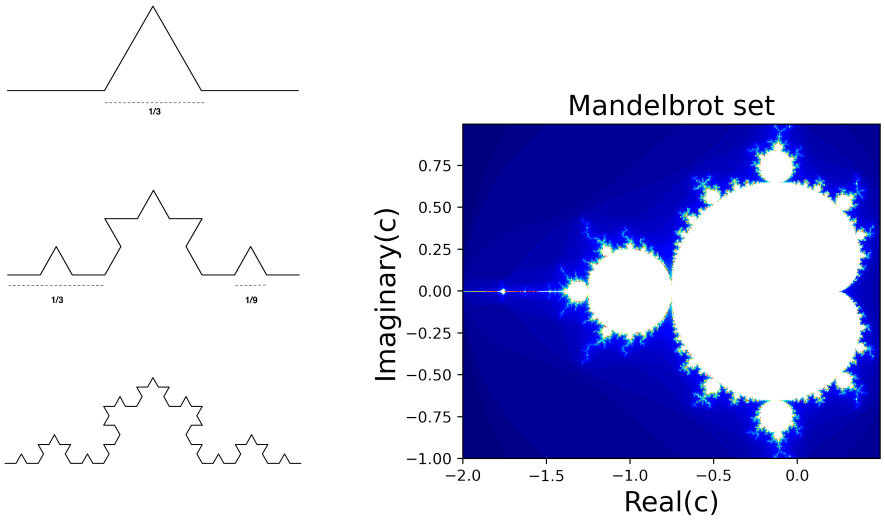

(a) Koch curve (b) The Mandelbrot set

Figure 2.1: Two fractal sets

There are several methods to estimate fractal dimension D_F, such as the box counting method. The most commonly theoretical definition is given as below [82, 85]:

$$D_F = \lim_{r \to 0} -\frac{logN}{log\ r(N)} \Longleftrightarrow N = r(N)^{-D_F} \tag{2.1.1}$$

where N is the number of parts that object exactly decomposed into, and $r(N)$ is the similarity ratio that divides object or inverse resolution. In this way, fractal dimension

D_F is no longer an integer number. And a large fractal dimension D_F indicates the structure is highly irregular.

Another decisive parameter in fractal geometry is co-dimension c, which is the intermittency exponent or Hurst exponent:

$$c = D - D_F \tag{2.1.2}$$

where D is Euclidean dimension. Contrary to fractal dimension D_F, the co-dimension c describes the degree of sparseness.

Here, one-dimensional fractal set Cantor set Fig.2.2 provides an illustration of fractal geometry and clarifies fractal dimension D_F.

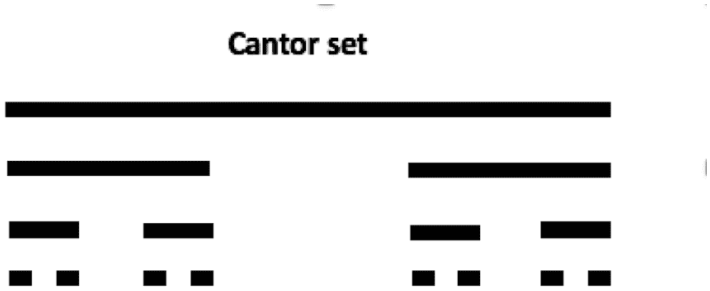

Figure 2.2: Cantor set

It is assumed that the initial scale of this Cantor set is l_0. Separating ratio λ is 3 and the scales after n steps l_n become $\frac{l_0}{\lambda^n}$ which indicates similarity ratio $r(N)$ equals $\frac{1}{\lambda^n}$. The number of small scale l_n is $N(l_n) = 2^n$. Hence, fractal dimension of Cantor set is estimated by

$$D_F = \lim_{n\to\infty} -\frac{log(N(l_n))}{log(\frac{1}{\lambda^n})} = \frac{log2}{log3} \approx 0.63, \tag{2.1.3}$$

which suggests that the co-dimension is $c \approx 0.37$.

Typically, the difficulty of directly obtaining fractal dimension requires estimating the co-dimension to describe irregular properties of fields.

2.2 Multiplicative Process

Following L.F.Richardson, the notion of multiplicative cascade was developed in statistical study of turbulence by Kolmogorov as a phenomenological framework to consider intermittency. Yaglom [137] exhibits an explicit cascade to take intermittency into account. It's a discrete procedure in which the breakdown of turbulent eddies occurs, which is named as "self-similar breakdown of turbulence eddies". He proposed that the distribution of ε is log–normal distribution. This result also testifies to one of the shortcomings of K41 theory. Although log-normal approximation is considered as a good solution for the problem of intermittency in hydrodynamic turbulence, its application has been questioned by other researches. The most common challenge [83, 84] is that tails of probability distribution generated by nonlinear cascade process [93, 62] deviate from the log-normal distribution, especially for high-order moments. And it was until 1980, the fact that these multiplicative cascade models [137, 94, 50] actually is general multifractal process, is realized.

Energy transfers from the large scale l_0 to small scale l by successive steps. Separate ratio in the whole process is assumed as a fixed value λ. After separating n steps, the length of small scales is

$$l_n = \frac{l_0}{\lambda^n} \tag{2.2.1}$$

Energy transfer rate ε_{l_n} at scale l_n should be calculated by the multiplicative method as shown in Fig.2.3:

$$\varepsilon_n = \varepsilon_{l_n} = \mu_n \cdot \varepsilon_{n-1}. \tag{2.2.2}$$

where μ_n is usually assumed to be a scale-independent increment μ.

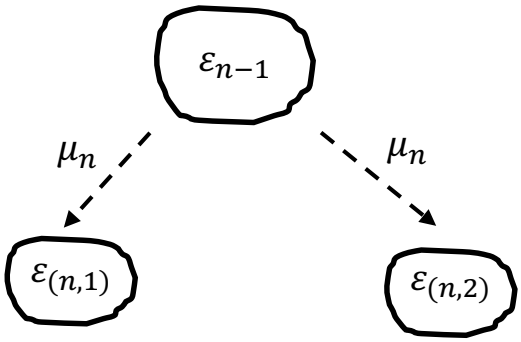

Figure 2.3: Multiplicative process whose separate ratio is 2. And increments for $\varepsilon_{(n,1)}$ and $\varepsilon_{(n,2)}$ are generally considered to be the same.

From Eq 2.2.2, it yields:

$$\varepsilon_n = \mu_n \mu_{n-1} \cdots \mu_1 \varepsilon_0 = (\prod_{m=1}^{n} \mu_m)\varepsilon_0 = \mu^n \varepsilon_0 \tag{2.2.3}$$

Since turbulence energy is conserved in inertial range, the total transfer rate is conserved

$$\langle \varepsilon_n \rangle = \langle \varepsilon_0 \rangle. \tag{2.2.4}$$

Besides, the scaling moment of energy flux density ε_n is:

$$\langle(\varepsilon_n)^q\rangle = \prod_{m=1}^{n}\langle(\mu_m)^q\rangle\langle\varepsilon_0\rangle^q = \langle\mu_1^q\rangle^n\langle\varepsilon_0\rangle^q \tag{2.2.5}$$

2.3 $\beta-$model

Based on Novikov-Stewart model [94], $\beta-$model [42] which is one of the fundamental cascade models considering intermittency is introduced. It has scaling law associated with fractal dimension and therefore provides more physical insight than the traditional approach based on probabilistic models of the dissipation. The idea is that part of the total space in scales is excited.

In the $\beta-$model, as shown in Fig 2.4, small eddies are either alive or dead, which is consistent with the disappearance of small eddies [8, 139] known as internal intermittency of turbulence.

Figure 2.4: $\beta-$cascade. Dash line represents dead eddies and the solid one is alive eddies.

The fraction of alive eddies at scale l_n is

$$\beta_n = \beta^n, \tag{2.3.1}$$

where β is the fraction of alive eddies decreasing by each step. This is the reason why it's named as $\beta-$model.

According to Eq.2.1.1, the alive fraction β_n can be expressed in fractal form:

$$\beta_n = \frac{N}{N(l_n)} = \frac{r(N)^{-D_F}}{r(N)^{-D}} = \frac{\lambda^{n \cdot D_F}}{\lambda^{n \cdot D}} = \lambda^{n \cdot (-c)}. \tag{2.3.2}$$

The alive fraction β at each step from Eq 2.3.1 is

$$\beta = \lambda^{-c}. \tag{2.3.3}$$

Considering this model in the probabilistic form, there are two states of the random increments μ. The probability of alive increment is:

$$Pr(\mu \neq 0) = \lambda^{-c}. \tag{2.3.4}$$

The probability of dead increment is:

$$Pr(\mu = 0) = 1 - \lambda^{-c}. \tag{2.3.5}$$

Here, the nonzero increment

$$\mu = \lambda^c, \tag{2.3.6}$$

which is assumed from the alive fraction β at each step, is larger than 1 to guarantee

the conservation of ε in whole process:

$$\langle \mu \rangle = \lambda^c \cdot Pr(\mu = \lambda^c) + 0 \cdot Pr(\mu = 0) = 1 \Longleftrightarrow \langle \varepsilon_n \rangle = \langle \varepsilon_0 \rangle. \tag{2.3.7}$$

After iterating n steps, there are two possible states at solution $r_n = \lambda^n$. The probability of alive state is:

$$Pr(\varepsilon_n = \mu \varepsilon_{n-1} = (r_n)^c = \lambda^{nc}) = \lambda^{-nc}. \tag{2.3.8}$$

The probability of dead state is:

$$Pr(\varepsilon_n = \mu \varepsilon_{n-1} = 0) = 1 - \lambda^{-nc}. \tag{2.3.9}$$

In the $\beta-$model, the activity of field ε depends on scale invariant fractal co-dimension. The larger co-dimension or high intermittent exponent c indicates more sparseness (less occupied fraction) of the set (See the black area of Fig 2.5).

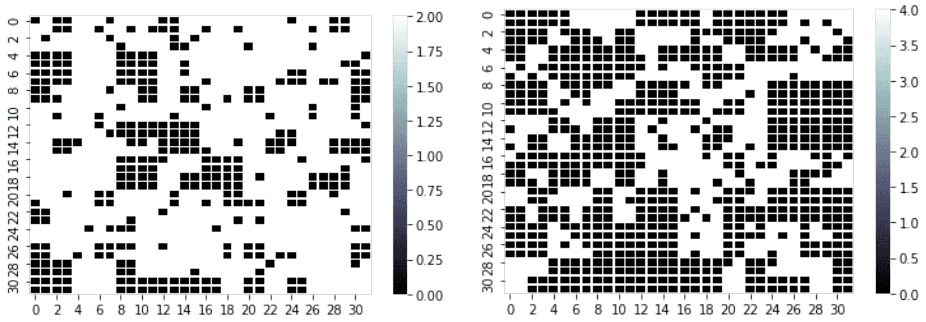

(a) Codimension $c = 0.2$ (b) Codimension $c = 0.4$

Figure 2.5: Examples of two dimensional $\beta-$model. The resolution is 2^5. The white area means alive area, while the black area is dead area.

Since scaling invariant is of great importance and $\beta-$model provides probability

distribution of intermittency, probabilistic conservation at different scales is studied. Due to the length of scales, there are two kinds of scale changes: up-scaling and down-scaling. The length of scales changes with a fixed number that is generally related to the scale ratio λ.

2.3.1 The probabilistic conservation of upscaled $\beta-$model

The up-scaling process is to study the field whose resolution is Λ at the smaller resolution $\frac{\Lambda}{\lambda^n}$ until reaching 1. As an illustration, a two-dimensional $\beta-$model is up-scaled. The field in Fig 2.6a has a resolution of $\Lambda = 2^5$. The resolution of upscaled field in Fig 2.6b is 2^3. Each event in the up-scaled field consists of all events at maximum resolution in the same location so that the mean of these events ε_Λ at maximum resolution Λ is the event in the up-scaled field.

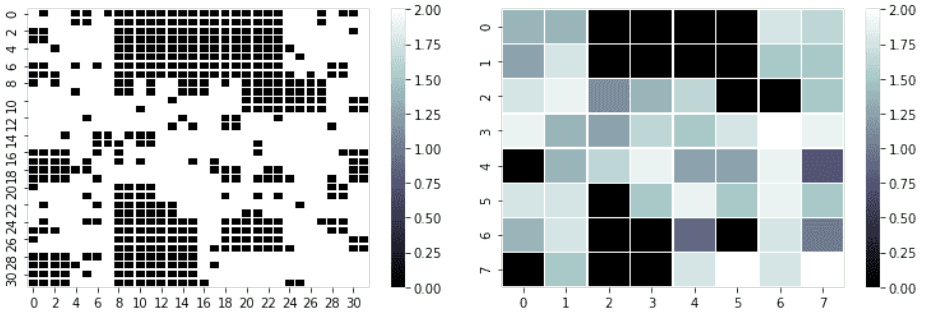

(a) The field (b) The upscaled field

Figure 2.6: The upscaling process of two dimensional $\beta-$model whose codimension is 0.2. The maximum resolution is 2^5.

In order to simplify writing, A_n represents the survival eddy at nth step whose energy flux density is $\varepsilon_n = \lambda^{nc}$

$$A_n : \varepsilon_n = \lambda^{nc}, \tag{2.3.10}$$

while A_n^c is complementary event of A_n corresponding to the dead eddy at nth step

whose energy flux density is $\varepsilon_n = 0$

$$A_n^c : \varepsilon_n = 0. \tag{2.3.11}$$

The number of alive eddies at nth step is denoted as r and s is the number of dead eddies. Eddies at nth step are independent. Upscaled steps is m. Therefore, $\overline{A_n^r (A_n^c)^s}$ is defined as possible upscaled event at $(n-m)$th step, which is generated by r alive eddies and s dead eddies at nth step ($r+s=2^m$). The energy flux density of $\overline{A_n^r (A_n^c)^s}$ is

$$\overline{A_n^r (A_n^c)^s} : \overline{\varepsilon}_{n-m} = \frac{r \cdot \varepsilon_n(A_n) + s \cdot \varepsilon_n(A_n^c)}{2^m} = \frac{r \cdot 2^{nc}}{2^m},\ \forall r + s = 2^m. \tag{2.3.12}$$

After upscaled one step ($m = 1$), there are three types of upscaled states:

$$\overline{A_n^2} : \overline{\varepsilon}_{n-1} = 2^{nc}; \tag{2.3.13a}$$

$$\overline{A_n A_n^c} : \overline{\varepsilon}_{n-1} = \frac{2^{nc}}{2}; \tag{2.3.13b}$$

$$\overline{(A_n^c)^2} : \overline{\varepsilon}_{n-1} = 0. \tag{2.3.13c}$$

According to the up-scaling process and independence, their probabilities are:

$$P(\overline{A_n^2}) = P(A_n)^2; \tag{2.3.14a}$$

$$P(\overline{(A_n^c)^2}) = P(A_n^c)^2; \tag{2.3.14b}$$

$$P(\overline{A_n A_n^c}) = 2P(A_n)P(A_n^c). \tag{2.3.14c}$$

Here, upscaled event $\overline{A_n A_n^c}$ could be produced by two possible arrangements of eddies at nth step: $(\underline{A_n}, \underline{A_n^c})$, $(\underline{A_n^c}, \underline{A_n})$, so the coefficient of its probability in Eq 2.3.14c

should be 2.

Moreover, the sum of upscaled events' probabilities equals 1, which ensures probabilistic conservation in upscaling process, as shown in following:

$$P(\overline{A_n^2}) + P(\overline{A_n A_n^c}) + P(\overline{(A_n^c)^2}) = (P(\overline{A_n}) + P(\overline{A_n^c}))^2 = 1. \tag{2.3.15}$$

For other cases ($m > 1$), the number of possible upscaled event $\overline{A_n^r (A_n^c)^s}$ increases and probability can be directly derived by the binomial coefficient theory, which indicates possible arrangements of eddies at nth step should be taken into consideration. Therefore, probability of upscaled event $\overline{A_n^r (A_n^c)^s}$ is given by:

$$P(\overline{A_n^r (A_n^c)^s}) = \binom{2^m}{r} P(A_n)^r P(A_n^c)^s. \tag{2.3.16}$$

The possibility field of up-scaled events is also conserved:

$$\sum_{r+s=2^m} P(\overline{A_n^r (A_n^c)^s}) = \sum_{r+s=2^m} \binom{2^m}{r} P(A_n)^r P(A_n^c)^s = (P(\overline{A_n}) + P(\overline{A_n^c}))^{2^m} = 1. \tag{2.3.17}$$

Fig 2.7 is the probability of events in two cascade step upscaled field. Energy flux density is normalized by $\varepsilon_n = \lambda^{nc}$ so that event 1 in Fig 2.7 is A_n and event 0 is A_n^c.

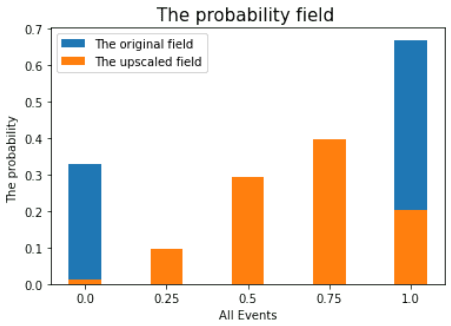

Figure 2.7: The probability of events in two cascade step upscaled field. The original field is one-dimensional $\beta-$model whose resolution is 2^8. The codimension is 0.2.

Now the statistical moments of up-scaled event $\overline{\varepsilon}_{n-m}$ could be calculated as follow:

$$\begin{aligned} E(\overline{\varepsilon}^q_{n-m}) &= \sum_{r+s=2^m} (\overline{\varepsilon}_{n-m}(\overline{A^r_N(A^c_N)^s}))^q P(\overline{A^r_N(A^c_N)^s}) \\ &= \sum_{r+s=2^m} (\frac{r}{2^m} \cdot 2^{nc})^q \binom{2^m}{r} P(A_N)^r P(A^c_N)^s. \end{aligned} \tag{2.3.18}$$

For the case $q = 1$:

$$\begin{aligned} E(\overline{\varepsilon}_{n-m}) &= \sum_{r=1}^{2^m} \frac{r}{2^m} \cdot 2^{nc} \binom{2^m}{r} P(A_N)^r P(A^c_N)^s \\ &= \sum_{r=1}^{2^m} \binom{2^m-1}{r-1} P(A_N)^{r-1} P(A^c_N)^{2^m-r} \\ &= (P(A_N) + P(A^c_N))^{2^m-1} = 1. \end{aligned} \tag{2.3.19}$$

The high statistical moments in study to describe distribution have $q \leq 4$. The upscaled step m is assumed large than 2 and it yields $q < 2^m$. From Eq 2.3.19, the

statistical moments function can be substituted into:

$$\begin{aligned} E(\overline{\varepsilon}_{n-m}^{q}) &= \sum_{r=1}^{2^m} (\frac{r}{2^m} \cdot 2^{nc})^{q-1} \binom{2^m-1}{r-1} P(A_N)^{r-1} P(A_N^c)^s \\ &= \sum_{r=1}^{2^m} (\frac{r}{2^m})^{q-1} \binom{2^m-1}{r-1} P(A_N)^{r-q} P(A_N^c)^s \\ &= \sum_{r=1}^{2^m} (\frac{r}{2^m})^{q-1} \cdot \frac{(2^m-1)!}{(2^m-r)! \cdot (r-1)!} P(A_N)^{r-q} P(A_N^c)^s. \end{aligned} \tag{2.3.20}$$

According to the inequality

$$\frac{1}{2^m} < \frac{1}{2^m-1} < \frac{1}{2^m-2}, \tag{2.3.21}$$

Eq 2.3.20 becomes

$$\begin{aligned} E(\overline{\varepsilon}_{n-m}^{q}) &< \sum_{r=1}^{2^m} r^{q-1} \cdot \frac{(2^m-q)!}{(2^m-r)! \cdot (r-1)!} P(A_N)^{r-q} P(A_N^c)^s \\ &< \frac{(2^m-q)!}{(2^m-1)!} P(A_N)^{1-q} P(A_N^c)^{2^m-1} + \sum_{r=2}^{2^m} r^{q-1} \cdot \frac{(2^m-q)!}{(2^m-r)! \cdot (r-1)!} P(A_N)^{r-q} \cdot \\ &\quad P(A_N^c)^s. \end{aligned} \tag{2.3.22}$$

The right hand side of Eq 2.3.22 is simply denoted as $E_{max}(\overline{\varepsilon}_{n-m}^{q})$. Considering

$r = 1 + r - 1$, $E_{max}(\overline{\varepsilon}^q_{n-m})$ turns into

$$\begin{aligned}
E_{max}(\overline{\varepsilon}^q_{n-m}) =& \frac{(2^m-q)!}{(2^m-1)!}P(A_N)^{1-q}P(A_N^c)^{2^m-1} + \sum_{r=2}^{2^m} r^{q-2}\cdot(1+r-1)\cdot\frac{(2^m-q)!}{(2^m-r)!\cdot(r-1)!}\cdot \\
& P(A_N)^{r-q}P(A_N^c)^s \\
=& \frac{(2^m-q)!}{(2^m-1)!}P(A_N)^{1-q}P(A_N^c)^{2^m-1} + \sum_{r=2}^{2^m} r^{q-2}\cdot\frac{(2^m-q)!}{(2^m-r)!\cdot(r-1)!}P(A_N)^{r-q}\cdot \\
& P(A_N^c)^s + \sum_{r=2}^{2^m} r^{q-2}\cdot\frac{(2^m-q)!}{(2^m-r)!\cdot(r-2)!}P(A_N)^{r-q}P(A_N^c)^s \\
& \vdots \\
=& \frac{(2^m-q)!}{(2^m-1)!}P(A_N)^{1-q}P(A_N^c)^{2^m-1} + \sum_{r=2}^{2^m} r^{q-2}\cdot\frac{(2^m-q)!}{(2^m-r)!\cdot(r-1)!}P(A_N)^{r-p}\cdot \\
& P(A_N^c)^s + \cdots + \sum_{r=q}^{2^m}\frac{(2^m-q)!}{(2^m-r)!\cdot(r-q)!}P(A_N)^{r-p}P(A_N^c)^s.
\end{aligned} \tag{2.3.23}$$

Obviously the last term in Eq 2.3.23 equals 1 and

$$E(\overline{\varepsilon}^q_{n-m}) < E_{max}(\overline{\varepsilon}^q_{n-m}),\ E_{max}(\overline{\varepsilon}^q_{n-m}) > 1. \tag{2.3.24}$$

When statistical moment is $q = 1$, the upscaling process of $\beta-$model is conserved. When the statistical moments q is larger than 1, the value of upscaled fields $E_{max}(\overline{\varepsilon}^q_{n-m})$ suggests the weight of the alive eddies in the up-scaled field gets higher.

2.3.2 The probabilistic conservation of $\beta-$model in the down-scaling

This part will discuss the conservation of down-scaled field whose probability is determined by the hierarchical path in downscaling.

The ancestor eddy must be alive $\varepsilon_0 = 1$ due to the fact that alive eddies cannot be generated by dead mother eddy. The probabilities of increments are simplified as:

$$Pr(\mu = \lambda^c) = \lambda^{-c} = P_1; \tag{2.3.25a}$$

$$Pr(\mu = 0) = 1 - \lambda^{-c} = 1 - P_1. \tag{2.3.25b}$$

The number of alive eddies at nth step is denoted by r_n in downscaling, which corresponds to energy flux density $\varepsilon_n = r_n \cdot 2^{nc}$, preventing to mislead with the alive number at other steps.

When $n = 1$, there are three kinds of possible states at 1st cascade step:

$$\textit{All small eddies are alive } (r_1 = 2) : \varepsilon_1 = 2 \cdot 2^c; \tag{2.3.26a}$$

$$\textit{One of the small eddies is alive } (r_1 = 1) : \varepsilon_1 = 1 \cdot 2^c; \tag{2.3.26b}$$

$$\textit{None of the small eddies is alive } (r_1 = 0) : \varepsilon_1 = 0 \cdot 2^c. \tag{2.3.26c}$$

The probability of state Eq.2.3.26b has to take arrangements of events into consideration too. So their probabilities are:

$$P(\varepsilon_1 = 2 \cdot 2^c) = \binom{2}{2} \cdot P_1^2; \tag{2.3.27a}$$

$$P(\varepsilon_1 = 1 \cdot 2^c) = \binom{2}{1} \cdot P_1^1 \cdot (1 - P_1)^1; \tag{2.3.27b}$$

$$P(\varepsilon_1 = 0 \cdot 2^c) = \binom{2}{0} \cdot (1 - P_1)^2. \tag{2.3.27c}$$

Plus, the sum of these events' probabilities is 1 ensuring probability conservation.

When $n > 1$, energy flux density at nth step that depends on states at former steps can be generated by different events, suggesting that probabilities should be obtained by conditional probability theory

$$P(A|B) = \frac{P(AB)}{P(B)}. \tag{2.3.28}$$

Event at nth step can be generated by numerous different states at $(n-1)$th step when only the state at $(n-1)$th step is taken into account. Therefore, events at the nth step can be generated by many possible paths by considering hierarchical former steps.

Alive number r_n could be either the odd number or the even number. These situations will be separately discussed. $r_n = 2^n - 2j$ $(0 \leq j < 2^{n-1})$ alive eddies at nth step, which is even, should be generated from event $r_{n-1} = 2^{n-1}$ or event $r_{n-1} = 2^{n-1} - j$ if we only consider the $(n-1)$th step. Meanwhile, event $r_{n-1} = 2^{n-1} - j$ could be generated through different paths from 1st step to $(n-2)$th step which exhibits hierarchical property in the downscaling. Because dead eddies only generate dead eddies instead of alive eddies that has an impact on the event at nth step. As a result, $2j$ dead eddies at nth step, which are generated by different former layers, could consist of dead eddies produced by the last step or the former steps. In this way, there are plenty of arrangements of dead eddies which will be represented by coefficient $a(m)$. $h_{(z)}$ dead eddies which are produced at $(n-z)$th step except those eddies generated by former steps could be referred as binomial coefficient $\binom{2^{n-z}-g_{(z)}}{h_{(z)}}$. And $g_{(z)}$ is the number of supposed dead eddies at $(n-z)$th step which is caused by former steps. Therefore $g_{(z)} = \sum_{m'=z+1} h_{(m')} \cdot 2^{m'-z}$ corresponds to the supposed

dead eddies at $(n-z)$th step which is caused by former step. So $\sum h_{(z)} \cdot 2^z = 2j$ is the number of dead eddies at nth step, whereas the sum of $\sum h_{(z)}$ is the index of the probabilities of dead eddy.

The following gives a clear formula of events probabilities:

$$\begin{aligned}
P(\varepsilon_n = (2^n - 2j)\cdot 2^{nc}) =& P(r_n = 2^n - 2j) \\
=& P(r_{n-1} = 2^{n-1}) \cdot \tbinom{2^n}{2j} \cdot P_1^{2^n-2j} \cdot (1-P_0)^{2j} + P(r_{n-1} = 2^{n-1}-1)\cdot \\
& \tbinom{2^n-2}{2j-2} \cdot P_1^{2^n-2j} \cdot (1-P_1)^{2j-2} + \cdots + P(r_{n-1} = 2^{n-1}-j) \cdot P_1^{2^n-2j} \\
=& \sum_{m'=0}^{j} P_{(r_{n-1}=2^{n-1}-m')} \cdot \tbinom{2^n-2m'}{2j-2m'} \cdot P_1^{2^n-2j} \cdot (1-P_1)^{2j-2m'} \\
=& \sum a(m) \cdot P_1^w \cdot (1-P_1)^v
\end{aligned} \tag{2.3.29}$$

where $a(m) = \prod_{z=0}^{n} \binom{2^{n-z}-g_{(z)}}{h_{(z)}}$, in which $\sum h_{(z)} = v$, $\sum h_{(z)} \cdot 2^z = 2j$, $g_{(z)} = \sum_{m'=z+1} h_{(m')} \cdot 2^{m'-z}$, $\sum(2^{n-z} - g_{(z)} - h_{(z)}) = w$.

Another case is $p_n = 2^n - 2j - 1$ alive eddies at nth step. The same procedure is easily adapted to obtain its probability.

$$\begin{aligned}
P(\varepsilon_n = (2^n - 2j - 1)\cdot 2^{nc}) =& P(p_n = 2^n - 2j - 1) \\
=& P(p_{n-1} = 2^{n-1}) \cdot \tbinom{2^n}{2j+1} \cdot P_1^{2^n-2j-1} \cdot (1-P_1)^{2j+1} + \\
& P(p_{n-1} = 2^{n-1}-1) \cdot \tbinom{2^n-2}{2j-2+1} \cdot P_1^{2^n-2j-1} \cdot (1-P_1)^{2j-2+1} + \\
& \cdots + P(p_{n-1} = 2^{n-1}-j)\tbinom{2^n-2j}{1} \cdot P_1^{2^n-2j-1} \cdot (1-P_1) \\
=& \sum_{t=0}^{j} P_{(p=2^{n-1}-m')} \cdot \tbinom{2^n-2m'}{2j+1-2m'} \cdot P_1^{2^n-2j-1} \cdot (1-P_1)^{2j+1-2m'} \\
=& \sum a(m) \cdot P_1^w \cdot (1-P_1)^v
\end{aligned} \tag{2.3.30}$$

where $a(m) = \prod_{z=0}^{n} \binom{2^{n-z}-g_{(z)}}{h_{(z)}}$, in which $\sum h_{(z)} = v$, $\sum h_{(z)} \cdot 2^z = 2j+1$, $g_{(z)} = \sum_{m'=z+1} h_{(m')} \cdot 2^{m'-z}$, $\sum 2^{n-z} - g_{(z)} - h_{(z)} = w$.

Moreover, the sum of probabilities of energy density at nth step equals 1 suggesting hierarchical theory exits in downscaling. Above two probabilities equations of down-scaled $\beta-$model provide probability without computing probabilities of former events.

The detailed probability of up-scaled and down-scaled $\beta-$model are presented. It shows that the measure of probability is conserved when scale changes.

2.4 $\alpha-$model

As known, two states are used to roughly describe eddies in $\beta-$model. However, Schertzer and Lovejoy in 1984 discovered that various thresholds is allowed for a hierarchy of many fractals to characterize irregular field, which is the idea of multifractal. Instead of that eddy is either "alive" or "dead", $\alpha-$model is introduced to reveal multifractal field by considering intensity of activity that eddy is going to act more active or less active, as shown in Fig 2.8.

Figure 2.8: $\alpha-$model. Compared with $\beta-$model, some eddies act more active and the rest acts less active.

Due to this detailed description of activities, $\alpha-$model is a better approximation and exponent α represents instability degree. The intensity of activity based on increments Eq 2.3.6 in $\beta-$model is related to threshold, which can be written in the form of singularity with separate ratio λ^{γ}.

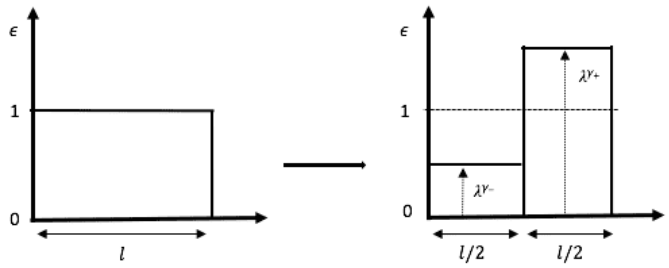

Figure 2.9: The separating process of $\alpha-$model when λ equals 2.

Therefore, increments of $\alpha-$model shown in Fig 2.9 are:

$$More\ active\ (\gamma_+ > 0) : \mu = \lambda^{\gamma+}; \tag{2.4.1a}$$

$$Less\ active\ (\gamma_- < 0) : \mu = \lambda^{\gamma-}; \tag{2.4.1b}$$

where

$$\gamma_+ = \frac{c}{\alpha}; \gamma_- = -\frac{c}{\alpha'}; \frac{1}{\alpha} + \frac{1}{\alpha'} = 1. \tag{2.4.2}$$

When $\gamma_- \to -\infty$, $\gamma_+ = c$ which is $\beta-$model. And there is only one unique singularity in $\beta-$model.

Due to Eq.2.3.4, 2.3.5, probabilities of increments are:

$$Pr(\mu = \lambda^{\gamma_+}) = \lambda^{-c}; \tag{2.4.3a}$$

$$Pr(\mu = \lambda^{\gamma_-}) = 1 - \lambda^{-c}. \tag{2.4.3b}$$

As the averaged increments should be conversed $\langle\mu\rangle = 1$, $\alpha-$model requires

$$\langle\mu\rangle = \lambda^{\gamma_+} \cdot Pr(\mu = \lambda^{\gamma_+}) + \lambda^{\gamma_-} \cdot Pr(\mu = \lambda^{\gamma_-}) = 1, \tag{2.4.4}$$

where parameters are (γ_+, γ_-, c) and two of them could be chosen freely. The singularities in separating process indicate $\alpha-$model is multifratal. Obviously, $\beta-$model is a special case that $\alpha = 1$ and $\alpha' = 0$, which suggests $\beta-$model is a fractal model.

After iterating $n = n_+ + n_-$ step, probability of states at nth step is:

$$Pr(\varepsilon_n = (\lambda^n)^{\gamma_n}) = \binom{n}{n_+}\lambda^{-cn_+}(1 - \lambda^{-c})^{n_-}. \tag{2.4.5}$$

where

$$\gamma_n = \frac{n_+\gamma_+ + n_-\gamma_-}{n_+ + n_-}; \tag{2.4.6}$$

n_+ is number of more active steps and n_- is number of less active steps.

For those intensity states, probability is summed as the following:

$$Pr(\varepsilon_n \geq (\lambda^n)^{\gamma_i}) = \sum_j p_{ij} (\lambda^n)^{-c_{ij}} \tag{2.4.7}$$

where p_{ij} is the prefactors in Eq 2.4.5, c_{ij} is the sub-codimensions.

2.5 Multifractal field

By re-normalizing $\alpha-$model, multifractal field is obtained. These n steps with two increment states cascade are replaced by a single step cascade with $n+1$ states. The new scale ratio λ' replaces λ^n and λ' will eventually approach ∞. Here, c_i is defined by

$$c_i = min\{c_{ij}\} = c(\gamma_i). \tag{2.5.1}$$

And Eq 2.4.7 turns into

$$Pr(\varepsilon_{\lambda'} \geq (\lambda')^{\gamma_i}) = p_i (\lambda')^{-c_i}. \tag{2.5.2}$$

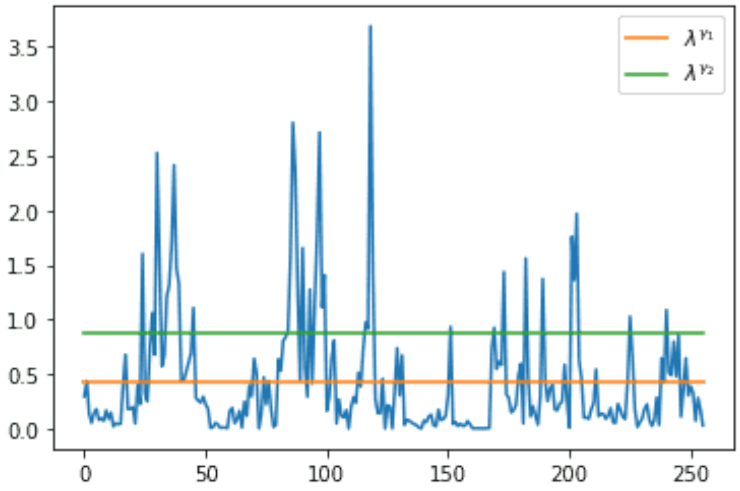

Figure 2.10: A irregular field showing the codimensions $c(\gamma)$ is associated to different singularities γ.

For uniform and continuous distribution, Eq 2.5.2 could be written as

$$Pr(\varepsilon_\lambda \geq \lambda^\gamma) \approx \lambda^{-c(\gamma)}, \tag{2.5.3}$$

where p_i is absorbed by $\approx$. It describes probabilities of events whose intensity exceeds the scale-dependant threshold λ^γ and yields a scale-invariant singularity γ, as shown in Fig 2.10. Since Eq 2.5.2 indicates there is an unique co-dimension corresponding to scaling threshold, $c(\gamma)$ in Eq 2.5.3 is an increasing function [116] of the singularity γ in Fig. 2.11. The multifractality of field is represented by codimension function $c(\gamma)$.

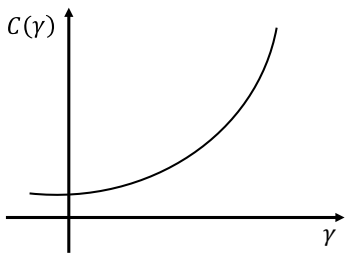

Figure 2.11: The codimension function $c(\gamma)$.

Now let's move to scaling statistical moments of energy dissipation rate. The statistical moments of energy dissipation rate $\langle(\varepsilon_\lambda)^q\rangle$ has been given in Eq 2.2.5. Schertzer and Lovejoy [79] obtained that the qth moment of energy dissipation rate $\langle(\varepsilon_\lambda)^q\rangle$ can be expressed with the resolution λ

$$\langle(\varepsilon_\lambda)^q\rangle \approx \lambda^{K(q)} \tag{2.5.4}$$

where $K(q)$ is moment scaling function which is convex. Moreover, Parisi and Frisch in 1985 [100] discovered the connection of scaling moment function $K(q)$ and the codimension function $c(\gamma)$ through Legendre transform (Appendix A.1):

$$c(\gamma) = \max_q(q\gamma - K(q)) = q_\gamma\gamma - K(q_\gamma); \tag{2.5.5a}$$

$$K(q) = \max_\gamma(q\gamma - c(\gamma)) = q\gamma_q - c(\gamma_q) \tag{2.5.5b}$$

where q_γ is defined by $K'(q_\gamma) = \gamma$ and γ_q is defined by $c'(\gamma_q) = q$. The statistical moment and singularity are unique corresponded. Because there are only convexity constraints, characteristic scaling function $K(q)$ and codimension function $c(\gamma)$ may

depend on infinite number of parameters.

2.6 Universal Multifractal

The idea that only a few parameters are crucial in determining "universality" classes caught scientists' attention in the middle of 1980s. Based on the central limit theorem of additive process, Schertzer and Lovejoy in 1987 [116] obtained that multiplicative cascade processes converge to a "universality" process under quite general conditions, which is named as Universal Multifractal (UM). For conservative processes, these infinite parameters determined scaling moment function $K(q)$ and codimension function $c(\gamma)$, can be reduced to two.

When scaling moment is $q = 1$ indicating it is the mean of process, corresponding singularity is γ_1. Due to Eq 2.5.5, it has

$$\langle \varepsilon_\lambda \rangle \approx \lambda^{\gamma_1 - c(\gamma_1)}. \tag{2.6.1}$$

As the field is conserved $\langle \varepsilon_\lambda \rangle = 1$, it has

$$\gamma_1 = c(\gamma_1) = C_1 \tag{2.6.2}$$

Therefore, C_1 is the codimension of singularity which related to the mean field. Moreover, Legendre transforms yield

$$c(\gamma_1) = c(C_1) = C_1,\ c'(\gamma_1) = c'(C_1) = 1 \tag{2.6.3a}$$

$$K(1) = \gamma_1 - c(\gamma_1) = 0,\ K'(1) = \gamma_1 = C_1. \tag{2.6.3b}$$

Then multifractality can be characterized by the deviations of $K(q)$ from the mean process $q = 1$. Since moment scaling function $K(q)$ is convex, local radius of curvature R_K at $q = 1$, which is local rate of change of slope, enables to define multifractality index α. The local radius of curvature R_K at $q = 1$ is

$$R_K(q = 1) = \frac{(1 + (K'(1))^2)^{3/2}}{K''(1)} = \frac{(1 + C_1^2)^{3/2}}{K''(1)} \tag{2.6.4}$$

And multifractality index α is defined as

$$\alpha = \frac{K''(1)}{K'(1)}. \tag{2.6.5}$$

Therefore C_1 is mean codimension measuring mean concentration of the activity. Typically, C_1 of irregular field couldn't be smaller than 0 ($C_1 \geq 0$). When C_1 equals 0, the process is homogeneous, and intermittency doesn't appear. Multifractality index α ($0 \leq \alpha \leq 2$) measures how quickly intermittency evolves when singularity slightly deviates from the singularity obtained from average field. $\alpha = 0$ is a monofractal field, such as $\beta-$model, while $\alpha = 2$ is the Log-normal model [137]. It's important to emphasize that α in UM is not the same as the one in $\alpha-$model.

So the moment scaling function $K(q)$ and codimension function $c(\gamma)$ described by UM parameters [79] are (See in Appendix A.2)

$$K(q) = \begin{cases} \frac{C_1}{\alpha - 1}(q^\alpha - q), & \alpha \neq 1 \\ C_1 q Ln(q), & \alpha = 1 \end{cases} \tag{2.6.6a}$$

$$c(\gamma) = \begin{cases} C_1(\frac{\gamma}{C_1 \alpha'} + \frac{1}{\alpha})^{\alpha'}, & \alpha \neq 1 \\ C_1 exp(\frac{\gamma}{C_1} - 1), & \alpha = 1 \end{cases} \tag{2.6.6b}$$

where

$$\frac{1}{\alpha} + \frac{1}{\alpha'} = 1. \tag{2.6.7}$$

Also included is multifractal impact on structural function $S_n(l)$ Eq 1.2.9 [123]. When a field is monofractal, scaling exponent $\zeta(q)$ is linear

$$\zeta(q) = qH, \tag{2.6.8}$$

however structure function of universal multifractal field exhibits deviations from linearity, which can be characterised by UM parameters

$$\zeta(q) = qH - \frac{C_1}{\alpha - 1}(q^\alpha - q), \tag{2.6.9}$$

where $H = \zeta(1)$ is scaling Hurst exponent corresponding to the scaling of average absolute fluctuations. UM parameters could be obtained from plot of $log_{10}(q\zeta'(0) - \zeta(q))$ and $log_{10}(q)$.

2.6.1 Double Trace Moment

UM parameters can be directly estimated by Double Trace Moment (DTM) method [70, 133]. Considering renormalized ηth power of field whose resolution is λ

$$\varepsilon_\lambda^{(\eta)} = \frac{\varepsilon_\lambda^\eta}{\langle \varepsilon_\lambda^\eta \rangle}, \tag{2.6.10}$$

and statistical qth moment of $\varepsilon_\lambda^{(\eta)}$ obtained from Eq 2.5.4 is

$$\langle \varepsilon_\lambda^{(\eta)q} \rangle = \frac{\langle \varepsilon_\lambda^{\eta q} \rangle}{\langle \varepsilon_\lambda^\eta \rangle^q} \approx \frac{\lambda^{K(\eta q)}}{\lambda^{qK(\eta)}} = \lambda^{K(q,\eta)} \tag{2.6.11}$$

where

$$K(q,\eta) = K(\eta q) - qK(\eta). \tag{2.6.12}$$

In UM framework, moment function has

$$K(q,\eta) = \eta^\alpha K(q) \tag{2.6.13}$$

and $K(q,\eta)$ turns into

$$K(q,\eta) = \eta^\alpha \frac{C_1}{\alpha - 1}(q^\alpha - q). \tag{2.6.14}$$

It suggests the slope of log-log plot of $K(q,\eta)$ and η is α and $C_1 = exp(b)\frac{\alpha-1}{q^\alpha - q}$, where b is the intercept shown in Fig. 2.12.

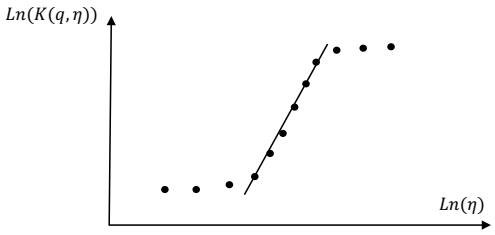

Figure 2.12: The function $K(q, \eta)$ obtained by DTM method. UM parameters is estimated by linear fit of empirical points.

2.6.2 Sampling dimension

It is crucial to note that statistical properties of multifractal process in above are defined for infinite statistical ensembles. However, empirically statistical analysis normally is supported by finite samples instead of infinities that don't capture the whole rare events. Thus, sample dimension D_s is introduced to describe finite samples by generating a maximum singularity γ_s and critical moment q_s, which is the maximum value that codimension and scaling moment function are reliable statistical estimated.

For a collection of N_s samples, the resolution of samples is λ and there are λ^D values for each $D-$dimensional sample. Based on the definition of codimension Eq 2.5.3, there is a maximum value of γ, which is denoted γ_s, and could be observed on at least one sample. Hence, it yields:

$$N_s \lambda^D \lambda^{c(\gamma_s)} \approx 1. \tag{2.6.15}$$

And the sampling definition is defined as

$$N_s = \lambda^{D_s} \Rightarrow D_s = \frac{log(N_s)}{log(\lambda)}. \tag{2.6.16}$$

From Eq 2.6.15, it has

$$c(\gamma_s) = D + D_s. \tag{2.6.17}$$

According to Fig 2.11, when the sampling dimension is considered, the maximum singularity gets large indicating that more rare events are studied.

The critical moment $q_s = c'(\gamma_s)$ which depends on number of samples, is always used to study scaling moment function. It is the highest order moment after which estimated moment scaling function $K(q)$ will become linear. The critical moment $q_s = c'(\gamma_s)$ obtained from the UM framework is:

$$q_s = (\frac{D + D_s}{C_1})^{\frac{1}{\alpha}}. \tag{2.6.18}$$

2.7 Summary of Chapter 2

In this chapter, the most basic phenomenological cascade $\beta-$model considering the intermittency is explained. Since many studies have attempted to understand the intermittency with its' probability distribution and the physical $\beta-$model gives the probabilistic representation, the probability conservation under the changing scales is studied. It demonstrates that probability conservation is a scaling invariant, which lays a solid foundation for the further developed multifractal field. However, the alive eddies at high moments will take more weights, causing the probability field to be

larger than 1.

Based on the $\beta-$model, the multifractal is introduced to provide a remarkable accuracy description of irregular fields. Meanwhile, UM framework, which is inspired by the multifractal process and the central limit theorem, is presented as a powerful framework for characterizing the multifractality of weather and climate on a large spatial and temporal scale. A detailed analysis is carried out in the next chapter.

Chapter 3

The Scaling Gyroscope Cascade model and numerical methods

The intermittency of natural turbulence is considered one of the most important phenomena in classical physics, nevertheless, for which neither a thorough theoretical foundation nor phenomenological knowledge is sufficient. Scaling Gyroscope Cascade (SGC) model [20, 21, 120] was motivated by Arnold's insight [4] that vorticity equation arising from NS equation is analogous to Euler's gyroscope equation. On the basis of this similarity, SGC model preserves the majority of fundamental properties of NS equation, such as the triad interaction and energy conservation. With its capacity to generate the intermittency and quantitative description of natural turbulence, SGC model is regarded as being extremely close to turbulence in nature and boosting the possibility to precisely study intermittency and its role in energy decay. Various numerical techniques are used to provide the velocity time evolution of SGC model,

deformation of NS equation, which is particularly difficult to obtain the general solution. These methods are the simplest explicit Euler method, the classic fourth-order Runge-Kutta method, and two methods considering physical properties. They are the semi-implicit Euler method, which is often used to describe the motion of rigid bodies, and the slaved Adams-Bashforth method, which takes into account the fast damping of waves with high wave numbers. Algorithm analysis is performed, and the results obtained from these three approaches are compared in order to identify effective numerical simulation approach.

3.1 Scaling Gyroscope Cascade (SGC) model

Scaling Gyroscopes Cascade (SGC) model [20, 21, 120] is a space-time gyroscope step-step model depicting evolution of the superposition coupling of daughter eddies in Fig.3.1, which is based on a parsimonious discretization of Bernoulli's form of NS equation. The model doesn't undergo an infinite number of iterations, and the maximum finite cascade step is n.

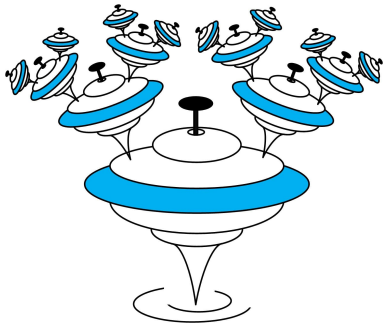

Figure 3.1: Gyroscope cascade whose separate ratio is $\lambda = 2$.

SGC model is developed as a result of nonlocal orthogonal approximation of NS

equation in Bernoulli form satisfying gyroscope equation (See Appendix B.1), in which velocity and vorticity are analogous to angular momentum $\boldsymbol{M}$ and rotation $\boldsymbol{\Omega}$. In the imcompressibility condition

$$div(\boldsymbol{u}(\boldsymbol{x},t)) = 0, \tag{3.1.1}$$

Bernoulli form of NS equation is

$$(\frac{\partial}{\partial t} - v\Delta)\boldsymbol{u}(\boldsymbol{x},t) = \boldsymbol{u}(\boldsymbol{x},t) \wedge \boldsymbol{\omega}(\boldsymbol{x},t) - grad(\alpha^*); \tag{3.1.2a}$$

$$\boldsymbol{\omega}(\boldsymbol{x},t) = curl(\boldsymbol{u}(\boldsymbol{x},t)) \tag{3.1.2b}$$

where $\boldsymbol{\omega}(\boldsymbol{x},t)$ is vorticity and α^* is kinematic pressure. Projector $P(\nabla)$ corresponding to $\widehat{P}(\boldsymbol{k})$ in Fourier space

$$P_{i,j}(\nabla) = \delta_{i,j} - \nabla_i \nabla_j \Delta^{-1} \ (\delta_{i,j} \ is \ Kronecker's \ \delta) \tag{3.1.3}$$

imposes the imcompressibility condition Eq.3.1.1 restriction on advection term, classic pseudospectral technique typically employed in DNS [102, 17], and Eq.3.1.2 in Fourier space turns into:

$$(\frac{\partial}{\partial t} + vk^2)\widehat{\boldsymbol{u}}(\boldsymbol{k},t) = \widehat{P}(\boldsymbol{k}) \cdot \int_{\boldsymbol{p}+\boldsymbol{q}=\boldsymbol{k}} \widehat{\boldsymbol{u}}(\boldsymbol{p},t) \wedge \widehat{\boldsymbol{\omega}}(\boldsymbol{q},t) d^d\boldsymbol{p}, \tag{3.1.4}$$

where $\boldsymbol{\omega}$ is vorticity:

$$\widehat{\boldsymbol{\omega}}^i_m = i\boldsymbol{k}^i_m \wedge \widehat{\boldsymbol{u}}^i_m. \tag{3.1.5}$$

Here, the velocity-vorticity vertex of triad interaction $(\boldsymbol{k},\boldsymbol{p},\boldsymbol{q})$ also only exits under

orthogonality condition

$$\boldsymbol{k} \cdot \widehat{\boldsymbol{u}}(\boldsymbol{k}, t) = 0. \tag{3.1.6}$$

Assuming arbitrary nonlocalness parameter λ_k in Eq.1.6.16, the orthogonality of vorticity-velocity vertex interaction is

$$|\boldsymbol{k}| \ll |\boldsymbol{p}| \approx |\boldsymbol{q}|, \boldsymbol{p} \perp \boldsymbol{k} \Longrightarrow \qquad (\widehat{\boldsymbol{u}}(\boldsymbol{p}) \wedge \widehat{\boldsymbol{\omega}}(\boldsymbol{q})) \perp \boldsymbol{k} \tag{3.1.7a}$$

$$|\boldsymbol{p}| \ll |\boldsymbol{k}| \approx |\boldsymbol{q}|, \widehat{\boldsymbol{u}}(\boldsymbol{p}) \parallel \boldsymbol{k} \Longrightarrow \quad (\widehat{\boldsymbol{u}}(\boldsymbol{p}) \wedge \widehat{\boldsymbol{\omega}}(\boldsymbol{q})) \perp \boldsymbol{k}, (\widehat{\boldsymbol{u}}(\boldsymbol{q}) \wedge \widehat{\boldsymbol{\omega}}(\boldsymbol{p})) \parallel \boldsymbol{k}. \tag{3.1.7b}$$

Therefore, Eq.3.1.4 turns into:

$$(\frac{\partial}{\partial t} + vk^2)\widehat{\boldsymbol{u}}(\boldsymbol{k}, t) = \int_{|\boldsymbol{p}|>\lambda_k|\boldsymbol{k}|} (\widehat{\boldsymbol{u}}(\boldsymbol{p}) \wedge \widehat{\boldsymbol{\omega}}(\boldsymbol{q}))d^d\boldsymbol{p} + (\int_{|\boldsymbol{p}|\leq\lambda_k^{-1}|\boldsymbol{k}|} \widehat{\boldsymbol{u}}(\boldsymbol{p})d^d\boldsymbol{p}) \wedge \widehat{\boldsymbol{\omega}}(\boldsymbol{q}). \tag{3.1.8}$$

Since the triad interaction of SGC model is chosen as its tree structure $(\boldsymbol{k}_m^i, \boldsymbol{k}_{m+1}^{2i}, \boldsymbol{k}_{m+1}^{2i+1})$, which has orthogonality constraints, Eq. 3.1.8 becomes

$$(\frac{\partial}{\partial t} + vk^2)\widehat{\mathbf{u}}_m^i = \widehat{\mathbf{u}}_{m+1}^{2i} \wedge \overline{\widehat{\boldsymbol{\omega}}}_{m+1}^{2i} + \widehat{\mathbf{u}}_{m+1}^{2i+1} \wedge \overline{\widehat{\boldsymbol{\omega}}}_{m+1}^{2i+1} + \widehat{\mathbf{u}}_{m-1}^{a(i)} \wedge \widehat{\boldsymbol{\omega}}_m^i. \tag{3.1.9}$$

The symmetric property of gyroscope equation yields

$$\mathbf{u}(\mathbf{k}, t) = \frac{i\mathbf{k} \wedge \widehat{\boldsymbol{\omega}}(\mathbf{k}, t)}{k^2}. \tag{3.1.10}$$

and the orthogonality in Appendix B.2 leads to

$$\mathbf{k}_{m+1}^{2i+1} = -\mathbf{k}_{m+1}^{2i}, \tag{3.1.11}$$

which is the last orthogonality triad.

Following the matrix representation of Eq.3.1.9 considering orthogonality, discrete SGC model is as follow:

$$(\frac{\partial}{\partial t} + vk_m^2)u_m^i = k_{m+1}[|u_{m+1}^{2i}|^2 - |u_{m+1}^{2i+1}|^2] + (-1)^{i+1}k_m u_m^i u_{m-1}^{a(i)} \tag{3.1.12}$$

where k_m is wave number at layer m $(0 \leq m \leq n)$; k_{m+1} is wave number at layer $m+1$; u_m^i is velocity of eddy in location i at layer m $(0 \leq i \leq 2^m - 1)$; $a(i)$ is location index of its mother eddy which is the integer part of real $\frac{i}{2}$.

It presents the temporal evolution of velocity field u_m^i, which is associated with mother eddies $u_{m-1}^{a(i)}$ and two daughter eddies u_{m+1}^{2i} and u_{m+1}^{2i+1}. Due to spatial structure, velocity equations for two special layer are given. Velocity at top layer u_0^0 without ancestor eddy is

$$\frac{\partial u_0^0(t)}{\partial t} = k_1[|u_1^0(t)|^2 - |u_1^1(t)|^2] - vk_0^2 u_0^0(t). \tag{3.1.13}$$

Velocities at last layer u_n^i without generating daughter eddies are

$$\frac{\partial u_n^i(t)}{\partial t} = (-1)^{i+1}k_n u_n^i(t)u_{n-1}^{a(i)}(t) - vk_n^2 u_n^i(t). \tag{3.1.14}$$

According to the invariant of gyroscope equation, turbulence energy corresponds to the square of the angular momentum $\boldsymbol{M}^2$ conserves.

Waleffe [134, 135] reported that the instability assumption for rapidly rotating turbulence, which is typically applicable for any sort of triad interaction, suggests direction of energy transferring - from the poles of the rotation axis to the equator. Furthermore, this instability assumption is made even more apparent with helical mode decomposition. As an alternative to the Craya-Herring decomposition, helical

mode decomposition [15, 112] allows for departures from isotropy caused by external rotational forces and the spectral energy to move from parallel to the normal wave vector, which seems to be compatible with trend toward two-dimensionality. Furthermore, Benzi et al. [9] investigated in detail various classes of helical shell models that arise from helical decomposition of interactions, and four different types were discussed. Two of them match the two-dimensional and three-dimensional shell models. Consequently, this helical decomposition might be applied to SGC model to provide more specific details.

3.2 The numerical methods

Four different numerical algorithms are discussed in this section to determine the scheme contributing to time developed velocity field of SGC model. Euler method, the simplest numerical approach, is presented first, followed by widely used, high precision fourth-order Runge-Kutta method. As a next step, slaved Adams-Bashforth method considering high dissipation at large wave numbers and the semi-implicit Euler scheme that maintains the rigid body property are studied. A brief overview of these methods will be provided, and the corresponding Python code and Pseudo-code will be provided in Appendix B.3.

3.2.1 The Euler method

Euler method [11], first reported by Leonhard Euler in 1768, utilizes the elementary difference methods to obtain approximate solutions to differential equations or

initial value problems. Theory underlying Euler's method of using the concept of local linearity of small line segments to approximate solutions is well illustrated by Taylor's theorem, which was published in 1714. Algorithm for Euler method is investigated since it is simple and its discretization of continuous variables can be easily calculated numerically.

Typical form of the first-order differential equation is

$$\frac{dy}{dt} = f(t, y(t)) \tag{3.2.1}$$

with initial condition $y(t_0) = y_0$. The classic first-order forward Euler method discretizes Eq.3.2.1 writing as

$$\begin{aligned} \frac{y(t+\Delta t) - y(t)}{\Delta t} &\cong f(t, y(t)) \\ y(t+\Delta t) &\cong y(t) + \Delta t \cdot f(t, y(t)), \end{aligned} \tag{3.2.2}$$

where Δt is the time step.

Numerically simulated velocity equations using Euler's method are categorized into three functions due to the spatial structure of SGC model. First of all, velocity at the top layer u_0^0 is computed by

$$u_0^0(t+\Delta t) = u_0^0(t) + \Delta t \cdot k_1[|u_1^0(t)|^2 - |u_1^1(t)|^2] - \Delta t \cdot v k_0^2 u_0^0(t). \tag{3.2.3}$$

External forcing is added to the code as forced turbulence is going to be studied in the next chapter, which is not necessary to repeat.

Velocities u_n^i located at the last layer are

$$u_n^i(t+\Delta t) = u_n^i(t) \cdot (1 - \Delta t \cdot v k_n^2) + \Delta t \cdot (-1)^{i+1} k_n u_n^i(t) u_{n-1}^{a(j)}(t). \tag{3.2.4}$$

As for velocities u_m^i whose cascade step m is between 1 and $n-1$, they are simulated by

$$\begin{aligned} u_m^i(t+\Delta t) =& u_m^i(t) \cdot [1 - \Delta t \cdot v k_m^2 + \Delta t \cdot (-1)^{i+1} k_m u_{m-1}^{a(i)}(t)] + \Delta t \cdot k_{m+1} [|u_{m+1}^{2i}(t)|^2 - \\ & |u_{m+1}^{2i+1}(t)|^2]. \end{aligned} \tag{3.2.5}$$

Furthermore, the numerical convergence of Euler's method has been demonstrated by Augustine Louis Cauchy in 1824, thus it's clear that time steps must be sufficiently small to ensure convergence. The absolute stability region of Euler method is

$$|1 + \frac{f(t, y(t))}{y} \cdot \Delta t| < 1, \tag{3.2.6}$$

3.2.2 Fourth-order Runge-Kutta method

Runge-Kutta method is a conventional, one-step approach that has been utilized extensively due to its high accuracy. It was initially proposed by Carl Runge in 1895 [109] and later extended to solve systems of differential equations by Martin Wilhelm Kutta in 1901[66]. To avoid computing higher order derivatives in Taylor expansion technique while still achieving higher order convergence, Runge-Kutta approach inserts a series of points into range $[t, t+\Delta t]$ to anticipate the slopes $k_1, k_2 \cdots$, and then takes their weighted average. Obviously, Euler method is Runge-Kutta method

of the first order. The discretized Eq.3.2.1 for fourth-order Runge-Kutta (RK4) is

$$y(t+\Delta t) = y(t) + \frac{\Delta t}{6}(k_1^* + 2k_2^* + 2k_3^* + k_4^*) \tag{3.2.7}$$

where

$$\begin{aligned} k_1^* &= f(t, y(t)) \\ k_2^* &= f(t + \frac{\Delta t}{2}, y(t) + \frac{\Delta t}{2} \cdot k_1^*) \\ k_3^* &= f(t + \frac{\Delta t}{2}, y(t) + \frac{\Delta t}{2} \cdot k_2^*) \\ k_4^* &= f(t + \Delta t, y(t) + \Delta t \cdot k_3^*). \end{aligned} \tag{3.2.8}$$

Except that RK4 method has to calculate the slope four times, numerical velocities equation is the same between the Euler and RK4 methods, therefore, Python code for RK4 method is directly provided. The equations describing velocity field of all layers for each time step are written in pseudo-code and Python code, which are quite similar to that of Euler and in Appendix B.3.2.

Besides, the absolute stability region of RK4 method is

$$|1 + \frac{f(t,y(t))}{y} \cdot dt + \frac{1}{2!} \cdot (\frac{f(t,y(t))}{y} \cdot dt)^2 + \frac{1}{3!} \cdot (\frac{f(t,y(t))}{y} \cdot dt)^3 + \frac{1}{4!} \cdot (\frac{f(t,y(t))}{y} \cdot dt)^4| < 1. \tag{3.2.9}$$

3.2.3 Slaved Adams-Bashforth Method

The linear multi-step method is another approach that is typically used to resolve ordinary differential equations. Unlike the one-step method, which simply discards former data in favor of the most recently acquired data, this method uses a linear combination of former points and derivative values to predict the next point. One of

the classic multi-step approaches is Adams-Bashforth method, commonly known as explicit Adam method. In order to account for the quick damping at high wave numbers, "slaved frog" scheme [44] has been implemented in two-step Adams-Bashforth method, which is slaved Adams-Bashforth (ABF) approach and has been applied to the investigation of shell model [101].

A simple linear model that displays fast damping at high wave numbers is

$$\frac{dU}{dt} = -aU + g(t). \tag{3.2.10}$$

After integrating, it turns into

$$\begin{aligned} U(t+\delta t) &= e^{-a\delta t}U(t) + \int^{t+\delta t} e^{-a(t+\delta t-s)}g(s)ds \\ U(t+\delta t) &= e^{-a\delta t}U(t) + \frac{1-e^{-a\delta t}}{a}g(t) \end{aligned} \tag{3.2.11}$$

Hence, the slaved Adams-Bashforth Method is:

$$U(t+\Delta t) = e^{-a\cdot\Delta t}u(t) + \frac{1-e^{-a\cdot\Delta t}}{a}(\frac{3}{2}g(t) - \frac{1}{2}g(t-\Delta t)). \tag{3.2.12}$$

The initial time t_0 is estimated by $g(t_0 - \Delta t) = g(t_0)$.

Velocity equation u_0^0 obtained from slaved ABF method is

$$u_0^0(t+\Delta t) = e^{-a_0\cdot\Delta t}u_0^0(t) + \frac{1-e^{-a_0\cdot\Delta t}}{a_0}(\frac{3}{2}g_0(t) - \frac{1}{2}g_0(t-\Delta t)), \tag{3.2.13}$$

where $a_0 = vk_0^2$ and $g_0(t) = k_1[|u_1^0(t)|^2 - |u_1^1(t)|^2]$.

Velocities at the end layer u_n^i are computed by

$$u_n^i(t+\Delta t) = e^{-a_n \cdot \Delta t} u_n^i(t) \tag{3.2.14}$$

where $a_n = vk_n^2 - (-1)^{i+1} k_n u_{n-1}^{a(j)}(t)$.

Velocities u_m^i $(1 \leq m \leq n-1)$ are computed from

$$u_m^i(t+\Delta t) = e^{-a_m \cdot dt} u_m^i(t) + \frac{1 - e^{-a_m \cdot \Delta t}}{a_m} (\frac{3}{2} g_m(t) - \frac{1}{2} g_m(t - \Delta t)) \tag{3.2.15}$$

where $a_m = vk_m^2 - (-1)^{i+1} k_m u_{m-1}^{a(j)}(t)$ and $g_m(t) = k_{m+1}[|u_{m+1}^{2i}(t)|^2 - |u_{m+1}^{2i+1}(t)|^2]$.

Despite the fact that two schemes are applied to increase the precision of turbulence numerical simulations, slaved ABF technique still has to adhere to the stability of ABF approach. The characteristic equation of ABF method satisfies root condition, suggesting that it is highly stable and avoids the round-off error from growing exponentially.

3.2.4 Semi-implicit Euler method

Semi-implicit Euler method known as Störmer-Verlet and symplectic-Euler [51] is commonly applied to the numerical simulations of rigid bodies, as it's more stable than classic explicit Euler schemes and preserves the nature of volume conservation of phase space volume element in physical system. Hence, semi-implicit Euler scheme is studied in the simulation of SGC model, which is obtained from the gyroscope equation- Euler's equation for a rigid body. Semi-implicit Euler scheme for SGC model, in which linear dissipation is implicit and nonlinear transfer term is explicit,

is as follows:

$$\begin{aligned}(\frac{1}{\Delta t}+vk_m^2)u_m^i(t+\Delta t)-\frac{u_m^i(t)}{\Delta t}&=g_m^i(t)\\ u_m^i(t+\Delta t)&=\frac{g_m^i(t)\Delta t+u_m^i(t)}{1+vk_m^2\Delta t}\end{aligned} \tag{3.2.16}$$

where the nonlinear transfer term is wrote as $g_m^i(t) = k_{m+1}[|u_{m+1}^{2i}|^2 - |u_{m+1}^{2i+1}|^2] + (-1)^{i+1}k_m u_m^i u_{m-1}^{a(i)}$.

Velocity $u_0^0(t+\Delta t)$ at the top layer is computed by:

$$u_0^0(t+\Delta t)=\frac{k_1[|u_1^0(t)|^2-|u_1^1(t)|^2]\cdot\Delta t+u_0^0(t)}{1+vk_0^2\cdot\Delta t} \tag{3.2.17}$$

Velocities u_n^i located at last layer are:

$$u_m^i(t+\Delta t)=\frac{(-1)^{i+1}k_n u_n^i(t)u_{n-1}^{a(i)}(t)\cdot\Delta t+u_m^i(t)}{1+vk_m^2\cdot\Delta t} \tag{3.2.18}$$

For velocities u_m^i whose cascade step m is between 1 and $n-1$, they are simulated by

$$u_m^i(t+\Delta t)=\frac{(k_{m+1}[|u_{m+1}^{2i}(t)|^2-|u_{m+1}^{2i+1}(t)|^2]+(-1)^{i+1}k_n u_n^i(t)u_{n-1}^{a(i)}(t))\cdot\Delta t+u_m^i(t)}{1+vk_m^2\Delta t} \tag{3.2.19}$$

3.3 Result analysis

In order to determine an optimal numerical method for SGC model, it is essential to compare velocity fields generated by different approaches, such as energy flux

utilized to study intermittency and it's multifractality analyzed by UM framework. Moreover, complexity of the principal function as well as the specific running time and space of these algorithms will be calculated in next section to evaluate numerical methods.

To begin, the specific equation for energy flux and required simulation parameters are presented. According to Kolmogorov's local stationary assumption, the inertial range has

$$\frac{\partial E(k,t)}{\partial t} = 0, \tag{3.3.1}$$

which suggests

$$\Pi(k_m) \approx \epsilon(t). \tag{3.3.2}$$

Energy flux, which refers to energy transfer rate from all wave number $k < k_m$ to the other wave number $k \geq k_m$ or the cumulative energy transfer rate above the wave number k_m, is calculated from

$$\begin{aligned} \Pi(k_m) &= -\sum_{m'=0}^{m-1} T(k_{m'},t) \\ &= \sum_{m'=m}^{n} T(k_{m'},t) \\ &\propto \sum_{m'=m}^{n} u(k_{m'},t)\cdot[\frac{\partial u(k_{m'},t)}{\partial t} + vk_{m'}^2 u(k_{m'},t)]. \end{aligned} \tag{3.3.3}$$

The energy flux through wave number k_m of SGC model is

$$\Pi(k_m) \propto \sum_{j=m}^{n}\sum_{i=0}^{2^m-1} u_j^i(t)\cdot[k_{j+1}[|u_{j+1}^{2i}(t)|^2 - |u_{j+1}^{2i+1}(t)|^2] + (-1)^{i+1}k_j u_j^i(t)u_{j-1}^{a(i)}(t)] \tag{3.3.4}$$

which is related to the nonlinear transfer term of SGC model.

The initial kinetic energy spectrum is assumed as Kolmogorov spectrum

$$E(k,0) = C_K \varepsilon^{\frac{2}{3}} k^{-\frac{5}{3}}, \tag{3.3.5}$$

where C_k is Kolmogorov constant. C_k and ε are taken to be 1 to start simulation. Initial velocities $u_m^i(0)$ are obtained from the assumed energy spectrum $E(k_m, 0)$ by

$$|u_m^i(0)|^2 = E(k_m^i, 0)k_m^i \equiv E(k_m, 0)k_m. \tag{3.3.6}$$

An artificial viscosity v is required to dissipate the energy and it can be derived from Reynolds number at Kolmogorov scale $Re(l_{\eta*}) \approx 1$

$$Re(l_{\eta*}) = \frac{u_{\eta*} l_{\eta*}}{v} = \frac{u_{\eta*}}{v k_{\eta*}} \approx 1. \tag{3.3.7}$$

Related artificial dissipation cascade step η^* is generally assumed as two steps before the maximum cascade step n.

Now, initial values for Case 3.1, which is used for the comparison, are shown in Table 3.1. Time step Δt should be small enough to guarantee the stability of numerical simulation methods. RK4 method has a broader absolute stability zone than Euler method, whereas slaved ABF method is strongly stable. As a result, time step of these approaches is uniformly assumed by the stability of Euler method. It is also limited by cascade steps. Hence, the restriction on time step Δt is that it should approximately obey $|1 - v k_n^2 \Delta t| < 1$, since the main dissipation term is viscous term and the convection term can be neglected. The running time Tmax is set as sufficient enough time to investigate the difference in results caused by numerical methods.

For simplicity's sake, the external forcing f is assumed to be 0, which eliminates the complexity of turbulent characteristics brought on by injecting forcing.

Table 3.1: Case 3.1

Case	n	$\eta*$	Δt	Tmax	f
3.1	12	10	0.0002	30000	0

Energy flux $\Pi(k_6)$ calculated from these different numerical methods is displayed in Fig 3.2. It reveals that energy fluxes at the initial time period are indistinguishable, whereas they become inconsistent as time goes on. The occurrence of this disparity is expected due to the chaotic nature and introduction of deviations in the velocity field by different numerical algorithms.

Figure 3.2: Energy flux $\Pi(k_6)$ for Case 3.1

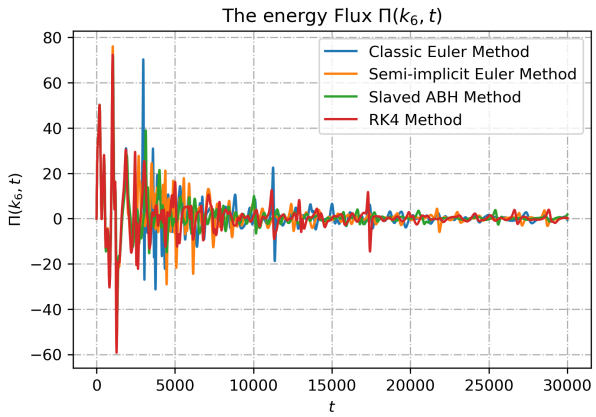

Furthermore, it's apparent that all energy fluxes exhibit fluctuation depicted in Fig.3.2. Multifractality of these fluctuations is studied by UM framework to clarify whether the properties of SGC model are impacted by numerical simulation approaches. UM parameters for Case 3.1 are displayed in Fig.3.3. The analysis is carried

out from all time steps, and UM parameters are determined by averaging results of three moments $\eta = 0.9, 1.5, 2$. These approaches have the same codimension C_1 but differ in multifractality index α. Multifractality index α for the classic Euler method is 1.52, while α obtained from RK4 method and slaved ABF method are 1.53 and 1.47, respectively. However, semi-implicit Euler method yields a multifractality index of 1.44, which differs from the classic Euler method by 0.08 and from Slaved ABF method by 0.03. It demonstrates that UM parameters estimations for explicit one-step approaches are quite close, and results for Slaved ABF method and Semi-implicit that take into account physical properties are close.

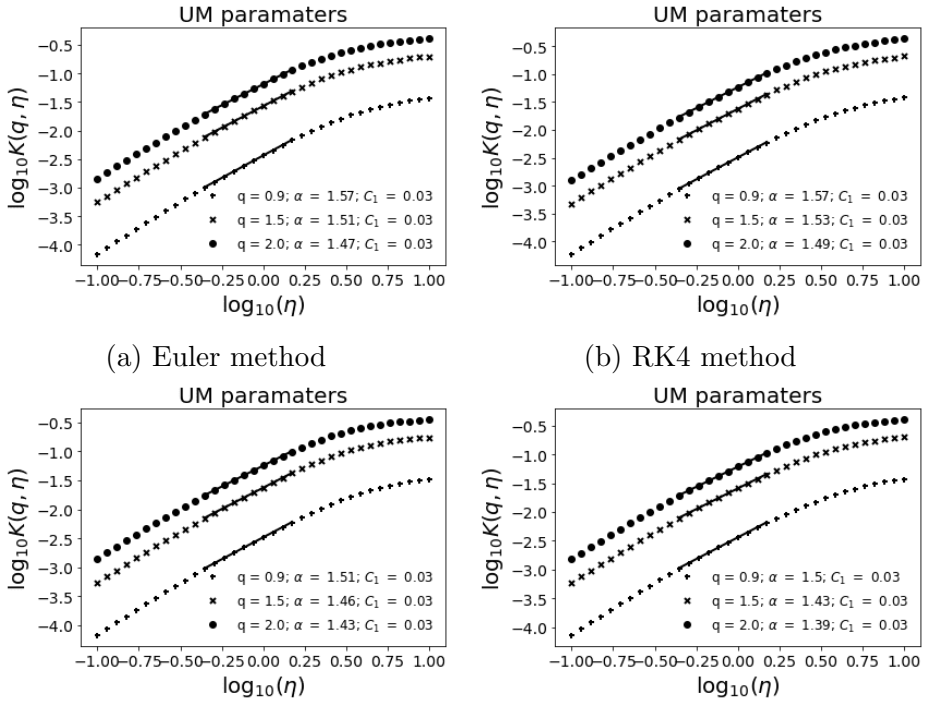

(a) Euler method (b) RK4 method

(c) Slaved ABF method (d) Semi-implicit Euler method

Figure 3.3: UM analysis of energy fluxes $\Pi(k_6)$ for Case 3.1. The UM parameters is obtained from ensemble analysis of samples whose resolution is 512.

3.4 Algorithm analysis

Algorithm analysis [125] is a quantitative evaluation of resources needed to run a task, which primarily takes execution time and memory usage into account. Due to the fact that it can be carried out in two stages: pre-implementation and post-implementation, priori analysis of these algorithms is performed first, and then the posterior analysis follows.

A priori analysis is an approach that does not rely on specific testing or data, so the pseudo-code of velocity function for previously presented algorithms is provided along with complexity analysis. Space complexity characterizes required storage space $S(n)$ for full execution, including temporary auxiliary space, input space, and output space, as a function of problem size n. It is defined as an asymptotic behavior by following generic formula :

$$\lim_{n\to\infty} \frac{S(n)}{f(n)} = \text{Cst} \neq 0, \tag{3.4.1}$$

where $f(n)$ is a statement function with regard to the storage space. Space complexity is denoted as $S(n) = O(f(n))$ merely preserving the highest order term without coefficient. The order of algorithm complexity from simplest to most complicated is

$$O(1) < O(log(n)) < O(n) < O(nlogn) < O(n^2) < O(n^3) < \ldots < O(2^n).$$

However, the empirical efficiency of algorithms not only depends on the complexity, but also problem size n, as shown in Fig.3.4.

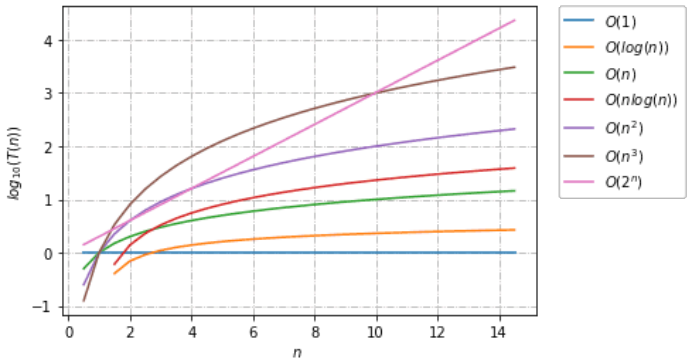

Figure 3.4: Comparing commonly used functions in the big O notation when $n \leq 15$.

Space complexity of these algorithms computing velocity for each step time is listed in Table.3.2. There are a total of $2^{n+1} - 1$ spatial eddies in SGC model, all of whose velocities must be calculated. Storage space $S(n)$ of Function 1 in Algorithm 1 becomes $2^{n+2} - 1$ after accounting for extra memory occupied in computation as well as new velocities needed to be written out. Except for velocities equations, Euler method including classic Euler method and semi-implicit Euler method share the same algorithm with RK4 method, hence space complexity of these one-step methods is $O(2^n)$. Storage space $S(n)$ of Function 1 in Algorithm 2 is $3 \cdot 2^{n+1} - 2$ and complexity is $O(2n)$ since slaved ABF method, in comparison to those one-step approaches, requires an additional set of inputs $U(t - \Delta t)$. Table.3.2 indicates that these four numerical methods have the same space complexity $O(2^n)$ due to spatial structure of SGC model.

Table 3.2: The space complexity for numerical methods.

Lines	$S(n)$	Space Complexity
Line 2,6,9,13	1	$O(1)$
Lines 3	$2^{n+1}-1$	$O(2^n)$
Function 1 in Algorithm 1	$2^{n+2}-1$	$O(2^n)$
Function 1 in Algorithm 2	$3\cdot 2^{n+1}-2$	$O(2^n)$

However, storage space $S(n)$ of slaved ABF method is larger than that of one-step methods, demonstrating that slaved ABF method requires more usage memory for each time step. And the difference in $S(n)$ rapidly grows as cascade step n enlarges as illustrated in Fig.3.5.

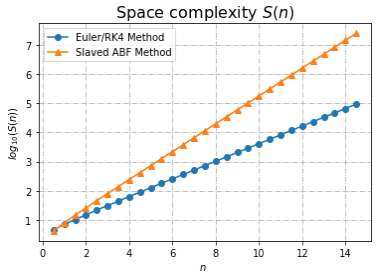

Figure 3.5: The storage space $S(n)$.

Asymptotic time complexity, as opposed to actual code execution time, is the tendency of code execution time growing with data size. Given that running time is proportional to statements executed number in algorithms, statements executed number is referred to as statement frequency or time-frequency $T(n)$, which also

depends on problem size n. If there is a function $g(n)$ satisfying

$$\lim_{n\to\infty} \frac{T(n)}{g(n)} = \mathrm{C} \neq 0, \tag{3.4.2}$$

then $T(n)$ is denoted as $T(n) = O(g(n))$ and $O(g(n))$ is asymptotic time complexity.

Below is Table 3.3 displaying time complexity of these algorithms. Simple operations, such as addition, have an execution number of 1 and time complexity of $O(1)$. Executions number of computing velocities for each cascade step m is 2^m. Subsequently, all eddies velocities $U(t + \Delta t)$ takes $T(n) = 2^{n+1} + 1$ iterations, which is the sum of all steps executions, and time complexity is $O(2^n)$.

Table 3.3: The time complexity for algorithms.

Lines	$T(n)$	Time Complexity
Line 2,3,6,9,13	1	$O(1)$
Lines 8-10	2^m	$O(2^m)$
Lines 12-14	2^n	$O(2^n)$
Function 1	$2^{n+1} + 1$	$O(2^n)$

Both space complexity and time complexity defined in terms of cascade step n are $O(2^n)$ for these algorithms, suggesting that spatial structure of SGC model determines its complexity. Time and storage space required to simulate SGC model increases exponentially when cascade step n grows, and numerical simulation approaches are incapable of improving SGC model's computation. Complexity analysis, however, is a rather rough evaluation of algorithms. A more thorough posterior analysis is presented to enhance the overall evaluation.

In order to conduct empirical investigation of algorithms, posterior analysis utilizes data to execute a coded algorithm on target computer and collect practical statistics such as running time and required space. The accuracy of this approach is reliant on testing environment and compiler languages. Indeed, computations for velocity equations distinguishing classical Euler algorithm from semi-implicit Euler technique are basic operations so that posterior analysis for these two approaches is almost identical. Posterior analysis of classical Euler algorithm representing semi-implicit Euler method is used in comparison with the other two algorithms.

Posterior analysis of Case 3.1 simulated by three numerical methods, including User time and the maximum resident set size (Max RSS), is shown in Table3.4 (See Appendix B.3.4). User time referred to the empirical time spent on execution process without taking into account any other processes or blocking condition is CPU time spent by process Case 3.1. According to User time in Table 3.4, the order from smallest to largest is classic Euler method, RK4 method and slaved ABF method. Max RSS is the maximum physical memory utilised by execution process at any given time. Max RSS of three approaches is extremely close as the maximum memory relies on velocity field that has to be written out and velocities for all eddies at each time step are saved in case 3.1. In terms of efficiency, the classic Euler method, which takes the least amount of time, is an good option, based on posterior analysis.

Table 3.4: The posterior analysis of three numerical methods for Case 3.1, which is obtained on the same server.

	Classic Euler Method	RK4 Method	Slaved ABF Method
User time	14872s	15664s	33910s
Max RSS	11590 Mb	11588 Mb	11590 Mb

3.5 Summary of Chapter 3

SGC model that preserves the most fundamental properties of NS equation, including triad interactions, is applied to characterize the properties of natural turbulent flows. In this chapter, four numerical methods—classic Euler approach, RK4 method, slaved ABF method (considering fast dissipation at high wave numbers), and semi-implicit Euler method (widely applied to the motion of rigid body) —are evaluated to determine the effective numerical simulation for SGC model and to provide simulated transient motion of eddies on the full-scale range for next chapters. Algorithms analysis consists of UM analysis, complexity analysis and empirical analysis.

UM parameters of Case 3.1 demonstrate that multifractality index of intermittency using classic Euler scheme is close to that of the fourth-order Runge Kutta scheme, while multifractality index of semi-implicit Euler method is close to the result obtained by Slaved ABH method. The definition of multifractality index makes it common for numerical approaches to result in relatively small difference. Priori analysis reveals that spatial-temporal complexity of these algorithms computing velocities for each time step is $O(2^n)$ because of spatial structure of SGC model. Execution time $T(n)$ and storage space $S(n)$ of SGC model grow exponentially when cascade step n increases. However, slaved ABF method per time step requires more memory than the other two methods. A more thorough empirical posterior analysis reveals that maximum memory for Case 3.1 which has a large enough time scale, is almost the same for all three methods because the output velocity field is preserved at all time steps. Euler method takes the least amount of time in terms of user time.

However, time scale used to compare algorithms in Case 3.1 isn't enough to perform properties analysis and time differences will be far more significant when time scale is extended. It also likely that the difference will increase as the cascade step increases, but that is not the focus of this study. Euler methods including classic Euler method and semi-implicit Euler method are effective numerical methods and are employed in the following chapters. In addition, simulation of SGC model is complex and can not be simply improved by numerical methods, as the complexity analysis demonstrates.

Chapter 4

Multifractal intermittency of forced SGC model analysed by UM framework

Numerous achievements in turbulence [38] are challenged by intermittency, which commonly refers to spatially and temporally unevenly distributed velocity fluctuations. Because of "the heavy tails" generated by extreme events, it is well acknowledged that intermittency is non-Gaussian distribution. Advance studies [1], such as K62, claim that it follows log-normal distribution, which has been proven in hydrodynamic turbulence. However, log-normal model is criticized by universal behavior [118, 49], UM framework based on the central limit theorem is then considered a powerful approach to characterize this intermittency. Empirical UM parameters estimated from various turbulence data, especially from laboratory experiments [121] and atmospheric in-situ/remotely sensed data [122], are multifractality index $\alpha \approx 1.5$ and

mean co-dimension $C_1 \approx 0.25$. Moreover, results of SGC model simulated by RK4 method [20, 120, 21] confirm that forced SGC model whose cascade step is 12 exhibits strong fluctuations in energy transfer process and UM parameters are consistent with those obtained from empirical data. Therefore, the existence of intermittency and its multifractality is firstly investigated by forced SGC model whose cascade step is 12 and then expanded to large cascade steps $14, 15$ in this chapter.

4.1 The forced SGC model

Forced SGC model instead of freely decaying SGC model is simulated to achieve quasi-equilibrium state, which prolongs turbulence motion and hence exhibits more information, such as strong fluctuations, for studying the intermittency. A quasi-equilibrium state [129] is a statistically stable condition in which viscous dissipation is not precisely balanced by external energy and system kinetic energy does not remain constant during the whole process, as it does in the equilibrium state. Despite the fact that the system is not self-preserving, it is nevertheless possible to obtain a similar law partly.

There are two fundamental approaches of forcing [128]: deterministic forcing and stochastic forcing [2, 32]. Evidence [20] suggests, however, that SGC model isn't largely dependent on the type of external forcing. Specifically, simple deterministic forcing f is utilized in the study. Forced SGC model is

$$\frac{\partial u_m^i}{\partial t} = k_{m+1}[|u_{m+1}^{2i}|^2 - |u_{m+1}^{2i+1}|^2] + (-1)^{i+1} k_m u_m^i u_{m-1}^{a(j)} - v k_m^2 u_m^i + f. \tag{4.1.1}$$

If external force is significantly larger than viscous term ($f \gg \nu k_m^2 u_m^i$), Eq 4.1.1 turns into

$$\frac{\partial u_m^i}{\partial t} = k_{m+1}[|u_{m+1}^{2i}|^2 - |u_{m+1}^{2i+1}|^2] + (-1)^{i+1} k_m u_m^i u_{m-1}^{a(j)} + f \tag{4.1.2}$$

which gives unstable state or even worse explodes the model. Conversely, when forcing is less than viscous term, Eq 4.1.1 is equivalent to freely decaying SGC model. To sum up, an appropriate forcing f is essential to achieve quasi-equilibrium state, and deterministic forcing is performed by merely adding forcing at the top layer.

4.2 Numerical parameters for the forced SGC model

Due to Eq 3.3.2, details of numerical simulations of SGC model are presented, as energy flux equaling kinetic energy dissipation rate reveals significant local fluctuation of turbulence. Energy spectrum is Kolmogorov spectrum assuming C_k and ε to be 1. Velocities as well as artificial viscosity are given according to Eq 3.3.6 and Eq 3.3.7 in Chapter 3.

Typical time unit of turbulence is initial large-eddy turnover time [39] that allows significant distortion of eddy to transfer energy:

$$\tau_e = \frac{L(0)}{(E(0))^{1/2}}, \tag{4.2.1}$$

where integral scale [5] measures the correlation distance between two points in terms of distance or time characterizing energy containing scale:

$$L(t) = \frac{\int_0^{k_{max}} k^{-1} E(k,t) dk}{\int_0^{k_{max}} E(k,t) dk} \tag{4.2.2}$$

and system energy is computed by

$$E(t) = \sum_{m=0}^{m=n} \sum_{i=0}^{2^m-1} |u_m^i(t)|^2. \tag{4.2.3}$$

Due to specific spatial structure of SGC model, time evolution of energy spectrum $E(k_m, t)$ is calculated by

$$E(k_m, t) = \frac{1}{2^m} \sum_{i=0}^{2^m-1} |u_m^i(t)|^2 \approx \overline{E_m}(t), \tag{4.2.4}$$

where

$$E_m(t) = \sum_{i=0}^{2^m-1} |u_m^i(t)|^2 \tag{4.2.5}$$

is energy at layer m whose wave number is k_m.

4.3 Cascade step 12

Table 4.1 lists key parameters of forced SGC model with a cascade step of 12 ensuring a sufficient inertial range in cascade model. External forcing f is limited to the range of 0.1 to 1.0 as a result of assumptions of C_k and ε in energy spectrum. Energy flux whose step is m has to be in inertial range. The time in simulation is displayed in terms of initial eddy turnover time τ_e with a large time scale t_f reaching 10^4.

Table 4.1: Parameters of Case 4.1 whose cascade step is $n = 12$.

Case 4.1				
	n	η^*	Δt	m
	12	10	0.0002	6
Case	f		t_f	
4.1.1	0.1		23810	
4.1.2	0.2		23810	
4.1.3	0.3		23810	
4.1.4	0.4		23810	
4.1.5	0.5		23810	
4.1.6	0.6		23810	
4.1.7	0.7		23810	
4.1.8	0.8		18000	
4.1.9	0.9		12000	
4.1.10	1		11000	

The following section will give out temporal evolution of energy fluxes injected with various forcings. Energy flux confirms the existence of intermittency and its probability distribution is provided to testify that it's non-Gaussian distribution and has a "heavy" tail. Then UM analysis is performed to describe the multifractality.

4.3.1 Intermittency of energy flux

Energy flux $\Pi(k_6)$ of Case 4.1 is shown in Fig 4.1. On a time frame of 23810, energy fluxes of Case 4.1.1- Case 4.1.7 displayed in Fig 4.1a- Fig 4.1g have achieved the expected time 23810. Extremely significant variations, as illustrated in Fig 4.1h, Fig 4.1i and Fig 4.1j, prevent energy fluxes of Case 4.1.8- Case 4.1.10 from reaching expected time scale 23810. Moreover, the larger forcing f is, the earlier energy flux $\Pi(k_6)$ stops.

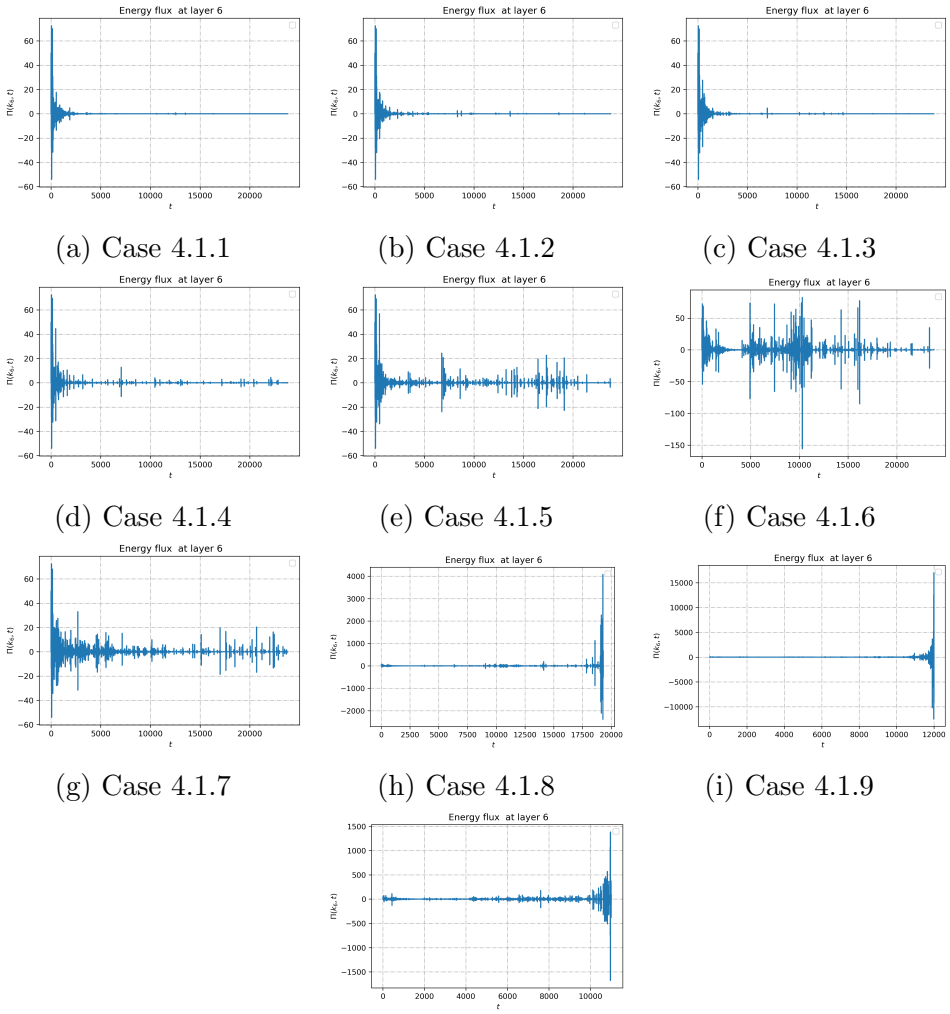

(a) Case 4.1.1 (b) Case 4.1.2 (c) Case 4.1.3

(d) Case 4.1.4 (e) Case 4.1.5 (f) Case 4.1.6

(g) Case 4.1.7 (h) Case 4.1.8 (i) Case 4.1.9

(j) Case 4.1.10

Figure 4.1: Energy flux $\Pi(k_6)$ of Case 4.1. Time unit is initial eddy turn over time. Vertical coordinate of energy fluxes is not uniform.

At the same time, energy fluxes in Fig 4.1e, Fig 4.1f and Fig 4.1g are directly indicative of intermittency behavior, whereas extreme values occurring at the beginning or the end time period make it difficult to observe fluctuations in the rest of Case 4.1. Thus, extreme values for Case 4.1 excluding Case 4.1.5- Case 4.1.7 are removed and shown in Fig 4.2.

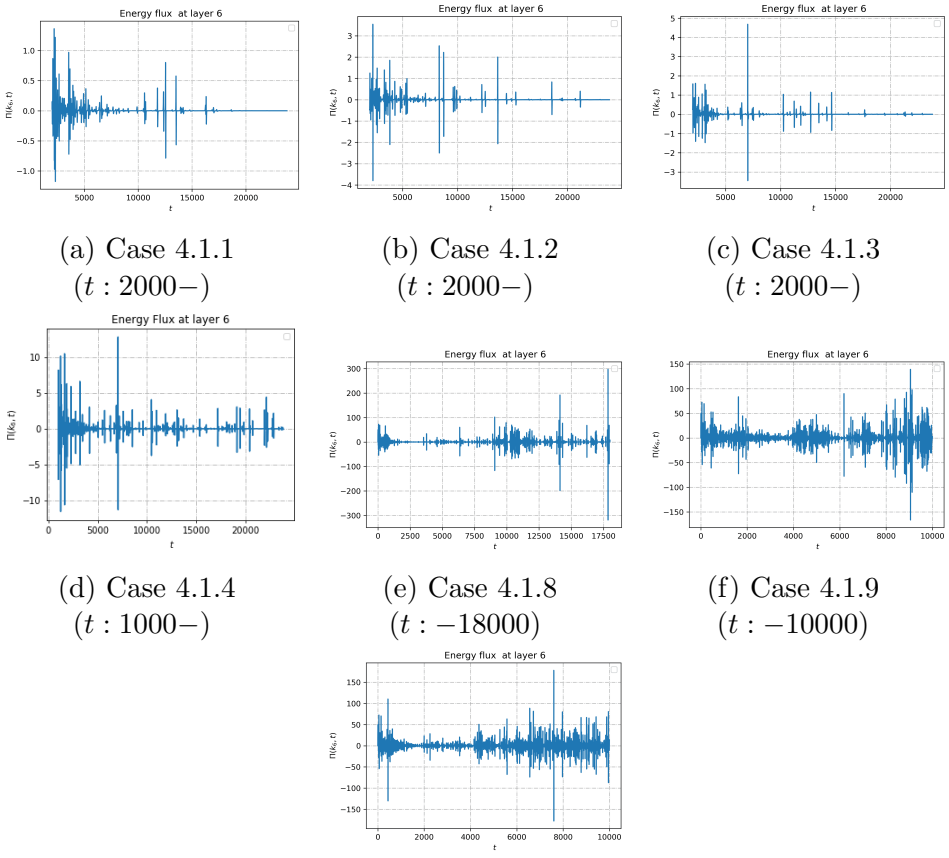

(a) Case 4.1.1 ($t : 2000-$)

(b) Case 4.1.2 ($t : 2000-$)

(c) Case 4.1.3 ($t : 2000-$)

(d) Case 4.1.4 ($t : 1000-$)

(e) Case 4.1.8 ($t : -18000$)

(f) Case 4.1.9 ($t : -10000$)

(g) Case 4.1.10 ($t : -10000$)

Figure 4.2: Energy flux $\Pi(k_6)$ of Case 4.1 getting rid of extremely high values.

Energy flux of Case 4.1.8-4.1.10 after cutting extreme value at the end shown in Fig.4.2e, Fig.4.2f and Fig.4.2g exhibits strong fluctuation, as do Case 4.1.1-4.1.4 in Fig.4.2a-Fig.4.2d when energy flux in initial transition period has been removed. Besides, fluctuations get weaker as forcing decreases. The range of energy flux in Fig.4.2a-Fig.4.2d is smaller than that in Fig. 4.2e-Fig.4.2g.

Even though energy fluxes $\Pi(k_6)$ of Cases 4.1.1–4.1.3 are weak, energy flux at former cascade step $\Pi(k_5)$ in Fig.4.3 exhibits strong fluctuations.

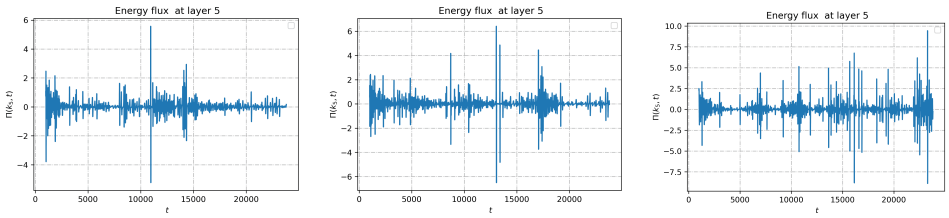

(a) Case 4.1.1 (b) Case 4.1.2 (c) Case 4.1.3

Figure 4.3: Energy flux $\Pi(k_5)$ of Case 4.1.1-4.1.3 ($t : 1000 - 23810$).

Existence of intermittency is confirmed by all energy fluxes in Case 4.1, and intensity of fluctuations is related to the value of forcing. Dramatically increased energy flux $\Pi(k_6)$ is evidence that SGC model with large injected force explodes. This might be the result of SGC model's unique spatial structure, which intensifies the energy exchange. SGC model with a medium-range forcing injection is able to reach expected large time scales, and energy flux $\Pi(k_6)$ directly displays high intermittent. Strong fluctuations appear in energy flux $\Pi(k_5)$ rather than energy flux $\Pi(k_6)$ when external forcing is small, indicating that injected forcing is insufficient to enlarge system energy and energy flux $\Pi(k_6)$, but intermittency exists. For this reason, energy flux $\Pi(k_6)$ is chosen to investigate property of fluctuations for various forcings. Given that conservative multiplicative cascades and UM framework are established in the positive field, energy flux $\Pi(k_6)$ has to be taken at absolute value in the following.

4.3.2 Non-Gaussian distribution and "heavy" tail

Probability distribution is given to confirm that fluctuations in turbulence are non-Gaussian distribution and have a "heavy" tail [38].

Probability distribution of fluctuations $\Delta|\Pi(k_6)|$ for Case 4.1 exceeding threshold

s is presented according to probability definition of multiplicative cascade Eq.2.5.3. As seen in Fig 4.4, probability distribution of Case 4.1 decays much more slowly than corresponding Gaussian distribution with the same mean and variance. The tails of PDF for Case 4.1 are heavier than those of the equivalent Gaussian distribution, which implies that extreme events occur far more frequently than those in Gaussian distribution. Besides, Fig 4.4 demonstrates that the mean and standard deviation resulting in different Gaussian distributions vary depending on the case. Nonetheless, variation in Gaussian distributions is not the focus of this thesis. The extreme events causing "heavy" tail are going to be studied next.

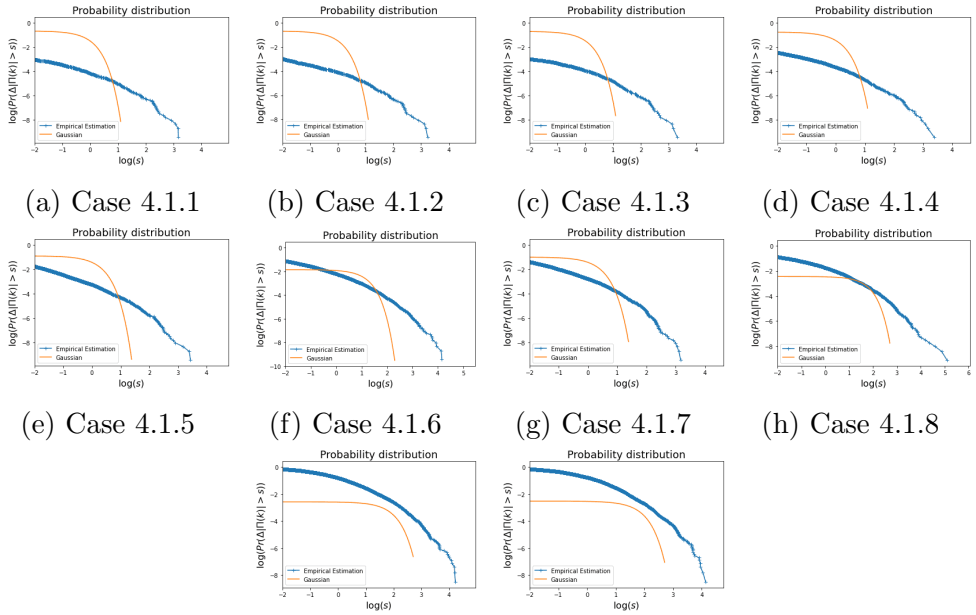

(a) Case 4.1.1 (b) Case 4.1.2 (c) Case 4.1.3 (d) Case 4.1.4

(e) Case 4.1.5 (f) Case 4.1.6 (g) Case 4.1.7 (h) Case 4.1.8

(i) Case 4.1.9 (j) Case 4.1.10

Figure 4.4: Log-log plot of probability $Pr(\Delta|\Pi(k_6)|) > s)$ exceeding a fixed reflectivity threshold s of Case 4.1.

4.3.3 Multifractality analyzed by UM framework

It has been demonstrated that, in accordance with the central limit theorem, the sum of random variables from "heavy" tail eventually converges to an α-stable distribution [38]. UM framework based on the central limit theorem and multiplicative cascade processes is a powerful tool [119] to describe this nonlinear high variability.

The entire time series of energy flux is divided into many sub-series to carry out the temporal evolution of UM parameters as well as corresponding frequency. Ensemble analysis is then conducted on all sub-series. Multifractality index obtained from ensemble analysis of all subsequences is represented as α_e, while mean codimension is written as C_{1_e}. $\overline{\alpha}$ is the average of multifractality index of all sub-series, and $\overline{C_1}$ represents the averaged mean codimension. q_{s_e} is critical moment obtained by ensemble analysis, and $\overline{q_s}$ is the mean of critical moment of all sub-series.

UM analysis of Case 4.1 starts with cases in which a middle range of forcings is imposing and high intermittent energy flux is directly observed. Cases injecting large forcing are analyzed next, followed by those in which small forcing is injected. UM parameters are estimated as the mean value of three scaling moment orders $q = 0.9$, $q = 1.5$, and $q = 2$. Absolute energy flux $|\Pi(k_6)|$ has to be normalized to maintain the conservation and perform the UM analysis.

Sample size and bias generated by fixed range estimation

To begin studying intermittency using UM analysis, a sample size has to be selected.

Case 4.1.6 in which strong fluctuation is directly observed is studied as an example. Time evolution of UM parameters for Case 4.1.6 at three different sizes of 1024, 512, and 256 is shown in Fig.4.5.

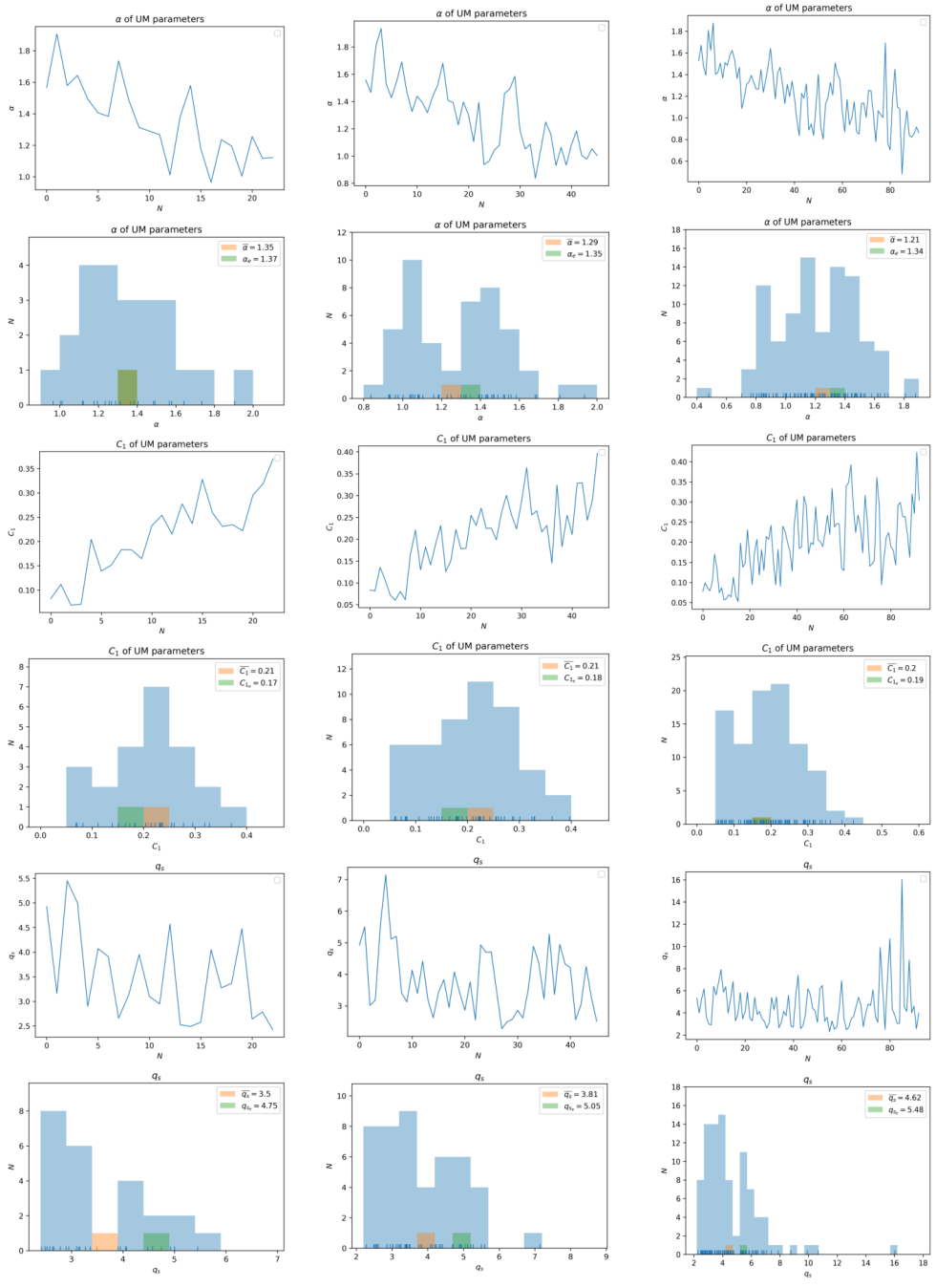

(a) Size 1024 (b) Size 512 (c) Size 256

Figure 4.5: Temporal evolution of UM parameters and critical moment q_s for Case 4.1.6 under size 1024 (a), 512 (b) and 256 (c).

Temporal evolution of UM parameters and critical moment q_s obtained from small sub-sequence size clearly reveals more detailed information, such as the trend, since results of size 512 in Fig.4.5b and size 256 in Fig.4.5c provide more elaborated descriptions than the analysis of size 1024 in Fig.4.5a. The trends of UM parameters and q_s for size 256 are largely similar to those for size 512 with the exception of α in the final period, which results in changes of q_s at the same time. UM parameters obtained by ensemble analysis are almost the same as shown by frequency histograms. $\overline{\alpha}$ varies as a result of changes in sample sizes, so does q_s derived by ensemble analysis, which would not be considered. Frequency histogram of α for size 512 is more comparable that for size 256 rather than size 1024. Almost identical $\overline{C_1}$ are found over all three sizes, and its frequency histogram shows nearly predicted double growth. In summary, size 512 is chosen for UM analysis of energy flux in the following case study.

It should be emphasized that UM parameters [1] in above is derived from a predefined range $\eta \approx 1$. Nevertheless, this statistical predefined range estimation does not precisely capture multifractality of intermittency, given energy flux varies dramatically over time. For instance, three sub-series of Case 4.1.6 are shown in Fig.4.6 whose UM parameters are determined from the fixed range $\eta \approx 1$. Fig.4.6a and Fig.4.6c display well-fitted UM parameters, whereas UM parameter estimations in Fig. 4.6b demonstrates that estimation derived from the fixed range is grossly unfit.

[1] The first two decimal places of UM parameters are retained for the sake of labeling concisely in figures, but q_s is calculated from the original UM parameters. q_s in figures and the one estimated from the labeled UM parameters, thus, differ slightly.

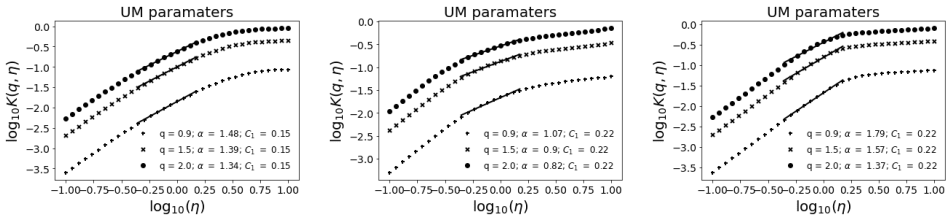

(a) Sub-series 16 (b) Sub-series 23 (c) Sub-series 29

Figure 4.6: Bias of UM parameters for Case 4.1.6.

The bias results from the fact that convergence of certain computational quantities is determined by field distribution [27]. Sometimes only a small fraction of the field primarily contributes to certain statistical moments. The convergence of trace moments may only occur at rather large scales and varies with sub-series, indicating that "flat" region at the upper right for each sub-series is different. For this reason, fit correlation coefficient for the plot is limited to a value larger than 0.995 in order to locate optimal range closest to 1 for each sub-series to ensure that slope is well fitted. Fig 4.7 illustrates the adjusted analysis for subseries 23. Compared to UM parameters estimated from the fixed range in Fig 4.6b, this approach reduce the bias effectively.

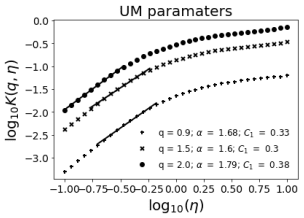

Figure 4.7: Adjustment of Sub-series 23 for Case 4.1.6.

Time evolution of UM parameters and q_s obtained from the optimal range method is now given in Fig 4.8.

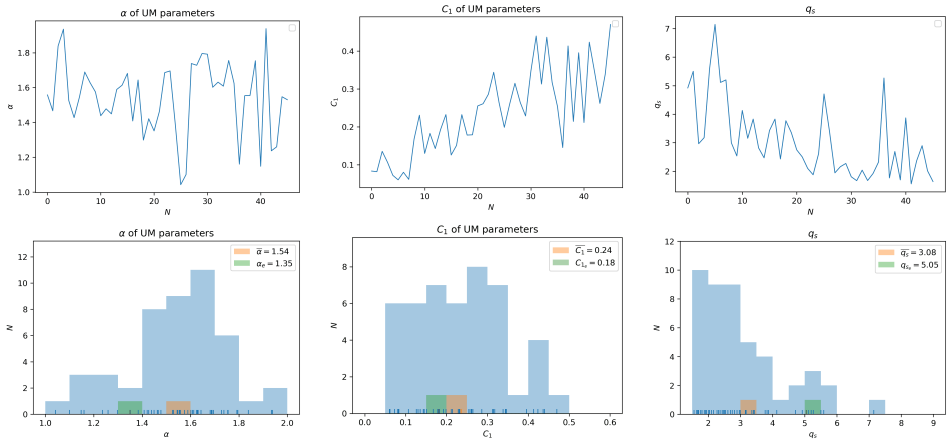

(a) Multifractality index α (b) Mean codimesnion C_1 (c) Critical moment q_s

Figure 4.8: Time evolution of UM parameters and critical moment q_s for Case 4.1.6 obtained by limiting correlation coefficient. Sub-series size is 512. The horizontal coordinate is sub-series number.

Difference in multifractality index α as well as its trend is observed when comparing the results shown in Fig.4.8 to Fig.4.5b. Alterations in the tendency of q_s occurs as a result of α since trend of C_1 has not changed noticeably. Frequency histogram of UM parameters, along with q_s, their means, and their ensemble values, all show that adjusted range technique improves the poor fit over fixed range method. α fluctuates constantly throughout the time shown in Fig.4.8, whereas C_1 increases initially and then floats steadily after $N = 30$. The tendency of q_s thus is decreasing, followed by end period of steadily fluctuating steadily.

α is between 1 and the Levy index in Log-normal model 2, while C_1 ranges between 0 and 0.5. Ensemble analysis considering number of samples yields larger values q_{s_e} than averaged q_s. As for UM parameters, it's typical for discrepancy between ensemble analysis and averaged values. Moreover, time evolution of UM parameters reflects time period close to atmospheric turbulence whose empirical parameters are

$\alpha \approx 1.5, C_1 \approx 0.25$. The number of subsequences centered around $\alpha \approx 1.5$ and $C_1 \approx 0.25$ is visible on frequency plots. q_s can also be utilized to study atmospheric turbulence whose q_s is around 2.5.

Analysis of Case 4.1

UM analysis results for Case 4.1.7 showing strong fluctuations are presented in Fig.4.9 [2].

Due to the range used to estimate UM parameters, difference between Fig.4.9a and Fig.4.9b is observed from trends of α and q_s. α decreases with time in Fig.4.9a, but fluctuates steadily in Fig.4.9b. In contrast to trend in Fig.4.9b, critical moment q_s in Fig.4.9a varies steadily after unstable initial state. Evidences from frequency histograms and mean values testify the necessity of adjusted range approach. Ensemble analysis gives the same UM parameters and q_s for these two different range estimation. The maximum α for Case 4.1.7 in Fig 4.9b does not exceed 2 and the minimum is not far from 1. C_1 grows over time, but it's less than 1. Both q_s suggesting by $\overline{q_s}$ and q_{s_e} because of large sample size are far away from that of the atmospheric turbulence. In the beginning, mean codimesnion C_1 is around 0.1 as injected forcing has not yet taken effect and the system is reaching quasi-equilibrium. UM analysis and frequency plots reveal the overlap period that α near 1.5 and C_1 close to 0.25 and subsequences number for ensemble analysis.

[2]The first set of results is time evolution of UM parameters and q_s obtained from fixed range method, while the second set of results is obtained from optimal range method. For each set, the first column displays time evolution of multifractality index α and its frequency, and mean codimension C_1 is the second column. Critical moment q_s is in the last column. The outcomes for remaining cases are organized in the same structure and won't be repeated.

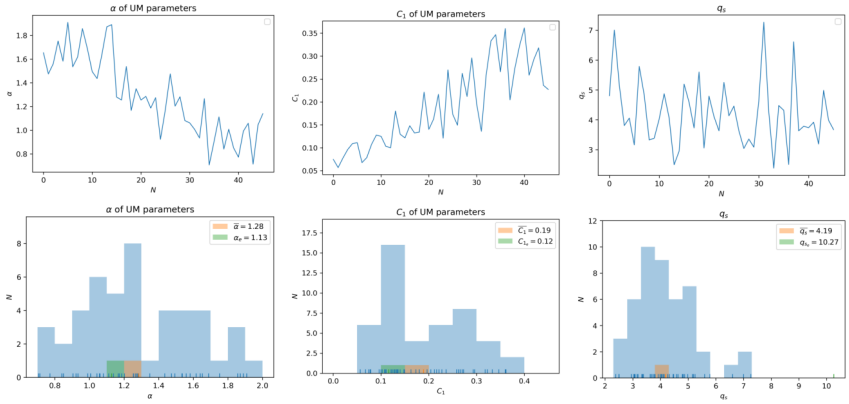

(a) Fixed range estimation

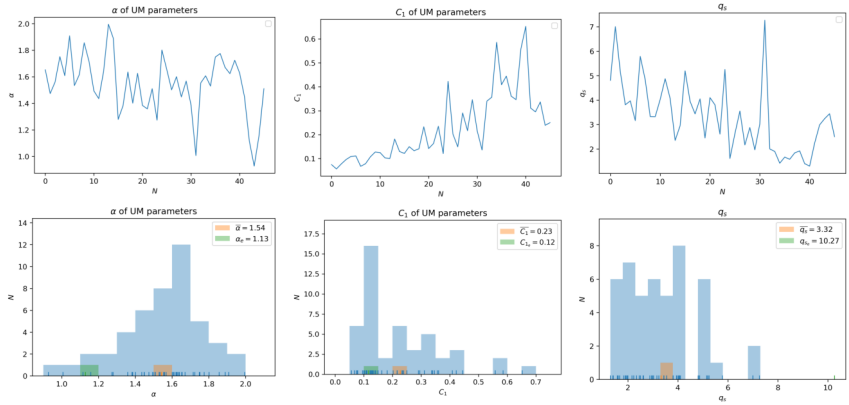

(b) Adjusted range estimation

Figure 4.9: Time evolution of UM parameters and critical moment q_s for Case 4.1.7. Sample size is 512.

UM analysis for Case 4.1.8, in which SGC model stops early because of slightly large forcing, is displayed in Fig.4.10. UM analysis is thus carried out from time 0 to 18000 before SGC model explodes. Multifractality index α in Fig.4.10a decrease, whereas α in Fig.4.10b becomes stable once the initial instability phase is passed. Even though two methods yield nearly identical trends for C_1 that float steadily in intermediate phases, mean values and frequency histograms of UM parameters as well as q_s testify the difference caused by estimation range. Ensemble analysis yields

identical UM parameters and q_s for two different range estimations.

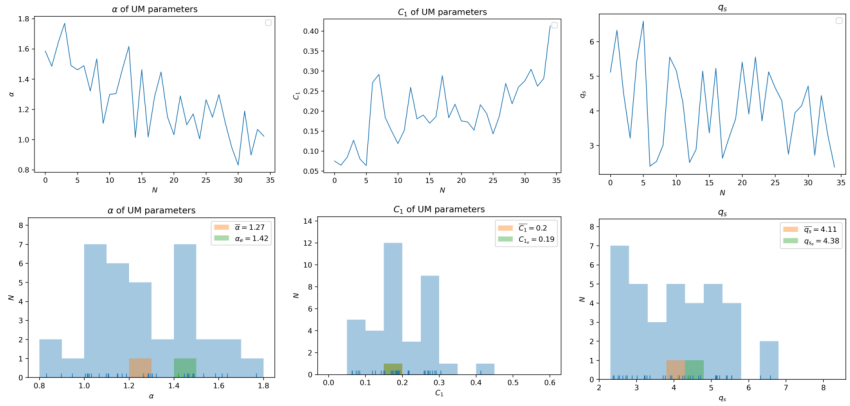

(a) Fixed range estimation

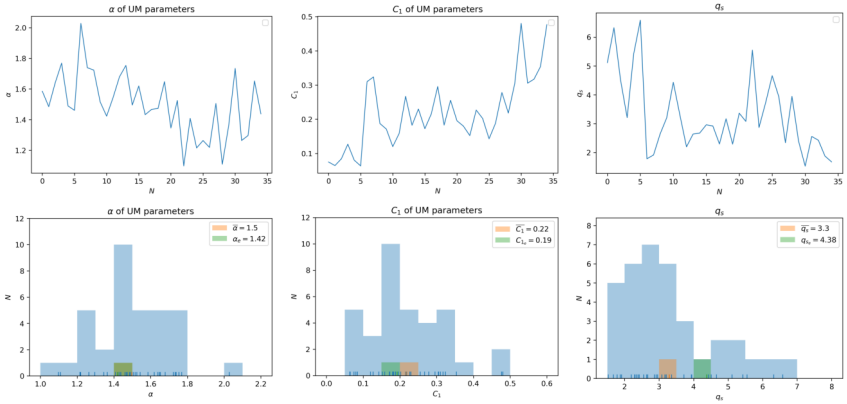

(b) Adjusted range estimation

Figure 4.10: Time evolution of UM parameters and critical moment of Case 4.1.8.

Multifractality index α ranges between 1 and 2, with the exception of subseries $N = 6$ in Fig 4.11. There are some extreme values in energy flux Fig 4.11a that dominate UM analysis. This leads to α of subseries $N = 6$ being larger than 2, as shown in Fig 4.11b. C_1 is small at the beginning and has an increment at the end. $\overline{q_s}$ is larger than 2.5, and is close to q_{s_e} as the number of sample is reduced. Time evolution of UM parameters indicates that the intermediate sub-series are close

to that of atmospheric turbulence, while frequency plots give the number of specific sub-series.

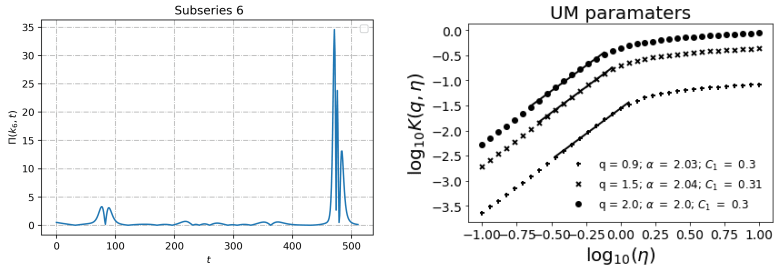

(a) Normalized flux (b) UM parameters

Figure 4.11: Sub-series $N = 6$ in Case 4.1.8.

Fig 4.12 is UM analysis for Case 4.1.9 with a large forcing resulting in an enormous energy flux and ending SGC model at time 12000. UM analysis is therefore performed from 0 to 10000. The trends of C_1 and q_s are quite similar when comparing Fig 4.12a and Fig 4.12b. Difference in α, which includes trend, the mean, and frequency plot, contributes to alteration of q_s. It indicates that the bias for Case 4.1.9 generated by fixed range estimation is non-negligible. In Fig 4.12b, multifractality index α varies from 1.3 to 1.8 and mean codimension C_1 ranges from 0.05 to 0.25. Due to the limitation of C_1, there is only one sub-series for Case 4.1.9 close to atmospheric turbulence, making it difficult to conduct ensemble analysis. This analysis concludes that forcing 0.9 is excessive not only stopping SGC model but also generating subseries far away from atmospheric turbulence.

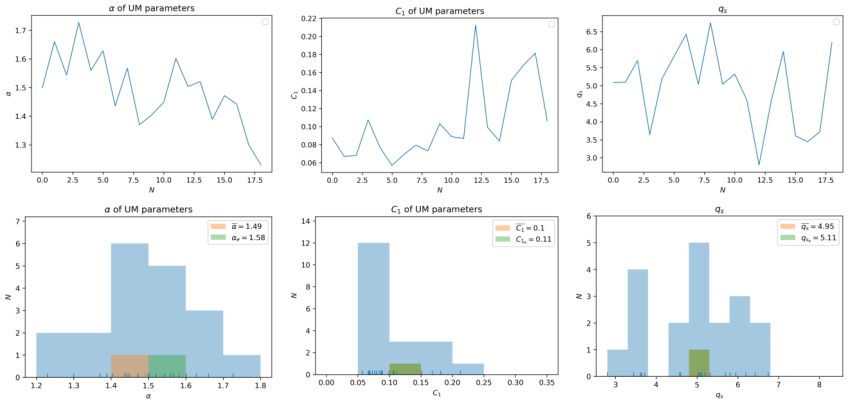

(a) Fixed range estimation

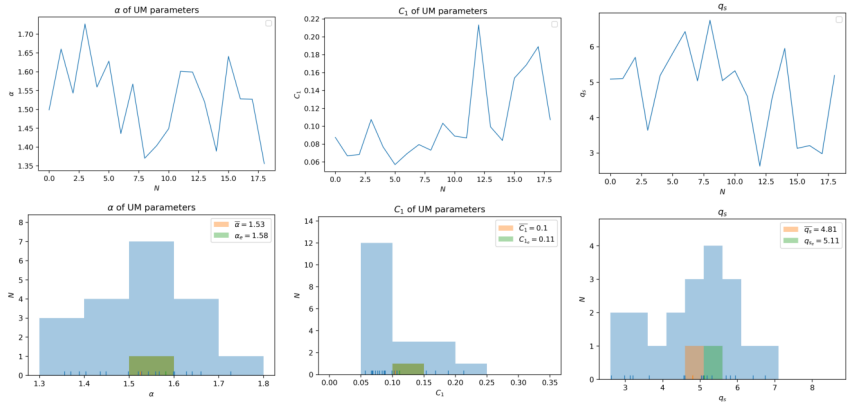

(b) Adjusted range estimation

Figure 4.12: Time evolution of UM parameters and critical moment of Case 4.1.9.

Case 4.1.10 has similar results to Case 4.1.9, in which forcing is too large that energy flux ends SGC model early. UM analysis of Case 4.1.10 is carried out from time 0 to 10000, as shown in Fig 4.13. The nearly identical results in Fig 4.13a and Fig 4.13b indicate that there is almost no difference for Case 4.1.10. Multifractality index α varies between 1.3 and 1.9, when mean codimension C_1 fluctuates around 0.1 and does not exceed 0.15. The fact that C_1 is less than 0.25 demonstrates that there are no subseries whose UM parameters are in agreement with the empirical values of

atmospheric turbulence. Analysis of Case 4.1.10 also proves that this forcing is too large to reach quasi-equilibrium state.

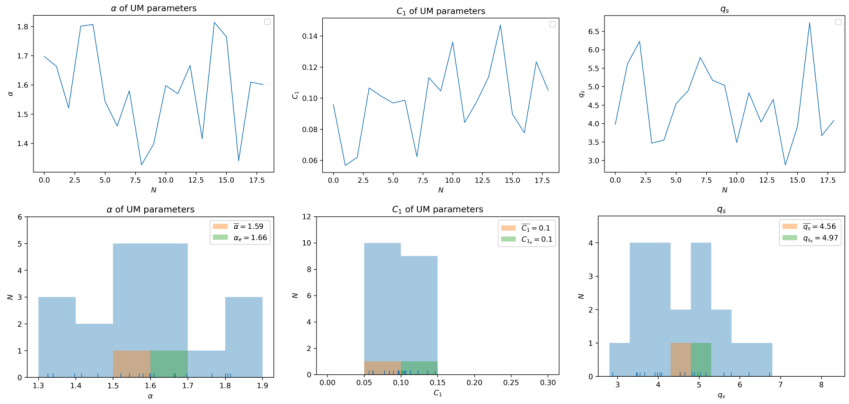

(a) Fixed range estimation

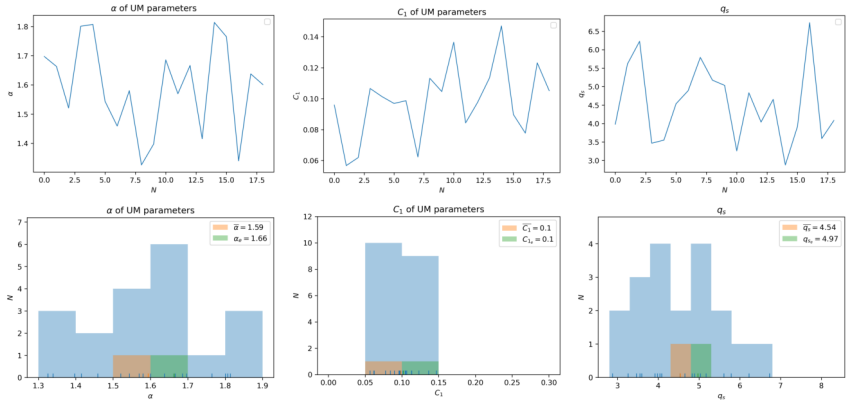

(b) Adjusted range estimation

Figure 4.13: Time evolution of UM parameters and critical moment of Case 4.1.10.

UM analysis for cases with forcing less than 0.6 is given below, from the largest to the smallest forcing.

UM analysis for Case 4.1.5 is in Fig 4.14.

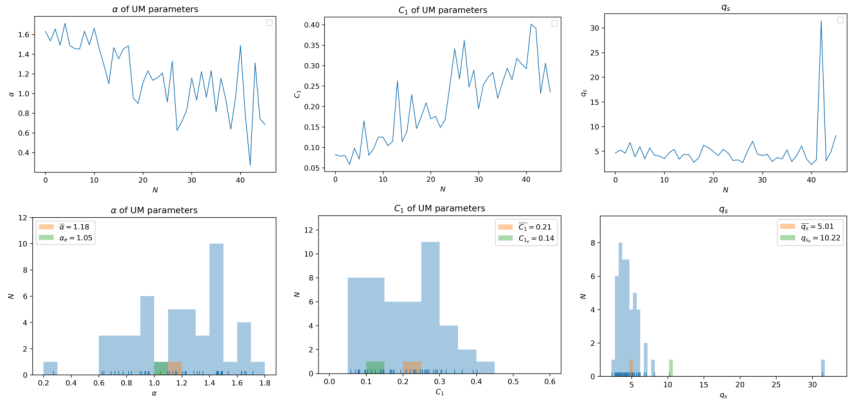

(a) Fixed range estimation

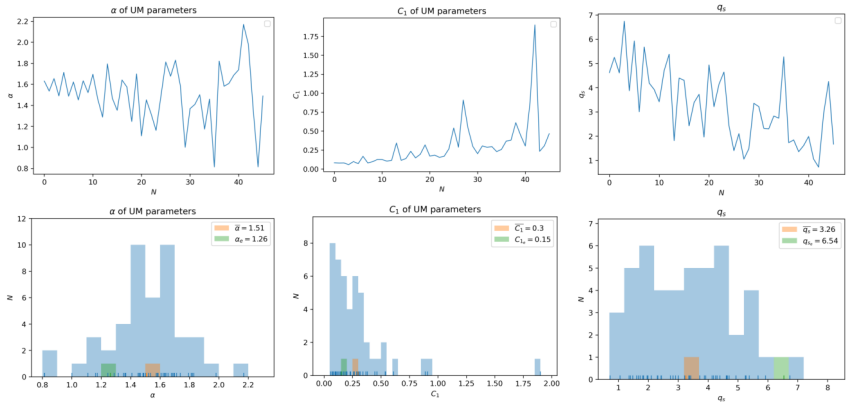

(b) Adjusted range estimation

Figure 4.14: Time evolution of UM parameters and critical moment of Case 4.1.5.

UM parameters and q_s as well as their tendencies derived by two range methods are completely different. Multifractality index α in Fig 4.14a is decreasing, whereas it fluctuates around the mean value in Fig 4.14b. q_s in Fig 4.14a is stable excluding the end, however, in Fig 4.14b decreasing before being stable. It confirms a huge disparity for Case 4.1.5, which is also manifested in averaged values as well as their frequency histograms. Surprisingly, mean codimension C_1 at $N = 42$ shown in Fig 4.14b is larger than 1. Due to extremely low energy flux of Case 4.1.5 in Fig 4.1e at the end,

almost 0, this abnormal value is brought on by weak fluctuations, which also generates α at $N = 41$ greater than 2. This explains why ensemble UM parameters obtained from adjusted range estimation are different from those from fixed range estimation and analysis after $N = 40$ should not be taken into account. UM parameters and its frequency plots in Fig 4.14b display the duration of energy flux that is close to atmospheric turbulence as well as number of subseries.

Vanishing flux and weak fluctuation are also what are responsible for abnormal C_1 at sub-series $N = 42$, as demonstrated in Fig 4.15a, which suggests that sub-series $N = 42$ is not a multifractal field.

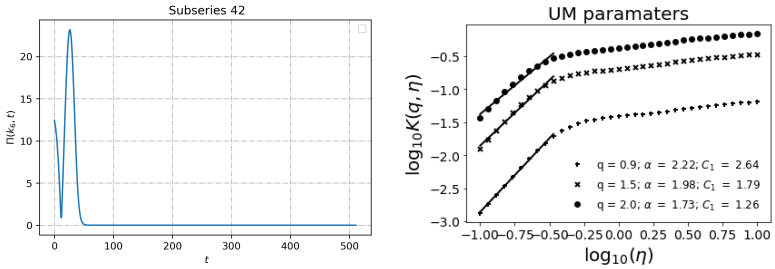

(a) Normalized flux (b) UM parameters

Figure 4.15: Subseries $N = 42$ in Case 4.1.5.

UM analysis of Case 4.1.4 is presented in Fig 4.16. New tendency for α and q_s emerge when estimation is obtained from adjusted range, with an abnormal value C_1 at the end. Statistics like averages and histograms of frequencies confirm the discrepancies caused by estimated range. Steadily fluctuating of multifractality index $\alpha$is observed in Fig 4.16b, which initially has values larger than 2. Mean codimension C_1 floats smoothly before $N = 35$ once the initial conditions are over. But Case 4.1.4 also has an abnormal value at $N = 42$ as a result of extraordinarily low value of energy flux and nearly nonexistent fluctuations. UM parameters and corresponding

frequency plots alao give out subseries that are in accordance with empirical value of atmospheric turbulence.

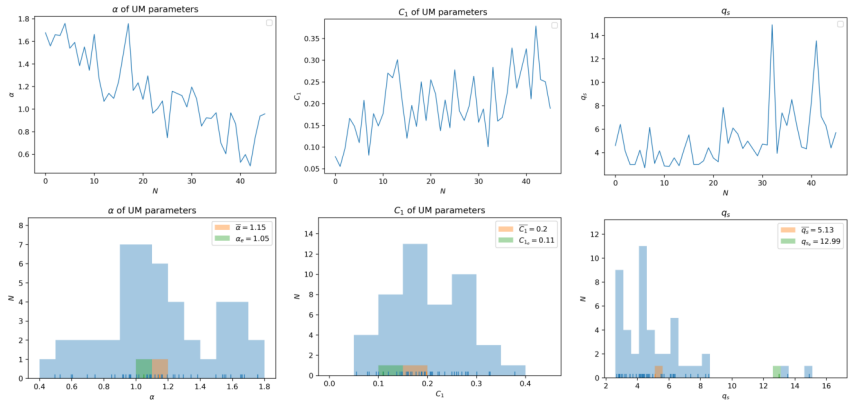

(a) Fixed range estimation

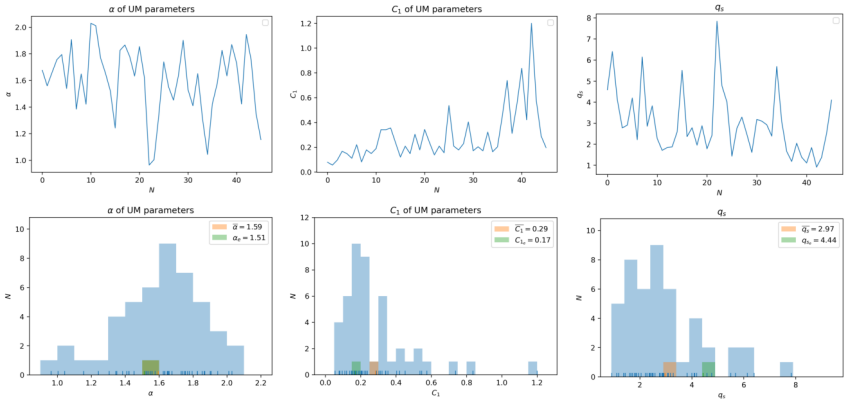

(b) Adjusted range estimation

Figure 4.16: Time evolution of UM parameters and critical moment of Case 4.1.4.

Fig 4.17 displays UM analysis performed on Case 4.1.3. Comparing Fig 4.17a with Fig 4.17b, for instance, UM parameters and their trends, reveals the disparity resulting from estimated range. It's evident that multifractality index *alpha* varies and the trend shifts from decreasing to stable floating. Several values greater than 0.4 for mean codimension C_1 are observed in Fig 4.17b. Hence, there is a clear disparity

in averaged UM parameters and frequency histograms and changes in q_s naturally follows from alteration of UM parameters. Besides, UM parameters in Fig 4.17b have more extreme values affecting ensemble analysis. Multifractality index α has many values below 1 or close to 2, while mean codimension C_1 has several values close to 0.8. This is due to energy flux of Case 4.1.3 in Fig 4.2c, in which energy flux is small and fluctuations disappear with time.

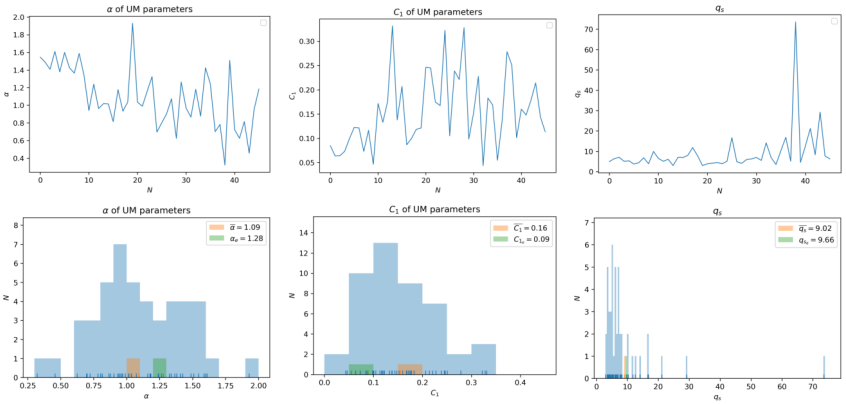

(a) Fixed range estimation

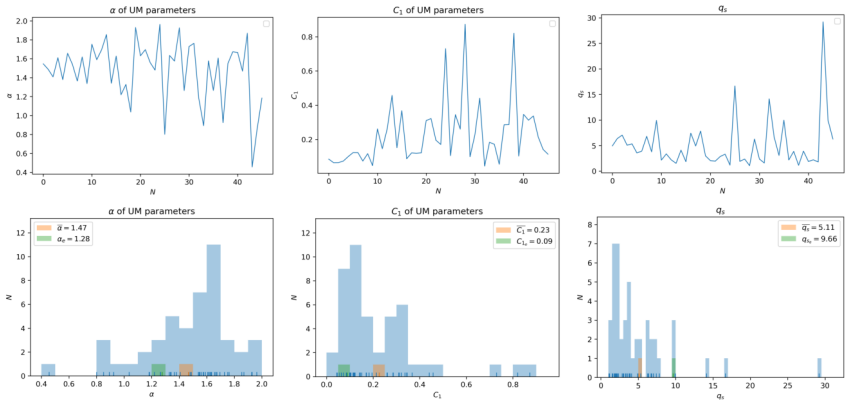

(b) Adjusted range estimation

Figure 4.17: Time evolution of UM parameters and critical moment of Case 4.1.3.

For Case 4.1.2, UM analysis is displayed in Fig 4.18. The estimating deviation

caused by fixed range is similar to analysis in Case 4.1.3. Because of small energy flux and gradually disappearing fluctuation, UM parameters in Fig 4.18b display unusual values that multifractal index α has many values around 2 and mean codimension C_1 is either close to 0.1 or close to 1. There is no sub-sequence for Case 4.1.2 that is consistent with atmospheric turbulence after leaving initial unstable condition.

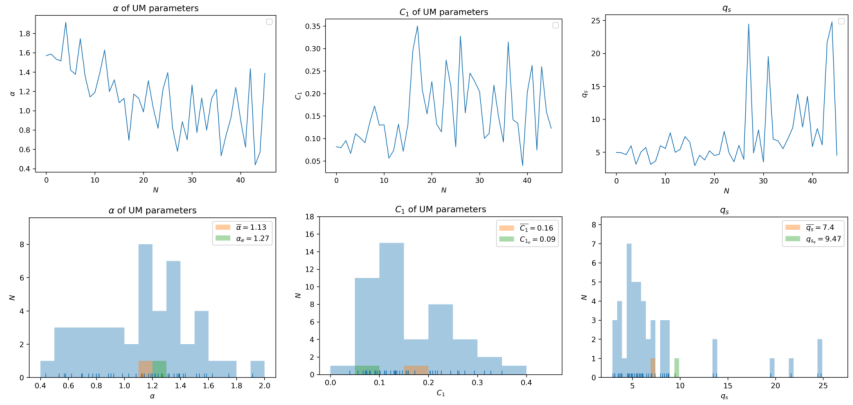

(a) Fixed range estimation

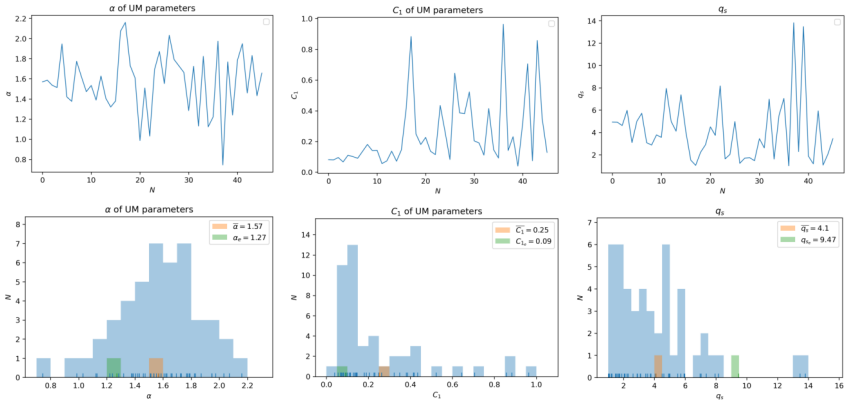

(b) Adjusted range estimation

Figure 4.18: Time evolution of UM parameters and critical moment of Case 4.1.2.

UM analysis for Case 4.1.1 is shown in Fig 4.19. Both difference of UM parameters and trends prove estimating deviation. Due to accelerated absence of fluctuations in energy flux, more values appear in Fig 4.19b after $N = 20$, such as multifractal index

α, which has values outside of the range of $1-2$, and mean codimension C_1, which has values near to 0.8. Thus abnormal value $q_s = 1000$ appears.

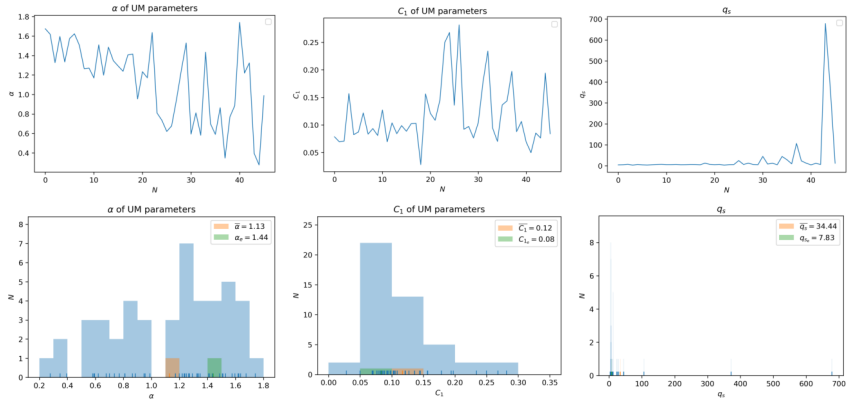

(a) Fixed range estimation

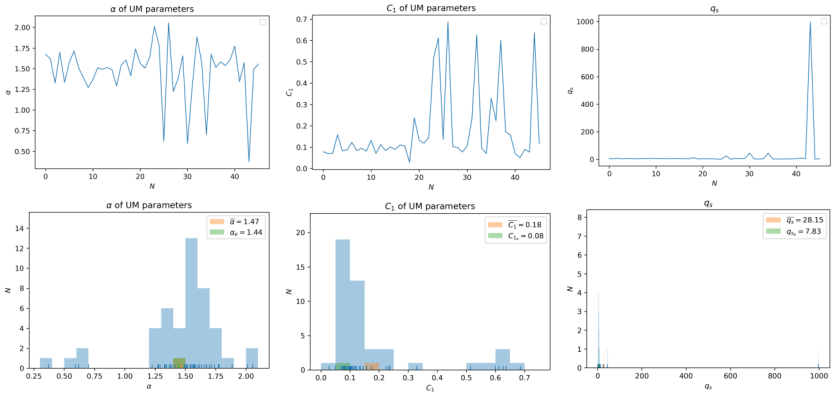

(b) Adjusted range estimation

Figure 4.19: Time evolution of UM parameters and critical moment of Case 4.1.1.

The frequency of UM parameters that is close to empirical values is summarised in Table 4.2 to study the effect of various forcing on intermittency. UM parameters are obtained from adjusted range estimation. The frequency of multifractality index α between 1.4 and 1.6 is denoted as N_α, and frequency of mean intermittency C_1 between 0.2 and 0.3 is written as N_{C_1}.

Table 4.2: Frequency of UM parameters of Case 4.1 closing to atmospheric turbulence.

Case 4.1								
	n	η^*	Δt	m	resolution			
	12	10	0.0002	6	512			
Case	f	t_f	N_α	N_{C_1}	$\overline{\alpha}$	$\overline{C_1}$	α_e	C_{1_e}
4.1.1	0.1	23810	17	3	1.13	0.12	1.44	0.08
4.1.2	0.2	23810	12	5	1.57	0.25	1.27	0.09
4.1.3	0.3	23810	11	7	1.47	0.23	1.28	0.09
4.1.4	0.4	23810	11	10	1.59	0.29	1.51	0.17
4.1.5	0.5	23810	16	10	1.51	0.3	1.26	0.15
4.1.6	0.6	23810	17	14	1.54	0.24	1.35	0.18
4.1.7	0.7	23810	14	9	1.54	0.23	1.13	0.12
4.1.8	0.8	18000	14	9	1.5	0.22	1.42	0.19
4.1.9	0.9	10000	11	1	1.53	0.1	1.58	0.11
4.1.10	1	10000	6	0	1.59	0.1	1.66	0.1

No sub-series consistent with atmospheric turbulence exists due to the limitation of N_{C_1} when external forcing is large, as in the range 0.9–1, or low, as in the range $f \leq 0.3$. Averaged UM parameters of Cases 4.1.4–4.1.8, along with N_α and N_{C_1}, imply that the middle range of forcing is appropriate to describe intermittency. UM parameters become stable once initial instability period is finished and injected forcing have maintained the system. Except for Case 4.1, averaged multifractality index $\overline{\alpha}$ is 1.55 ± 0.05, on the other hand, most of $\overline{C_1}$ is 0.25 ± 0.05. However, UM parameters obtained by ensemble analysis are inaccurate, since it is performed on all sub-series including initial unstable time, averaged UM parameters instead of ensemble values are sufficient to study the entire time series.

4.3.4 Time scale closing to atmospheric turbulence

This section presents ensemble analysis of energy flux, whose UM parameters are consistent with those of atmospheric turbulence. Time series is determined from time evolution of UM parameters and critical moment q_s. Number of sub-series is suggested by Table 4.2 satisfying $\alpha \approx 1.5$ and $C_1 \approx 0.25$ simultaneously. Therefore, ensemble analysis can not be performed on Case 4.1.9 and Case 4.1.10 due to explosions of SGC model, and neither Case 4.1.1 nor Case 4.1.2 are provided because of small energy flux. Forcings from $f = 0.3$ to the maximum forcing $f = 1$ requiring at least 3 sub-series for ensemble analysis are shown below.

Figure 4.20 illustrates UM analysis of sub-series $N = 12$ to sub-series $N = 14$ in Case 4.1.3, when fluctuation exists. It confirms that adjusted range estimation provides better fitted UM parameters. Mean codimension C_1 is between 0.14 and 0.45, and multifractality index α ranges from 1.3 to 1.9. So empirical scaling moment function $K(q)$ deviates from theoretical moment function [3] after the first order moment $q = 1$.

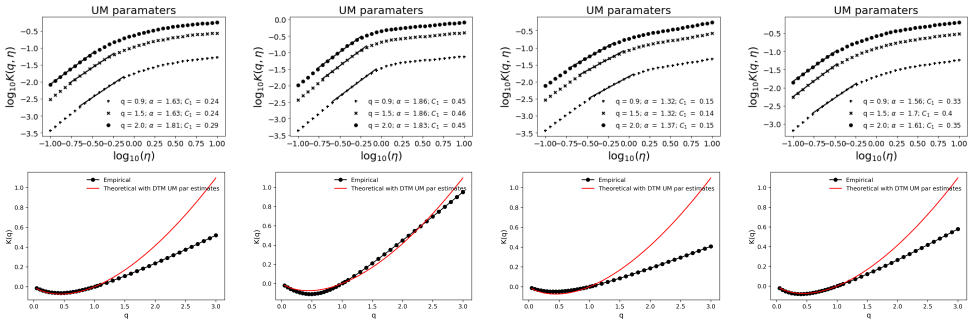

(a) Sub-series $N = 12$ (b) Sub-series $N = 13$ (c) Sub-series $N = 14$ (d) Sub-series $N = 15$

Figure 4.20: Sub-series of Case 4.1.3 for ensemble analysis. Theoretical scaling moment function is defined by empirical UM parameters for atmospheric turbulence $\alpha \approx 1.5, C_1 \approx 0.25$.

[3] If not specifically noted, theoretical UM parameters remain the same.

Ensemble analysis of sub-series $N = 12 - 14$ of Case 4.1.3 is shown in Fig.4.21 with estimated UM parameters $\alpha = 1.54,\ C_1 = 0.27$.

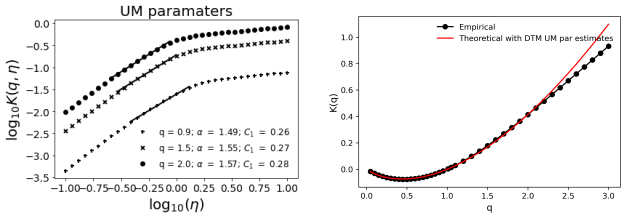

(a) UM parameters (b) Scaling moment function $K(q)$

Figure 4.21: Ensemble analysis of Case 4.1.3.

It implies that multifractality of energy flux during this time is close to that of the atmospheric turbulence. After this time period, system energy decreases, weakening energy flow and fluctuations as a result of injected forcing failing to compensate for dissipation and causing UM parameters to deviate from general empirical value. Scaling moment equation $K(q)$ is indistinguishable from theoretical scaling moment equation until critical moment $q_s = 2.67$, after which empirical curve becomes linear.

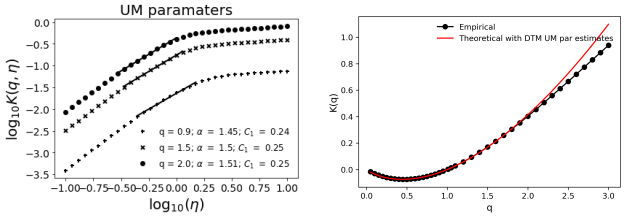

(a) UM parameters (b) Scaling moment function $K(q)$

Figure 4.22: Ensemble analysis of Case 4.1.4.

UM analysis of four subsequences for Case 4.1.4 is $N = 12 - 15$. α varies from 1.2 and 1.8, and C_1 is between 0.11 and 0.35. Ensemble analysis, shown in Fig.4.22,

illustrates that UM parameters $\alpha = 1.49,\ C_1 = 0.25$ of energy flux at this time period is consistent with empirical values.

Fluctuations of Case 4.1.3 and 4.1.4 are weak because of small amount of external forcing, while forcing amplify fluctuation of Case 4.1.5. Overlap time restriction limits the number of subsequences for ensemble analysis, even if UM analysis indicates more subseries with UM parameters $\alpha \approx 1.5,\ C_1 \approx 0.25$. Thus, no ensemble analysis available for Case 4.1.5.

Energy flux of Case 4.1.6 is highly intermittent, increasing the number of subseries for ensemble analysis to 8. Ensemble study of subseries 23 to 30 in Fig.4.23 suggested $\alpha \approx 1.39,\ C_1 \approx 0.26$ which are close to empirical UM parameters of atmospheric turbulence. And empirical scaling moment function is identical to the theoretical function up to $q = 2.1$.

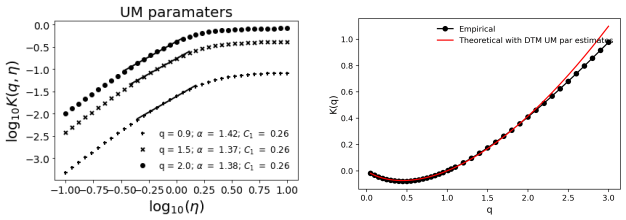

(a) UM parameters

(b) Scaling moment function $K(q)$

Figure 4.23: Ensemble analysis of Case 4.1.6.

Since energy fluxes in Cases 4.1.7 and Case 4.1.8 exhibit strong fluctuations, just like Case 4.1.6, the number of sub-series for ensemble analysis is 8, which used in Case 4.1.6. Ensemble analysis for subseries $N = 26$ to $N = 33$ of Case 4.1.7 shown in Fig 4.24a is $\alpha \approx 1.49,\ C_1 \approx 0.26$, which gives critical moment $q_s = 3$.

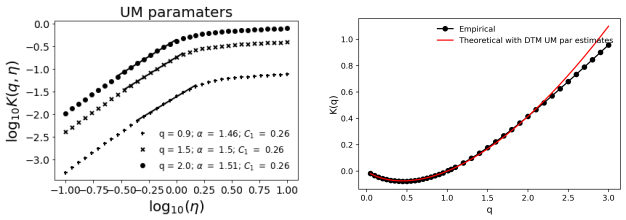

(a) UM parameters (b) Scaling moment function $K(q)$

Figure 4.24: Ensemble analysis of Case 4.1.7.

Fig 4.25 gives out UM parameters of Case 4.1.8 estimated by ensemble analysis $\alpha \approx 1.52,\ C_1 \approx 0.23$, which is performed on subseries $N = 12 - 17$.

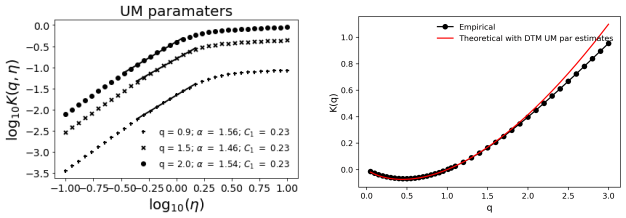

(a) UM parameters (b) Scaling moment function $K(q)$

Figure 4.25: Ensemble analysis of Case 4.1.8.

4.3.5 Summary of cascade step 12

Different forcings are injected into SGC model with cascade step $n = 12$ to study the intermittency of natural turbulence. Fluctuations in energy flux occur and gradually vanish when forcing is between 0.1 and 0.3, whereas extraordinarily large energy flux generated by forcing f larger than 0.8 stopped SGC model, which could be as a result of spatial structure of SGC model amplifying energy exchange. All energy fluxes

whose forcing is between 0.4 and 0.8 display highly intermittent. Probability distribution function of these fluctuations has a "heavy" tail, resulting in non-Gaussian distribution and allowing UM framework as an effective tool to study multifractality. According to UM analysis of Case 4.1.6, sample size 512 is chosen to display properties of fluctuations over the entire time series. UM parameters and critical moment q_s confirm the difference brought on by fixed range estimation because of different fluctuations for each subseries. Hence, adjusted range estimation method yields better fitted UM parameters. There aren't many subseries whose UM parameters are $\alpha \approx 1.5$ and $C_1 \approx 0.25$ when forcing is either small or large, but number of subseries closing to empirical UM parameters for atmospheric turbulence increases for the rest cases. Temporal evolution of UM parameters reveals the time of energy flux which is consistent with the atmospheric turbulence, and frequency plots suggests UM parameters for most cases centered on $\alpha \approx 1.5$ and $C_1 \approx 0.25$. Averaged UM parameters are $\overline{\alpha} \approx 1.55 \pm 0.05$ and $\overline{C_1} \approx 0.25 \pm 0.05$ except forcing 0.1. At last, ensemble analyze of energy flux whose parameters consistent to empirical UM parameters is carried out.

4.4 Cascade step 14

Intermittency of forced SGC model with a large cascade step $n = 14$ is investigated, and the range of external forcings is from 0.1 to 1.1 because of larger cascade step. Time step and dissipation step have both been reset. Initial values are presented in Table 4.3 as well as extended cascade step that was used to study energy flux. The study is divided into three parts: intermittency, non-Gaussian distribution, and time evolution of multifractality.

Table 4.3: Case 4.2 whose cascade step is $n = 14$

Case 4.2				
	n	η^*	Δt	m
	14	12	0.0001	8
Case	f		τ	
4.2.1	0.1		25001	
4.2.2	0.2		25001	
4.2.3	0.3		25001	
4.2.4	0.4		25001	
4.2.5	0.5		25001	
4.2.6	0.6		25001	
4.2.7	0.7		21371	
4.2.8	0.8		14000	
4.2.9	0.9		20974	
4.2.10	1		19000	
4.2.11	1.1		7000	

4.4.1 Intermittency of energy flux

Energy flux $\Pi(k_8)$ of Case 4.2 is displayed in Fig 4.26.

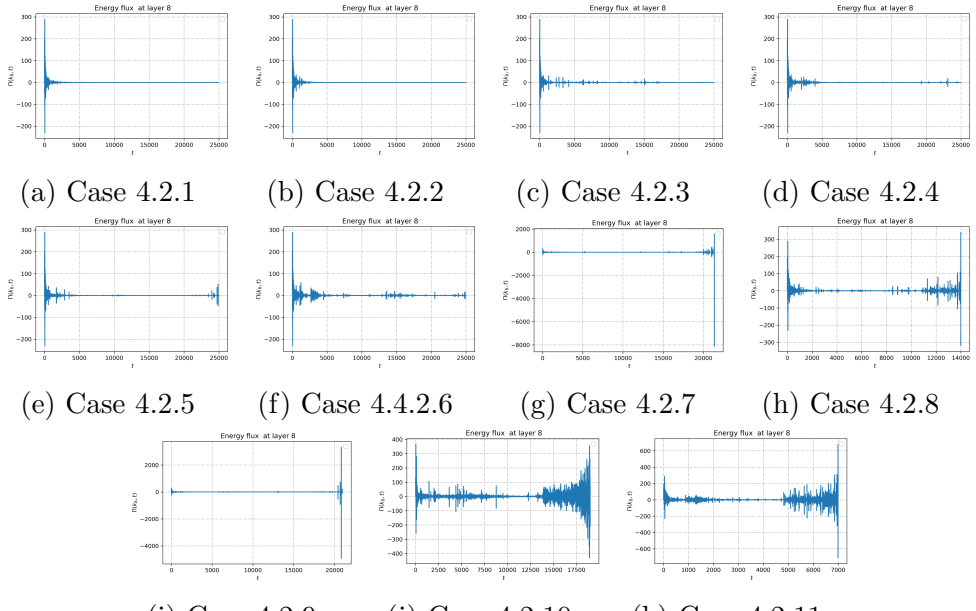

(a) Case 4.2.1 (b) Case 4.2.2 (c) Case 4.2.3 (d) Case 4.2.4

(e) Case 4.2.5 (f) Case 4.4.2.6 (g) Case 4.2.7 (h) Case 4.2.8

(i) Case 4.2.9 (j) Case 4.2.10 (k) Case 4.2.11

Figure 4.26: Energy flux $\Pi(k_8)$ of Case 4.2.

When injected forcing is larger than 0.7 due to incredibly high energy flux, SGC model ends before expected time scale 25001 and more quickly as the forcing increases. Energy fluxes with forcing below 0.7 show that SGC model doesn't generate excessively huge value and can be numerically simulated up to expected time. Cases 4.2.1-Case 4.2.6 begin in an unstable condition, as shown in Fig 4.26a-Fig 4.26f, thereby making it difficult to directly observe fluctuations. Meanwhile, large energy fluxes at the end shown in Fig 4.26g-Fig 4.26i pose a difficulty to observe the intermittency.

Energy flux $\Pi(k_8)$ of Case 4.2 is shown in Fig 4.27, where intermittency is evident, once extreme energy fluxes at the beginning or end are removed. Fig 4.27f-Fig 4.27k show that there are strong fluctuations in Cases 4.2.6-4.2.11 throughout the time period. Fluctuations with large forcing get stronger towards the end, as it is in Case 4.2.7–Case 4.2.11. The beginning time period needs to be removed to study intermittency of Case 4.1.1-4.1.5 whose injected forcing is small. In contrast to cases injecting large forcing, Fig 4.27d and Fig 4.27e demonstrate weak fluctuations as a result of injected forcing. Fig 4.27c shows that intermittency disappears near the end, but this behavior disappears at much earlier times in Fig 4.27a and Fig 4.27b. Energy flux implies that intermittency is affected by external forcing.

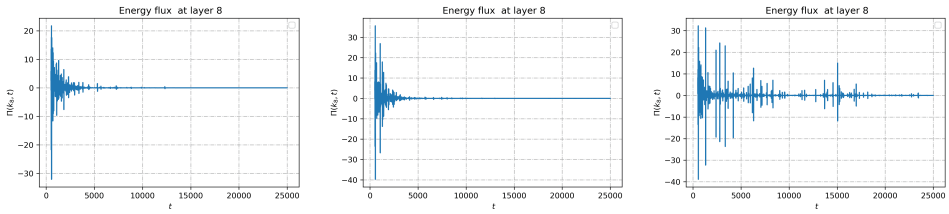

(a) Case 4.2.1 ($t : 500-$) (b) Case 4.2.2 ($t : 500-$) (c) Case 4.2.3 ($t : 500-$)

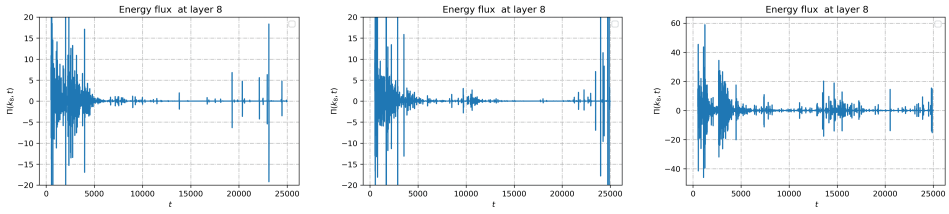

(d) Case 4.2.4 ($t : 500-$) (e) Case 4.2.5 ($t : 500-$) (f) Case 4.2.6 ($t : 500-$)

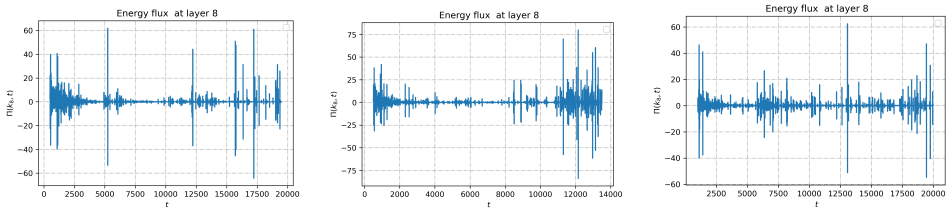

(g) Case 4.2.7 ($t : 500 - 19500$) (h) Case 4.2.8 ($t : 500 - 13500$) (i) Case 4.2.9 ($t : 1000 - 20000$)

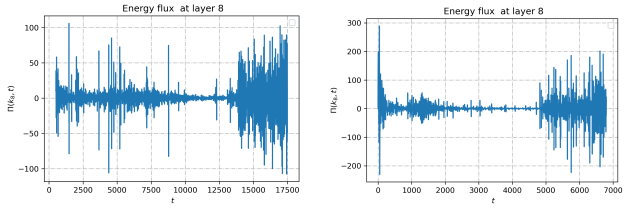

(j) Case 4.2.10 ($t : 500 - 17500$) (k) Case 4.2.11 ($t : 0 - 6800$)

Figure 4.27: Energy flux $\Pi(k_8)$ of Case 4.2 removing unstable time.

4.4.2 Non-Gaussian distribution and "heavy" tail

After observing fluctuations in energy flux of Case 4.2, probability distribution of

$\Delta|\Pi(k_8)|$ exceeding a fixed reflectivity threshold s is shown in Fig 4.28.

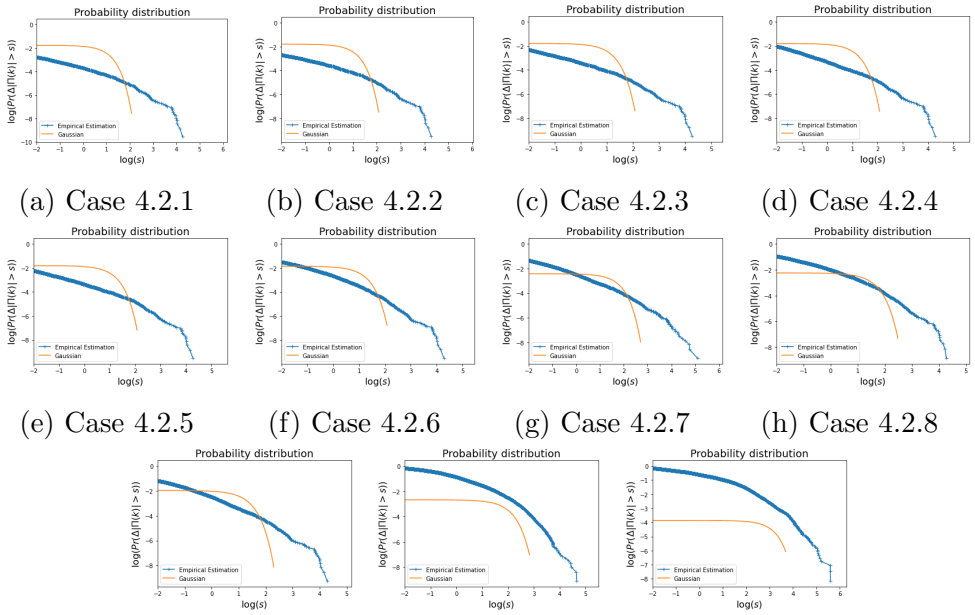

(a) Case 4.2.1 (b) Case 4.2.2 (c) Case 4.2.3 (d) Case 4.2.4

(e) Case 4.2.5 (f) Case 4.2.6 (g) Case 4.2.7 (h) Case 4.2.8

(i) Case 4.2.9 (j) Case 4.2.10 (k) Case 4.2.11

Figure 4.28: Log-log plot of probability $Pr(\Delta|\Pi(k_8)| > s)$ exceeding a fixed reflectivity threshold s of Case 4.2

The probability distribution compared with corresponding Gaussian distribution displays "heavy" tails for Case 4.2. Hence, UM framework is applied to study this extreme events causing "heavy" tails.

4.4.3 Multifractality described by UM framework

UM parameters for Case 4.2 are provided below to investigate multifractality of fluctuations over time. Energy flux is analysed in the same way as in cascade step 12 and analysis is presented from the largest forcing to the smallest forcing.

UM analysis for Case 4.2.11 is displayed in Fig 4.29.

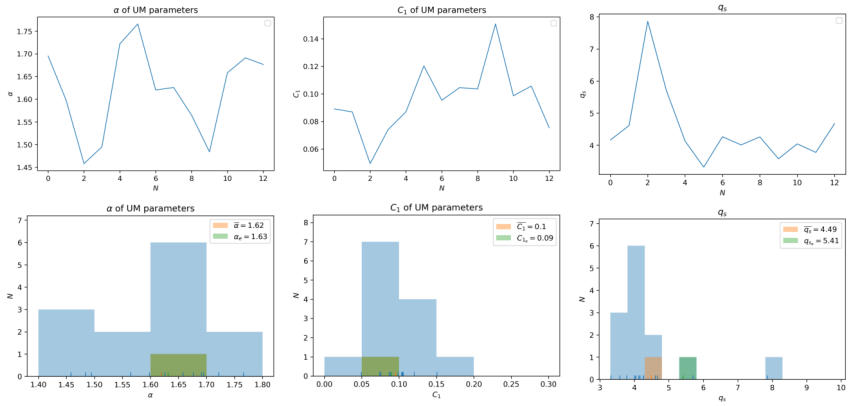

(a) Fix range method

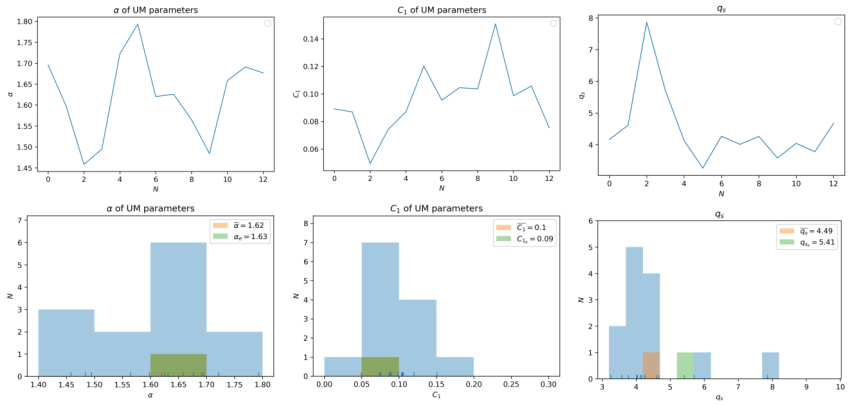

(b) Adjusted range method

Figure 4.29: Time evolution of UM parameters and critical moment of Case 4.2.11.

Both Fig 4.29a and Fig 4.29b show the same pattern for critical moments q_s as well as UM parameters. Mean values, frequency plots, and UM parameters obtained from ensemble analysis are identical, which naturally leads to same critical moments q_s. The difference caused by estimation range for Case 4.2.11 is negligible. Frequency plots in Fig 4.29b show that multifractality index α ranges from 1.45 to 1.80 and mean codimension C_1 varies under 0.25, indicating that energy flux $\Pi(k_8)$ of Case 4.2.11 does not match the characteristics of atmospheric turbulence. Besides, UM parameters

obtained from ensemble analysis are close to mean values, while q_s obtained from ensemble analysis are much larger than mean values, which is consistent with the definition of q_s taking into account sample dimension.

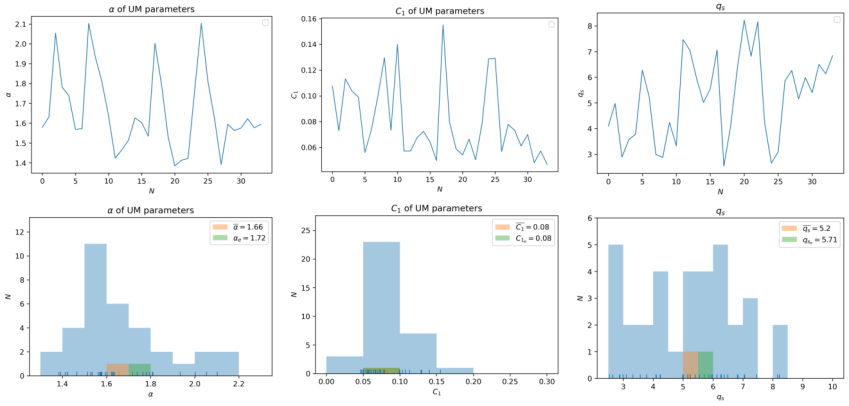

(a) Fix range method

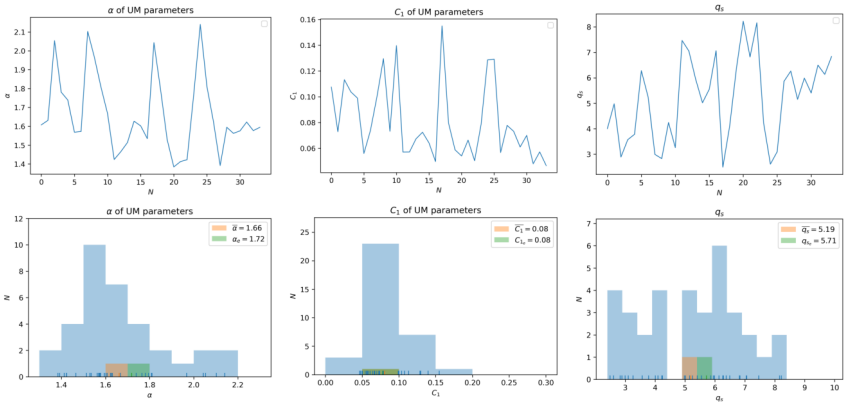

(b) Adjusted range method

Figure 4.30: Time evolution of UM parameters and critical moment of Case 4.2.10.

UM analysis for Case 2.10 with large forcing $f = 1$ is displayed in Fig.4.30. Similar to disparity analysis of Case 2.11, results in Fig.4.30a and Fig.4.30b are quite similar, demonstrating that the difference for Case 2.10 is negligible. Since mean codimension C_1 in Fig.4.30b is less than 0.20, it can be concluded that no time period reflects

atmospheric turbulence. Even though, there are four sub-series with α greater than 2.

UM analysis of Case 4.2.9 is shown in Fig 4.31.

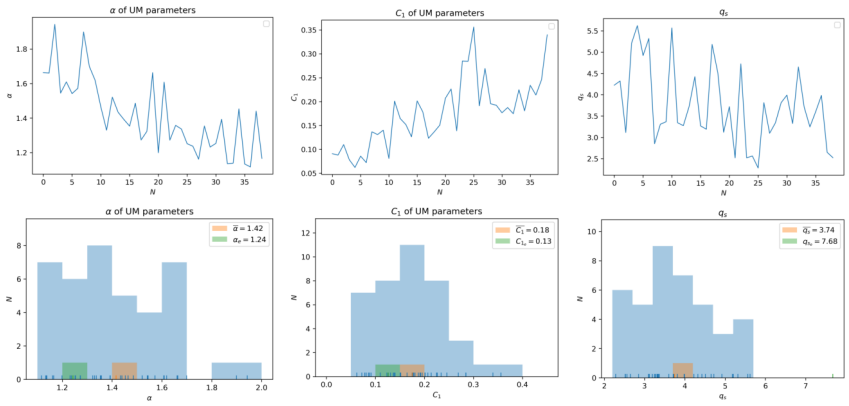

(a) Fix range method

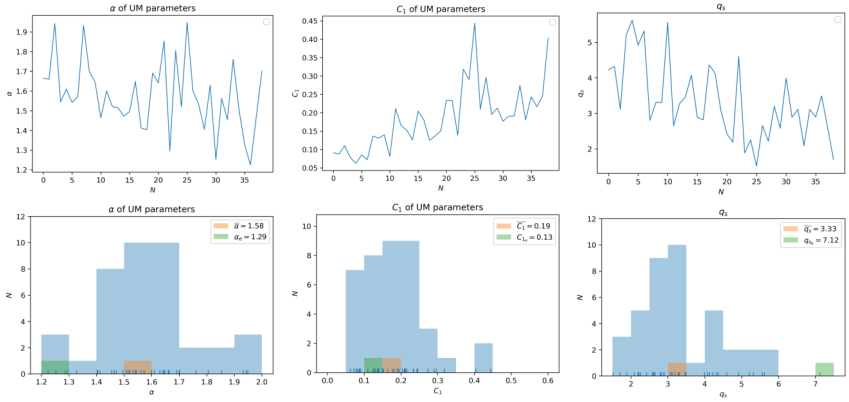

(b) Adjusted range method

Figure 4.31: Time evolution of UM parameters and critical moment of Case 4.2.9.

Fig 4.31a shows a decreasing multifractality index α, whereas Fig 4.31b displays α varying around the average. Comparing these two range estimations, both the average and frequency plot of α change. Similar tendencies are seen in Fig 4.31 for mean codimension C_1. As a result, q_s exhibits significant variation. This significantly

disparity that differs from Cases 4.2.10 and 4.2.11, implying that adjusted range estimation provides well fitted UM analysis. According to Fig 4.31b, α varies between 1.2 and 2, but does not exceed 2. C_1 is in the range of 0.05 and 0.45 and q_s stabilizes after getting rid of initial unstable state.

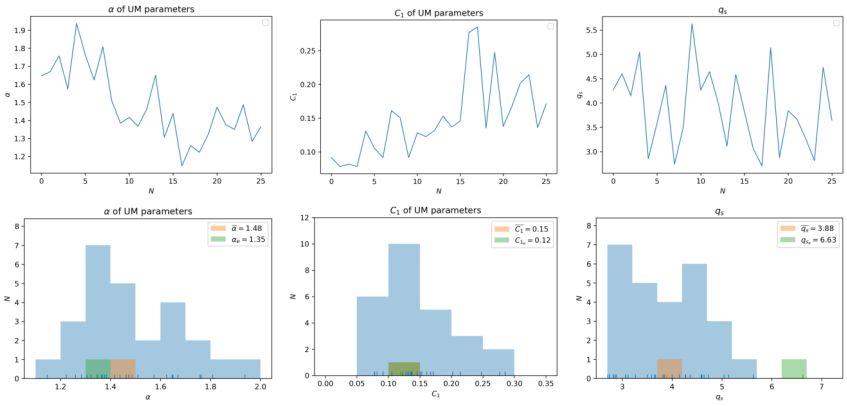

(a) Fix range method

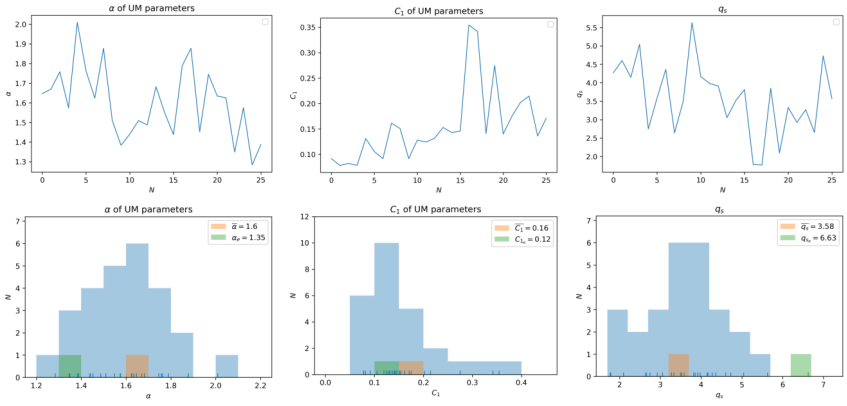

(b) Adjusted range method

Figure 4.32: Time evolution of UM parameters and critical moment of Case 4.2.8.

Case 4.2.8 is shown in Fig 4.32. There aren't many noticeable deviations in tendencies of UM parameters and q_s between Fig 4.32a and Fig 4.32b. The difference yielded by range estimation is, nevertheless, confirmed by mean values. After initial

unstable condition, α in Fig 4.32b is in the range of 1 to 2, but only three subsequences have C_1 between 0.2 and 0.3. As a result, there are few sub-series in Case 4.2.8 whose UM parameters are comparable to those of atmospheric turbulence.

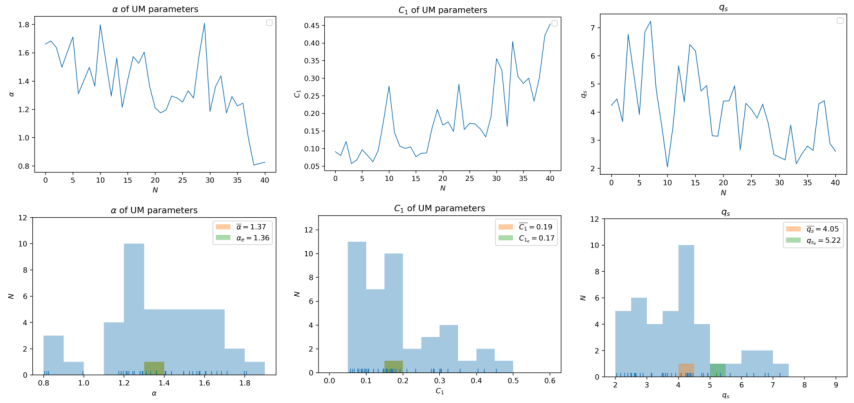

(a) Fix range method

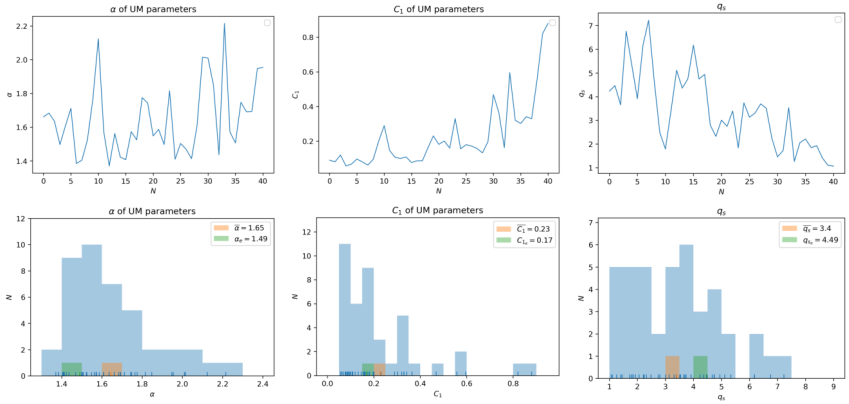

(b) Adjusted range method

Figure 4.33: Time evolution of UM parameters and critical moment of Case 4.2.7.

Fig.4.33 is the UM analysis of Case 4.2.7. α in Fig 4.33b compared to Fig 4.33a increases, as indicated by mean value. C_1 is greater than 0.8 at the end in Fig 4.33b, whereas it is close to 0.5 in Fig 4.33a. Thus, q_s in Fig 4.33b is without a doubt different from those in Fig 4.33a, as shown by mean values and frequency plots, even

though curves are similar. These differences confirm that adjusted range estimation is a well fitted UM parameters technique. Additionally, three subseries with α greater than 2 caused by the same reason as in Case 2.10. Based on temporal evolution of UM parameters, subseries exist in which UM parameters are in agreement with empirical value for atmospheric turbulence.

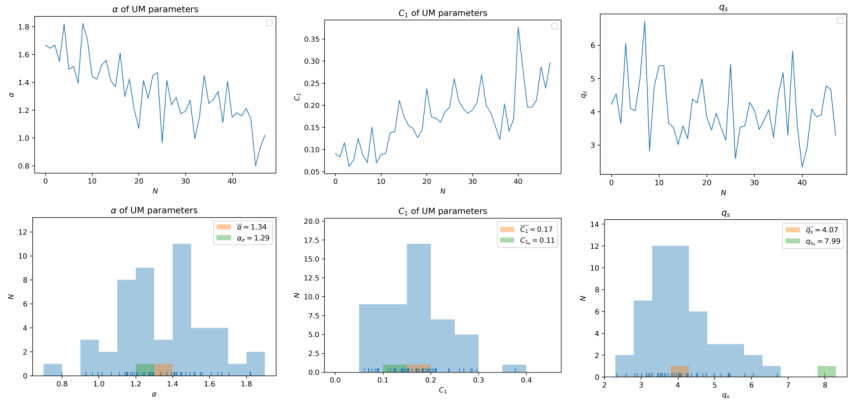

(a) Fix range method

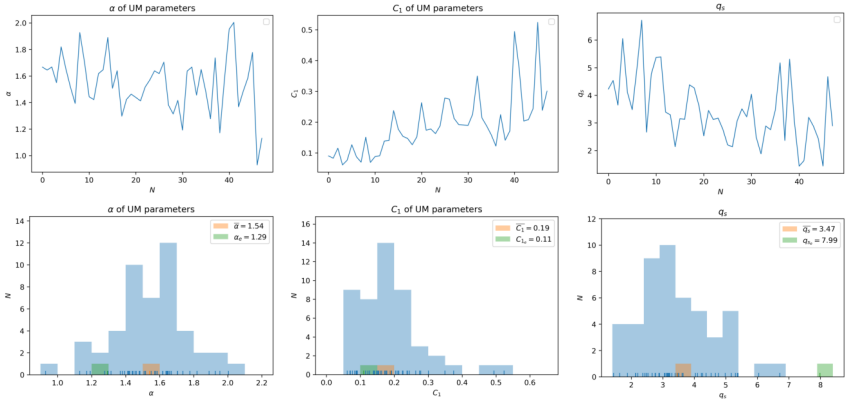

(b) Adjusted range method

Figure 4.34: Time evolution of UM parameters and critical moment of Case 4.2.6.

Time evolution of UM parameters for Case 4.2.6 exhibiting highly intermittent energy flux is shown in Fig 4.34. α decreases and then stabilizes in Fig 4.34a, but swings steadily around the mean in Fig 4.34b. Disparity in α caused by estimation

range is demonstrated by frequency plot and mean value. C_1 in Fig 4.34b is almost identical to that in Fig 4.34a. Change in q_s results from the variation in α. All these results testify difference generated by estimation range for Case 4.2.6. In Fig 4.34b, α is in the range of 1 and 2 before $N = 40$, whereas there are two extreme values after $N = 40$: one larger than 2 at $N = 41$ and another less than 1 at $N = 46$. C_1 is less than 0.4 before $N = 40$ and has two values approaching 0.5 after $N = 40$.

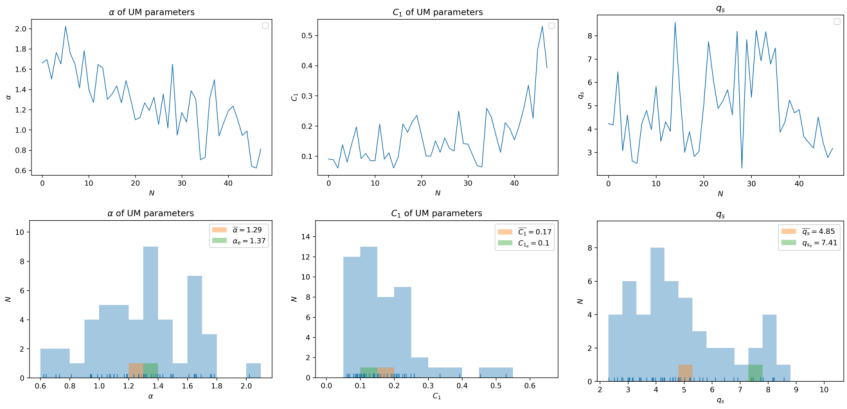

(a) Fix range method

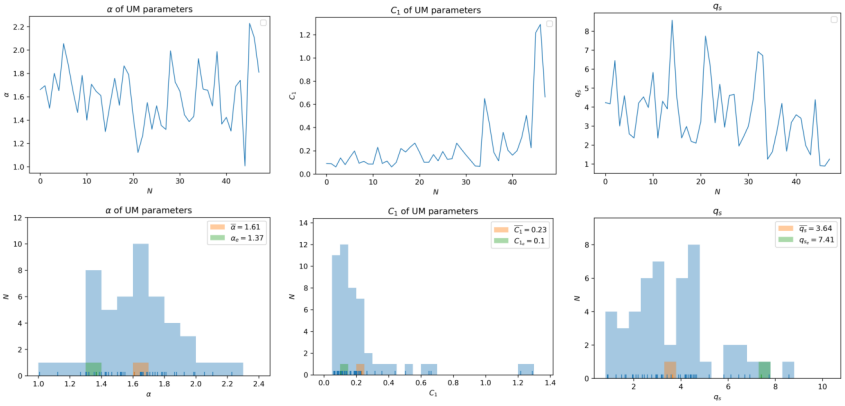

(b) Adjusted range method

Figure 4.35: Time evolution of UM parameters and critical moment of Case 4.2.5.

UM analysis for Case 4.2.5 is shown in Fig 4.35. Variations in UM parameters

and q_s implies the difference caused by estimation range. α is decreasing in Fig 4.35a, whereas it is fluctuating around the mean in Fig 4.35b. C_1 increases to almost 0.6 in Fig 4.35a, but exceeds abnormal value 1.2 in Fig 4.35b. The disparity resulting from estimation range is evident in both frequency plots and mean values of UM parameters. Therefore, q_s has a significantly change after $N = 20$ in Fig 4.35b compared to Fig 4.35a. In addition, three α large than 2 after $N = 40$ are shown in Fig 4.35b.

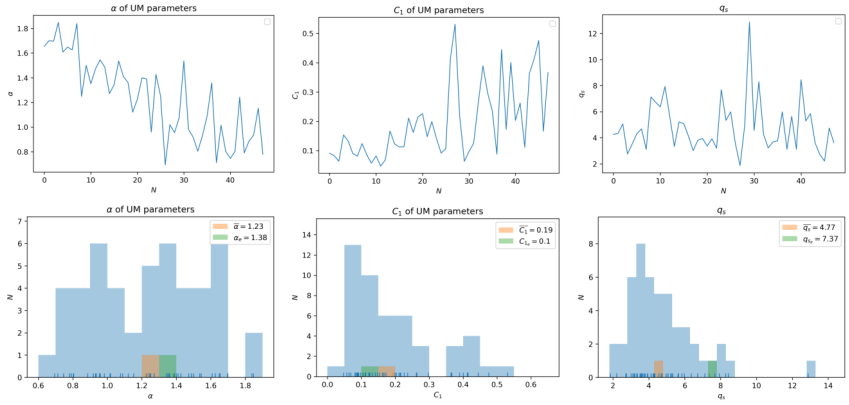

(a) Fix range method

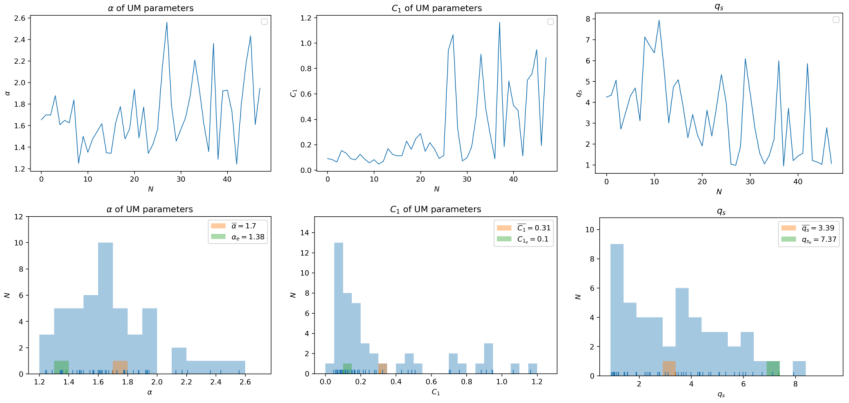

(b) Adjusted range method

Figure 4.36: Time evolution of UM parameters and critical moment of Case 4.2.4.

UM analysis of Case 4.2.4 is provided in Fig 4.36. Similar to Case 4.2.5, both tendencies and frequency plots of UM parameters demonstrate difference caused by estimation range for Case 4.2.4. α has six values larger than 2 after $N = 20$, and C_1 has two abnormal value which is greater than 1. These extreme values indicate that Case 4.2.4 with forcing 0.4 generates many non-multifractal subseries and appeared earlier than Case 4.1.5. Unfortunately, there is no overlap time satisfying $\alpha \approx 1.5$ and $C_1 \approx 0.25$, according to time evolution of UM parameters. So Case 4.2.4 doesn't have enough subseries to perform ensemble analysis.

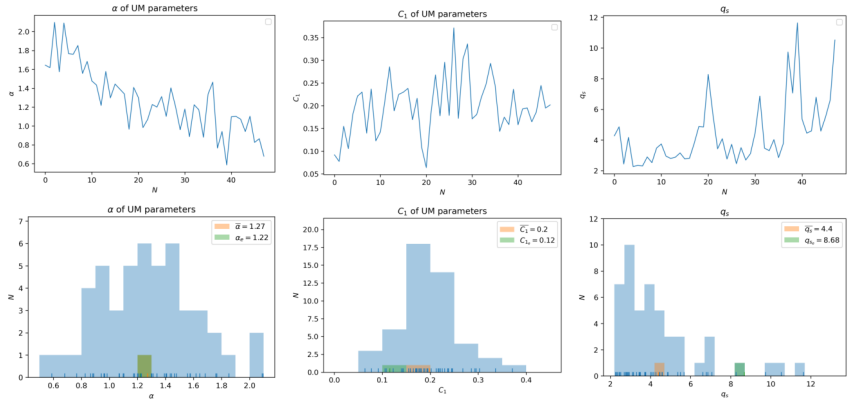

(a) Fix range method

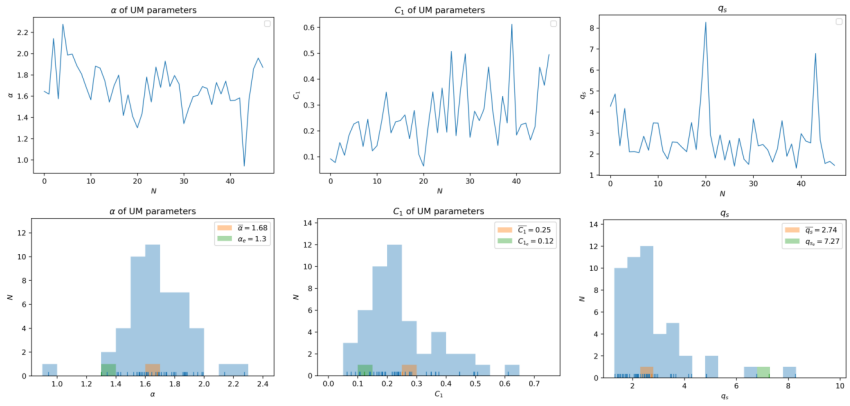

(b) Adjusted range method

Figure 4.37: Time evolution of UM parameters and critical moment of Case 4.2.3.

UM analysis of Case 4.2.3, in which forcing is 0.3 and fluctuations vanish over time, is shown in Fig.4.37. In Fig 4.37a, α has a downward trend and C_1 is centered around the mean. q_s is stable before the final upward trend. Averaged UM parameters in Fig 4.37b is greater than those in Fig 4.37a. Frequency diagrams further confirm disparity caused by well fitted UM estimation. After forced SGC model has been fully developed, α is less than 2, and has a value less than 1 at the end which is in agreement with disappearing fluctuations. C_1 is between 0 and 1, with no abnormal value. Frequency diagrams of UM parameters for Case 4.2.3 suggests that there are subsequences satisfying $\alpha \approx 1.5$ and $C_1 \approx 0.25$ before fluctuations vanishes. Overlapping time is confirmed by time evolution of UM parameters, indicating that energy flux exhibits atmospheric turbulence-like properties.

UM analysis of Case 4.2.2 is shown in Fig 4.38. Disparity in trend of UM parameters and q_s is obvious when Fig 4.38a and Fig 4.38b are compared, and their frequency plots and averages verify this difference. Although α in Fig.4.38b is around the mean, there are two values greater than 2. The number of subseries whose C_1 is in the range of 0.2 to 0.3 is 1. Forcing injected in Case 4.2.2 thus is not enough to provide ensemble analysis because of low values energy flux and weak fluctuations.

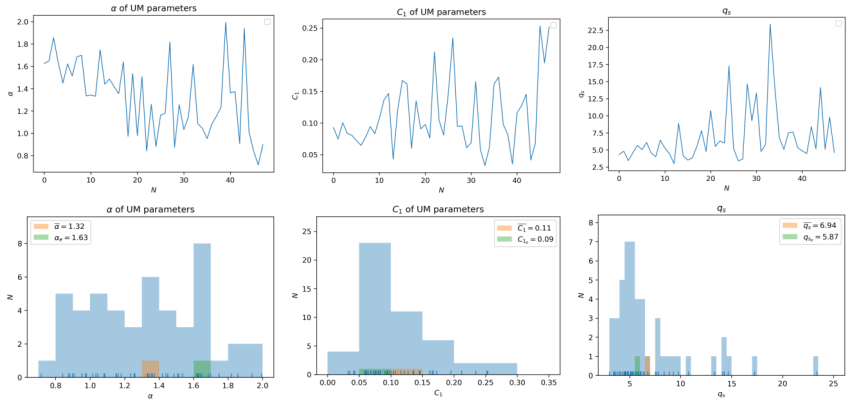

(a) Fix range method

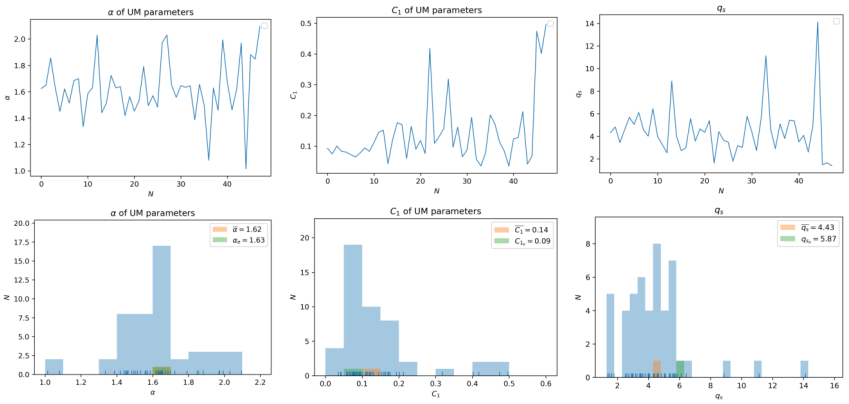

(b) Adjusted range method

Figure 4.38: Time evolution of UM parameters and critical moment of Case 4.2.2.

Fig 4.39 displays UM analysis of Case 4.2.1. The existence of range estimation-generated difference is proved by UM analysis comparison. C_1 suggests that energy flux of Case 4.2.1 does not have subseries to approximate empirical UM parameters, despite the frequency plot in Fig 4.39b indicating subseries satisfying $\alpha \approx 1.5$.

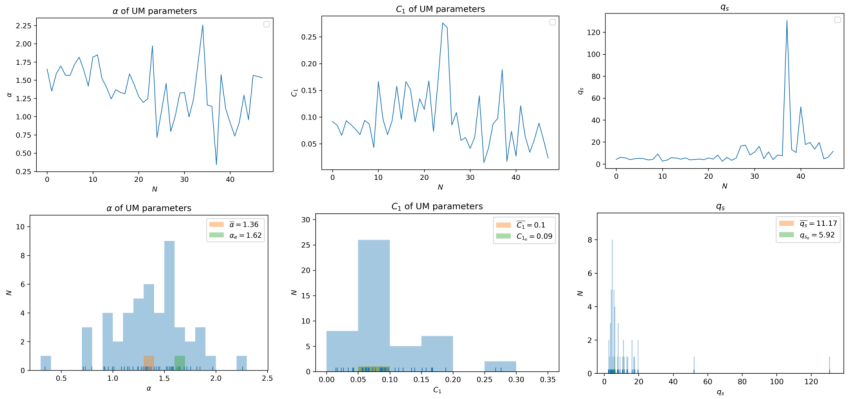

(a) Fix range method

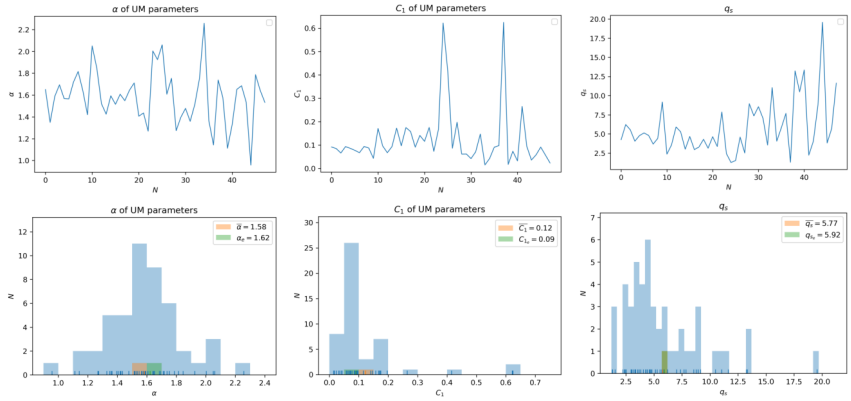

(b) Adjusted range method

Figure 4.39: Time evolution of UM parameters and critical moment of Case 4.2.1.

Frequency for subseries of Case 4.2 whose UM parameters are close to $\alpha \approx 1.5$ and $C_1 \approx 0.25$ is listed in Table 4.4. Case 4.2.7 - Case 4.2.11, whose forcing is large, doesn't reach expected time because of enormous energy flux. And few subseries satisfy $C_1 \approx 0.25$ with the exception of Case 4.2.9 resulting in mean values below 0.25. Case 4.2.1 and Case 4.2.2, on the other hand, have relatively few cases satisfying $C_1 \approx 0.25$ due to small forcings, as indicated by mean values. As for Case 4.2.3– Case 4.2.6, there are many subseries whose UM parameters are close to $\alpha \approx 1.5$ and $C_1 \approx 0.25$. Case 4.2 with sample size 512 has many subseries $\alpha > 2$, which is caused

by extreme values dominating scaling properties and leads to $\overline{\alpha}$ being larger than 1.5. Since averaged values are obtained over all subseries, including unstable state at the beginning or the end, it cannot be used to determine whether or not the entire time series is close to atmospheric turbulence. Time period of Case 4.2 that is consistent with atmospheric turbulence is displayed in the following.

Table 4.4: Frequency of UM parameters of Case 4.2 closing to atmospheric turbulence.

Case 4.2								
	n	η^*	Δt	m	resolution			
	14	12	0.0001	8	512			
Case	f	t_f	N_α	N_{C_1}	$\overline{\alpha}$	$\overline{C_1}$	α_e	C_{1_e}
4.2.1	0.1	25001	16	1	1.58	0.12	1.62	0.09
4.2.2	0.2	25001	16	2	1.62	0.14	1.63	0.09
4.2.3	0.3	25001	14	17	1.68	0.25	1.3	0.12
4.2.4	0.4	25001	11	10	1.7	0.31	1.38	0.1
4.2.5	0.5	25001	11	9	1.61	0.23	1.37	0.1
4.2.6	0.6	25001	17	12	1.54	0.19	1.29	0.11
4.2.7	0.7	21000	19	4	1.65	0.23	1.49	0.17
4.2.8	0.8	13500	9	3	1.6	0.16	1.35	0.12
4.2.9	0.9	20000	10	12	1.58	0.19	1.29	0.13
4.2.10	1	19000	14	0	1.66	0.08	1.72	0.08
4.2.11	1.1	7000	2	0	1.62	0.1	1.63	0.09

4.4.4 Time scale closing to atmospheric turbulence

Due to UM analysis for time evolution of fluctuations in the last section, this part presents ensemble analysis for the time exhibiting atmospheric turbulence-like properties. It starts with cases with small forcing. Here it has to point out that time scale for ensemble analysis doesn't necessarily have to be slot subseries from time evolution UM analysis. Due to the limitation of C_1, cases whose time scales reflect

the nature of atmospheric turbulence are Case 4.2.3-Case 4.2.6 and Case 2.9.

Ensemble analysis for subseries $N = 21$ to $N = 30$ in Case 4.2.3 is shown in Fig 4.40. UM parameters are close to empirical general value for atmospheric turbulence with $\alpha = 1.45$ and $C_1 = 0.26$.

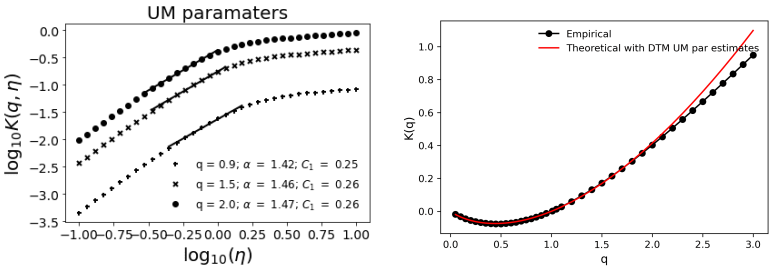

(a) UM parameters (b) Scaling moment function $K(q)$

Figure 4.40: Ensemble analysis of Case 4.2.3.

In spite of small forcing and weak fluctuations, Case 4.2.3 has a time period with UM parameters close to empirical general values. As stated, there is no time period for Case 4.2.4.

Ensemble analysis of Case 4.2.6 from time 18000 to 24145, with estimated UM parameters of $\alpha = 1.57,\ C_1 = 0.27$, as shown in Fig 4.41.

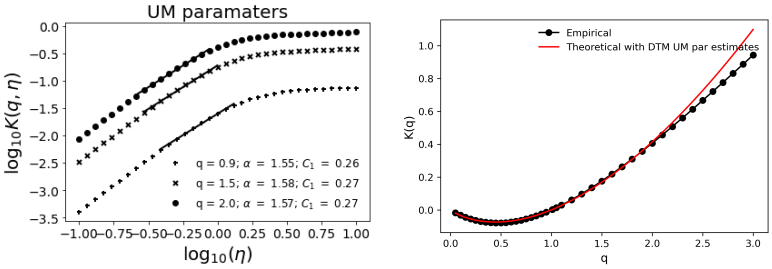

(a) UM parameters (b) Scaling moment function $K(q)$

Figure 4.41: Ensemble analysis of Case 4.2.6.

Ensemble analysis for Case 4.2.9 is shown in Fig 4.42. UM parameters obtained from ensemble analysis of subseries $N = 22$ to $N = 33$ are consistent with empirical UM parameters for atmospheric turbulence. Estimated UM parameters are $\alpha = 1.51, C_1 = 0.24$ yielding critical moment $q_s = 3.21$. And the empirical function is indistinguishable from the theoretical function.

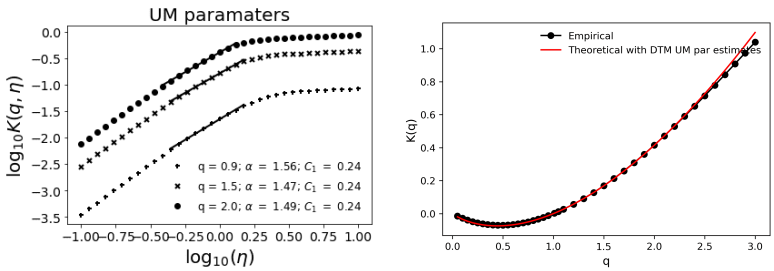

(a) UM parameters

(b) Scaling moment function $K(q)$

Figure 4.42: Ensemble analysis of subseries $N = 22 - 33$ in Case 4.2.9.

4.4.5 Summary of cascade step 14

SGC model with a large cascade step $n = 14$ injecting various forcing is studied. In all cases, energy fluxes exhibit fluctuations. Excessive energy flux is generated stopping SGC model when forcing is large, whereas fluctuations vanish for small forcing. For the remaining forcings, SGC model is capable of reaching expected numerical simulation time scale, and intermittency is present throughout the entire time series. The probability distribution function for these fluctuations doesn't follow Gaussian distribution, as indicated by the occurrence of a "heavy" tail. UM parameters and q_s of Case 4.2 also demonstrate the disparity brought on by estimation range. $\overline{\alpha}$ of Case

4.2 is $\overline{\alpha} \approx 1.66 \pm 0.06$, as there are several values $\alpha > 2$ caused by the extreme values in the field dominating scaling properties. Frequency plots, as well as Table 4.4, reveal that there are more subseries with UM parameters close to $\alpha \approx 1.5, C_1 \approx 0.25$ for middle-range forcings. Mean codimension C_1 is 0.25 ± 0.05 with the exception of small forcing Case 4.2.1-Case 4.2.2, large forcing Case 4.2.10-Case 4.2.11, and Case 4.2.8. Temporal evolution provides time periods and ensemble analysis confirms that part of time evolution is in agreement with atmospheric turbulence.

4.5 Cascade step 15

Numerical simulations of forced SGC model which has a large cascade step $n = 15$ are displayed with forcing ranging from 0.5 to 1.1. Simulation time grows exponentially with the maximum cascade step n in SGC model because of its spatial structure (see Chapter 3), so simulation is limited by computing devices. The initial condition is presented in Table.4.5.

Table 4.5: Case 4.3 whose cascade step is $n = 15$.

Case 4.3				
	n	η^*	Δt	m
	15	13	0.00007	9
Case	f		t_f	
4.3.1	0.5		25001	
4.3.2	0.6		25001	
4.3.3	0.7		13233	
4.3.4	0.8		25001	
4.3.5	0.9		19000	
4.3.6	1		18000	
4.3.7	1.1		11203	

4.5.1 Intermittency of energy flux

Energy flux of Case 4.3 is shown in Fig 4.43 to study the existence of fluctuations. In Case 4.3.1, Case 4.3.2, and Case 4.3.4, the simulation is able to complete computation within expected time frame. For Case 4.3.6 and Case 4.3.7 with large forcing, the simulation yields enormously large energy flux and ends running. Regardless, extreme values in either the initial unstable state or the end state, make it difficult to clearly observe fluctuations in Fig 4.43.

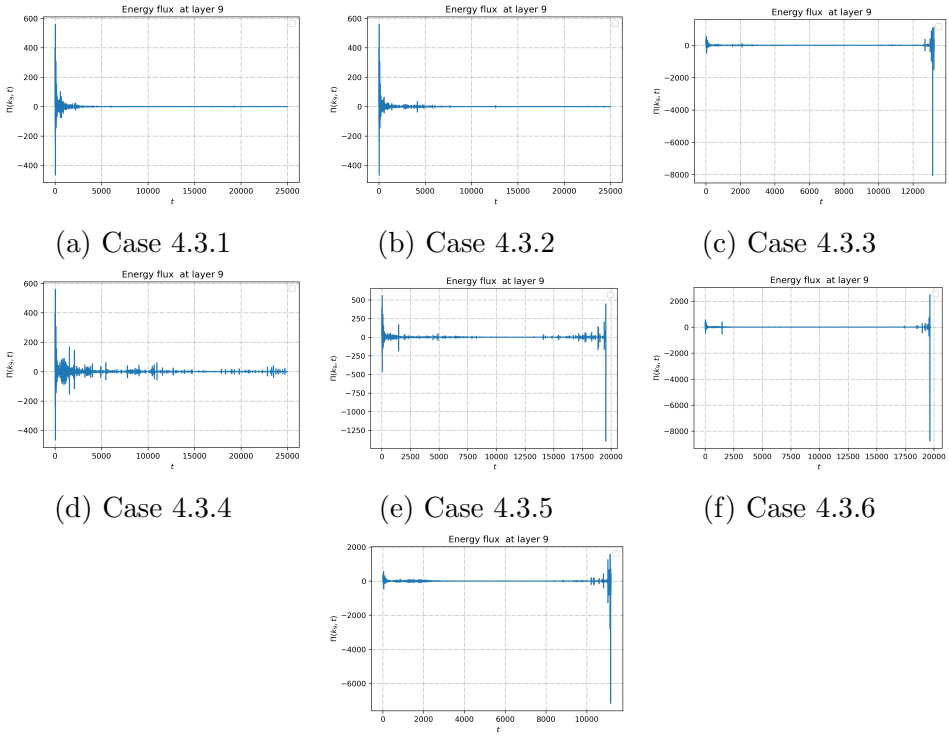

(a) Case 4.3.1 (b) Case 4.3.2 (c) Case 4.3.3

(d) Case 4.3.4 (e) Case 4.3.5 (f) Case 4.3.6

(g) Case 4.3.7

Figure 4.43: Energy flux $\Pi(k_9)$ whose cascade step $n = 15$.

Energy fluxes $\Pi(k_9)$ after removing these extreme values are shown in Fig 4.44. Energy fluxes in Case 4.3.1 and Case 4.3.2 display fluctuations, whereas intermittency

is observed in Case 4.3.3-Case 4.3.7 all the time series.

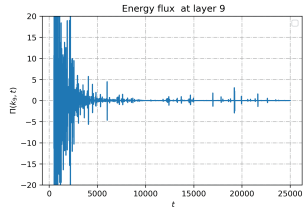

(a) Case 4.3.1 ($t : 500-$)

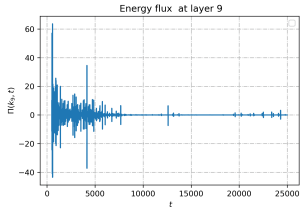

(b) Case 4.3.2 ($t : 500-$)

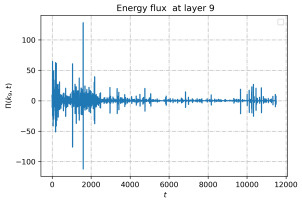

(c) Case 4.3.3 ($t : 500 - 12000$)

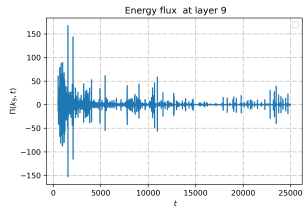

(d) Case 4.3.4 ($t : 500-$)

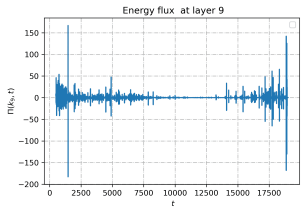

(e) Case 4.3.5 ($t : 500 - 19000$)

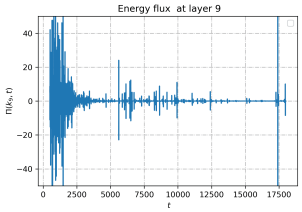

(f) Case 4.3.6 ($t : 500 - 18000$)

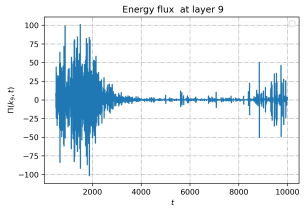

(g) Case 4.3.7 ($t : 500 - 10000$)

Figure 4.44: Energy flux $\Pi(k_9)$ of Case 4.3.

4.5.2 Non-Gaussian distribution and "heavy" tail

Probability distribution of fluctuations for Case 4.3 is given in this part. Fig 4.45 verify "heavy" tail for Case 4.3 by comparing probability distribution of $Pr(\Delta|\Pi(k_9)| > s)$ with Gaussian distribution that has the same mean and variance.

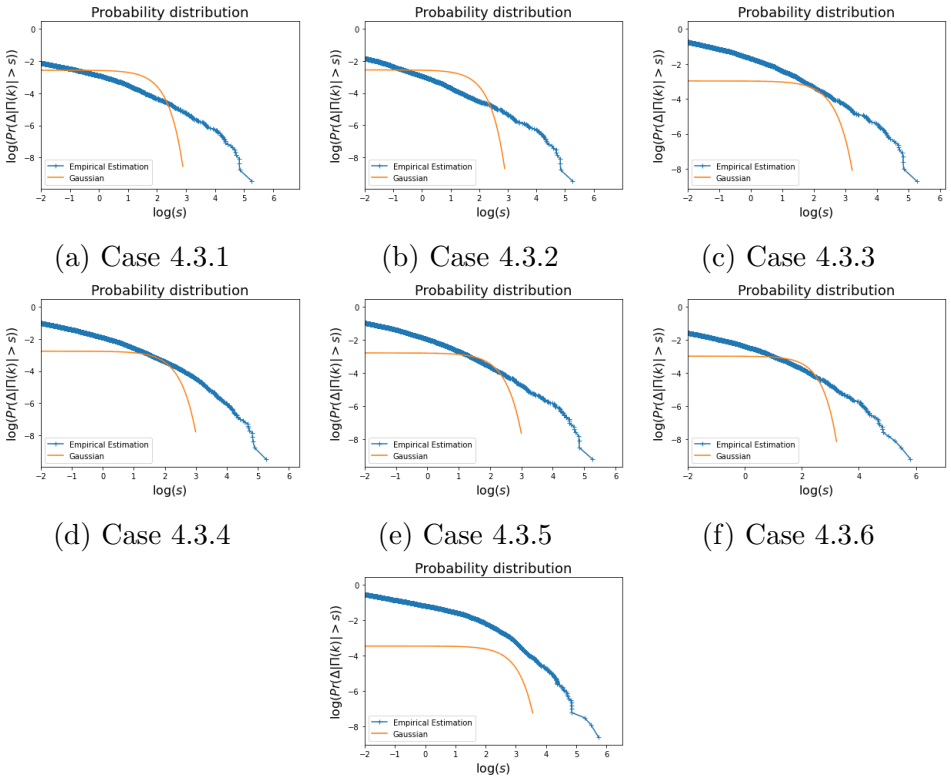

(a) Case 4.3.1 (b) Case 4.3.2 (c) Case 4.3.3

(d) Case 4.3.4 (e) Case 4.3.5 (f) Case 4.3.6

(g) Case 4.3.7

Figure 4.45: Log-log plot of probability $Pr(\Delta|\Pi(k_9)| > s)$ exceeding a fixed reflectivity threshold s of Case 4.3

4.5.3 Multifractality described by UM framework

Extreme events resulting in "heavy" tails are analyzed by UM framework to study multifractality over time and UM analysis of Case 4.3 is presented in descending order of forcing.

Case 4.3.7 with forcing $f = 1.1$ is shown in Fig 4.46.

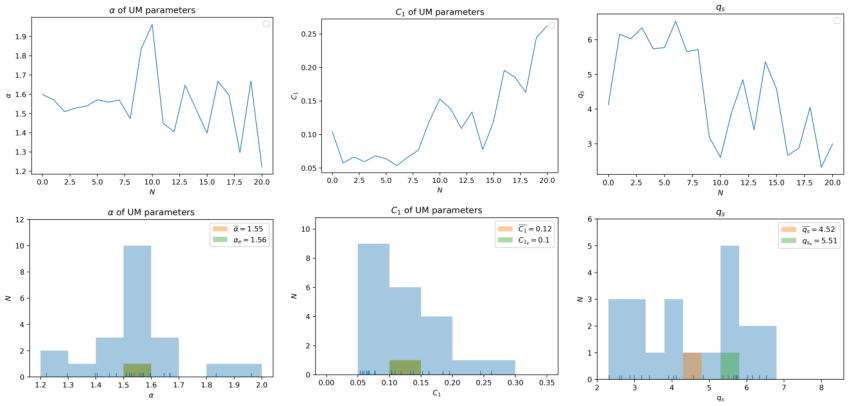

(a) Fix range estimation

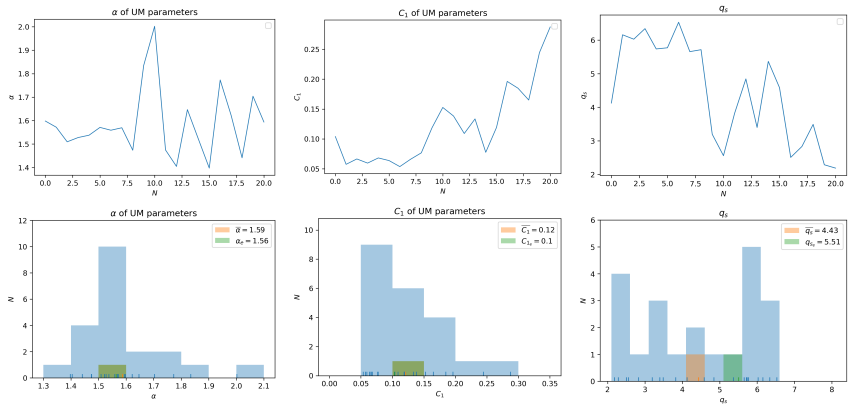

(b) Adjusted range estimation

Figure 4.46: Time evolution of UM parameters and critical moment of Case 4.3.7.

Two range estimation methods yield nearly identical trend curves for UM parameters and q_s. Frequency plots suggest that the means haven't changed significantly, but a few modifications have been made to C_1. Changes in α lead to adjustments of the frequency plot and the mean of q_s q_s obtained from ensemble analysis is larger than the mean due to sample number. UM parameters in the early phase have one value α greater than 2 and several C_1 lower than 0.1 as the model is trying to reach quasi-equilibrium before injected forcing is not yet acting. When forcing is large, the

time scale for analysis cannot reach expected time, preventing it from providing more information. Considering that C_1 has only two subseries around 0.25, there are no more than three subseries approaching atmospheric turbulence for ensemble analysis.

Analysis of Case 4.3.6 is shown in Fig 4.47, whose time scale reaches its maximum around 20000 and is adequate to study intermittency.

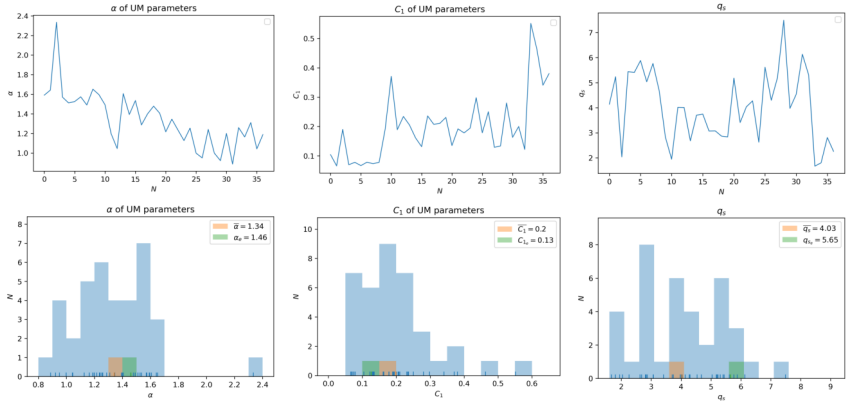

(a) Fix range estimation

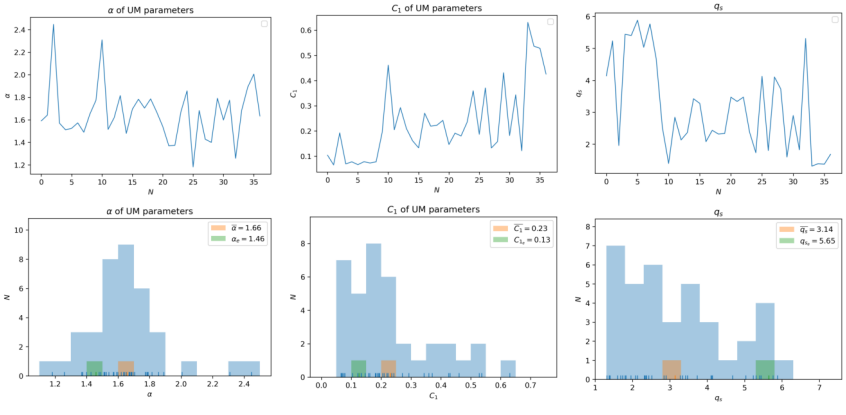

(b) Adjusted range estimation

Figure 4.47: Time evolution of UM parameters and critical moment of Case 4.3.6.

In contrast to α in Fig.4.47a, it in Fig.4.47b varies around mean. There is a disparity for subseries $N = 25 - 30$ between Fig.4.47b and Fig.4.47a. The definition

of q_s implies that it is normal for Case 4.3.6 that q_s yielded from these range estimation methods are different. In addition, UM parameters indicate that there is an overlap time that satisfies α around 1.5 and C_1 around 0.25.

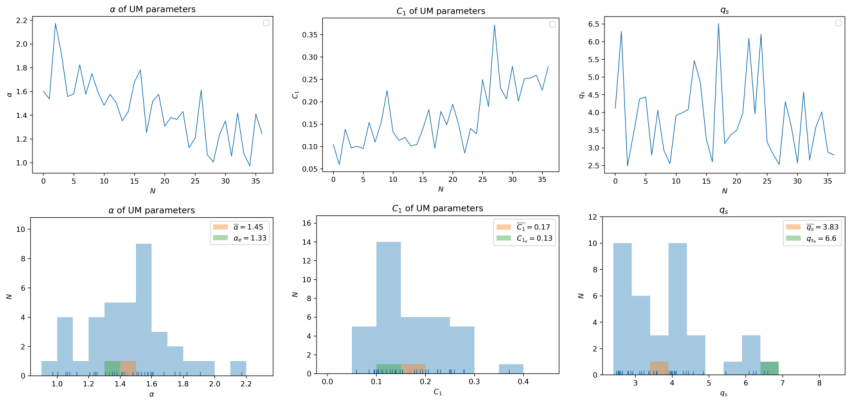

(a) Fix range estimation

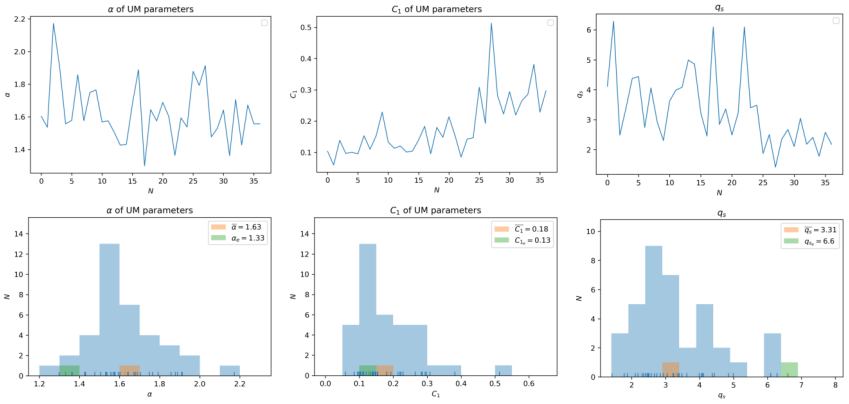

(b) Adjusted range estimation

Figure 4.48: Time evolution of UM parameters and critical moment of Case 4.3.5.

Fig 4.48 illustrates UM analysis of Case 4.3.5, which demonstrates the observed changes in α and q_s, including trends, frequency plots, and mean values. For instance, the trend of α after $N = 20$ in Fig 4.48b is much more stable than that in Fig 4.48a. This confirms the difference caused by range estimation. Besides, time evolution

of UM parameters reveals an overlap time satisfying $\alpha \approx 1.5$ and $C_1 \approx 0.25$, and ensemble analysis is carried out in the following part.

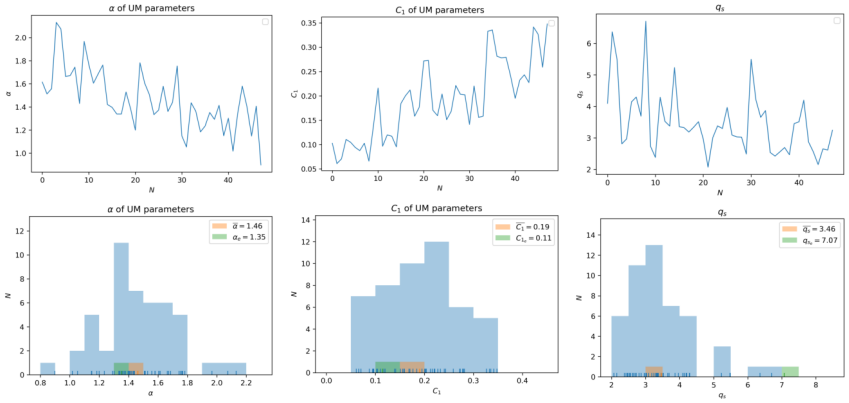

(a) Fix range method

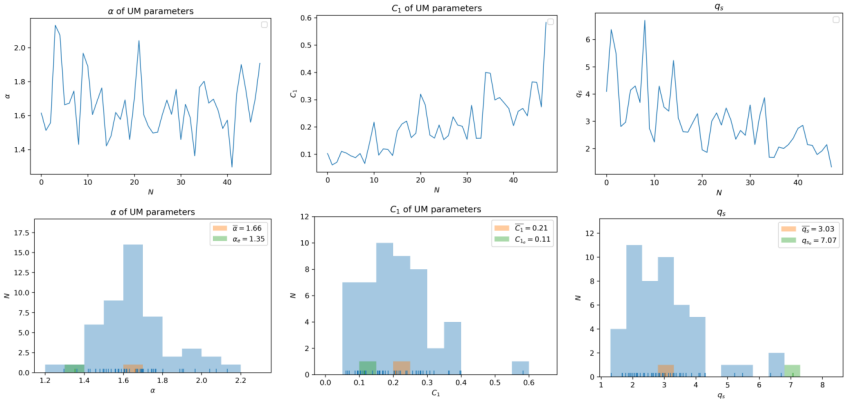

(b) Adjusted range method

Figure 4.49: Time evolution of UM parameters and critical moment of Case 4.3.4.

The result of Case 4.3.4, whose analysis is similar to that of Case 4.3.6, is displayed in Fig 4.49. Multifractality index α, including the trend, frequency plot, and mean, clearly reveals the difference between these two range estimations, which is further supported by changes in trend and the mean of q_s. Fig 4.49b shows a higher frequency of subsidies whose α is close to 1.5 and C_1 is close to 0.25, and overlap time periods

agreeing with empirical UM parameters.

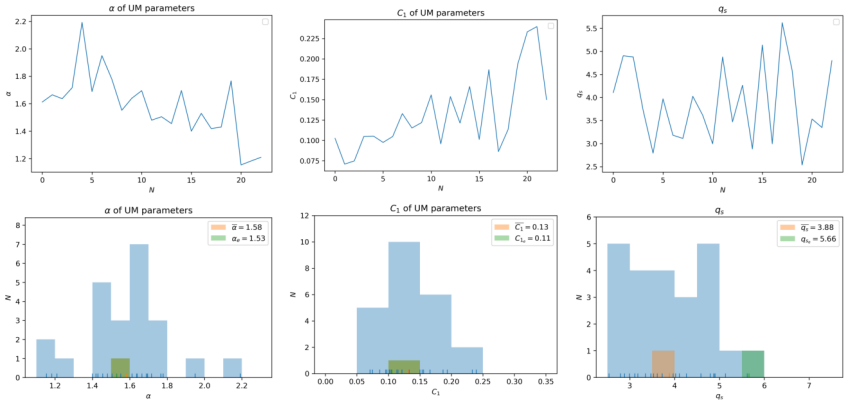

(a) Fix range estimation

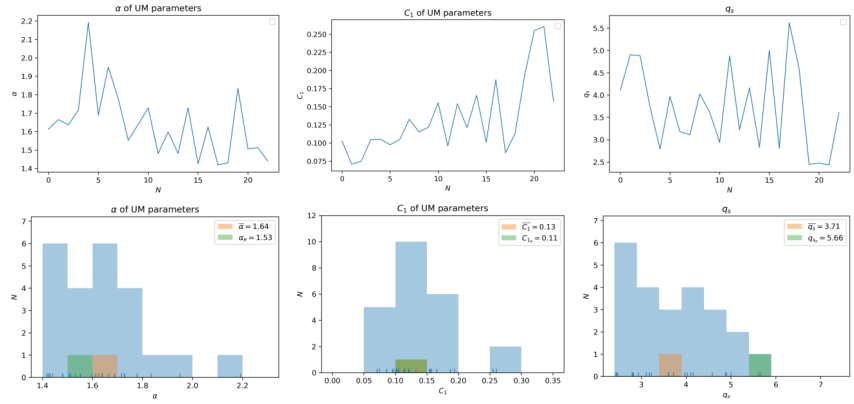

(b) Adjusted range estimation

Figure 4.50: Time evolution of UM parameters and critical moment of Case 4.3.3.

UM analysis for Case 4.3.3 is presented in Fig 4.50. Due to limitation of time scales, the difference resulting from estimated range is less visible than it is in the previous cases and there won't be sufficient time scale to provide ensemble analysis. Plus, frequency histogram of α displays an increment of $\overline{\alpha}$ resulting in changes of q_s.

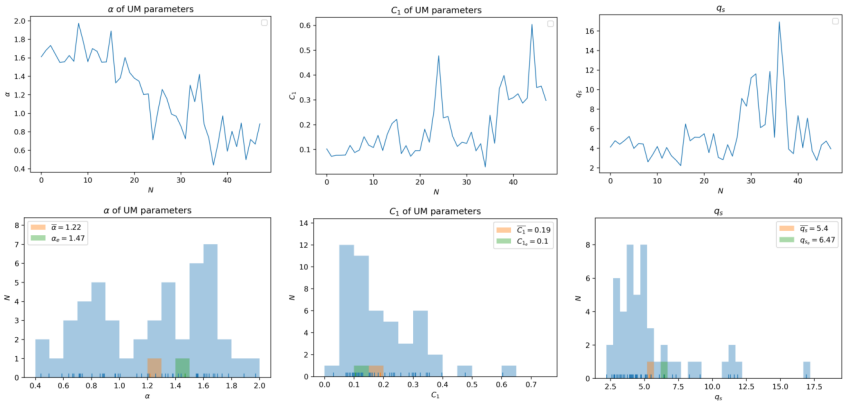

(a) Fix range estimation

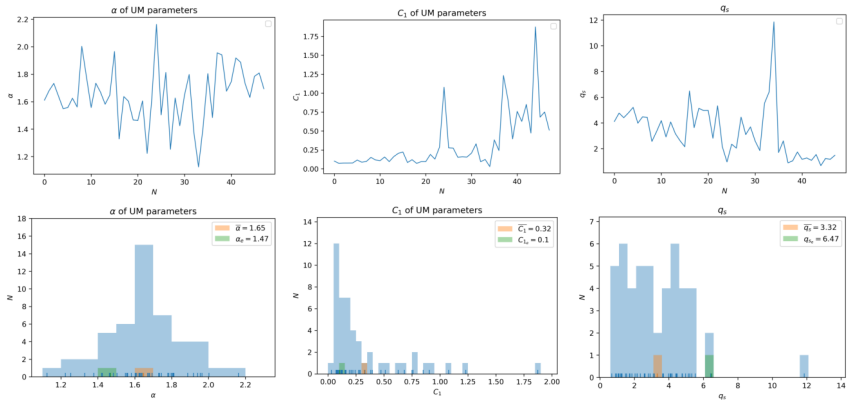

(b) Adjusted range estimation

Figure 4.51: Time evolution of UM parameters and critical moment of Case 4.3.2.

In Fig 4.51, UM analysis of Case 4.3.2 exhibiting vanishing fluctuation is displayed. α changes from decreasing in Fig 4.51a to floating around the mean in Fig.4.51b, and its frequency concentrates more closely around the mean. C_1 in Fig.4.51b reaches abnormal values toward the end instead of values closer to 0.6 in Fig.4.51a. So q_s in Fig.4.51b is approximately decreasing. Mean values of UM parameters and q_s also confirm the disparity generated by range estimation. But there are three subsequences $C_1 > 1$ indicating that they are not multifractal fields.

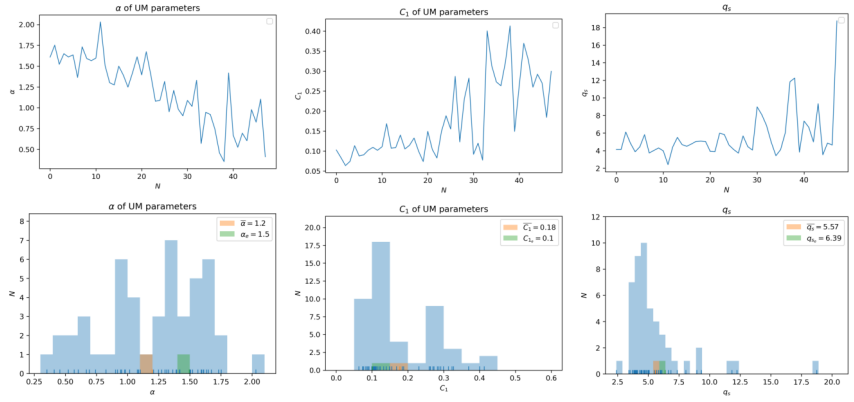

(a) Fix range estimation

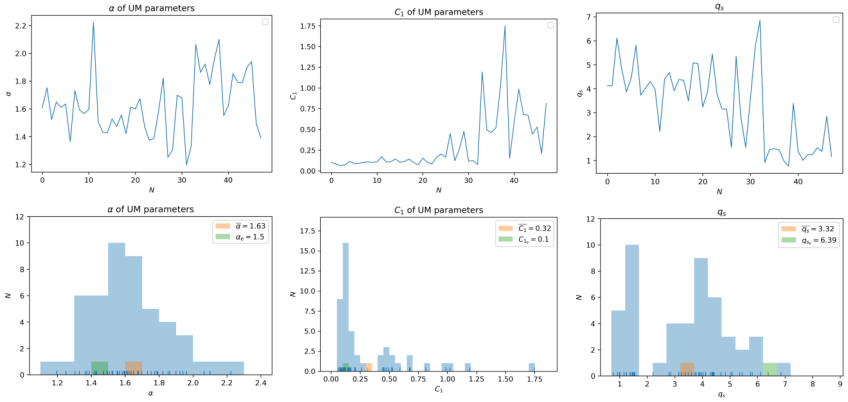

(b) Adjusted range estimation

Figure 4.52: Time evolution of UM parameters and critical moment of Case 4.3.1.

UM analysis for Case 4.3.1 is shown in Fig 4.52. Multifractality index α decreases gradually in Fig 4.52a, but not in Fig 4.52b, which is centered around the mean. Mean codimension C_1 increases below 0.5 in Fig 4.52a, whereas an abnormal value greater than 1 appears in Fig 4.52b. Critical moment q_s is stable except at the end in Fig 4.52a, while it falls off after subseries $N = 30$ in Fig 4.52b. The difference is also confirmed by averaged UM parameters. Besides, there are two subseries whose α is greater than 2 and three subseries with C_1 greater than 1 at the end in Fig 4.52b, indicating subseries with abnormal C_1 are not multifractal fields. Frequency of

$C_1 \approx 0.25$ as shown in Fig 4.52b limits subseries exhibiting properties of atmospheric turbulence.

The number of subseries with $\alpha \approx 1.5$ and $C_1 \approx 0.25$, as shown by frequency histograms, is summarized in Table 4.6. N_{C_1} of Case 4.3.7 whose forcing is extremely large causing SGC model stops at time 11000 is 2, while it is 3 for Case 4.3.1 whose fluctuations vanish. Because the energy flux of spatial eddies is so large that results in an early stopping, Case 4.3.3 only has two subseries satisfying $C_1 \approx 0.25$. These cases demonstrate the absence of a large time scale with UM parameters that are consistent with empirical UM parameters. For the rest, N_α and N_{C_1} in the table suggest that energy flux reflecting properties of atmospheric turbulence has sufficient time scale, and ensemble analysis is presented in the following part. The mean of multifractality index $\overline{\alpha}$ is 1.63 ± 0.04, which is greater than the empirical value 1.5 as many values $\alpha > 2$ appears in Case 4.3. $\overline{C_1}$ is 0.25 ± 0.07 excluding Case 4.3.1, Case 4.3.3, and Case 4.3.7.

Table 4.6: Frequency of UM parameters of Case 4.3 closing to atmospheric turbulence.

Case 4.3								
	n	η^*	Δt	m	resolution			
	15	13	0.00007	9	512			
Case	f	t_f	N_α	N_{C_1}	$\overline{\alpha}$	$\overline{C_1}$	α_e	C_{1_e}
4.3.1	0.5	25001	16	3	1.63	0.32	1.5	0.1
4.3.2	0.6	25001	11	7	1.65	0.32	1.47	0.1
4.3.3	0.7	12000	10	2	1.64	0.13	1.53	0.11
4.3.4	0.8	25001	15	17	1.66	0.21	1.35	0.11
4.3.5	0.9	19000	17	10	1.63	0.18	1.33	0.13
4.3.6	1	19000	11	8	1.66	0.23	1.46	0.13
4.3.7	1.1	11000	14	2	1.59	0.12	1.56	0.1

4.5.4 Time scale closing to atmospheric turbulence

Ensemble analysis for Case 4.3 is presented in this part. Case 4.3.1, Case 4.3.3, and Case 4.3.7 have inadequate time scales whose UM parameters agree with empirical UM parameters, according to N_{C_1} in Table 4.6. Overlapping time scale is not enough for Case 4.3.2, since Case 4.3.2 exhibiting gradually vanishing intermittency has abnormal C_1 after subseries $N = 20$ and α greater than 2 in the first half of time series. Ensemble analysis of Case 4.3.4-Case 4.3.6 is therefore carried out to demonstrate partial time series reflecting the characteristics of empirical atmospheric turbulence.

Ensemble analysis of Case 4.3.4 is shown in Fig 4.53. UM parameters performed on subseries $N = 30 - 45$ are $\alpha = 1.56$ and $C_1 = 0.26$, which implies scaling moment function $K(q)$ after critical moment function $q_s = 2.99$ is linear. And empirical scaling moment function is identical to the theoretical scaling moment function, as shown in Fig 4.55b.

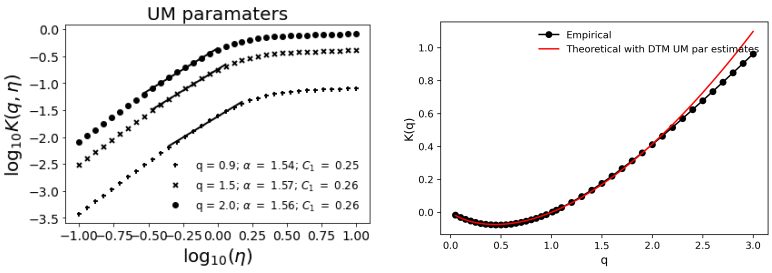

(a) UM parameters (b) Scaling moment function $k(q)$

Figure 4.53: Ensemble analysis of Case 4.3.4.

Fig 4.54 is ensemble analysis of subseries $N = 30 - 38$ in Case 4.3.5. UM parameters are $\alpha = 1.47$ and $C_1 = 0.27$ with critical moment function is $q_s = 2.96$.

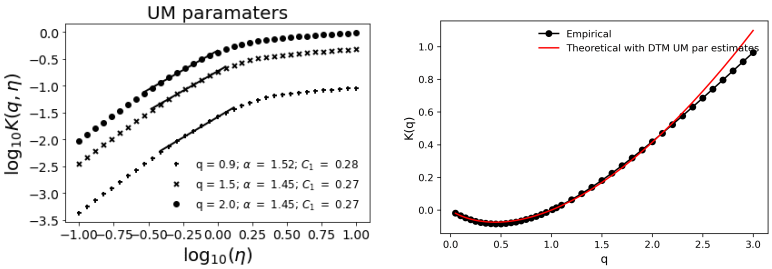

(a) UM parameters (b) Scaling moment function $k(q)$

Figure 4.54: Ensemble analysis of Case 4.3.5.

Ensemble analysis of Case 4.3.6 at time $12200 \leq t \leq 16800$ is shown in Fig 4.55. Estimated UM parameters are $\alpha = 1.5$ and $C_1 = 0.25$.

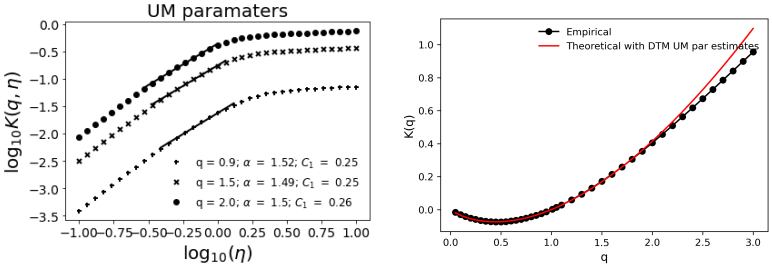

(a) UM parameters (b) Scaling moment function $k(q)$

Figure 4.55: Ensemble analysis of Case 4.3.6.

4.5.5 Summary of cascade step 15

In consideration of the complexity analysis of SGC model, the maximum cascade step using DNS in our study is $n = 15$. Case 4.3 exhibits fluctuations in energy flux in reaction to injected forcing. Except for Case 4.3.3, fluctuations get stronger and even end SGC model when forcing enlarges. Probability distribution function of these fluctuations has a "heavy" tail, allowing UM framework to be used to analyze them.

As statistically uniform estimating range may not be well fitted for every subseries, adjusted range estimation is utilized to estimate UM parameters and critical moments q_s. The number of subseries with UM parameters close to $\alpha = 1.5$ and $C_1 = 0.25$ is summarized in Table 4.6, which suggests both large forcing and small forcing will result in a low number satisfying $C_1 \approx 0.25$, whereas middle-range forcing has a large number of subsequences. Averaged multifractality index is 1.63 ± 0.04. C_1 is between 0.12 and 0.32, and $\overline{C_1}$ is 0.25 ± 0.07 excluding Case 4.3.1 with small forcing, Case 4.3.7 as well as Case 4.3.3 with large forcing. Corresponding ensemble analysis confirms that cases injecting forcing in the middle range do have time whose UM parameters are consistent with those of empirical atmospheric turbulence.

4.6 Computational instability by comparing semi-implicit Euler method

Computational instability has been revealed in three cases utilizing the classic Euler method. Case 4.1 is simulated by the semi-implicit Euler technique, which is more stable than the classic Euler approach, to investigate the reason for instability in this section.

Energy flux $\Pi(k_6)$ of Case 3.1 simulated by the semi-implicit Euler method is presented in Fig 4.56. Energy flux of Case 4.1.6 and Case 4.1.8 - Case 4.1.10 deviates significantly from what was simulated by classic Euler method in Fig 4.1. Case 4.1.6 stops at time 21856 and doesn't reach the expected time, which is earlier than that simulated by classic Euler method. Extremely large energy flux in Case 4.1.10 stopped

the computation in advance. However, Case 4.1.8 has a prolonged time series and significant values at the end, while Case 4.1.9 ends at the expected time.

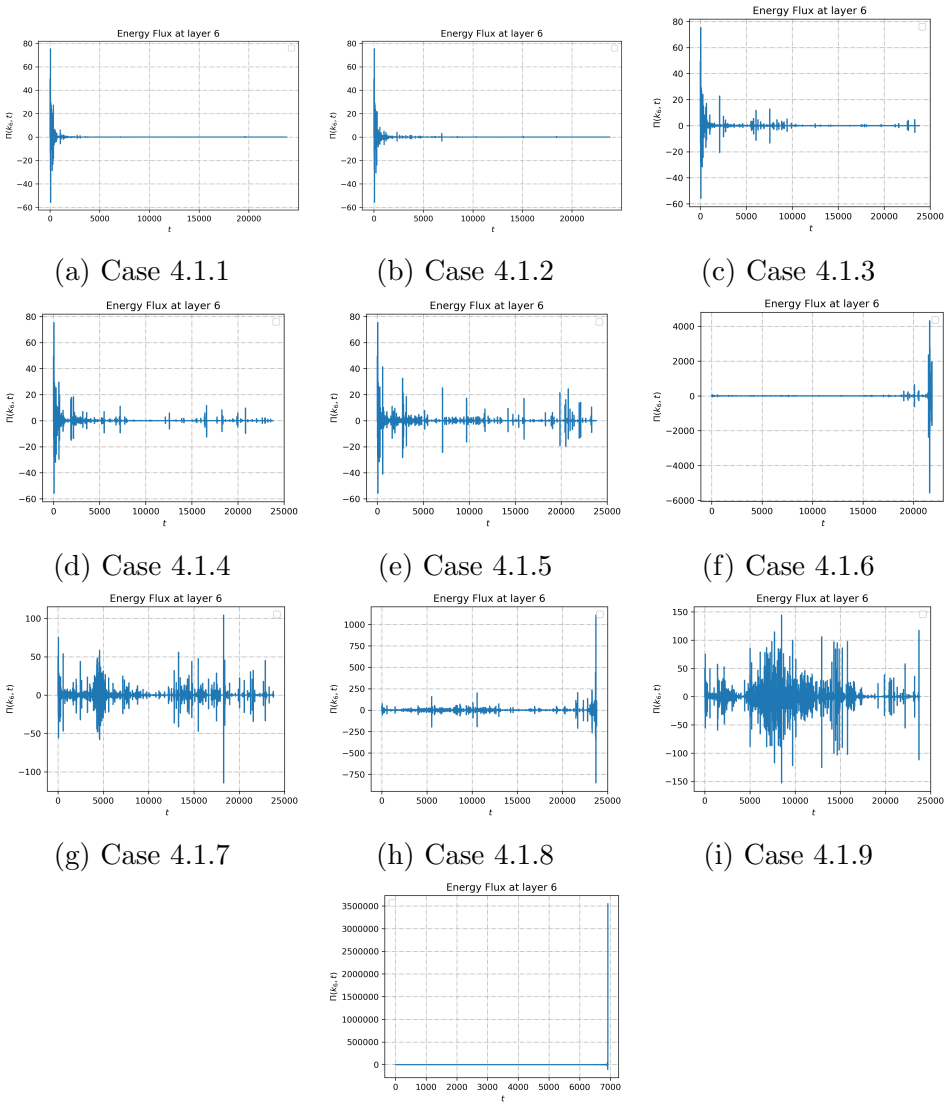

(a) Case 4.1.1 (b) Case 4.1.2 (c) Case 4.1.3

(d) Case 4.1.4 (e) Case 4.1.5 (f) Case 4.1.6

(g) Case 4.1.7 (h) Case 4.1.8 (i) Case 4.1.9

(j) Case 4.1.10

Figure 4.56: Energy flux $\Pi(k_6)$ of Case 4.1 simulated by semi-implicit Euler method.

Except for obvious fluctuations in Case 4.1.7 and Case 4.1.9, energy flux in the rest cases removing unstable state is presented in Fig 4.57. All cases exhibit fluctuations.

Especially, strong fluctuations are observed in most of Case 4.1 excluding Case 4.1.1 and Case 4.1.2.

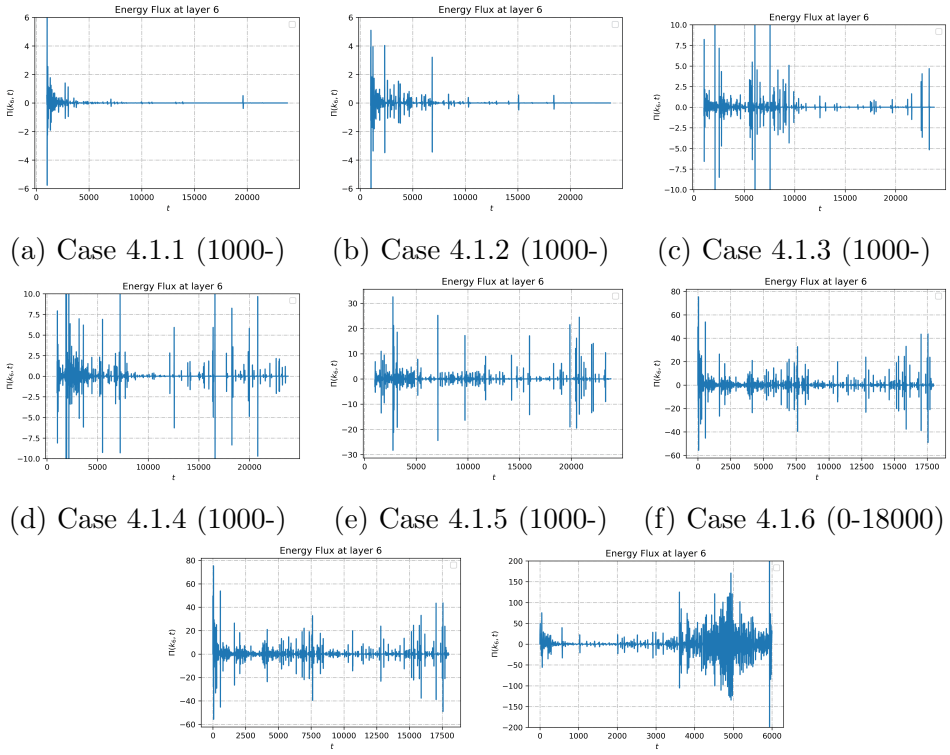

(a) Case 4.1.1 (1000-) (b) Case 4.1.2 (1000-) (c) Case 4.1.3 (1000-)

(d) Case 4.1.4 (1000-) (e) Case 4.1.5 (1000-) (f) Case 4.1.6 (0-18000)

(g) Case 4.1.8 (0-18000) (h) Case 4.1.10 (0-6000)

Figure 4.57: Energy flux $\Pi(k_6)$ of Case 4.1 which is simulated by the semi-implicit Euler method and removed the extreme values.

Non-Gaussian distribution of these fluctuations and heavy tails are not given in this section. UM analysis of all cases will be provided in Appendix B.4 and summarised UM parameters are given in Table 4.7. Averaged multifractaility index $\overline{\alpha}$ is 1.55 ± 0.07 and averaged mean codimension $\overline{C_1}$ is 0.25 ± 0.05 except the largest forcing case 4.1.10. It also confirms that multifractality index is smaller less than 2.

Table 4.7: Frequency of UM parameters of Case 4.1 simulated by semi-implicit Euler method.

Case 4.1 simulated by semi-implicit Euler method.								
	n	η^*	Δt	m	resolution			
	12	10	0.0002	6	512			
Case	f	t_f	N_α	N_{C_1}	$\overline{\alpha}$	$\overline{C_1}$	α_e	C_{1_e}
4.1.1	0.1	23810	14	5	1.61	0.2	1.35	0.09
4.1.2	0.2	23810	14	5	1.61	0.2	1.35	0.09
4.1.3	0.3	23810	10	14	1.62	0.28	1.21	0.13
4.1.4	0.4	23810	12	8	1.61	0.3	1.32	0.15
4.1.5	0.5	23810	19	6	1.57	0.28	1.36	0.17
4.1.6	0.6	18000	17	7	1.58	0.2	1.5	0.17
4.1.7	0.7	23810	16	11	1.48	0.24	1.21	0.16
4.1.8	0.8	18000	16	12	1.48	0.23	1.5	0.2
4.1.9	0.9	23810	17	8	1.52	0.24	1.37	0.15
4.1.10	1	6000	7	4	1.62	0.12	1.34	0.08

4.7 Summary of Chapter 4

Intermittency of forced SGC model with three large cascade steps $n = 12, 14, 15$, which is simulated by classic Euler method, is investigated in this chapter by injecting forcing at top layer to achieve quasi-equilibrium state. Forcing is $0.1 \leq f \leq 1$ for cascade step $n = 12$, and ranges from $f = 0.1$ to $f = 1.1$. Cascade step 15 with forcing from 0.5 to 1.1 is studied. The proof of intermittency is given out first, followed by its multifractality, and then the investigation about computational instability.

With the exception of one special case, energy flux in the inertial range for these three cascade steps yields extraordinarily high values as forcing increases, even bringing an early ending to SGC model. All these cases confirm the existence of intermittency. Strong intermittency is clearly observed in cases injecting the medium value

forcings. Cases with large forcings demonstrate strong fluctuations after removing extraordinarily large value of energy flux strengthened by forcings at the end are visible. On the other hand, energy flux in instability state at the beginning prevents direct observation of intermittency in cases with small forcing, but these noticeable fluctuations become weaker and eventually vanish as time goes on. Probability distribution function of energy flux in all cases verifies the "heavy" tail caused by extreme events.

UM framework is therefore used to analyze the multifractality of intermittency. Properties of time slots are presented first, followed by ensemble analysis, due to the lack of additional independent cases to perform general ensemble analysis on. Sample size 512 is chosen by comparing UM analysis of three sample sizes 1024, 512, and 256. As subsequences have different scale-invariant features and statistical fixed range estimation $\eta \approx 1$ doesn't fit well, adjusted range estimation is introduced by improving the plot fit of UM parameters. Results reveal that disparity caused by fixed range estimation is either negligible or non-existent for cases injecting large forcings, whereas in the other cases, UM parameters as well as critical moment q_s, confirm the difference, e.g. trends, frequency histograms, mean values.

Multifractality index α obtained from adjusted range estimation swings around the mean, mostly between 1 and 2. Subseries with α larger than 2 appear either at the beginning or the end since some extreme values in energy flux dominate the scale-invariant properties. More α greater than 2 are observed as cascade step enlarges, most likely as a result of the expansion of spatial eddies in SGC model, which accelerates energy exchange. Mean codimension C_1 is small at the beginning as SGC model is quitting from an ad-hoc initial state and forcing is not yet functioning, followed

by stable and rising at the end. The occurrence of abnormal values $C_1 > 1$ when forcing is small suggests that these subseries are not multifractal fields, but this does not happen when forcing is extremely small.

The analysis of these three cascade steps reveals that the multifractality index is significantly smaller than 2. Averaged multifractality index of cascade step 12 except the minimum forcing 0.1 is $\overline{\alpha} = 1.53 \pm 0.06$ and is 1.66 ± 0.06 for cascade step 14. It is also confirmed by averaged multifractality index 1.63 ± 0.04 for cascade step 15. There are many cases for these three cascade steps whose energy flux is consistent with the empirical atmospheric turbulence $\alpha \approx 1.5, C_1 = 0.25$. Time scale for ensemble analysis is limited when forcing is either large or small because of few subseries satisfying $C_1 \approx 0.25$ As for forcings of medium value, many subseries satisfying $\alpha \approx 1.5, C_1 \approx 0.25$, which is supported by ensemble analysis, demonstrates that there is a temporal scale at which UM parameters obtained from ensemble analysis confirms empirical UM parameters from various measurements.

Last but not least, computation instability in classic Euler method simulation is investigated by comparing the simulation of cascade step $n = 12$ obtained by more stable semi-implicit Euler method that is commonly used for rigid bodies. It turns out that semi-implicit Euler method couldn't reduce computational instability. Furthermore, strong fluctuations are observed in most cases and UM analysis confirms a multifractality index of significantly less than 2.

Chapter 5

Backscatter term and energy decay law

5.1 Global scaling and the decay law of free turbulence

Since at least the empirical observations made by Leonardo da Vinci, turbulence has been known to be dissipative, i.e. without external forcing it will decay. At the mathematical level, this is due to the presence of dissipative term $\nu\Delta u$ in the Navier-Stokes equation. However, it has also been observed that this decay is slow, in fact much slower than an exponential law that would result from neglecting all the other terms of these equations. More precisely it was empirically found and theoretically argued that the decay of free turbulence follows a power law for the whole period

where it remains fully developed, i.e. with a high Reynolds number. The exponent of this decay law can be obtained with the help of only two hypotheses:

- global self-similarity of the energy spectrum and transfer, with the possible exception of the dissipation range [113]
- stationarity of the energy spectrum of big eddies, i.e. those corresponding to vanishing wave numbers ($k \to 0$)

Indeed, these hypotheses yield the two equations that follow:

$$E(k,t) = v^2(t)\ell(t)F(x);\ T(k,t) = v^3(t)G(x) :\ x = k\ell(t); \tag{5.1.1a}$$

$$E(k,t) = C_s(t_0)k^s + O(k^{s+1}), k \to 0; \tag{5.1.1b}$$

where $F(x)$ and $G(x)$ are dimensionless functions of the dimensionless wavevector x, $v^2(t)/2$ is the average energy $K(t)$ (Eq.1.5.1); $\ell(t)$ is a rather arbitrary scale of the energy-containing eddies (e.g. the integral scale); s is the exponent of stationary of big eddies and C_s is its prefactor. The latter, via Eq.5.1.1b, yields a first scaling relation between $v(t) \propto t^{\alpha_v}$ and $\ell(t) \propto t^{\alpha_\ell}$:

$$v(t)^2\ell(t)^{s+1} = Const. \Rightarrow 2\alpha_v + (s+1)\alpha_\ell = 0. \tag{5.1.2}$$

A second scaling relation is obtained by considering the phenomenological relation of energy dissipation to the velocity ε (Eq.1.4.1):

$$\varepsilon(t) = -\frac{d}{dt}v^2(t) \approx \frac{v^3}{\ell} \Rightarrow \alpha_v - \alpha_\ell + 1 = 0. \tag{5.1.3}$$

Combining both scaling relations (Eqs.5.1.2, 5.1.3) yields:

$$\alpha_v = -\frac{s+1}{s+3};\ \alpha_\ell = \frac{2}{s+3}. \tag{5.1.4}$$

A more rigorous and more general derivation was obtained by Schertzer in 1980 [113] by firstly introducing a modified dissipativity [76] $\alpha_D \neq 1$ to enable to obtain a strict global self-similarity, i.e., including in the dissipation range. The spectral equation is then generalized to:

$$\left(\frac{\partial}{\partial t} + 2\,\nu_{\alpha_D} k^{2\alpha_D}\right) E(k,t) = T(k,t) \tag{5.1.5}$$

The scales of dissipation ℓ_{d,α_D} and of energy containing eddies ℓ are linked through the modified Reynolds number R_{α_D}:

$$\ell_{d,\alpha_D}(t) \propto \ell(t) R_{\alpha_D}(t)^{-3/2(3\alpha_D-1)};\ R_{\alpha_D}(t) = v(t)\ell(t)^{2\alpha_D-1}/\nu_{\alpha_D} \tag{5.1.6}$$

Then it is assumed that the modified dissipativity $\alpha_D \neq 1$ can be chosen to obtain a strict global self-similarity. Spectral equation Eq.5.1.5 can be expressed with the help of functions F and G:

$$v^{-3}\frac{d(v^2\ell)}{dt}F(x) + v^{-1}\frac{d\ell}{dt}xF'(x) + \frac{2}{R_{\alpha_D}}\ x^{2\alpha_D}F(x) = G(x). \tag{5.1.7}$$

Deriving this equation only with respect to time, one faces then the alternative:

- the three functions $F, xF', x^{2\alpha_D}F(x)$ are linearly dependent
- they are linearly independent

The first hypothesis yields solutions of type:

$$F(x) = a_0 x^i - a_2/a_1 e^i - x^{2\alpha_D}/a_1 \tag{5.1.8}$$

that was rejected by Schertzer [113] as non-physically interesting, despite they were investigated in the physical space by [124].

The second hypothesis yields the following form of spectral equation:

$$(\frac{1}{\beta} - a)F(x) + v^{-1}\frac{1}{\beta}xF'(x) + \frac{2}{R_{\alpha_D}}\, x^{2\alpha_D}F(x) = G(x) \tag{5.1.9}$$

with the series of constant positive prefactors:

$$\frac{1}{\beta} = v^{-1}\frac{d\ell}{dt} = Const. > 0;\ a = \frac{\ell}{v^3}\varepsilon = Const. > 0; R_{\alpha_D} = Const. > 0 \tag{5.1.10}$$

The two first prefactors are equivalent to the aforementioned phenomenological relation and the resulting relation between scaling exponents of v and ℓ (Eq.5.1.3). Together with the assumed stationarity of big eddies (Eq.5.1.2), they yield the expressions of scaling exponents α_v and α_ℓ with respect to big eddies stationary exponent s. The third prefactor, which is the (modified) Reynolds number, provides the expression of adequate modified dissipativity α_D with respect to the exponent s:

$$\alpha_D(s) = (1 - \frac{\alpha_v}{\alpha_\ell})/2 = \frac{s+3}{4} \tag{5.1.11}$$

In this respect, the case $s = 1$ is the unique case that does not require any modification of the dissipativity to ensure strict global self-similarity. It confirms a remark made by [75] on the fact that in this case the analysis of free decay can be performed with

a non-negligible viscosity. On the contrary, the often studied case $s = 4$, see below, requires a significantly modified dissipativity $\alpha_D(s) = 1.75$ to be in the situation of strict global self-similarity.

5.2 Stationarity of big eddies and energy backscattering

The stationarity of big eddies was largely discussed by Kolmogorov [58] and Landau and Lifchitz [67] in relation with the so-called Loitsianski's invariant or Loitsianski's integral Eq.1.5.5:

$$I =< u^2(t) > \int_0^\infty r^4 f(r) dr \tag{5.2.1}$$

where $f(r)$ is the longitudinal correlation.

Some physical arguments [24] have been put forward, notably by [69] to ensure that this integral is indeed time-invariant, however, no mathematical proof has yet been provided and there is reason to believe that it will be not done. Indeed, a basic feature of Loitsianski's integral is that it is proportional to the prefactor $C_4(t)$ of k^4 term of energy spectrum expansion at $k \to 0$, while the analytical closures, starting with Quasi-Normal approximation [89] point out [103] that:

$$T(k,t) = \mathcal{A}(t)k^4 + O(k^{s+1}),\ k \to 0;\ s > -1; \mathcal{A} > 0 \tag{5.2.2}$$

The fact that $\mathcal{A}(t)$ is positive implies that the largest eddies are growing and storing energy and thus have the potential to slow down turbulence decay. This is very

effective if initially $s \geq 4$, particularly if $s \gg 4$, modifying the scaling exponent expressions (Eq.5.1.4). On the contrary, it will have a negligible impact for $s < 4$ and the scaling exponent expressions (Eq.5.1.4) will apply unchanged. The non-realisability of Quasi-Normal approximation at long times does not bring into question this behavior for short times. This is more than being confirmed by Lesieur and Schertzer [74] with the help of Eddy Damped Quasi-Nomal Markovianized model (EDNM) [97]. They demonstrated that for all times:

$$\mathcal{A}(t) = \frac{7}{15}\int_{k/a}^{\infty} \theta_{k,p,p} \frac{E(p,t)^2}{p^2} dp, \tag{5.2.3}$$

where $\theta_{k,p,q}$ is the correlation relaxation time of the triad k, p, q. The main contribution to $\mathcal{A}(t)$ comes from energy-containing eddies of wave numbers $p \sim \ell^{-1}$ and therefore does not depend on either of wavenumber k or the non-locality parameter a ($k \leq ap, q \sim p$). This term was initially called 'beating term' because it corresponds to interactions between two wavenumbers very close to each other $p \sim q$. But, due to the fact that it scatters energy from energy-containing eddies back to the largest eddies, it became known as 'backscatter term'.

For initial $s \geq 4$, Lesieur and Schertzer [74] introduced the scaling exponent $\gamma > 0$ of the Loitsianski's integral and the corresponding prefactor $C_4(t)$:

$$C_4(t) = C_4(t_0)(t/t_0)^{\gamma}, \tag{5.2.4}$$

which modifies the scaling exponents of v and ℓ (Eq.5.1.4) into:

$$\alpha_v = -\frac{5-\gamma}{7};\ \alpha_\ell = \frac{2+\gamma}{7}, \tag{5.2.5}$$

with the following numerical estimates:

$$\alpha_e = -2\alpha_v = 1.38;\ \alpha_\ell = 0.31;\ \gamma \approx 0.17. \tag{5.2.6}$$

Lesieur and Schertzer [74] also argued that the fact that backscatter is in k^4 is also obtained by the renormalization group [35]. It is also worthwhile to note that most of the aforementioned results on the velocity field were extended by Herring et al.,[54] to the passive scalar field, not only with the help of EDQNM, but also with the Test Field Model (TFM), which can be understood as somewhat more elaborated. Frisch et al [43] showed also these results could be also obtained with the less markovianised version of the Quasi-Normal model (QNM) [130], which is fully realizable contrary to the original QN, but still fails to renormalize the Green functions, contrary to the Test-Field-Model(TFM).

5.3 Other studies of backscatter term

More detailed research achievements are given in the following since global scaling law and the role of backscatter term in the stationarity of big eddies have been explained in the previous two sections.

The permanence of large eddies has been extensively investigated using the classic two-point closure theories, and thus indirectly confirms the existence of energy backscatter term. Except for closure analysis methods, the existence of energy backscatter is studied by the commonly numerical approach for turbulence. Using

large eddy simulation (LES) [72], Ossia and Lesieur [99] examined energy backscattering in free decay of three-dimensional incompressible isotropic turbulence and confirmed the non-negligible energy backscattering term Eq.5.2.2 for initial power spectrum $s = 4$. The exponent of energy decay law is -1.4 which is between -1.38 proposed by EDQNM and -1.43 predicted by Kolmogorov. However, the quantitative measure of energy backscatter intensity γ relies on the resolution and integration time. Chasnov [19] observed the continuous energy backscattering term and obtained the estimated exponent $\gamma \approx 0.25$ from spectral velocity field, when the finite size effects are negligible, through computing 1024 independent cases and large resolution 643 to improve statistical convergence of the infrared modes.

Another interesting argument is the threshold for destabilizing stationarity of large eddies, which is commonly acknowledged as an integer 4. With EDQNM framework, Eyink and Thomson [33] suggested the threshold is $s_c \approx 3.45$, above which backscatter term k^4 can be clearly observed and a new energy decay law is derived. Lesieur and Ossia [73] conducted EDQNM analysis of three-dimensional isotropic turbulence (without helicity) to study this backscatter term issue with cases whose noninteger s is from 3.2 to 3.9. The computation doesn't yield significant observed backscatter term indicating that big eddies are stationary when $s < 3$, which is consistent with energy decay exponent α_e and scaling law Eq.5.1.4. The slope of energy spectrum with non-integer exponent $3 < s < 4$ over time evolution is somewhat higher than s and backscatter does gradually observed. The exponent of energy decay law ranges from $-\frac{4}{3}$ to -1.38. However, they didn't find evidence of backscatter term k^4 above threshold $s = 3.45$ suggested by Eyink and Thomson. Furthermore, Ossia and Lesieur [99] utilized LES approach and claimed that backscatter term k^4 did not appear at

$s = 3.5$ despite an increase in the energy spectrum. Briard et al. [12] developed an extension of EDQNM to anisotropic flows in relation to the interplay between third-order statistics and anisotropy of turbulent flow [16]. See also the analysis of freely decaying rotating turbulence by Delache et al. 2014 [26].

5.4 New challenge

The crucial role of backscatter term in the stationarity of big eddies [113], which leads to the reversed energy cascade phenomenon and modifies free energy decay process, has been revealed within the framework of EDQNM. Even though the backscatter term has been observed and quantified its impact in many kinds of research, a strong limitation of EDQNM theory is that it is based on a quasi-normal approximation preventing it from being able to generate intermittency. This fundamental property [127] poses questions about the dynamics of turbulence, in particular, the stationarity of large eddies and scaling law.

SGC model preserving the nonlocal triad interaction, which can generate intermittency proven in the last chapter, is applied to investigate the existence of backscatter terms taking intermittency into account. More precisely, the selected NS interactions for SGC model are semi-local interactions rather than strongly nonlocal interactions generating backscatter term. Therefore, this study will provide some insight into whether semi-local interactions can indirectly establish the nonlocal interactions to observe backscatter term in simulation.

5.5 SGC model and its backscatter term

5.5.1 Theoretical insights

Due to the triads interaction of SGC model, the evidence for backscatter term is theoretically hypothesized to be derived directly from the nonlinear transfer term.

Since the nonlocal transfer term revealing backscatter term is generated by the nonlocal triad interaction Eq.1.6.15c, the nonlinear transfer term of eddy $\widehat{u}_m^i$ (Eq.3.1.9) generated by same triad interaction which actually is semi-local is:

$$T_{U_m^i}^{NL}(\mathbf{k},t) = \widehat{u}_{m+1}^{2i}(\boldsymbol{k},t) \wedge \overline{\widehat{w}}_{m+1}^{2i}(\boldsymbol{k},t) + \widehat{u}_{m+1}^{2i+1}(\boldsymbol{k},t) \wedge \overline{\widehat{w}}_{m+1}^{2i+1}(\boldsymbol{k},t). \tag{5.5.1}$$

Hence, the nonlocal transfer term in wave number space can be obtained from the velocity equation Eq.5.5.1 and its conjugate, as

$$\frac{\partial E(\boldsymbol{k},t)}{\partial t} = \overline{\widehat{u}}(\boldsymbol{k},t) \cdot \frac{\partial \widehat{u}(\boldsymbol{k},t)}{\partial t} + \widehat{u}(\boldsymbol{k},t) \cdot \frac{\partial \overline{\widehat{u}}(\boldsymbol{k},t)}{\partial t}. \tag{5.5.2}$$

The velocity field in Fourier space has:

$$\forall\ \boldsymbol{k}:\ \widehat{u}(-\boldsymbol{k}) = \overline{\widehat{u}}(\boldsymbol{k}), \tag{5.5.3}$$

and Eq3.1.10 considering the complex conjugation symmetry of SGC model yields

$$\forall\ \boldsymbol{k}:\ \widehat{w}(-\boldsymbol{k}) = \overline{\widehat{w}}(\boldsymbol{k}); \tag{5.5.4}$$

$$\forall\ \boldsymbol{k}:\ \overline{\widehat{u} \wedge \overline{\widehat{w}}} = \overline{\widehat{u}} \wedge \widehat{w}. \tag{5.5.5}$$

Then, the conjugation of $T^{NL}_{U^i_m}(\mathbf{k}, t)$ is:

$$\overline{T}^{NL}_{U^i_m}(\boldsymbol{k}, t) = \overline{\widehat{u}}^{2i}_{m+1}(\boldsymbol{k}, t) \wedge \overline{\widehat{w}}^{2i}_{m+1}(-\boldsymbol{k}, t) + \overline{\widehat{u}}^{2i+1}_{m+1}(\boldsymbol{k}, t) \wedge \overline{\widehat{w}}^{2i+1}_{m+1}(-\boldsymbol{k}, t). \tag{5.5.6}$$

The nonlocal transfer term $T_{NL}(\mathbf{k}, t)$ producing backscatter term for spatial eddy $\widehat{u}^i_m$ is

$$\begin{aligned} T_{NL}(\boldsymbol{k}^i_m, t) =& \overline{\widehat{u}}^i_m(\boldsymbol{k}, t) \cdot \widehat{u}^{2i}_{m+1}(\boldsymbol{k}, t) \wedge \overline{\widehat{w}}^{2i}_{m+1}(\boldsymbol{k}, t) + \overline{\widehat{u}}^i_m(\boldsymbol{k}, t) \cdot \widehat{u}^{2i+1}_{m+1}(\boldsymbol{k}, t) \wedge \overline{\widehat{w}}^{2i+1}_{m+1}(\boldsymbol{k}, t) + \\ & \widehat{u}^i_m(\boldsymbol{k}, t) \cdot \overline{\widehat{u}}^{2i}_{m+1}(\boldsymbol{k}, t) \wedge \overline{\widehat{w}}^{2i}_{m+1}(-\boldsymbol{k}, t) + \widehat{u}^i_m(\boldsymbol{k}, t) \cdot \overline{\widehat{u}}^{2i+1}_{m+1}(\boldsymbol{k}, t) \wedge \overline{\widehat{w}}^{2i+1}_{m+1}(-\boldsymbol{k}, t). \end{aligned} \tag{5.5.7}$$

After the matrix representation, the nonlocal transfer term $T_{NL}(k^i_m, t)$ is

$$\begin{aligned} T_{NL}(k^i_m, t) =& u^i_m(k, t) \cdot k_{m+1} \cdot (|u^{2i}_{m+1}(k, t)|^2 - |u^{2i+1}_{m+1}(k, t)|^2) + \\ & u^i_m(k, t) \cdot k_{m+1} \cdot (|u^{2i}_{m+1}(k, t)|^2 - |u^{2i+1}_{m+1}(k, t)|^2) \\ =& 2u^i_m(k, t) \cdot k_{m+1} \cdot |u^{2i}_{m+1}(k, t)|^2 - 2u^i_m(k, t) \cdot k_{m+1} \cdot |u^{2i+1}_{m+1}(k, t)|^2 \end{aligned} \tag{5.5.8}$$

For power spectrum k^s ($k \to 0$), $T_{NL}(k_m^i, t)$ is

$$\begin{aligned} T_{NL}(k_m^i, t) \approx & 2k_m^{s/2} \cdot k_{m+1} E(k_{m+1}^{2i}, t) - 2k_m^{s/2} \cdot k_{m+1} E(k_{m+1}^{2i+1}, t) \\ \approx & 2k_m^{s/2} \cdot k_{m+1}^{s+1} - 2k_m^{s/2} \cdot k_{m+1} E(k_{m+1}^{2i+1}, t). \end{aligned} \tag{5.5.9}$$

Unfortunately, Eq.5.5.9 fails to provide backscatter term yet. It is important to note that energy lost during the elimination of initial ah-hoc state is not considered, which might be a determining factor. Tree structure of SGC model whose semi-local triad interaction is ($\boldsymbol{k}_m^i, \boldsymbol{k}_{m+1}^{2i}, \boldsymbol{k}_{m+1}^{2i+1}$) makes the separating of backscatter term more complex. But Eq.5.5.9 suggests there is a positive term that will slow down the energy decay. The simulation thus will be carried out in the next section to study the energy decay law considering intermittency.

5.5.2 Numerical results

Initial condition for free decaying SGC model

In this part, energy spectrum and initial simulation parameters are presented to investigate the impact of intermittency on backscatter term as well as energy decay law. The energy spectrum has to include both power spectrum k^s resulting in backscatter term and $k^{-\frac{5}{3}}$ inertial spectrum exhibiting extreme intermittency. Energy

spectrum shown in Fig 5.1 is

$$E(k,0) = \begin{cases} C_s k^s, 0 < k_m \leq k_L, \\ k^{-\frac{5}{3}}, k_L \leq k_m \leq k_n, \end{cases} \tag{5.5.10}$$

where C_s is $k_L^{-(s+\frac{5}{3})}$ required by connected wave number k_L. Comte-Bellot, G and Corrsin, S [23] also proposed energy spectrum Eq.5.5.10 and studied the connection between $-10/7$ decay law and integral scale $2/7$ law.

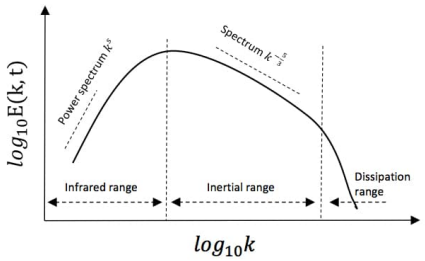

Figure 5.1: Energy spetcrum Eq 5.5.10.

But the energy spectrum for SGC model in simulation is

$$E(k,0) = \begin{cases} C_s k^s, 1 \leq k_m \leq k_{peak}, \\ k^{-\frac{5}{3}}, k_{peak} \leq k_m \leq k_n. \end{cases} \tag{5.5.11}$$

It requires the numerical simulated energy spectrum Eq.5.5.11 to be normalized by $E(k_{peak}, 0)$:

$$E_r(k_m, t) = \frac{E(k_m, t)}{E(k_{peak}, 0)}, \tag{5.5.12}$$

which is the time evolution of energy spectrum Eq.5.5.10. Initial velocities for spatial eddies are obtained from energy spectrum Eq 5.5.11, as described in Chapter 4. So do

the artificial viscosity, time step, and time units. The classic Euler method is chosen in the simulation of this Chapter.

Corresponding compensated spectrum, as well as the local Reynolds number, can be calculated. The compensated spectrum for inertial spectrum is defined as:

$$E_c(k_m/k_{peak}, t) = k^{\frac{5}{3}} E_r(k_m, t). \tag{5.5.13}$$

To emphasize that the exponent of energy decay is obtained through a sufficiently high local Reynolds number Re_L, the local Reynolds number Re_L of SGC model is computed by:

$$Re_L(k_m/k_{peak}, t) = \frac{UL}{v} = \frac{(k_m/k_{peak} E_r(k_m, t))^{1/2}}{v k_m/k_{peak}}. \tag{5.5.14}$$

The high Reynolds number implies that the inertial force is many times greater than the viscosity force, so the viscosity force can be neglected and the flow is fully developed turbulent.

Meanwhile, two crucial properties in the dynamic of turbulence remain the same after normalization, which are the exponent of integral scale and energy decay law. According to the definition of integral scale Eq.4.2.2, integral scale is

$$L(t) = \frac{\sum_{m=0}^{n} k_m^{-1} K_m}{\sum_{m=0}^{n} K_m} = k_{peak}^{-1} \cdot \frac{\sum_{m=0}^{n} (k_m/k_{peak})^{-1} K_m/K_{peak}}{\sum_{m=0}^{n} K_m/K_{peak}}, \tag{5.5.15}$$

which indicates the exponent of integral scale obtained from energy spectrum Eq.5.5.11 and energy spectrum Eq.5.5.10 is equivalent. The deduction of energy decay law is not going to repeat. In this way, the exponent of integral scale and energy decay can

be directly estimated from energy spectrum Eq.5.5.11 instead of using the normalized value.

Free energy decay law of spectrum $k^{-\frac{5}{3}}$

Before studying the role of intermittency, free energy decay law of SGC model without power spectrum is checked to compare with that of energy spectrum Eq.5.5.10. n_{peak} is assumed as 0 to ensure energy spectrum Eq.5.5.10 without power spectrum, and initial parameters are listed in Table 5.1.

Table 5.1: Cases without power spectrum

Case	n	n_{peak}	$\eta*$	Δt	Tmax
5.1	11	0	9	0.0002	6000
5.2	12	0	10	0.0002	6000

Since there is no independent case to perform an ensemble average, statistical descriptions for time slots are carried out with resolution 10.

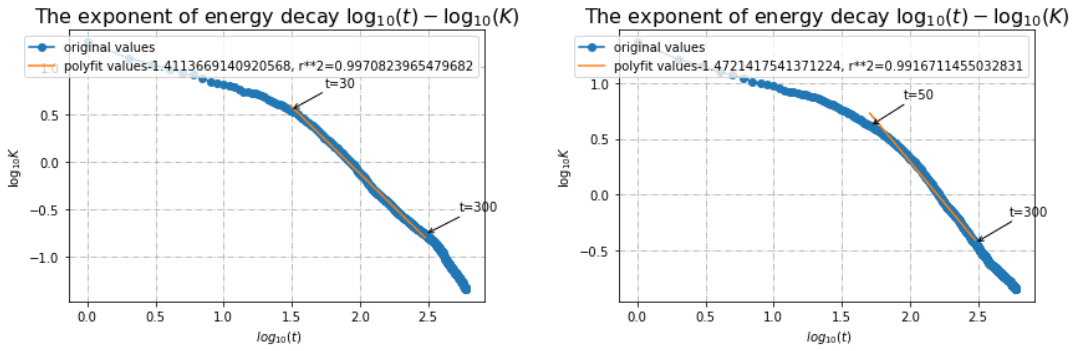

(a) Case 5.1 (b) Case 5.2

Figure 5.2: Log-log plot of energy $E(t)$ of Case 5.1 and Case 5.2. Time unit of time t is the initial large eddy turnover time. K is system energy $E(t)$.

Fig.5.2 presents the log-log plot of system energy for these two cases without power spectrum. Apart from the initial unstable phase, exponent of energy decay law at time $t = 30 - 300$ in Fig.5.2a is $\alpha_e = 1.41$, and $\alpha_e = 1.47$ at time t between $50 - 300$ in Fig.5.2b. The following are the other characteristics of same time period.

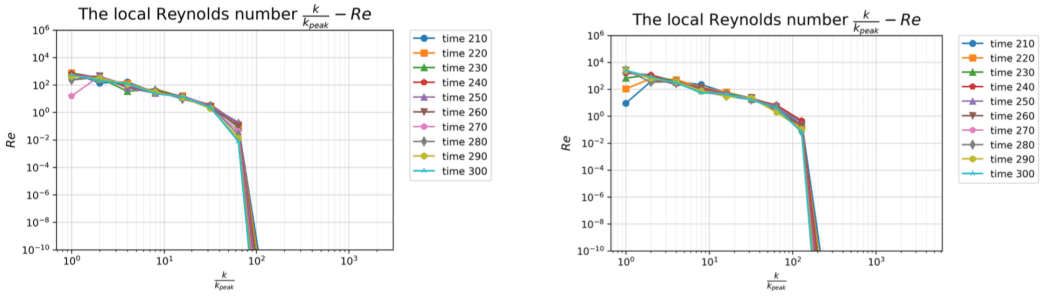

(a) Case 5.1 (b) Case 5.2

Figure 5.3: Local Reynolds number Re of Case 5.1 and Case 5.2.

At time $210 - 300$, Case 5.1 in Fig.5.3a has a Reynolds number close to 10^3, while the Reynolds number of Case 5.2 is around 10^4, demonstrating that the Reynolds numbers of Case 5.1 and Case 5.2 are sufficient to guarantee full developed SGC model.

Meanwhile, the energy spectrum of Case 5.1 and Case 5.2 as well as the compensation spectrum are given in Fig.5.4. It's clear that energy spectrum of Case 5.1 in Fig.5.4a and Case 5.2 in Fig.5.4c is $-\frac{5}{3}$ spectrum, which is confirmed by their compensation spectrum. Energy loss during the initial unstable time prevents compensated spectrum from reaching 1.

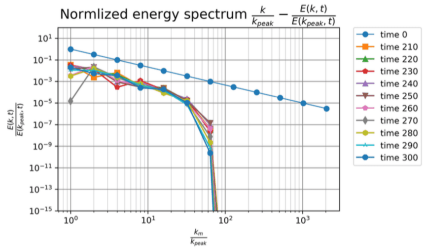

(a) Energy spectrum of Case 5.1

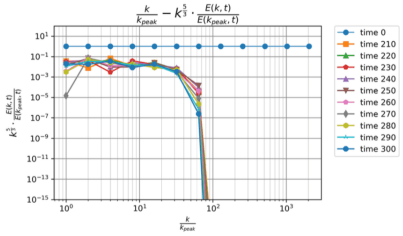

(b) Compensated spectrum of Case 5.1

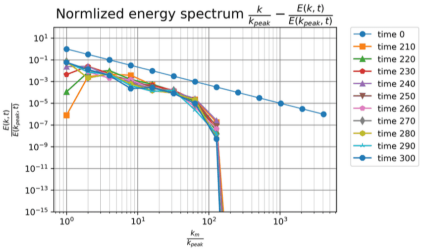

(c) Energy spectrum of Case 5.2

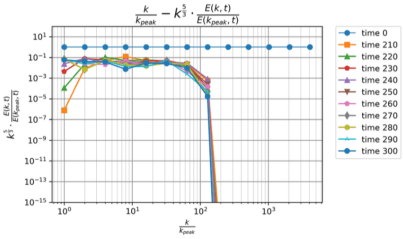

(d) Compensated spectrum of Case 5.2

Figure 5.4: Energy spectrum of Case 5.1 and Case 5.2, as well as their compensated spectrum.

Integral scale of Case 5.1 and Case 5.2, which is the weighted average of inverse wave numbers describing the characteristic length scale of energy-containing eddies, is simulated and shown in Fig 5.5. The scaling law of integral scale $L(t)$ with spectrum $k^{-\frac{5}{3}}$ is $L(t) \propto t^{\frac{2}{7}}$. The simulation reveals that exponent of integral scale for Case 5.1 and Case 5.2 is larger than $\frac{2}{7}$ resulting from wavering log-log plot of integral scale.

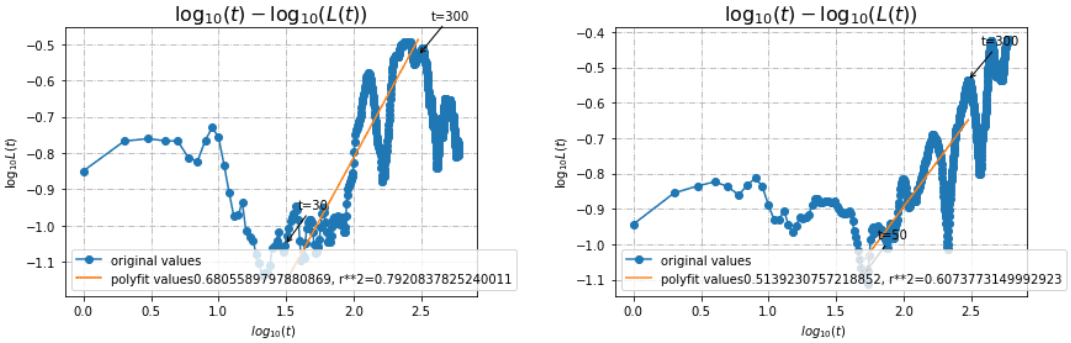

(a) Case 5.1 (b) Case 5.2

Figure 5.5: Log-log plot of integral scale $L(t)$ of Case 5.1 and Case 5.2 .

Energy decay law of spectrum injecting power spectrum

Now, free energy decay law of energy spectrum Eq.5.5.11 is investigated and cases are given in Table 5.2. Cases 5.3, Case 5.4, and Case 5.1 have the same inertial range length, and another group sharing the same inertial range length is Case 5.5, Case 5.6, and Case 5.2. Not only does time step follow the stability of classic Euler method, but it's also less than the initial eddy turnover time.

Table 5.2: Cases with power spectrum k^4

Case	n	n_{peak}	$\eta*$	Δt	Tmax
5.3	12	1	10	0.0001	6000
5.4	13	2	11	0.00006	6000
5.5	13	1	11	0.0001	6000
5.6	14	2	12	0.00001	6000

The study will start with Case 5.3. Ensemble-averaged spectrum $E_r(k_m, t)$ of Case 5.3 to time scale 3000 is shown in Fig 5.6. Spectrum coefficient in the infrared range increases and the power spectrum vanishes at the end 300 in Fig 5.6c as time evolves,

which indicates that energy in the infrared range of Case 5.3 grows due to backscatter term.

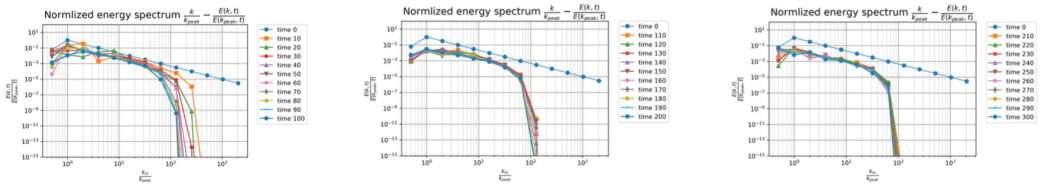

(a) Time $0 - 100$ (b) Time $110 - 200$ (c) Time $210 - 300$

Figure 5.6: Time evolution of ensemble averaged spectrum $E_r(k_m, t)$ of Case 5.3.

Compensated spectrum shown in Fig 5.7a confirms the vanishing power spectrum and consistency with $-5/3$ spectrum. Meanwhile, Reynolds number in Fig 5.7b suggests that the maximum Reynolds number almost reaches 10^4 even at the end ensuring Case 5.3 is a fully developed turbulent flow.

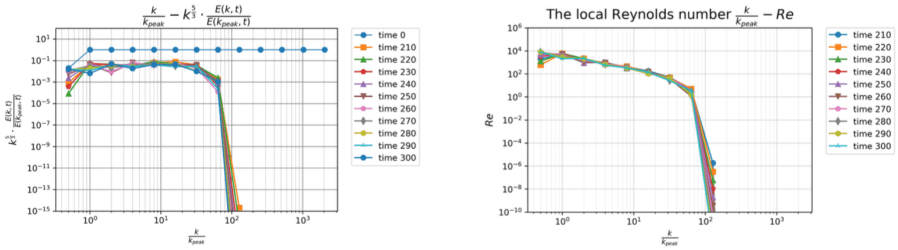

(a) Compensated spectrum (b) Local Reynolds number

Figure 5.7: Compensated spectrum and local Reynolds number of Case 5.3

Fig 5.8 displays the log-log plot of system energy and integral scale. The slope of log-log plot of energy at time $100 - 300$ in Fig 5.8a is -1.56, much smaller than $-\frac{5}{2}$, implying that Case 5.3 is not capable of comparison. Corresponding exponent of the integral scale is shown in Fig 5.8b as 0.77. All these results suggest the infrared range of Case 5.3 is insufficient to analyze theoretical energy spectrum Eq.5.5.10.

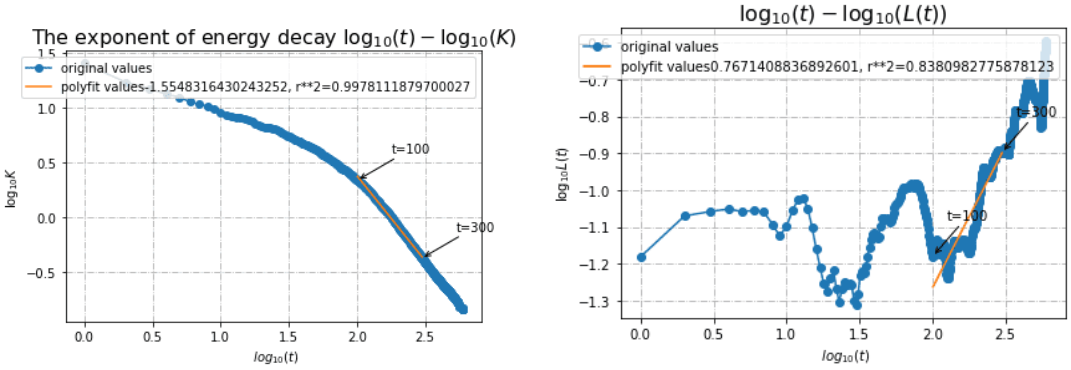

(a) Exponent of energy decay law $(100 - 300)$

(b) Exponent of integral scale $(100 - 300)$

Figure 5.8: Log-log plot of system energy and integral scale of Case 5.3

Ensemble averaged $E_r(k_m, t)$ of Case 5.4 whose infrared range is two cascade steps, is shown in Fig 5.9.

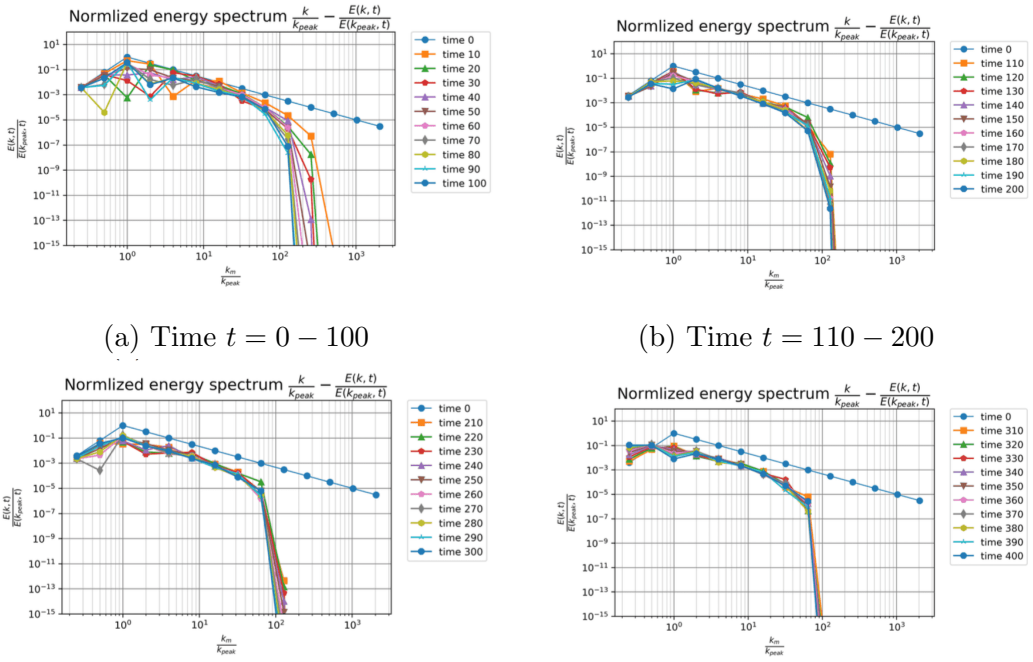

(a) Time $t = 0 - 100$

(b) Time $t = 110 - 200$

(c) Time $t = 210 - 300$

(d) Time $t = 310 - 400$

Figure 5.9: Ensemble averaged spectrum $E_r(k_m, t)$ of Case 5.4.

In Fig 5.9d, the infrared range maintains two cascade steps until time 300, then drops to one cascade step. Increased spectrum coefficient in infrared range is observed in Fig 5.9c confirming the existence of backscatter term that scatters back energy in the infrared range. Power spectrum obviously lasts longer than it does in Case 5.3.

The exponent of power spectrum in Case 5.4 for time period $160 - 190$ is given in Fig 5.10, which shows spectrum in infrared range st time $170 - 180$ is k^4.

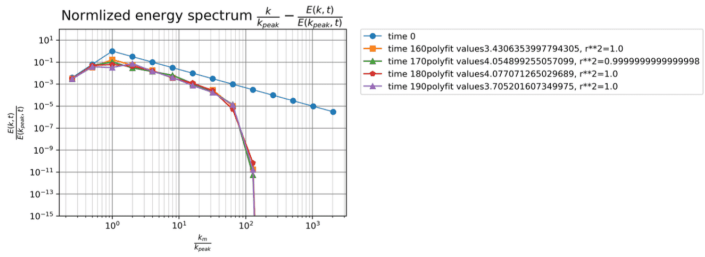

Figure 5.10: Ak^4 energy spectrum of Case 5.4

Compensated spectrum of Case 5.4 at time $310 - 400$ as well as Reynolds number are presented in Fig 5.11.

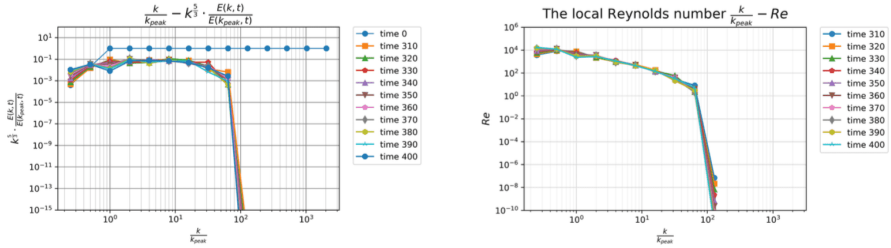

(a) Compensated spectrum (b) Reynolds number

Figure 5.11: Compensated spectrum and Reynolds number of Case 5.4 from time 310 to 400.

Compensated spectrum in Fig 5.11a supports $-5/3$ spectrum in inertial range, and flattening compensated spectrum in infrared range reveals the disappearance of

power spectrum. A sufficient Reynolds number for Case 5.4 is guaranteed by the maximum Reynolds number in Fig 5.11b exceeding 10^4.

Fig 5.12 displays system energy and integral scale of Case 5.4. The log-log plot of energy at time $100 - 400$ in Fig 5.12a has a slope of -1.04, while corresponding exponent of integral scale is 0.19.

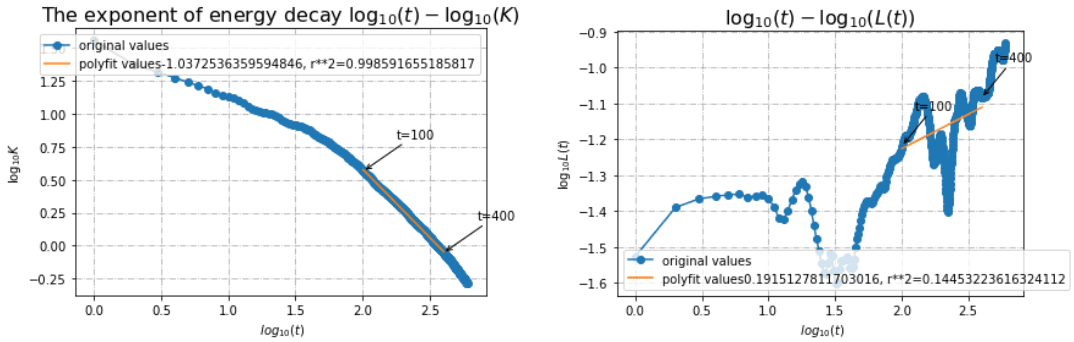

(a) Exponent of energy decaying law $t = 100 - 400$

(b) Integral scale $t = 100 - 400$

Figure 5.12: The Log-log plot of energy and integral scale of Case 5.4

Now let's discuss inserting power spectrum into Case 5.2.

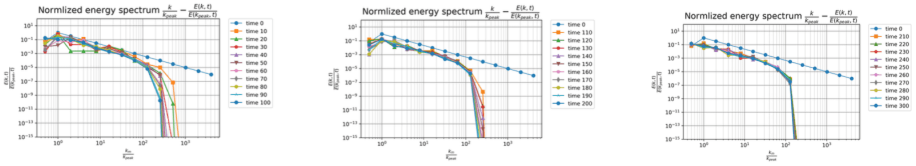

(a) Time $t = 0 - 100$ (b) Time $t = 110 - 200$ (c) Time $t = 210 - 300$

Figure 5.13: Energy spectrum of Case 5.5.

Fig 5.13 is time evolution of ensemble-averaged energy spectrum of Case 5.5 which is similar to Case 5.3 that spectrum coefficient in infrared range rises due to the reversed energy and has vanished between time 200 and 300 in Fig 5.13c.

Power spectrum of Case 5.5 has dissipated since time 200 that is confirmed by compensated spectrum in Fig 5.14a And the maximum Reynolds number exceeding 10^4 in Fig 5.14b indicates Case 5.5 is fully developed.

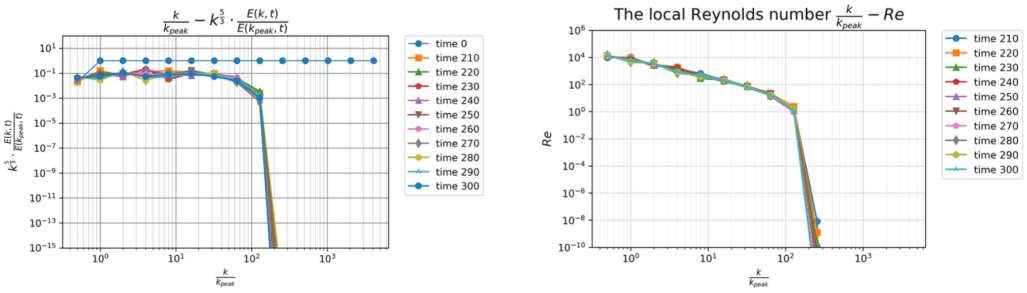

(a) Compensated spectrum (b) Reynolds number

Figure 5.14: Compensated spectrum and Reynolds number of Case 5.5 at time $210 - 300$.

At time $100 - 300$, Fig 5.15 shows the exponent of energy decay for Case 5.5 is -1.08 and exponent of integral scale is 0.35.

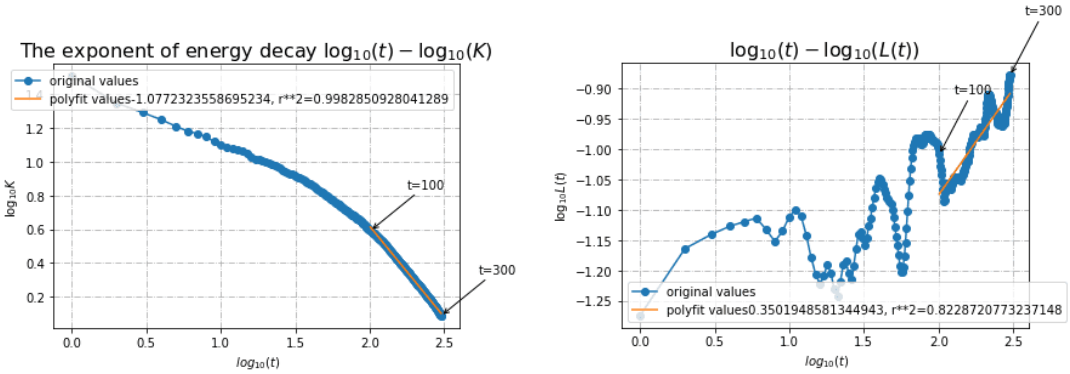

(a) System energy (b) Integral scale

Figure 5.15: Energy decay and integral scale of Case 5.5.

Finally, the temporal evolution of ensemble-averaged energy spectrum of Case 5.6 is presented in Fig 5.16. It's evident that the infrared range decrease over time

because it has two cascade steps at time $0-300$ and one step at time $310-600$. The increased infrared spectrum coefficient suggests that part of energy in inertial range is reversed to the infrared range. Depending on the degree of parallelism with energy spectrum at time 0, energy spectrum of k^4 appears at time 390, unfortunately it does not last for a large time scale.

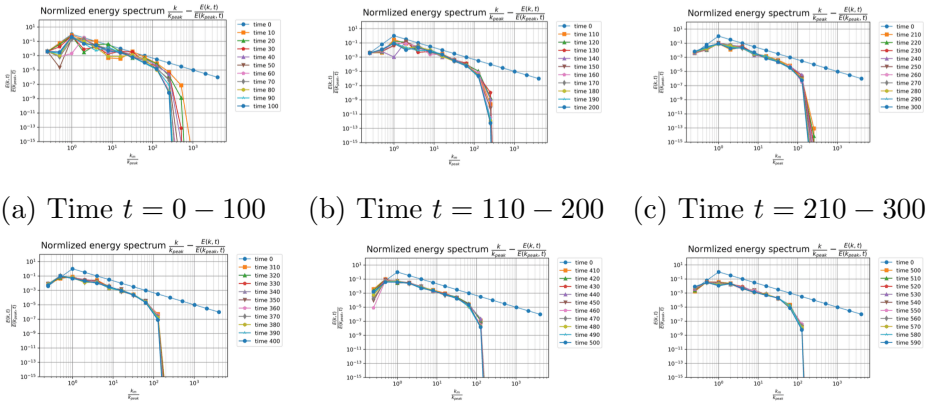

(a) Time $t = 0-100$ (b) Time $t = 110-200$ (c) Time $t = 210-300$

(d) Time $t = 310-400$ (e) Time $t = 410-500$ (f) Time $t = 510-600$

Figure 5.16: Energy spectrum of Case 5.6.

The slope of log-log plot in Fig 5.17 verifies that infrared spectrum of Case 5.6 at time 390 is k^4.

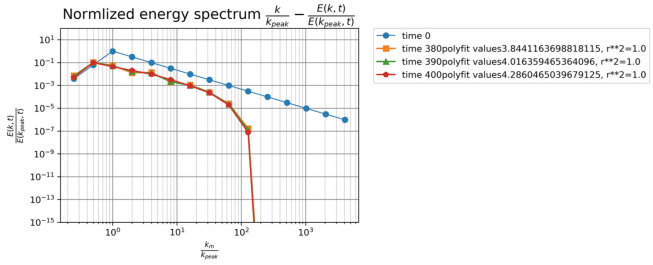

Figure 5.17: Exponent of infrared spectrum of Case 5.6.

Reynolds number and compensated spectrum for Case 5.6 after time 500 are

shown in Fig 5.18. The highest Reynolds number is over 10^4, as shown in Fig 5.18a which is sufficient. Compensated spectrum in Fig 5.18b demonstrates that the inertial spectrum is $-5/3$ spectrum.

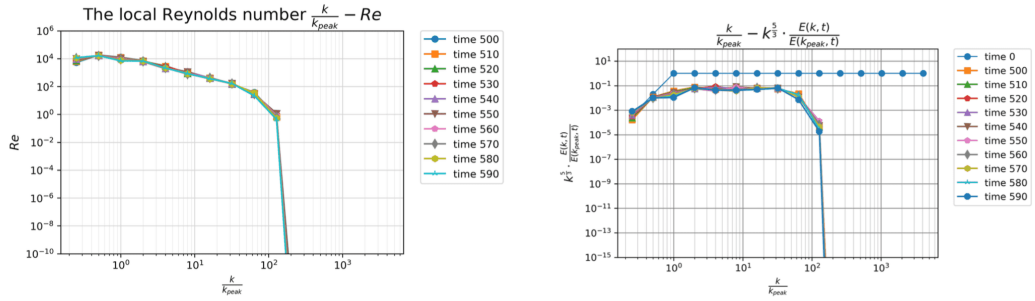

(a) Reynolds number (b) Compensated spectrum

Figure 5.18: Reynolds spectrum and compensated spectrum of Case 5.6.

The energy decay process of Case 5.6 is given in Fig 5.19, which suggests that exponent of energy decay obtained from time $100 - 400$ is -0.84 and corresponding exponent of integral scale estimated from wavering slope is 0.12.

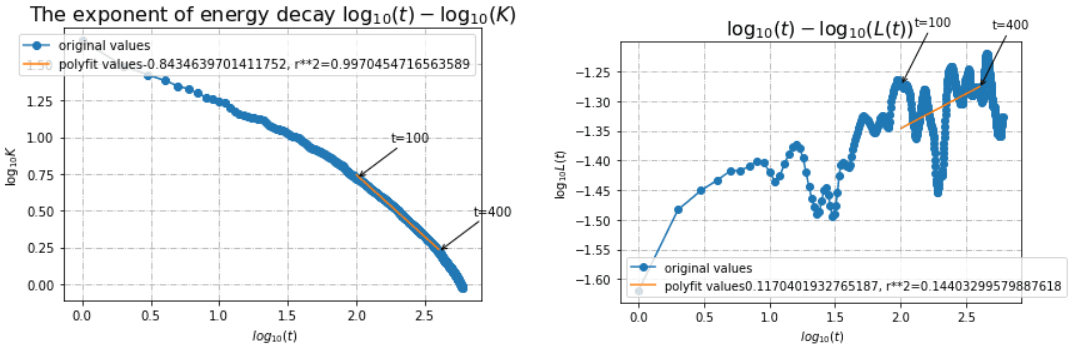

(a) System energy (b) Integral scale

Figure 5.19: Energy decay and integral scale of Case 5.6.

At the end, the exponent of energy decay and integral scale of Case 5.3-Case 5.6 is summarised in Table 5.3. The dynamic of these four cases is different due to various

infrared ranges and inertial ranges. According to energy decay exponent α_e of Case 5.4 and Case 5.5, the energy of spectrum Eq.5.5.10 decays slower than that of case without infrared spectrum, which is also supported by Case 5.6. The infrared range for Case 5.3 is too small, resulting in strange value for α_e and integral scale exponent.

Table 5.3: The exponent of energy decay and integral scale of cases with power spectrum k^4

Case	t	α_e	$\gamma*$
5.3	100-300	-1.56	0.77
5.4	100-400	-1.04	0.19
5.5	100-300	-1.08	0.35
5.6	100-400	-0.84	0.12

5.6 Conclusions of Chapter 5 and prospects

Due to the fact that SGC model preserves the triad interaction generating intermittency, the stationarity of large eddies and scaling laws taking intermittency into consideration are studied by such a model. Theoretical backscatter term is initially tried to be derived from SGC equations, but the semi-local interaction might prevents direct verification. The study thus is carried out with the classic Euler method numerical simulation of SGC model whose two-range spectrum contains power spectrum k^4 and inertial spectrum $k^{-5/3}$. Reynolds number of all cases is sufficient to guarantee that SGC model is full developed. It's typical that infrared range decreases and vanishes with time, as evidenced by four cases whose two-range spectrum includes power spectrum k^4. But phenomena including the conservation of large eddies and

the increased exponent of infrared spectrum are observed although with intermittency effects. Compensated spectrum confirms the change of infrared spectrum and inertial spectrum $k^{-5/3}$. With the exception of Case 5.3, exponents of energy decay law for case containing infrared spectrum are larger than those for cases lacking infrared spectrum, indicating that backscatter term slows down the energy decay. The buffs happened in the integral scale of these four cases, which suggests the energy is stored at large scales in a discontinuous way. Besides, k^4 at large eddies is observed over a short time scale and with a small wave number length, making it impossible to estimate the significance of backscattering term by Loitsiansky index that slowing down the energy decay.

More work needs to be done on energy backscatter term to provide both theoretical and numerical simulation evidence. It's challenging to obtain theoretical backscatter term from semi-local triad interactions of SGC model. Besides, it will be interesting to study SGC model by helical modes decompositions, which is typically used to analyze the non-isotropic effects of solid-body rotation on homogeneous turbulence, to provide detailed information about the dynamics of SGC model, such as the manner in which energy is transferred. As for numerical simulation, stable semi-implicit Euler method is worth considering for SGC model, as numerical results in this chapter are achieved by the classical Euler method. Due to time restrictions, results of the semi-implicit Euler simulation have not yet been sorted out and included in this chapter. It's also important to look into the energy decay using only k^4 infrared spectrum to enlarge infrared range, revealing the effect brought on by semi-local interaction of SGC model.

Chapter 6

Conclusion and perspectives

In this chapter, the most relevant findings and challenges encountered in this research are reported below, along with a list of future study directions.

With the advancement of turbulence study, the significance of intermittency of turbulence has been progressively realized. However, there are some disagreements regarding its properties and contribution to the mechanism of turbulence, for instance, it was initially assumed to be uniform, and later investigations suggested that it is a log-normal distribution. Aiming at filling part of this gap, SGC model which is more close to NS equation than the well known shell model, is simulated in this study, since it preserves the most important energy transfer structure-triad interactions, which is able to generate intermittency and backscatter term.

To begin, different numerical simulation approaches are investigated thorough complexity analysis, UM analysis and empirical analysis to determine the effective one. Two of them are the classic Euler method and classical RK4 method. The third one is slaved ABF method, which takes into account the rapid damping of high

wave numbers of turbulence, and the last one is semi-implicit Euler method which is commonly applied to the motion of rigid body. These four numerical methods have spatial and temporal complexity $O(2^n)$ implying running time increases exponentially when cascade step enlarges. UM parameters of Case 3.1, test case of freely decaying SGC model, show that multifractality index of intermittency by classic Euler scheme is close to that of RK4 scheme, while multifractality of fluctuations of semi-implicit Euler method is close to results achieved by Slaved ABH technique. Given the definition of multifractality index, it's natural that different numerical schemes bring variations in multifractality index. On the other hand, empirical analysis of Case 3.1 including computing time and maximum memory suggests classic Euler technique is the most efficient numerical simulation approach among these schemes, which is also supported by complexity analysis. The numerical simulation method for SGC model is thus obtained from classic Euler method to provide time evolution of velocity field.

The existence of intermittency and its multifractality are investigated by forced SGC model with different large cascade steps $n = 12, 14, 15$ as adding forcing at top cascade step will prolong the motion revealing the properties of turbulence. Forcing for cascade step $n = 12$ ranges from $f = 0.1$ to $f = 1$, while forcing for $n = 14$ is between $f = 0.1$ and $f = 1.1$. Cascade step $n = 15$ with forcing $f = 0.5$ to $f = 1.1$ is carried out due to time-consuming computation supported by complexity analysis. The existence of intermittency and "heavy" tail of its probability distribution are confirmed by all cases, which suggests UM framework is a powerful tool to describe this nonlinear extreme events. The intensity of fluctuations is related to injected forcing, which is normal considering forcing has to prevent energy from losing to prolong running time. Fluctuations in cases with small forcing vanish over time, however in other

cases with large forcing, enormous fluctuations emerge and even stop the simulation, resulting in computational instability. Strong fluctuations are obviously observed in cases injecting medium value forcing. Therefore, part of cases supports empirical UM parameters for atmospheric turbulence. Averaged multifractality index for all cases as well as ensemble value is significantly smaller than 2 casting doubt on the log-normal model. Besides, computation instability displayed by these three cascade steps using classic Euler method is investigated by cascade step $n = 12$ simulated by semi-implicit Euler method, becasue semi-implicit Euler method preserves many symmetries and is more stable than the Euler method, widely utilizing in the motion of rigid body. The outcomes demonstrate that computation instability still exists in the simulation of semi-implicit Euler method. Strong fluctuations are exhibited in the majority of cases $n = 12$ and UM analysis confirms the conclusion carried out by classic Euler method that multifractality index is significantly less than 2.

Last but not least, the role of intermittency in backscattering energy ans scaling laws are investigated by energy spectrum containing power spectrum k^4 and the inertial spectrum, since energy is backscattering for power spectrum $k^s (s \leq 4)$ with the help of EDQNM, a closure approach without considering intermittency. Time evolution of four cases exhibits the conserved large eddies and increased spectrum exponent in infrared range, supporting that phenomenology resulting from power spectrum remains the same, although with intermittency effects. It also confirmed by observed slower energy decay, when energy decay process is compared to the energy decay of case with same inertial range but no infrared spectrum. Besides, integrals scale demonstrates the energy is stored at large scales by buffs, no longer in a continuous manner. Unfortunately, neither theoretical evidence nor numerical

evidence of backscatter term is presented.

Complexity analysis of SGC model suggests that it's challenging to improve the execution time as well as memory massively from algorithms. An effective eddy viscosity [63, 22] which is a typical two-point closures technique, applies to predict the large scales without information beyond cutoff wave number. However, this method doesn't consider intermittency. It would be meaningful to improve this method, allowing to shorten the running time and memory of large cascade steps to provide more cases to study the role of intermittency in scaling laws.

Regarding intermittency, forced SGC model in the study has been injected the deterministic forcing at the top layer. Recently the linear forcing proposed by Lundgren [80] has been considered as a useful alternative [108] to classic forcing, as it's simple and can be easily applied to numerical codes in physics, but provides the same results. This linear forcing raises questions about the ability to maintain intermittency, so adding linear forcing to SGC model to test the properties of intermittency will be intriguing. It is important to emphasize that multifractality analysis is performed on the entire time series, including the initial ah-hoc states. This instability state actually has an impact on UM parameters. A hypothesis that UM parameters will be well in agreement with empirical values if this instability state is removed, which has been supported by some cases. Further detailed study will be carried out soon. Another study worth further consideration is reducing the sensitivity of multifractality index estimates caused by algorithms since semi-implicit Euler method is as efficient as classical Euler method. The simulation had finished, as demonstrated in Chapter 4, and further in-depth research will be summarized and published in related paper.

Large infrared range research will provide a clear insight into the impact of semi-local interactions of SGC model on basckscatter term and scaling laws. Until now, more cases with large infrared range are limited by the drawbacks of cutoff wave number method, as well as successfully assessing the role of backscatter term in slowing energy decay by Loitsiansky exponent over large time scales and a wide range of k^4 energy spectrum. Besides, helical modes decompositions which is explored for the non-isotropic impacts of solid-body rotation on homogeneous turbulence, appears consistent with a trend toward two-dimensionalityas a result of allowing a departure from isotropy via external rotation effects and the loss of spectral energy from the parallel to the normal wave vectors (relative to the rotation axis). It will provide new perspectives on the dynamics of SGC model, such as the manner in which energy is transferred.

In conclusion, this research provides some insight on the effective numerical simulation method for SGC model. The existence of spatial-temporal intermittency is confirmed and the multifractality of intermittency questions the log-normal model. Moreover, some findings-the role of intermittency on backscatter term and scaling laws is investigated. We must acknowledge, nevertheless, that much more research is needed to fully understand the impact of intermittency on energy decay, even if it is challenging, which will be crucial for empirical utilization of energy in the future.

Appendix A

A.1 Legendre Transform

The connection between the scaling moment function $K(q)$ and the codimension function $c(\gamma)$ through the Legendre transform is explained.

From Eq 2.4.5, the probability of ε

$$Pr(\varepsilon_\lambda = \lambda^\gamma) \simeq \lambda^{-c(\gamma)}, \tag{A.1.1}$$

where the field has many variables γ. The qth moment of ε has

$$\langle \varepsilon_\lambda^q \rangle = \int dP(\varepsilon) \cdot \varepsilon_\lambda^q \simeq \int \lambda^{-c(\gamma)} \lambda^{q\gamma} d\gamma. \tag{A.1.2}$$

Since Eq.2.5.4 suggests $\langle \varepsilon_\lambda^q \rangle$ can be expressed by the resolution λ, it yields

$$\langle \varepsilon_\lambda^q \rangle = \lambda^{K(q)} = e^{K(q)log(\lambda)} = \int_{-\infty}^{+\infty} e^{\xi f(\gamma)} d\gamma \tag{A.1.3}$$

where $\xi = log(\lambda)$. Due to Eq A.1.2, the function $f(\gamma)$ is

$$f(\gamma) = q\gamma - c(\gamma). \tag{A.1.4}$$

Considering the mathematical technique of "steepest descents", the dominant term of Eq A.1.3 is $exp[\xi max_{\gamma}(f(\gamma))]$. Therefore, the corresponded moment equation is

$$K(q) = \max_{\gamma}\{q\gamma - c(\gamma)\}. \tag{A.1.5}$$

Eq A.1.5 describing the moment equation $K(q)$ and the codimsion function $c(\gamma)$ is a Legendre transform. Following same method, another Legendre transform is obtained

$$c(\gamma) = \max_{q}(q\gamma - K(q)). \tag{A.1.6}$$

For a given q, γ_q is defined by the maximum value that increase $q\gamma - c(\gamma)$. q_γ is defined as same way.

A.2 Universal Multifractal

The general form of scaling moment function $K(q)$ and codimension function $C(\gamma)$ which relates to the UM parameters α, C_1 are explained.

Based on the Taylor expansion, the moment function $K(q)$ is obtained corresponding to a pure log-normal cascade

$$\langle \varepsilon_{\lambda}^{q} \rangle = \lambda^{A_2 q^2} \tag{A.2.1}$$

where A_2 is coefficient. In order to make sure the small scale cascade limit is well behaved, the field has to be normalized by $\varepsilon \to \varepsilon/\langle\varepsilon\rangle$, so that $K(q) \to K(q) - qK(1)$. And the moment function $K(q)$ is

$$K(q) = C_1(q^2 - q) \tag{A.2.2}$$

where A_2 is replaced by C_1 due to Eq 2.6.3 $K'(1) = C_1$.

However, this is not sufficient to describe the cascade process. A random generator following an "extremely asymmetric" Lévy distribution is added. And it yields

$$K(q) = \frac{C_1}{\alpha - 1}(q^\alpha - q) \ (0 \leq \alpha \leq 2) \tag{A.2.3}$$

For $\alpha = 1$, $K(q) = C_1 qLn(q)$ is obtained from L'Hopital's rule for the limit $\alpha \to 1$.

Taking the Legendre transformation of the moment function $K(q)$, the codimension function $c(\gamma)$ is obtained

$$c(\gamma) = \begin{cases} C_1(\frac{\gamma}{C_1\alpha'} + \frac{1}{\alpha})^{\alpha'}, & \alpha \neq 1 \\ C_1 exp(\frac{\gamma}{C_1} - 1), & \alpha = 1 \end{cases} \tag{A.2.4}$$

where

$$\frac{1}{\alpha} + \frac{1}{\alpha'} = 1. \tag{A.2.5}$$

When $\alpha = 0$, it's the monofractal $\beta-$model. And $\alpha = 2$ is the Log-normal model which is the upper limit .

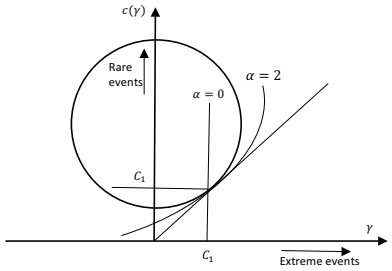

Figure A.1: The illustration that shows $c(\gamma)$ could be locally characterized by the singularity C_1 and the local radius of curvature $R_c(C_1)$ at C_1. $K(q)$ can be characterized through same method.

Appendix B

B.1 Gyroscope Equation

The Euler's equation for a rigid body is known as the gyroscope equation. There are two invariant, the square of the angular momentum and the kinetic energy.

The gyroscope equation is

$$\frac{d\boldsymbol{M}}{dt} = \boldsymbol{M} \wedge \boldsymbol{\Omega} \tag{B.1.1}$$

where $\boldsymbol{M}$ is the angular momentum of a rigid body; $\boldsymbol{\Omega}$ is its rotation; $\wedge$ is the vector product. The linear relationship between angular momentum $\boldsymbol{M}$ and rotation $\boldsymbol{\Omega}$ is symmetric

$$\boldsymbol{M} = I \cdot \boldsymbol{\Omega}; \boldsymbol{\Omega} = I^{-1} \cdot \boldsymbol{M} \tag{B.1.2}$$

where I is the moment of inertial tensor.

Considering Eq. B.1.1 in $so(3)$, the components of the fundamental asymmetric tensor I is the structure constants and the vector product $\wedge$ corresponds to the Lie bracket [,]. Now Eq. B.1.1 equals to an adjoint action on Lie algebra a

$$\frac{\partial X}{\partial t} = -ad_Y(X) \equiv [X, Y]; X, Y \in a \tag{B.1.3}$$

where [,] is defined by $[E_i, E_j] = C_{ij}^k E_k$; E_i is the basis; C_{ij} is the structure constant.

An invariant is the square of the angular momentum $\boldsymbol{M}^2$

$$\frac{d\boldsymbol{M}^2}{dt} = 2\boldsymbol{M} \cdot (\boldsymbol{M} \wedge \boldsymbol{\Omega}) = 0. \tag{B.1.4}$$

Another invariant is the kinetic energy

$$T = \frac{1}{2}\boldsymbol{M} \cdot \boldsymbol{\Omega} = \frac{1}{2}\boldsymbol{M} \cdot (I^{-1} \cdot \boldsymbol{M}), \tag{B.1.5}$$

since

$$\frac{dT}{dt} = 2\boldsymbol{\Omega} \cdot \frac{d\boldsymbol{M}}{dt} = 2\boldsymbol{\Omega} \cdot (\boldsymbol{M} \wedge \boldsymbol{\Omega}) = 0. \tag{B.1.6}$$

B.2 The orthogonality of SGC model

The orthogonality is crucial to obtain the SGC model. First of all, the impressibility condition yields

$$\boldsymbol{k} \cdot \widehat{\boldsymbol{u}}(\boldsymbol{k}, t) = 0. \tag{B.2.1}$$

The velocity $\widehat{\boldsymbol{u}}_m^i$ and its the vorticity $\widehat{\boldsymbol{\omega}}_m^i$ has the orthogonal triad $(\boldsymbol{k}_m^i,\ \widehat{\boldsymbol{u}}_m^i,\ \widehat{\boldsymbol{\omega}}_m^i)$ Fig.B.2a. In order to make Eq. 3.1.9 link to gyroscope equation Eq. B.1.1, the $\boldsymbol{M}_m^i$ and $\boldsymbol{\Omega}_m^i$ has the orthogonal decomposition $(\widehat{\boldsymbol{u}}_m^i,\ \widehat{\boldsymbol{u}}_{m+1}^{2i},\ \widehat{\boldsymbol{u}}_{m+1}^{2i+1})$ Fig.B.2b and $(\boldsymbol{k}_{m+1}^{2i},\ \widehat{\boldsymbol{\omega}}_{m+1}^{2i+1},\ \widehat{\boldsymbol{\omega}}_{m+1}^{2i})$ Fig.B.2c. These orthogonality conditions yield

$$\boldsymbol{k}_{m+1}^{2i+1} = -\boldsymbol{k}_{m+1}^{2i}. \tag{B.2.2}$$

The velocity field and the wave vector has

$$\widehat{\boldsymbol{u}}_m^i = \widehat{\boldsymbol{u}}(\boldsymbol{k}_m^i) = \widehat{u}_m^i \boldsymbol{e}_m^i \tag{B.2.3a}$$

$$\boldsymbol{e}_m^i = \frac{\boldsymbol{k}_m^i}{k_m^i} \tag{B.2.3b}$$

$$k_m^i = |\boldsymbol{k}_m^i| \tag{B.2.3c}$$

The last orthogonality triad is Fig.B.2d

$$\boldsymbol{e}_m^i \wedge \boldsymbol{e}_{m+1}^{2i} = \boldsymbol{e}_{m+2}^{2i}. \tag{B.2.4}$$

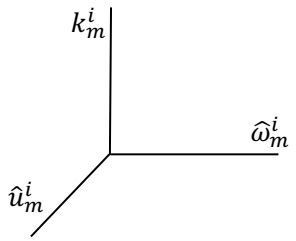

(a) Orthogonal triad $(\boldsymbol{k}_m^i,\ \widehat{\boldsymbol{u}}_m^i,\ \widehat{\boldsymbol{\omega}}_m^i)$

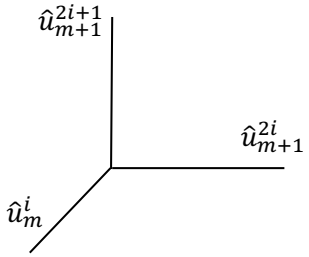

(b) Orthogonal triad $((\widehat{\boldsymbol{u}}_m^i,\ \widehat{\boldsymbol{u}}_{m+1}^{2i},\ \widehat{\boldsymbol{u}}_{m+1}^{2i+1})$

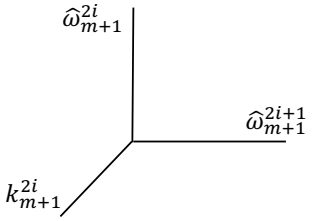

(c) Orthogonal triad $(\boldsymbol{k}_{m+1}^{2i},\ \widehat{\boldsymbol{\omega}}_{m+1}^{2i+1},\ \widehat{\boldsymbol{\omega}}_{m+1}^{2i})$

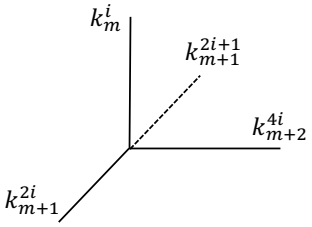

(d) Orthogonal triad of wave vector $\boldsymbol{k}_m^i$

Figure B.2: The orthogonality interaction of SGC model

The matrix representation of velocity $\widehat{\boldsymbol{u}}_m^i$ and its vorticity $\widehat{\boldsymbol{\omega}}_m^i$ are

$$\begin{bmatrix} \widehat{u}_{m+1}^{2i+1} \\ \widehat{u}_m^i \\ \widehat{u}_{m+1}^{2i} \end{bmatrix} = i[M_m^i] = i \begin{bmatrix} u_{m+1}^{2i+1} \\ u_m^i \\ u_{m+1}^{2i} \end{bmatrix} \tag{B.2.5a}$$

$$\begin{bmatrix} \widehat{\omega}_{m+1}^{2i} \\ 0 \\ \widehat{\omega}_{m+1}^{2i+1} \end{bmatrix} = [\Omega_m^i] = ik_{m+1} \begin{bmatrix} \widehat{u}_{m+1}^{2i} \\ 0 \\ \widehat{u}_{m+1}^{2i+1} \end{bmatrix}. \tag{B.2.5b}$$

And the inverse of the inertia tensor I^{-1} corresponds to

$$I^{-1} = k_m J; J = \begin{bmatrix} 0 & 0 & 1 \\ 0 & 0 & 0 \\ 1 & 0 & 0 \end{bmatrix}. \tag{B.2.6}$$

B.3 Algorithms

This part gives the pseudo-code for the numerical methods of the SGC model and the specific Python code for the main function contributing to the velocity field.

B.3.1 Euler method

The pseudo-code is provided first to better comprehend the following python code.

Algorithm 1 The Euler method

Input: The initial velocity U, The wave number K, The time steps Δt, The viscosity v, The computation time T, The maximum cascade step n, The ratio l

Output: The velocities U_T for all locations at time $0 - T$

function COMPUTING VELOCITIES $(U(t + \Delta t))$ ▷ By the former velocity $U(t)$

  Set L as the size of U ▷ Number of eddies at all layers

  Set the working list $Q = [0 \dots L - 1]$

  for $m = 0, \dots, n$ **do**

    if $m = 0$ **then** ▷ Selecting velocity equation at layer 0

      Compute $Q[0] = U_0^0(t + \Delta t)$ according to Eq. 3.2.3

    else if $m < n$ **then** ▷ Selecting velocity equation at layer m

for $i = 0, \ldots, K[m] - 1$ **do** ▷ i is the location at layer m
Compute $Q[l^m - 1 + i] = U_m^i(t + \Delta t)$ according to Eq.3.2.5
end for
else ▷ Selecting velocity equation at layer n
for $i = 0, \ldots, K[m] - 1$ **do** ▷ i is the location at layer m
Compute $Q[l^m - 1 + i] = U_n^i(t + \Delta t)$ according to Eq.3.2.4
end for
end if
end for
return Q
end function
function COMPUTING VELOCITIES (U_T)
Set the final velocity list $U_T := U$ ▷ The final velocity includes the initial value
for $t = 0, \ldots, T$ **do** ▷ Computing velocities for each location at time t
Compute $U(t + \Delta t)$ by Function 1
Store $U(t + \Delta t)$ in U_T
end for
return U_T
end function

The Python codes for velocities equations using classic Euler's scheme are given. First of all, the associated Python code for the velocity at top layer u_0^0 Eq.3.2.3 is:

```
### v0 is the initial value of the top layer
### v is the viscosity
### v1,v2 is v0's sub-eddies
```

```
### k0 is the wave number at top layer
### k1 is the wave number at cascade step 1
def Velocity_function0(v0, v1, v2, k1, k0,v, time_step,Force):
    a = 1 - v*np.power(k0,2)*time_step
    d = np.power(v1,2)-np.power(v2,2)
    new_velocity = v0*a +(k1 * d+Force ) * time_step
    return new_velocity
```

Code Listing B.1: Computing velocity at top layer $u_0^0(t+\Delta t)$ by Euler method

The corresponded Python code for the velocities u_n^i which are located at last layer Eq.3.2.4 is presented:

```
### i is the location in (n)th step
### v_n0 is the initial velocity
### a_n is the ancestor eddy
### k_n is the wave number at layer n
def Velocity_function2(v_n0,i,a_n,k_n,v,time_step,Force):
    a=(-1)**(i+1)
    b=a*k_n*v_n0*a_n
    c=v*np.power(k_n,2)
    B=1-c*time_step
    new_velocity=v_n0*B+(b+Force)*time_step
    return new_velocity
```

Code Listing B.2: Computing velocity $u_n^i(t+\Delta t)$ by Euler method

The Python code for the velocities u_m^i whose cascade step m is between 1 and $n-1$ Eq.3.2.5 are simulated by :

```
### i is the location at (s)th step
### v_s0 is the initial velocity
```

```
### a_s is it's ancestor eddy
### v_s1,v_s2 is it's sub-eddies
### v is the viscosity
### k_s is the wave number at cascade step s
### k_s1 is the wave number at cascade step s+1
def Velocity_function1(v_s0,i,a_s,v_s1,v_s2,k_s1,k_s,v,time_step,
    Force):
      a=(-1)**(i+1)
      b=np.power(v_s1,2)-np.power(v_s1,2)
      c=v*k_s**2
      C=1-c*time_step+a*k_s*a_s*time_step
      new_velocity=v_s0*C+(k_s1*b+Force)*time_step
      return new_velocity
```

Code Listing B.3: Computing velocity $u_m^i(t+\Delta t)(1 \leq m \leq n-1)$ by Euler method

Python code for Function 1 of Algorithm 1 computing $U(t+\Delta t)$ is presented in the following.

```
### n is the maximum cascade step, l is the separating ratio
### wave_number is the wave number for all cascade steps
### v is the viscosity
### Former_velocities is the velocity at time t
def Time_function(n, l, wave_number, Former_velocities, v, time_step
    , Force):
     length=len(Former_velocities) ### the number of eddies needs to
        compute
     New_velocities =[[]]* length ### Prepare array for new
        velocities
     for layer in range(n+1): ### Selecting the velocities equation
        by cascade step
```

```
9         if layer == 0: ### Special of the top layer
10            y = Velocity_function0(Former_velocities[0][0],
                  Former_velocities[1][0],Former_velocities[2][0],
                  wave_number[1],wave_number[0],v,time_step,Force)
11            New_velocities[0]=[y]### Store the new velocity
12        elif layer<n: ### From cascade step 1 to (n-1)th step
13            w_layer=wave_number[layer] ### Wave number for cascade
                  step (layer)
14            a=int(l**(layer-1))
15            b=int(l**layer)
16            B=Former_velocities[a-1:b-1] ### Eddies for (layer-1)th
                  step at time t
17            c=int(l**(layer+1))
18            C=Former_velocities[b-1:c-1] ### Eddies for (layer)th
                  step at time t
19            d=int(l**(layer+2))
20            D=Former_velocities[c-1:d-1] ### Eddies for (layer+1)th
                  step at time t
21            w_layer1=wave_number[layer+1]### Wave number for (layer
                  +1)th step
22            for i in range (l**layer):### Computing the velocities
                  for all locations at cascade step (layer)
23                h=int(i/2.) ### Computing the location of ancestor
24                a_layer=B[h][0] ### The velocity of ancestor eddy at
                      time t
25                v_layer1=D[2*i][0] ### The velocity of sub-eddies at
                      time t
26                v_layer2=D[2*i+1][0]
27                v_layer0=C[i][0] ### The initial velocity at time t
```

```
28                f=0
29                y=Velocity_function1(v_layer0,i,a_layer,v_layer1,
                      v_layer2,w_layer1,w_layer,v,time_step,f)
30                New_velocities[l**layer-1+i]=[y]### Store the new
                      velocity
31            else:### Cascade step n
32                w_layer=wave_number[layer] ###Wave number for cascade
                      step (layer)
33                a=int(l**(layer-1))
34                b=int(l**layer)
35                B=Former_velocities[a-1:b-1] ### Eddies for (n-1)th step
                       at time t
36                c=int(l**(layer+1))
37                C=Former_velocities[b-1:c-1] ### Eddies for (n)th step
                      at time t
38                for m in range (l**layer): ### Computing velocities for
                      all location at cascade step n
39                    H=int(m/2.) ### Computing the location of ancestor
40                    a_n=B[H][0] ### The velocity of ancestor eddy at
                          time t
41                    v_n0=C[m][0]### The initial velocity at time t
42                    y=Velocity_function2(v_n0,m,a_n,w_layer,v,time_step
                          ,0)
43                    New_velocities[l**layer-1+m]=[y]### Store the new
                          velocity
44        return New_velocities
```

Code Listing B.4: Euler method. The velocities U_m^i for all layers ($0 \leq m \leq n$) at each time step

The Python codes for velocities equations using semi-implicit Euler's scheme are given. First of all, the associated Python code for the velocity at top layer u_0^0 Eq.3.2.17 is:

```
### v0 is the initial value of the top layer
### v is the viscosity
### v1,v2 is v0's sub-eddies
### k0 is the wave number at top layer
### k1 is the wave number at cascade step 1
def Velocity_function0(v0, v1, v2, k1, k0,v, time_step,Force):
    a = 1+ v*np.power(k0,2)*time_step
    d = Square(v1)-Square(v2)
    b = v0 +(k1 * d+Force ) * time_step
    new_velocity = b/a
    return new_velocity
```

Code Listing B.5: Computing velocity at top layer $u_0^0(t + \Delta t)$ by Semi-implicit Euler method

The corresponded Python code for the velocities u_n^i which are located at last layer Eq.3.2.18 is presented:

```
### i is the location in (n)th step
### v_n0 is the initial velocity
### a_n is the ancestor eddy
### k_n is the wave number at layer n
def Velocity_function2(v_n0,i,a_n,k_n,v,time_step,Force):
    a=(-1)**i
    b= a*k_n*v_n0*a_n
    c= v*k_n**2
    d= v_n0 +(b+Force)*time_step
```

```
10      B= 1 +c*time_step
11      new_velocity= d/B
12      return new_velocity
```

Code Listing B.6: Computing velocity $u_n^i(t+\Delta t)$ by Semi-implicit Euler method

The Python code for the velocities u_m^i whose cascade step m is between 1 and $n-1$ Eq.3.2.19 are simulated by :

```
1  ### i is the location at (s)th step
2  ### v_s0 is the initial velocity
3  ### a_s is it's ancestor eddy
4  ### v_s1,v_s2 is it's sub-eddies
5  ### v is the viscosity
6  ### k_s is the wave number at cascade step s
7  ### k_s1 is the wave number at cascade step s+1
8  def Velocity_function1(v_s0,i,a_s,v_s1,v_s2,k_s1,k_s,v,time_step,
       Force):
9        a=(-1)**i
10       b= Square(v_s1)-Square(v_s2)
11       A= k_s1* b +a *k_s *v_s0 *a_s
12       c= v* k_s**2
13       d= v_s0+ (A+Force)* time_step
14       C= 1+ c* time_step
15       new_velocity= d/C
16       return new_velocity
```

Code Listing B.7: Computing velocity $u_m^i(t+\Delta t)(1 \leq m \leq n-1)$ by Semi-implicit Euler method

B.3.2 The fourth order Runge-Kutta method

The pseudo-code for the RK4 method is the same as the Euler method except for the equations for computing the velocity field. So the specific Python code instead of the pseudo-code is shown.

The Python code for the velocity at top layer is:

```
### v0 is the initial value of the top layer
### v is the viscosity
### v1,v2 is v0's sub-eddies
### k0 is the wave number at top layer
### k1 is the wave number at cascade step 1
def Runge_0(v0, v1, v2, k1, k0,v, time_step,Force):
    a = -v*np.power(k0,2)
    d = np.power(v1,2)-np.power(v2,2)
    k_1= v0*a+(k1*d+Force) ### the derivative function
    y_1 = time_step*k_1 ### y_1 = dx * f( x,y)
    ### y2 = dx * f( x + 0.5 * dx, y + 0.5 * y1)
    c = v0+0.5*y_1
    k_2 = c*a +(k1 * d+Force )
    y_2 = time_step*k_2
    ### y3 = dx * f(x + 0.5 * dx, y + 0.5 * y2)
    f = v0+0.5*y_2
    k_3 = f*a +(k1 * d+Force )
    y_3 = time_step*k_3
    ### y4 = dx * f( x + dx, y + y3)
    g = v0+y_3
    k_4 = g*a +(k1 * d+Force )
    y_4=time_step*k_4
```

```
    ### the new Velocity y + (y1 + 2 * y2 + 2 * y3 + y4) / 6.
    V = v0+(y_1 + 2 * y_2 + 2 * y_3 + y_4) / 6.
    return V
```

Code Listing B.8: Computing velocity $u_0^0(t + \Delta t)$ simulated by RK4 method

The Python code for the velocity u_n^i is:

```
### i is the location in (n)th step
### v_n0 is the initial velocity
### a_n is the ancestor eddy
### k_n is the wave number at layer n
def Runge_2(v_n0,i,a_n,k_n,v,time_step,Force):
    ### y1 = dx * f( x,y)
    a=(-1)**(i+1)
    b=a*k_n*a_n
    c=-v*k_n**2+b
    k_1=v_n0*c+Force
    y_1=time_step*k_1
    ### y2 = dx * f(x + 0.5 * dx, y + 0.5 * y1)
    C=v_n0+0.5*y_1
    k_2=C*c+Force
    y_2=time_step*k_2
    ### y3 = dx * f( x + 0.5 * dx, y + 0.5 * y2)
    f=v_n0+0.5*y_2
    k_3=f*c+Force
    y_3=time_step*k_3
    ### y4 = dx * f( x + dx, y + y3 )
    g=v_n0+y_3
    k_4=g*c+Force
    y_4=time_step*k_4
```

```
    ### y + (y1 + 2 * y2 + 2 * y3 + y4) / 6.
    V=v_n0+(y_1 + 2 * y_2 + 2 * y_3 + y_4) / 6.
    return V
```

Code Listing B.9: Computing velocities u_n^i by RK4 method

The Python code for the velocities u_m^i from layer 1 to $n-1$ is:

```
### i is the location at (s)th step
### v_s0 is the initial velocity
### a_s is it's ancestor eddy
### v_s1,v_s2 is it's sub-eddies
### v is the viscosity
### k_s is the wave number at cascade step s
### k_s1 is the wave number at cascade step s+1
def Runge_1(v_s0,i,a_s,v_s1,v_s2,k_s1,k_s,v,time_step,Force):
    ### y1 = dx * f(x,y)
    a=(-1)**(i+1)
    b=np.power(v_s1,2)-np.power(v_s2,2)
    A=k_s1*b
    c=-v*k_s**2+a*k_s*a_s
    k_1=v_s0*c+A+Force
    y_1=time_step*k_1
    ### y2 = dx * f(x + 0.5 * dx ,y + 0.5 * y1)
    C=v_s0+0.5*y_1
    k_2=C*c+A+Force
    y_2=time_step*k_2
    ### y3 = dx * f( x + 0.5 * dx, y + 0.5 * y2)
    f=v_s0+0.5*y_2
    k_3=f*c+A+Force
    y_3=time_step*k_3
```

```
    ### y4 = dx * f( x + dx, y + y3 )
    g=v_s0+y_3
    k_4=g*c+A+Force
    y_4=time_step*k_4
    ### y + (y1 + 2 * y2 + 2 * y3 + y4) / 6.
    V=v_s0+(y_1 + 2 * y_2 + 2 * y_3 + y_4) / 6.
    return V
```

Code Listing B.10: Computing velocities $u_m^i(t+\Delta t)(1 \leq m \leq n-1)$ simulated by RK4 method

The Python code for the velocities for each time step is:

```
### n is the maximum cascade step, l is the separating ratio, v is
    the viscosity
### wave_number is the wave number for all cascade steps
### Former_velocities is the velocity at time t
def Time_function(n, l, wave_number, Former_velocities, v, time_step
    , Force):
    length=len(Former_velocities) ### the number of eddies needs to
        compute
    New_velocities =[[]]* length ### Prepare array for new
        velocities
    for layer in range(n+1): ### Selecting the velocities equation
        by cascade step
        if layer == 0: ### Special of the top layer
            y = Runge_0(Former_velocities[0][0],Former_velocities
                [1][0],Former_velocities[2][0],wave_number[1],
                wave_number[0],v,time_step,Force)
            New_velocities[0]=[y]### Store the new velocity
        elif layer<n: ### From cascade step 1 to (n-1)th step
```

```
12              w_layer=wave_number[layer] ### Wave number for cascade
                    step (layer)
13              a=int(l**(layer-1))
14              b=int(l**layer)
15              B=Former_velocities[a-1:b-1] ### Eddies for (layer-1)th
                    step at time t
16              c=int(l**(layer+1))
17              C=Former_velocities[b-1:c-1] ### Eddies for (layer)th
                    step at time t
18              d=int(l**(layer+2))
19              D=Former_velocities[c-1:d-1] ### Eddies for (layer+1)th
                    step at time t
20              w_layer1=wave_number[layer+1]### Wave number for (layer
                    +1)th step
21              for i in range (l**layer):### Computing the velocities
                    for all locations at cascade step (layer)
22                  h=int(i/2.) ### Computing the location of ancestor
23                  a_layer=B[h][0] ### The velocity of ancestor eddy at
                        time t
24                  v_layer1=D[2*i][0] ### The velocity of sub-eddies at
                        time t
25                  v_layer2=D[2*i+1][0]
26                  v_layer0=C[i][0] ### The initial velocity at time t
27                  f=0
28                  y=Runge_1(v_layer0,i,a_layer,v_layer1,v_layer2,
                        w_layer1,w_layer,v,time_step,f)
29                  New_velocities[l**layer-1+i]=[y]### Store the new
                        velocity
30          else:### Cascade step n
```

```
31              w_layer=wave_number[layer] ###Wave number for cascade
                    step (layer)
32              a=int(l**(layer-1))
33              b=int(l**layer)
34              B=Former_velocities[a-1:b-1] ### Eddies for (n-1)th step
                     at time t
35              c=int(l**(layer+1))
36              C=Former_velocities[b-1:c-1] ### Eddies for (n)th step
                    at time t
37              for m in range (l**layer): ### Computing velocities for
                    all location at cascade step n
38                  H=int(m/2.) ### Computing the location of ancestor
39                  a_n=B[H][0] ### The velocity of ancestor eddy at
                        time t
40                  v_n0=C[m][0]### The initial velocity at time t
41                  y=Runge_2(v_n0,m,a_n,w_layer,v,time_step,0)
42                  New_velocities[l**layer-1+m]=[y]### Store the new
                        velocity
43      return New_velocities
```

Code Listing B.11: RK4 method. Velocities U_m^i for all layers ($0 \leq m \leq n$) at each time step

B.3.3 The slaved Adams Bashforth method

Since the input required by the slaved ABF method is different from that of the one-step methods, the pseudo-code for the slaved ABF method is given.

Algorithm 2 The slaved Adams-Bashforth Method

Input The initial velocity U, The wave number K, The time steps Δt, The viscosity v, The computation time T, The maximum cascade step n, The ratio l

Output The velocities U_T for all locations at time $0 - T$

function COMPUTING VELOCITIES($U(t + \Delta t)$) ▷ By the former velocities $U(t), U(t - \Delta t)$

  Set L as the size of U ▷ Number of eddies for all layers

  Set the working list $Q = [0 \dots L - 1]$ ▷ Velocities $U(t + \Delta t)$

  for $m = 0, \dots, n$ **do** ▷ Selecting velocities equations by cascade step m

    if $m = 0$ **then** ▷ Using velocity equation at top layer

      Compute $Q[0] = U_0^0(t + \Delta t)$ according to Eq.3.2.13 ▷ The velocity at layer 0

    else if $m < n$ **then** ▷ Selecting velocity equation at layer m

      for $i = 0, \dots, K[m] - 1$ **do** ▷ i is the location at layer m

        Compute $Q[l^m - 1 + i] = U_m^i(t + \Delta t)$ according to Eq.3.2.15

      end for

    else ▷ Selecting velocity equation at layer n

      for $i = 0, \dots, K[m] - 1$ **do** ▷ i is the location at layer n

        Compute $Q[l^m - 1 + i] = U_n^i(t + \Delta t)$ according to Eq.3.2.14

      end for

    end if

  end for

  return Q

end function

function COMPUTING VELOCITIES (U_T)

20: Set the final velocity list $U_T := U$ ▷ The final velocity includes the initial value

21: **for** $t = 0, \ldots, T$ **do** ▷ Computing velocities for each location at time t

22: Compute $U(t + \Delta t)$ by Function 3 ▷ When $t = 0$, the former velocities $U(t - \Delta t)$ is $U(t)$

23: Store $U(t + \Delta t)$ in U_T

24: **end for**

25: **return** U_T

26: **end function**

Python code for Eq.3.2.13 is:

```
### v0 is the initial value of the top layer
### v is the viscosity
### v1,v2 are v0's sub-eddies, v1_0,v2_0 are former velocities
### k0 is the wave number at top layer
### k1 is the wave number at cascade step 1
def Velocity_function0_1(v0, v1, v2, k1, k0,v, time_step,Force,v1_0,
    v2_0):
     a = v*np.power(k0,2)
     b = np.power(math.e,-a*time_step)
     d = k1 * (np.power(v1,2)-np.power(v2,2))+Force
     d_0 = k1 * (np.power(v1_0,2)-np.power(v2_0,2))+Force
     c=(3*d-d_0)/2
     new_velocity = v0*b+(1-b)/a*c
     return new_velocity
```

Code Listing B.12: Computing velocity $u_0^0(t + \Delta t)$ by slaved ABF method

The Python code for the velocities $u_n^i(t + \Delta t)$ at last cascade step is:

```
### i is the location in (n)th step
### v_n0 is the initial velocity
### a_n is the ancestor eddy
### k_n is the wave number at layer n
def Velocity_function2_1(v_n0,i,a_n,k_n,v,time_step,Force):
    a = v*k_n**2-(-1)**(i+1)*k_n*a_n
    b = np.power(math.e,-a*time_step)
    new_velocity = v_n0*b+(1-b)/a*Force
    return new_velocity
```

Code Listing B.13: Computing velocities $u_n^i(t+\Delta t)$ by slaved ABF method

The Python code for the velocities $u_m^i(t+\Delta t)$ $(1 \leq m \leq n-1)$ is:

```
### i is the location at (s)th step
### v_s0 is the initial velocity
### a_s is it's ancestor eddy
### v_s1,v_s2 are it's sub-eddies, v_s1_0,v_s2_0 are former
    velocities
### v is the viscosity
### k_s is the wave number at cascade step s
### k_s1 is the wave number at cascade step s+1
def Velocity_function1_1(v_s0,i,a_s,v_s1,v_s2,k_s1,k_s,v,time_step,
    Force,v_s1_0,v_s2_0):
    a =  v*k_s**2-(-1)**(i+1)*k_s*a_s
    b = np.power(math.e,-a*time_step)
    d = k_s1*(np.power(v_s1,2)-np.power(v_s2,2))+Force
    d_0 = k_s1*(np.power(v_s1_0,2)-np.power(v_s2_0,2))+Force
    c = (3*d-d_0)/2
    new_velocity = v_s0*b+(1-b)/a*c
```

```
15     return new_velocity
```

Code Listing B.14: Computing velocities $u_m^i(t+\Delta t)$ $(1 \leq m \leq n-1)$ by slaved ABF method

The Python code for Function 1 in Algorithm 2 is exhibited in the below.

```
1  ### n is the maximum cascade step, l is the separating ratio, v is
       the viscosity
2  ### wave_number is the wave number for all cascade steps,
       Former_velocities is the velocity at time t,
       Former_two_velocities is velocity at time t-dt
3  def Time_function(n, l, wave_number, Former_velocities, v, time_step
       , Force,Former_two_velocities):
4      New_velocities =[[]]* len(Former_velocities) ### Array for new
           velocities
5      for layer in range(n+1): ### Selecting the velocities equation
           by cascade step
6          if layer == 0: ### Special of the top layer
7              y = Velocity_function0_1(Former_velocities[0][0],
                   Former_velocities[1][0],Former_velocities[2][0],
                   wave_number[1], wave_number[0],v, time_step,0,
                   Former_two_velocities[1][0],Former_two_velocities
                   [2][0])
8              New_velocities[0]=[y]### Store the new velocity
9          elif layer<n: ### From cascade step 1 to (n-1)th step
10             w_layer=wave_number[layer] ### Wave number for cascade
                   step (layer)
11             a=int(l**(layer-1))
12             b=int(l**layer)
```

```
13              B=Former_velocities[a-1:b-1] ### Eddies for (layer-1)th
                    step at time t
14              c=int(l**(layer+1))
15              C=Former_velocities[b-1:c-1] ### Eddies for (layer)th
                    step at time t
16              d=int(l**(layer+2))
17              D=Former_velocities[c-1:d-1] ### Eddies for (layer+1)th
                    step at time t
18              F=Former_two_velocities[c-1:d-1] ### (layer+1)th step at
                     time t-dt
19              w_layer1=wave_number[layer+1]### Wave number for (layer
                    +1)th step
20              for i in range (l**layer):### Computing the velocities
                    for all locations at cascade step (layer)
21                  h=int(i/2.) ### Computing the location of ancestor
22                  a_layer=B[h][0] ### The velocity of ancestor eddy at
                        time t
23                  v_layer1=D[2*i][0] ### The velocity of sub-eddies at
                        time t
24                  v_layer2=D[2*i+1][0]
25                  v_layer0=C[i][0] ### The initial velocity at time t
26                  y=Velocity_function1_1(v_layer0,i,a_layer,v_layer1,
                        v_layer2,w_layer1,w_layer,v,time_step,0,F[2*i
                        ][0],F[2*i+1][0])
27                  New_velocities[l**layer-1+i]=[y]### Store the new
                        velocity
28          else:### Cascade step n
29              w_layer=wave_number[layer] ###Wave number for cascade
                    step (layer)
```

```
30              a=int(l**(layer-1))
31              b=int(l**layer)
32              B=Former_velocities[a-1:b-1] ### Eddies for (n-1)th step
                    at time t
33              c=int(l**(layer+1))
34              C=Former_velocities[b-1:c-1] ### Eddies for (n)th step
                   at time t
35              for m in range (l**layer): ### Computing velocities for
                   all location at cascade step n
36                  H=int(m/2.) ### Computing the location of ancestor
37                  a_n=B[H][0] ### The velocity of ancestor eddy at
                       time t
38                  v_n0=C[m][0]### The initial velocity at time t
39                  y=Velocity_function2_1(v_n0,m,a_n,w_layer,v,
                       time_step,0)
40                  New_velocities[l**layer-1+m]=[y]### Store the new
                       velocity
41      return New_velocities
```

Code Listing B.15: Slaved ABF method: Velocities U_m^i for all layers $(0 \leq m \leq n)$ at each time step

B.3.4 Results

The computing time and maximum memory of Euler method:

```
        Command being timed: "./Euler_computing_time.py"
        User time (seconds): 14871.78
        System time (seconds): 85.73
        Percent of CPU this job got: 99%
        Elapsed (wall clock) time (h:mm:ss or m:ss): 4:09:34
        Average shared text size (kbytes): 0
        Average unshared data size (kbytes): 0
        Average stack size (kbytes): 0
        Average total size (kbytes): 0
        Maximum resident set size (kbytes): 11867844
        Average resident set size (kbytes): 0
        Major (requiring I/O) page faults: 0
        Minor (reclaiming a frame) page faults: 2870008
        Voluntary context switches: 45780
        Involuntary context switches: 10522
        Swaps: 0
        File system inputs: 0
        File system outputs: 3839808
        Socket messages sent: 0
        Socket messages received: 0
        Signals delivered: 0
        Page size (bytes): 4096
        Exit status: 0
~
~
~
~
~
~
~
~
~
~
~
~
~
~
"Euler_computing_1.sh.e14709" 23L, 765C
```

Figure B.3: Euler method

The computing time and maximum memory of RK4 method:

```
        Command being timed: "./Runge_Kutta_computing_time.py"
        User time (seconds): 15663.66
        System time (seconds): 80.29
        Percent of CPU this job got: 99%
        Elapsed (wall clock) time (h:mm:ss or m:ss): 4:22:40
        Average shared text size (kbytes): 0
        Average unshared data size (kbytes): 0
        Average stack size (kbytes): 0
        Average total size (kbytes): 0
        Maximum resident set size (kbytes): 11866452
        Average resident set size (kbytes): 0
        Major (requiring I/O) page faults: 0
        Minor (reclaiming a frame) page faults: 2747993
        Voluntary context switches: 80490
        Involuntary context switches: 15154
        Swaps: 0
        File system inputs: 0
        File system outputs: 3839808
        Socket messages sent: 0
        Socket messages received: 0
        Signals delivered: 0
        Page size (bytes): 4096
        Exit status: 0
~
~
~
~
~
~
~
~
~
~
~
~
~
~
"Runge_Kutta_computing.sh.e14710" 23L, 771C
```

Figure B.4: RK4 method

The computing time and maximum memory of Slaved ABF method:

```
        Command being timed: "./slaved_adam_bash_forth_computing.py"
        User time (seconds): 33909.67
        System time (seconds): 510.66
        Percent of CPU this job got: 99%
        Elapsed (wall clock) time (h:mm:ss or m:ss): 9:33:56
        Average shared text size (kbytes): 0
        Average unshared data size (kbytes): 0
        Average stack size (kbytes): 0
        Average total size (kbytes): 0
        Maximum resident set size (kbytes): 11867664
        Average resident set size (kbytes): 0
        Major (requiring I/O) page faults: 85
        Minor (reclaiming a frame) page faults: 209083854
        Voluntary context switches: 32248
        Involuntary context switches: 39384
        Swaps: 0
        File system inputs: 10544
        File system outputs: 3839808
        Socket messages sent: 0
        Socket messages received: 0
        Signals delivered: 0
        Page size (bytes): 4096
        Exit status: 0
~
~
~
~
~
~
~
~
~
~
~
~
~
~
~
"Slaved_Adams_forth_computing.sh.e14711" 23L, 785C
```

Figure B.5: Slaved ABF method

B.4 The cascade step $n = 12$ simulated by semi-implicit Euler method

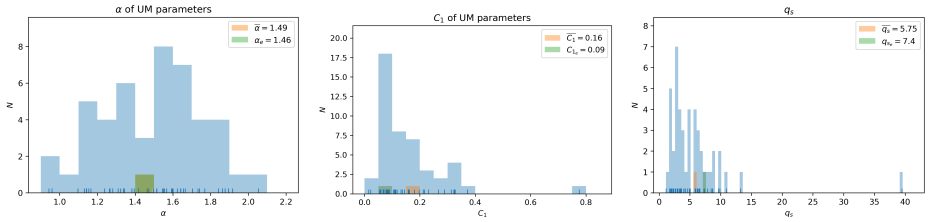

(a) Case 4.1.1

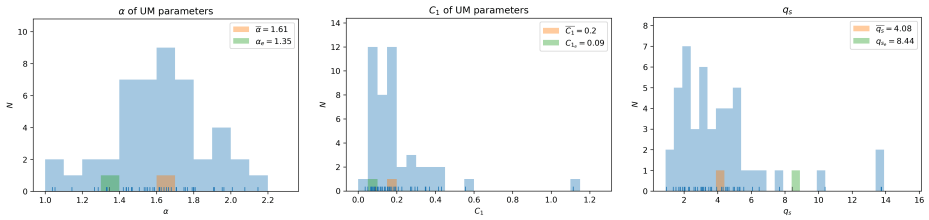

(b) Case 4.1.2

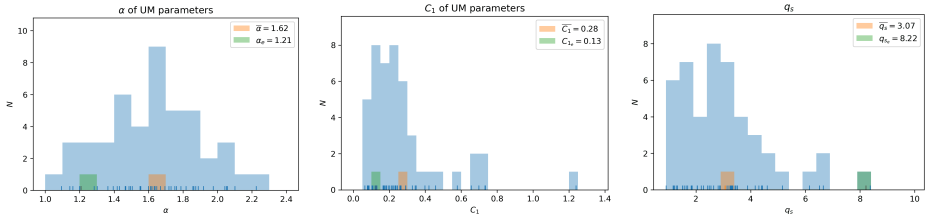

(c) Case 4.1.3

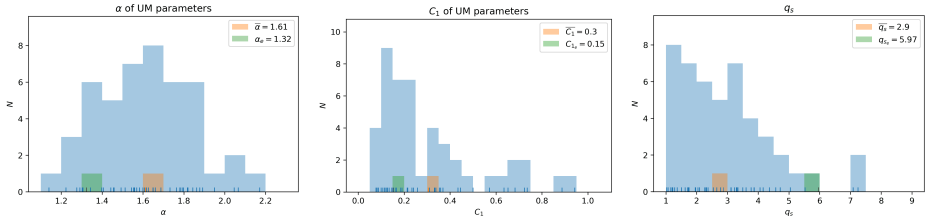

(d) Case 4.1.4

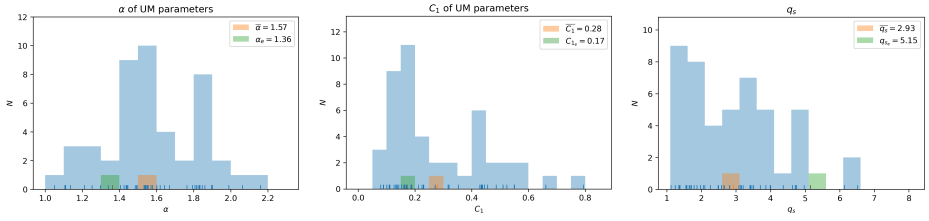

(e) Case 4.1.5

Figure B.6: The UM parameters of Cases 4.1.1-4.1.5 simulated by the semi-implicit Euler method.

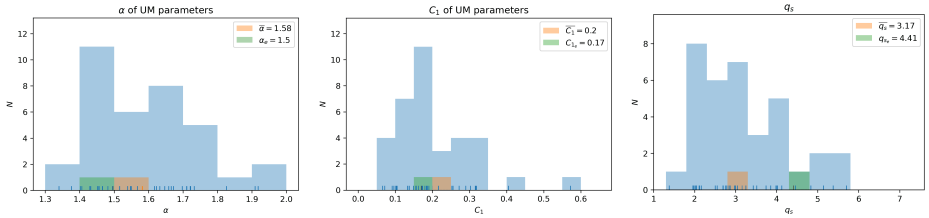

(a) Case 4.1.6

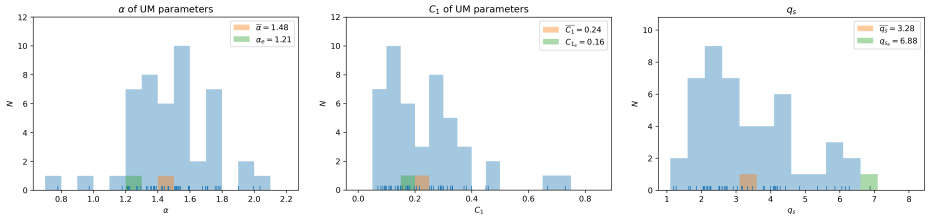

(b) Case 4.1.7

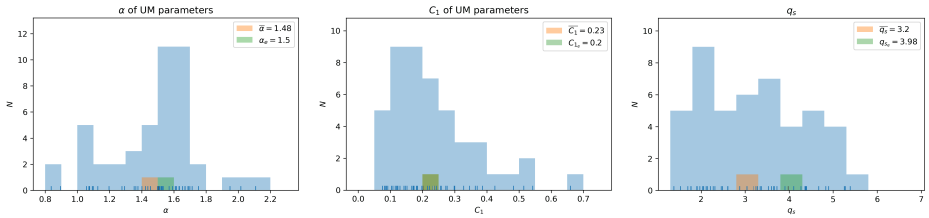

(c) Case 4.1.8

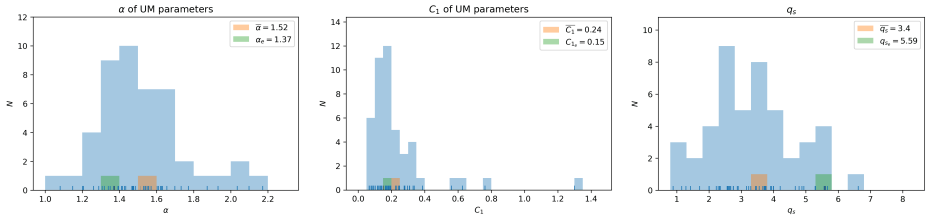

(d) Case 4.1.9

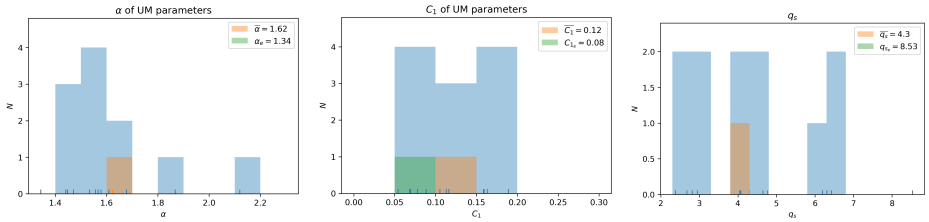

(e) Case 4.1.10

Figure B.7: The UM parameters of Cases 4.1.6-4.1.10 simulated by the semi-implicit Euler method.

Declaration of Academic Achievement

[1] Li X, Schertzer D, Roustan Y, et al. Multifractals, free turbulence decay laws and the Scaling Gyroscopes Cascade model[C]//EGU General Assembly Conference Abstracts. 2021: EGU21-10920. (Corresponded paper is preparing.)

[2] Li X, Schertzer D, Roustan Y, et al. Intermittency, stochastic Universal Multifractals and the deterministic Scaling Gyroscope Cascade model[C]//EGU General Assembly Conference Abstracts. 2022: EGU22-7783. (Corresponded paper is preparing.)

Bibliography

[1] J. Aitchison and J. Brown. Ac (1957) the lognormal distribution. *Cambridge University Press, Cambridge*, 1957.

[2] K. Alvelius. Random forcing of three-dimensional homogeneous turbulence. *Physics of Fluids*, 11(7):1880–1889, 1999.

[3] F. Anselmet, Y. Gagne, E. Hopfinger, and R. Antonia. High-order velocity structure functions in turbulent shear flows. *Journal of Fluid Mechanics*, 140: 63–89, 1984.

[4] V. Arnold. Sur la géométrie différentielle des groupes de lie de dimension infinie et ses applications à l'hydrodynamique des fluides parfaits. In *Annales de l'institut Fourier*, volume 16, pages 319–361, 1966.

[5] G. K. Batchelor. *The theory of homogeneous turbulence*. Cambridge university press, 1953.

[6] G. K. Batchelor and I. Proudman. The large-scale structure of homogenous turbulence. *Philosophical Transactions of the Royal Society of London. Series A, Mathematical and Physical Sciences*, 248(949):369–405, 1956.

[7] G. K. Batchelor and A. A. Townsend. Decay of isotropic turbulence in the initial period. *Proceedings of the Royal Society of London. Series A. Mathematical and Physical Sciences*, 193(1035):539–558, 1948.

[8] G. K. Batchelor and A. A. Townsend. The nature of turbulent motion at large wave-numbers. *Proceedings of the Royal Society of London. Series A. Mathematical and Physical Sciences*, 199(1057):238–255, 1949.

[9] R. Benzi, L. Biferale, R. Kerr, and E. Trovatore. Helical shell models for three-dimensional turbulence. *Physical Review E*, 53(4):3541, 1996.

[10] S. R. Bistafa. On the development of the navier-stokes equation by navier. *Revista Brasileira de Ensino de Física*, 40(2), 2018.

[11] B. Biswas, S. Chatterjee, S. Mukherjee, and S. Pal. A discussion on euler method: A review. *Electronic Journal of Mathematical Analysis and Applications*, 1(2):2090–2792, 2013.

[12] A. Briard, T. Gomez, and C. Cambon. Spectral modelling for passive scalar dynamics in homogeneous anisotropic turbulence. *Journal of Fluid Mechanics*, 799:159–199, 2016.

[13] T. Burton, N. Jenkins, D. Sharpe, and E. Bossanyi. *Wind energy handbook*. John Wiley & Sons, 2011.

[14] R. Calif and F. G. Schmitt. Modeling of atmospheric wind speed sequence using a lognormal continuous stochastic equation. *Journal of Wind Engineering and Industrial Aerodynamics*, 109:1–8, 2012.

[15] C. Cambon and L. Jacquin. Spectral approach to non-isotropic turbulence subjected to rotation. *Journal of Fluid Mechanics*, 202:295–317, 1989.

[16] C. Cambon, L. Danaila, F. S. Godeferd, and J. F. Scott. Third-order statistics and the dynamics of strongly anisotropic turbulent flows. *Journal of Turbulence*, 14(3):121–160, 2013.

[17] C. Canuto, M. Y. Hussaini, A. Quarteroni, A. Thomas Jr, et al. *Spectral methods in fluid dynamics*. Springer Science & Business Media, 2012.

[18] T.-P. Chang, H.-H. Ko, F.-J. Liu, P.-H. Chen, Y.-P. Chang, Y.-H. Liang, H.-Y. Jang, T.-C. Lin, and Y.-H. Chen. Fractal dimension of wind speed time series. *Applied Energy*, 93:742–749, 2012.

[19] J. Chasnov. Computation of the loitsianski integral in decaying isotropic turbulence. *Physics of Fluids A: Fluid Dynamics*, 5(11):2579–2581, 1993.

[20] Y. Chigirinskaya and D. Schertzer. Cascade of scaling gyroscopes: Lie structure, universal multifractals and self-organized criticality in turbulence. In *Stochastic Models in Geosystems*, pages 57–81. Springer, 1997.

[21] Y. Chigirinskaya, D. Schertzer, and S. Lovejoy. Scaling gyroscopes cascade: universal multifractal features of 2-d and 3-d turbulence. *Fractals and Chaos in Chemical Engineering. World Scientific, Singapore*, pages 371–384, 1997.

[22] J.-P. Chollet and M. Lesieur. Parameterization of small scales of three-dimensional isotropic turbulence utilizing spectral closures. *Journal of Atmospheric Sciences*, 38(12):2747–2757, 1981.

[23] G. Comte-Bellot and S. Corrsin. The use of a contraction to improve the isotropy of grid-generated turbulence. *Journal of fluid mechanics*, 25(4):657–682, 1966.

[24] P. Davidson. Was loitsyansky correct? a review of the arguments. *Journal of Turbulence*, 1(1):006, 2000.

[25] T. De Karman and L. Howarth. On the statistical theory of isotropic turbulence. *Proceedings of the Royal Society of London. Series A-Mathematical and Physical Sciences*, 164(917):192–215, 1938.

[26] A. Delache, C. Cambon, and F. Godeferd. Scale by scale anisotropy in freely decaying rotating turbulence. *Physics of Fluids*, 26(2):025104, 2014.

[27] N. Desaulniers-Soucy. Empirical test of the multifractal continuum limit in rain. 1999.

[28] J. A. Domaradzki. Analysis of energy transfer in direct numerical simulations of isotropic turbulence. *The Physics of fluids*, 31(10):2747–2749, 1988.

[29] J. A. Domaradzki. Nonlocal triad interactions and the dissipation range of isotropic turbulence. *Physics of Fluids A: Fluid Dynamics*, 4(9):2037–2045, 1992.

[30] J. A. Domaradzki and R. S. Rogallo. Local energy transfer and nonlocal interactions in homogeneous, isotropic turbulence. *Physics of Fluids A: Fluid Dynamics*, 2(3):413–426, 1990.

[31] S. Douady, Y. Couder, and M. Brachet. Direct observation of the intermittency of intense vorticity filaments in turbulence. *Physical review letters*, 67(8):983, 1991.

[32] V. Eswaran and S. B. Pope. An examination of forcing in direct numerical simulations of turbulence. *Computers & Fluids*, 16(3):257–278, 1988.

[33] G. L. Eyink and D. J. Thomson. Free decay of turbulence and breakdown of self-similarity. *Physics of Fluids*, 12(3):477–479, 2000.

[34] K. Falconer. *Fractal geometry: mathematical foundations and applications*. John Wiley & Sons, 2004.

[35] D. Forster, D. R. Nelson, and M. J. Stephen. Large-distance and long-time properties of a randomly stirred fluid. *Physical Review A*, 16(2):732, 1977.

[36] A. Fouquet, M. Lesieur, J. André, and C. Basdevant. Evolution of high reynolds number two-dimensional turbulence. *Journal of Fluid Mechanics*, 72(2):305–319, 1975.

[37] France. Gestionnaire du réseau de transport d'electricité. `https://bilan-electrique-2020.rte-france.com`.

[38] C. L. Franzke, S. Barbosa, R. Blender, H.-B. Fredriksen, T. Laepple, F. Lambert, T. Nilsen, K. Rypdal, M. Rypdal, M. G. Scotto, et al. The structure of climate variability across scales. *Reviews of Geophysics*, 58(2):e2019RG000657, 2020.

[39] U. Frisch and A. N. Kolmogorov. *Turbulence: the legacy of AN Kolmogorov*. Cambridge university press, 1995.

[40] U. Frisch and R. Morf. Intermittency in nonlinear dynamics and singularities at complex times. *Physical review A*, 23(5):2673, 1981.

[41] U. Frisch and G. Parisi. Fully developed turbulence and intermittency. *New York Academy of Sciences, Annals*, 357:359–367, 1980.

[42] U. Frisch, P.-L. Sulem, and M. Nelkin. A simple dynamical model of intermittent fully developed turbulence. *Journal of Fluid Mechanics*, 87(4):719–736, 1978.

[43] U. Frisch, M. Lesieur, and D. Schertzer. Comments on the quasi-normal markovian approximation for fully-developed turbulence. *Journal of Fluid Mechanics*, 97(1):181–192, 1980.

[44] U. Frisch, Z. S. She, and O. Thual. Viscoelastic behaviour of cellular solutions to the kuramoto-sivashinsky model. *Journal of Fluid Mechanics*, 168:221–240, 1986.

[45] W. K. George. The decay of homogeneous isotropic turbulence. *Physics of Fluids A: Fluid Dynamics*, 4(7):1492–1509, 1992.

[46] A. Gires, J. Jose, I. Tchiguirinskaia, and D. Schertzer. Combined high-resolution rainfall and wind data collected for 3 months on a wind farm 110 km southeast of paris (france). *Earth System Science Data*, 14(8):3807–3819, 2022.

[47] H. Grant, A. Moilliet, and R. Stewart. A spectrum of turbulence at very high reynolds number. *Nature*, 184(4689):808–810, 1959.

[48] B.-J. Gréa, J. Griffond, and A. Burlot. The effects of variable viscosity on the decay of homogeneous isotropic turbulence. *Physics of Fluids*, 26(3):035104, 2014.

[49] V. K. Gupta and E. C. Waymire. A statistical analysis of mesoscale rainfall as a random cascade. *Journal of Applied Meteorology and Climatology*, 32(2): 251–267, 1993.

[50] A. Gurvich and A. Yaglom. Breakdown of eddies and probability distributions for small-scale turbulence. *The Physics of Fluids*, 10(9):S59–S65, 1967.

[51] E. Hairer, C. Lubich, and G. Wanner. Structure-preserving algorithms for ordinary differential equations. *Geometric numerical integration*, 31, 2006.

[52] F. Hausdorff. Dimension und äußeres maß. *Mathematische Annalen*, 79(1): 157–179, 1918.

[53] F. Hausdorff. Der wertvorrat einer bilinearform. *Mathematische Zeitschrift*, 3 (1):314–316, 1919.

[54] J. Herring, D. Schertzer, M. Lesieur, G. Newman, J. Chollet, and M. Larcheveque. A comparative assessment of spectral closures as applied to passive scalar diffusion. *Journal of Fluid Mechanics*, 124:411–437, 1982.

[55] F. Hvelplund. Renewable energy and the need for local energy markets. *Energy*, 31(13):2293–2302, 2006.

[56] S. Kida, R. H. Kraichnan, R. Rogallo, F. Waleffe, and Y. Zhou. Triad interactions in the dissipation range. *Stanford Univ., Studying Turbulence Using Numerical Simulation Databases. 4: Proceedings of the 1992 Summer Program*, 1992.

[57] A. N. Kolmogorov. On degeneration (decay) of isotropic turbulence in an incompressible viscous liquid. In *Dokl. Akad. Nauk SSSR*, volume 31, pages 538–540, 1941.

[58] A. N. Kolmogorov. The local structure of turbulence in incompressible viscous fluid for very large reynolds numbers. *Cr Acad. Sci. URSS*, 30:301–305, 1941.

[59] A. N. Kolmogorov. A refinement of previous hypotheses concerning the local structure of turbulence in a viscous incompressible fluid at high reynolds number. *Journal of Fluid Mechanics*, 13(1):82–85, 1962.

[60] R. H. Kraichnan. Irreversible statistical mechanics of incompressible hydromagnetic turbulence. *Physical Review*, 109(5):1407, 1958.

[61] R. H. Kraichnan. Inertial-range transfer in two-and three-dimensional turbulence. *Journal of Fluid Mechanics*, 47(3):525–535, 1971.

[62] R. H. Kraichnan. Convection of a passive scalar by a quasi-uniform random straining field. *Journal of fluid mechanics*, 64(4):737–762, 1974.

[63] R. H. Kraichnan. Eddy viscosity in two and three dimensions. *Journal of Atmospheric Sciences*, 33(8):1521–1536, 1976.

[64] P.-Å. Krogstad and P. Davidson. Is grid turbulence saffman turbulence? *Journal of Fluid Mechanics*, 642:373–394, 2010.

[65] J. A. Krommes. Fundamental statistical descriptions of plasma turbulence in magnetic fields. *Physics Reports*, 360(1-4):1–352, 2002.

[66] W. Kutta. Beitrag zur naherungsweisen integration totaler differentialgleichungen. *Z. Math. Phys.*, 46:435–453, 1901.

[67] L. Landau and E. Lifschitz. Lehrbuch der theoretischen physik, band vi. *Buch, Springer-Verlag*, 1991.

[68] L. Landau and E. Lifshitz. Mechanics of fluids. *Course of Theoretical Physics*, 6, 1987.

[69] L. D. Landau and E. M. Lifshitz. *Fluid Mechanics: Landau and Lifshitz: Course of Theoretical Physics, Volume 6*, volume 6. Elsevier, 2013.

[70] D. Lavallée, S. Lovejoy, D. Schertzer, and F. Schmitt. On the determination of universal multifractal parameters in turbulence. In *Topological aspects of the dynamics of fluids and plasmas*, pages 463–478. Springer, 1992.

[71] M. Lesieur. Turbulence in fluids: stochastic and numerical modeling. *NASA STI/Recon Technical Report A*, 91:24106, 1990.

[72] M. Lesieur and O. Metais. New trends in large-eddy simulations of turbulence. *Annual review of fluid mechanics*, 28(1):45–82, 1996.

[73] M. Lesieur and S. Ossia. 3d isotropic turbulence at very high reynolds numbers: Edqnm study. *Journal of Turbulence*, 1(1):007, 2000.

[74] M. Lesieur and D. Schertzer. Amortissement autosimilaire d'une turbulence à grand nombre de reynolds. *Journal de mecanique*, 17(4):609–646, 1978.

[75] M. Lesieur and D. Schertzer. Self-similar damping of turbulence at large reynolds number. *Journal de Mecanique*, 17(4):609–646, 1978.

[76] J.-L. Lions. Quelques méthodes de résolution de problemes aux limites non linéaires. 1969.

[77] I. T. W. London, September 2018. International air transport association, montreal, canada. `https://www.iata.org`.

[78] S. Lovejoy and D. Schertzer. Generalized scale invariance in the atmosphere and fractal models of rain. *Water Resources Research*, 21(8):1233–1250, 1985.

[79] S. Lovejoy and D. Schertzer. *The weather and climate: emergent laws and multifractal cascades*. Cambridge University Press, 2018.

[80] T. S. Lundgren. Linearly forces isotropic turbulence. Technical report, MINNESOTA UNIV MINNEAPOLIS, 2003.

[81] A. A. Mailybaev and S. Thalabard. Hidden scale invariance in navier–stokes intermittency. *Philosophical Transactions of the Royal Society A*, 380(2218): 20210098, 2022.

[82] B. Mandelbrot. How long is the coast of britain? statistical self-similarity and fractional dimension. *science*, 156(3775):636–638, 1967.

[83] B. B. Mandelbrot. Possible refinement of the lognormal hypothesis concerning the distribution of energy dissipation in intermittent turbulence. In *Statistical models and turbulence*, pages 333–351. Springer, 1972.

[84] B. B. Mandelbrot. Intermittent turbulence in self-similar cascades: divergence of high moments and dimension of the carrier. *Journal of fluid Mechanics*, 62 (2):331–358, 1974.

[85] B. B. Mandelbrot and B. B. Mandelbrot. *The fractal geometry of nature*, volume 1. WH freeman New York, 1982.

[86] J. F. Manwell, J. G. McGowan, and A. L. Rogers. *Wind energy explained: theory, design and application*. John Wiley & Sons, 2010.

[87] C. Meneveau. Big wind power: seven questions for turbulence research. *Journal of Turbulence*, 20(1):2–20, 2019.

[88] O. Métais and M. Lesieur. Statistical predictability of decaying turbulence. *Journal of the atmospheric sciences*, 43(9):857–870, 1986.

[89] M. Millionshchikov. On the theory of homogeneous isotropic turbulence. In *Dokl. Akad. Nauk SSSR*, volume 32, pages 611–614, 1941.

[90] M. Millionshtchikov. On the role of the third moments in isotropic turbulence. *CR Acad. Sci. SSSR*, 32:619, 1941.

[91] C. Morize and F. Moisy. Energy decay of rotating turbulence with confinement effects. *Physics of Fluids*, 18(6):065107, 2006.

[92] C. Navier. Mémoire sur les lois du mouvement des fluides. *Mémoires de l'Académie Royale des Sciences de l'Institut de France*, 6(1823):389–440, 1823.

[93] M. Nelkin. Scaling theory of hydrodynamic turbulence. *Physical Review A*, 11 (5):1737, 1975.

[94] E. Novikov and R. Stewart. The intermittency of turbulence and the spectrum of energy dissipation fluctuations. *Izv. Geophys. Ser*, 3:408–413, 1964.

[95] A. Obukhov. On the distribution of energy in the spectrum of turbulent flow. *Bull. Acad. Sci. USSR, Geog. Geophys.*, 5:453–466, 1941.

[96] K. Ohkitani and S. Kida. Triad interactions in a forced turbulence. *Physics of Fluids A: Fluid Dynamics*, 4(4):794–802, 1992.

[97] S. Orszag, R. Balian, and J. Peube. Statistical theory of turbulence in fluid dynamics 1973 les houches summer school of theoretical physics, 1977.

[98] S. A. Orszag. Analytical theories of turbulence. *Journal of Fluid Mechanics*, 41(2):363–386, 1970.

[99] S. Ossia and M. Lesieur. Energy backscatter in large-eddy simulations of three-dimensional incompressible isotropic turbulence. *Journal of Turbulence*, 1(1): 010, 2000.

[100] G. Parisi and U. Frisch. On the singularity spectrum of fully developed turbulence (1985) turbulence and predictability in geophysical fluid dynamics. *Proceedings of the International Summer School in Physics Enrico Fermi*, pages 84–87.

[101] D. Pisarenko, L. Biferale, D. Courvoisier, U. Frisch, and M. Vergassola. Further results on multifractality in shell models. *Physics of Fluids A: Fluid Dynamics*, 5(10):2533–2538, 1993.

[102] S. B. Pope and S. B. Pope. *Turbulent flows*. Cambridge university press, 2000.

[103] I. Proudman and W. H. Reid. On the decay of a normally distributed and homogenous turbulent velocity field. *Philosophical Transactions of the Royal*

Society of London. Series A, Mathematical and Physical Sciences, 247(926): 163–189, 1954.

[104] O. Reynolds. Xxix. an experimental investigation of the circumstances which determine whether the motion of water shall be direct or sinuous, and of the law of resistance in parallel channels. *Philosophical Transactions of the Royal society of London*, (174):935–982, 1883.

[105] L. Richardson. Weather prediction by numerical processes, cambridge univ. *P., London*, 1922.

[106] L. F. Richardson. Atmospheric diffusion shown on a distance-neighbour graph. *Proceedings of the Royal Society of London. Series A, Containing Papers of a Mathematical and Physical Character*, 110(756):709–737, 1926.

[107] J. C. Robinson, J. L. Rodrigo, and W. Sadowski. *The three-dimensional Navier–Stokes equations: Classical theory*, volume 157. Cambridge university press, 2016.

[108] C. Rosales and C. Meneveau. Linear forcing in numerical simulations of isotropic turbulence: Physical space implementations and convergence properties. *Physics of fluids*, 17(9):095106, 2005.

[109] C. Runge. Über die numerische auflösung von differentialgleichungen. *Mathematische Annalen*, 46(2):167–178, 1895.

[110] S. G. Saddoughi and S. V. Veeravalli. Local isotropy in turbulent boundary layers at high reynolds number. *Journal of Fluid Mechanics*, 268:333–372, 1994.

[111] P. Saffman. The large-scale structure of homogeneous turbulence. *Journal of Fluid Mechanics*, 27(3):581–593, 1967.

[112] P. Sagaut and C. Cambon. *Homogeneous turbulence dynamics*, volume 10. Springer, 2008.

[113] D. Schertzer. Comportements auto-similaires en turbulence homogene et isotrope. 1980.

[114] D. Schertzer and S. Lovejoy. The dimension and intermittency of atmospheric dynamics. In *Turbulent Shear Flows 4*, pages 7–33. Springer, 1985.

[115] D. Schertzer and S. Lovejoy. Generalised scale invariance in turbulent phenomena. *PhysicoChemical Hydrodynamics*, 6(5-6):623–635, 1985.

[116] D. Schertzer and S. Lovejoy. Physical modeling and analysis of rain and clouds by anisotropic scaling multiplicative processes. *Journal of Geophysical Research: Atmospheres*, 92(D8):9693–9714, 1987.

[117] D. Schertzer and S. Lovejoy. Nonlinear variability in geophysics: Multifractal simulations and analysis. In *Fractals' Physical Origin and Properties*, pages 49–79. Springer, 1989.

[118] D. Schertzer and S. Lovejoy. Nonlinear variability in geophysics. *Scaling and Multifractal processes*, 1991.

[119] D. Schertzer, S. Lovejoy, and F. Schmitt. Structures in turbulence and multifractal universality. In *Small-Scale Structures in Three-Dimensional Hydrodynamic and Magnetohydrodynamic Turbulence*, pages 137–144. Springer, 1995.

[120] D. Schertzer, S. Lovejoy, F. Schmitt, Y. Chigirinskaya, and D. Marsan. Multifractal cascade dynamics and turbulent intermittency. *Fractals*, 5(03):427–471, 1997.

[121] F. Schmitt, D. La Vallee, D. Schertzer, and S. Lovejoy. Empirical determination of universal multifractal exponents in turbulent velocity fields. *Physical review letters*, 68(3):305, 1992.

[122] F. Schmitt, D. Schertzer, S. Lovejoy, and Y. Brunet. Estimation of universal multifractal indices for atmospheric turbulent velocity fields. In *Fractals in Natural Sciences*, pages 274–281. World Scientific, 1994.

[123] F. Schmitt, S. Lovejoy, and D. Schertzer. Multifractal analysis of the greenland ice-core project climate data. *Geophysical research letters*, 22(13):1689–1692, 1995.

[124] L. Sedov. Methods of similitude and dimensional analysis in mechanics, 1972.

[125] C. A. Shaffer. *A practical introduction to data structures and algorithm analysis*. Prentice Hall Upper Saddle River, NJ, 1997.

[126] B. Song, X. Zhi, M. Pan, M. Hou, C. He, and K. Fraedrich. Turbulent heat flux reconstruction in the north pacific from 1921 to 2014. *Journal of the Meteorological Society of Japan. Ser. II*, 2019.

[127] K. Sreenivasan. On the fine-scale intermittency of turbulence. *Journal of Fluid Mechanics*, 151:81–103, 1985.

[128] N. P. Sullivan, S. Mahalingam, and R. M. Kerr. Deterministic forcing of homogeneous, isotropic turbulence. *Physics of Fluids*, 6(4):1612–1614, 1994.

[129] T. Tatsumi. Theory of homogeneous turbulence. *Advances in Applied Mechanics*, 20:39–133, 1980.

[130] T. Tatsumi, S. Kida, and J. Mizushima. The multiple-scale cumulant expansion for isotropic turbulence. *Journal of Fluid Mechanics*, 85(1):97–142, 1978.

[131] G. I. Taylor. Statistical theory of turbulence-ii. *Proceedings of the Royal Society of London. Series A-Mathematical and Physical Sciences*, 151(873):444–454, 1935.

[132] G. I. Taylor and A. E. Green. Mechanism of the production of small eddies from large ones. *Proceedings of the Royal Society of London. Series A-Mathematical and Physical Sciences*, 158(895):499–521, 1937.

[133] D. Veneziano and P. Furcolo. A modified double trace moment method of multifractal analysis. *Fractals*, 7(02):181–195, 1999.

[134] F. Waleffe. The nature of triad interactions in homogeneous turbulence. *Physics of Fluids A: Fluid Dynamics*, 4(2):350–363, 1992.

[135] F. A. Waleffe. The helical decomposition and the instability assumption. *Annual Research Briefs, 1992*, 1993.

[136] P. D. Williams and M. M. Joshi. Intensification of winter transatlantic aviation turbulence in response to climate change. *Nature Climate Change*, 3(7):644–648, 2013.

[137] A. Yaglom. The influence of fluctuations in energy dissipation on the shape of turbulence characteristics in the inertial interval. In *Sov. Phys. Dokl.*, volume 11, pages 26–29, 1966.

[138] Y. Zhou. Interacting scales and energy transfer in isotropic turbulence. *Physics of Fluids A: Fluid Dynamics*, 5(10):2511–2524, 1993.

[139] Y. Zhou. Turbulence theories and statistical closure approaches. *Physics Reports*, 935:1–117, 2021.